

Plastic Deformation and Ductile Fracture of 2024-T351 Aluminum under Various  
Loading Conditions

Dissertation

Presented in Partial Fulfillment of the Requirements for the Degree Doctor of Philosophy  
in the Graduate School of The Ohio State University

By

Jeremy Daniel Seidt, M.S.

Graduate Program in Mechanical Engineering

The Ohio State University

2010

Dissertation Committee:

Amos Gilat, Advisor

Mark E. Walter

Brian Harper

Mo-How Herman Shen

Copyright by  
Jeremy Daniel Seidt  
2010

## Abstract

The plastic deformation and ductile fracture behavior of 12.7 mm thick 2024-T351 aluminum plate is investigated. Tension, compression and shear experiments are conducted at strain rates ranging from  $10^{-4} \text{ s}^{-1}$  to  $5000 \text{ s}^{-1}$  and temperatures ranging from  $-50 \text{ }^{\circ}\text{C}$  to  $450 \text{ }^{\circ}\text{C}$ . Anisotropy in the plate is studied by conducting tension and compression tests on specimens oriented in multiple directions within the plate. An anisotropic plasticity model is used in numerical simulations of select experiments. Comparison of the simulation results to the actual test data shows that the material behavior can be adequately captured in tension, compression and shear. Anisotropic plastic deformation behavior in an impacted target panel is also investigated. Numerical simulations using both a von Mises and anisotropic yield functions are compared to previously published experimental data. The choice of yield function has a dramatic effect on the predicted projectile residual velocities. Experimental impact data shows evidence of anisotropic behavior, the trends of which can be captured in simulations using the anisotropic yield function. The dependence of equivalent plastic fracture strain on the state of stress is studied through mechanical experiments on specimens with various geometries, subjected to multiple load conditions. Tension tests of plane stress (thin) specimens, axisymmetric specimens and plane strain (thick) specimens are conducted for this purpose. Combined tension – torsion, pure shear and compression – torsion tests as well as dynamic punch experiments are also used. The three dimensional digital image correlation (DIC) technique is used to determine the specimen surface strains in many of the experiments. A coupled experimental – numerical approach is used to generate fracture locus data points for the tension and punch experiments. The equivalent fracture strain dependence on three stress state parameters: stress triaxiality, Lode parameter and product triaxiality is determined. The stress triaxiality parameter alone is insufficient to describe the equivalent plastic fracture strain for all of the stress states examined. A fracture locus in the triaxiality – Lode parameter stress space is presented.

## Dedication

Dedicated to my wife, Cara, and my family.

## Acknowledgements

Many people have helped me with this research. Thanks to my wife, Cara. I would not have been able to accept this opportunity without her, and for this, I will always be grateful. Thanks to my family and friends who have all been very supportive the past several years. I would also like to acknowledge my advisor, Professor Amos Gilat. His advice has been invaluable and it has truly been a pleasure working with him. Thanks also to the members of my committee: Professors Mark Walter, Brian Harper and Herman Shen.

Thanks also to Andy Walker, Tom Matrka, Bob Lowe, Frank Jenner, Mikko Hokka, Hakan Ozaltun, Wasim Tarar, Ravi Yatnalkar and Chris Cooley. These students and post-doctoral researchers in the Mechanical Engineering Department at The Ohio State University have helped me immensely with both technical discussions regarding the research and the friendship they provided. I also sincerely appreciate Gary Gardner's assistance. He machined the majority of the test specimens and fixtures described in this document and his work was always accurate and efficient.

This research was funded by the Federal Aviation Administration. Thanks to Don Altobelli, Bill Emmerling and Chip Queitzsch who oversaw a remarkable team of researchers for this project. Thanks to Mike Pereira, Kelly Carney, Duane Revilock, Chuck Ruggeri and Brad Lerch of NASA Glenn Research Center. Thanks also to John Leach, Kapil Nandwana, Paul Dubois, Jeanne He, Steve Kan, Murat Buyuk, Tim Schmidt and Alistair Tofts.

This work was supported in part by an allocation of computing time from the Ohio Supercomputer Center (OSC).

## Vita

- 1994.....St. Charles High School, Columbus, OH
- 1999.....B.S., Aeronautical and Astronautical  
Engineering, The Ohio State University
- 1999 to 2001.....Graduate Research Associate, Department  
of Aeronautical and Astronautical  
Engineering, The Ohio State University
- 2001.....M.S., Aeronautical and Astronautical  
Engineering, The Ohio State University
- 2001 to present.....Research Scientist, Energetic Systems and  
Security Technology Group, Battelle  
Memorial Institute
- 2006 to present.....Graduate Research Associate, Department of  
Mechanical Engineering, The Ohio State  
University

## Publications

Seidt, J.D.; “Development of a Novel Vibration Based High Cycle Fatigue Test Method”, Master of Science, Aeronautical and Astronautical Engineering, The Ohio State University, 2001.

George, T.J.; Seidt, J.; Shen, M.-H.; Nicholas, T.; Cross, C.J.; “Development of a Novel Vibration-Based Fatigue Testing Methodology”, *International Journal of Fatigue*, Vol. 26, 2004, pp477-486.

Seidt, J.D., Trott, B.D., “Design of a Blast Chamber for Repeated Use”, *Proceedings of the ASME Pressure Vessels and Piping Conference (PVP2005)*, Denver, CO, 2005.

Seidt, J.D., Gilat, A., Klein, J.A., Leach, J.R., “High Strain Rate, High Temperature Constitutive and Failure Models for EOD Impact Scenarios”, *Proceedings of the 2007 SEM Annual Conference and Exposition on Experimental and Applied Mechanics*, Springfield, MA, June, 2007.

Seidt, J.D.; Gilat, A.; “Characterization of 2024-T351 Aluminum for Dynamic Loading Applications”, *Proceedings of the 11<sup>th</sup> International Congress and Exhibition on Experimental and Applied Mechanics*, Orlando, FL, June, 2008.

Schmidt, T.; Gilat, A.; Walker, A.; Seidt, J.; Tyson, J.; “3D Image Correlation Studies of Geometry and Material Property Effects during Split Hopkinson Bar Experiments”, *Proceedings of the 11<sup>th</sup> International Congress and Exhibition on Experimental and Applied Mechanics*, Orlando, FL, June, 2008.

Seidt, J.D.; Gilat, A.; “Experimental Investigation of the Failure Characteristics of 2024-T351 Aluminum”, *Proceedings of the 2009 SEM Annual Conference and Exposition on Experimental and Applied Mechanics*, Albuquerque, NM, June, 2009.

Kokkonen, J.; Kuokkala, V.-T.; Seidt, J.D.; Walker, A.; Gilat, A.; Olejnik, L.; Rosochowski, A.; “High Strain Rate Deformation Analysis of UFG Aluminum Sheet Samples”; *Proceedings of the 2009 SEM Annual Conference and Exposition on Experimental and Applied Mechanics*, Albuquerque, NM, June, 2009.

Gilat, A., Seidt, J.D., “Dynamic Punch Testing of 2024-T351 Aluminum”, *Proceedings of the 16<sup>th</sup> Biennial International conference of the APS Topical Group on Shock Compression of Condensed Matter*, Nashville, TN, June/July, 2009.

Gilat, A., Seidt, J.D., “Dynamic Punch Test”, *Proceedings of the 9<sup>th</sup> International Conference on the Mechanical and Physical Behaviour of Materials under Dynamic Loading*, Brussels, Belgium, September, 2009.

Clelland, N.L., Seidt, J.D., Daroz, L.G., McGlumphy, E.A., “Comparison of Strains for Splinted and Non-Splinted Implant Prostheses using 3D Image Correlation Photogrammetry”, *International Journal of Oral & Maxillofacial Implants*, In Press.

## Fields of Study

Major Fields: Mechanical Engineering, Experimental Mechanics, Dynamic Behavior of Materials, Computational Mechanics, Aerospace Engineering

## Table of Contents

Abstract.....	ii
Dedication.....	iii
Acknowledgements.....	iv
Vita.....	v
Table of Contents.....	vii
List of Tables.....	ix
List of Figures.....	x
Chapter 1: Introduction.....	1
Significance of the Problem.....	2
Scope and Objectives of the Research.....	5
Literature Review.....	7
Chapter 2: Methodology and Experimental Program.....	14
Plastic Deformation of 2024-T351 Aluminum.....	14
Anisotropic 2024 Aluminum Sheet and Plate under Impact Loading.....	17
Ductile Fracture of 2024-T351 Aluminum.....	17
Chapter 3: Experimental Techniques.....	27
Low Strain Rate Experiments.....	27
High Strain Rate Experiments.....	48
Impact Experiments Conducted by NASA Researchers.....	66
Digital Image Correlation (DIC).....	68
Chapter 4: Experimental Characterization and Anisotropic Modeling of the Plastic Deformation of 2024-T351 Aluminum in Tension, Compression and Shear.....	73
Experimental Data.....	73
Constitutive Modeling and Parameter Determination.....	81
Finite Element Simulations and Results.....	85
Chapter 5: The Effect of Anisotropic Strength Properties on Ballistic Impact and Penetration of 2024 Aluminum Sheet and Plate.....	94
Chapter 6: Dynamic Ductile Fracture of 2024-T351 Aluminum in Punch Experiments.....	107
Failure Mode Evolution of Disk Specimens under Dynamic Punch Loads.....	107
Finite Element Simulations and Results.....	110
Chapter 7: Fracture Locus Construction for 2024-T351 Aluminum.....	118
Tension Experiments.....	118
Combined Loading Experiments.....	122
Fracture Locus Data and Discussion.....	123
Chapter 8: Summary and Conclusions.....	128
Appendix A: Repeatability of the Experimental Data Recorded in the Plastic Deformation Test Series.....	132
Appendix B: Finite Element Meshes Used for the Tension Ductile Fracture Test Series.....	149
Appendix C: Comparison of Simulated and Experimental Data from Tension Ductile Fracture Tests.....	154
Appendix D: Additional Experimental Data for Combined Loading Experiments.....	168

Appendix E: Additional Views of the Fracture Locus for 2024-T351 Aluminum .....	172
References.....	175

## List of Tables

Table 1. Reported composition of 12.7 mm thick 2024-T351 aluminum plate.....	5
Table 2. Plastic deformation experimental program.....	16
Table 3. Ductile fracture experimental program: tensile tests conducted on plane stress test specimens.....	22
Table 4. Ductile fracture experimental program: tensile tests conducted on axisymmetric specimens.....	23
Table 5. Ductile fracture experimental program: tensile tests conducted on plane strain specimens.....	24
Table 6. Ductile fracture experimental program: pure shear (torsion) and combined loading (tension / torsion, compression / torsion) experiments conducted on thin walled tube specimens.....	25
Table 7. Ductile fracture experimental program: dynamic punch tests.....	26
Table 8. DIC extensometer gage lengths used for all tension specimen geometries.....	36
Table 9. Parameters for the anisotropic yield function for 12.7 mm thick 2024-T351 aluminum plate and 0.3 mm thick 2024-T3 aluminum sheet.....	84
Table 10. Run list of impact simulations.....	96
Table 11. Simplified Johnson Cook model parameters and other physical properties for various materials in the impact simulations.....	96

## List of Figures

Figure 1. The uncontained engine debris threat: (a) damage to a DC-9 aircraft from uncontained engine debris and subsequent fire, after [14], (b) damage to an aircraft from an uncontained turbine blade, after [15], (c) recovered debris from a fan disk failure event, after [15], (d) an uncontained fan blade experiment, after [14].	3
Figure 2. Failure modes of impacted targets, after [16].	4
Figure 3. Tension, compression and torsion specimens fabricated from 12.7 mm thick 2024-T351 aluminum plate.	15
Figure 4. Combined axial and torsional loading of a thin walled tube specimen.	19
Figure 5. Stress triaxiality and Lode parameter vs axial stress to shear stress ratio for combined axial and torsional loading of a thin walled spool specimen.	21
Figure 6. Instron 1321 bi-axial servohydraulic load frame: (a) equipped with the Lebow cell and hydraulic wedge grips, (b) equipped with the Interface cell and Inconel 718 push rods.	28
Figure 7. (a) Tension test specimen dimensions (0.762 mm thick), (b) specimen clamped in Inconel 718 attachment fixture, (c) Epsilon 3442 axial extensometer attached to specimen. (Continued)	30
Figure 8. Sample data from a servohydraulic tension experiment: (a) engineering stress and engineering strain history data, (b) engineering and true stress strain curves.	31
Figure 9. Plane stress notched specimen tension experiment: (a) specimen instrumented with a bi-axial strain gage rosette, (b) experimental data.	32
Figure 10. Maximum principal (a) and minimum principal (b) strains on the surface of a notched, plane stress tension specimen.	32
Figure 11. Experimental setup for axisymmetric and plane strain tensile tests.	33
Figure 12. Three dimensional surface features of (a) a notched axisymmetric tension specimen and (b) a notched plane strain tension specimen.	34
Figure 13. Tension specimen surface strains just prior to fracture: maximum (a) and minimum (b) principal strains of a notched axisymmetric specimen, maximum (c) and minimum (d) principal strains of a notched plane strain specimen.	34
Figure 14. Sample data from a tension test on a notched axisymmetric specimen: (a) force and strain history data, (b) force versus displacement data.	35
Figure 15. Low strain rate compression experimental setup: (a) specimen placed between inconel 615 platens, (b) push-rod and platen setup with secondary LVDT fixture.	38
Figure 16. Sample data from a servohydraulic compression experiment: (a) engineering stress and engineering strain history data, (b) engineering and true stress strain curves. (Continued)	38
Figure 17. Spool-shaped torsion specimen.	41
Figure 18. Torsion specimen and adaptors (a)-(b), specimen-adaptor assembly (c), instrumentation (d) and grip fixtures (e).	41
Figure 19. Sample data from a servohydraulic torsion experiment: (a) shear stress and shear strain history data, (b) shear and effective stress strain curves.	42
Figure 20. Surface strains on a combined loading specimen: (a) maximum principal strain, (b) minimum principal strain.	44

Figure 21. Experimental data from a combined loading experiment: (a) axial force versus displacement, (b) torque versus rotation, (c) strain versus time. (Continued) .....	44
Figure 22. Instron 1321 load frame equipped for (a) elevated temperature testing and (b) low temperature testing.....	47
Figure 23. Elevated or low temperature experiments instrumented with thermocouples: (a) tension, (b) compression, (c) torsion.....	47
Figure 24. Compression split Hopkinson bar: (a) schematic representation of a typical compression SHB apparatus, (b) compression SHB used in this research. ....	50
Figure 25. Sample data from a compression SHB experiment on 2024-T351 aluminum: (a) wave data, (b) reduced history data, (c) stress strain data. (Continued).....	51
Figure 26. Experimental setup for dynamic punch testing on a compression SHB apparatus, (a) configured for unrestricted displacement, (b) configured for restricted displacement. ....	54
Figure 27. Experimental results from an unrestricted punch test (2.39 mm punch radius): (a) split Hopkinson bar wave data, (b) reduced history data including transmitted force, relative velocity and relative displacement, (c) 1-wave and 2-wave force vs displacement data.....	55
Figure 28. Sketch of a direct-tension SHB apparatus. ....	59
Figure 29. A direct-tension SHB apparatus and a stored-torque torsion SHB apparatus. ....	59
Figure 30. Specimen attachment for a tension SHB experiment: (a) top view of a specimen instrumented with a strain gage, (b) side view of the specimen, (c) post-test photo. ....	60
Figure 31. Sample data from a tension SHB experiment on 2024-T351 aluminum: (a) wave data, (b) reduced history data, (c) stress strain data. (Continued) .....	60
Figure 32. Sketch of a stored-torque SHB apparatus. ....	64
Figure 33. Spool-shaped, thin-walled tube specimen for torsion SHB experiments: (a) drawing, (b) specimen epoxied between incident and transmitter bars, (c) post test photograph.....	65
Figure 34. Sample data from a torsion SHB experiment on 2024-T351 aluminum: (a) wave data, (b) reduced history data, (c) stress strain data. (Continued) .....	65
Figure 35. 2024 aluminum target panel, (a) showing the through holes for the 330 mm bolt circle constraint, (b) close-up view of the target panel instrumented with five strain gages, after [43]. .	67
Figure 36. Cylindrical Ti-6Al-4V projectile used to impact the 3.175 mm target panels. ....	67
Figure 37. Sketch illustrating that two cameras are necessary to resolve three dimensional features: (a) one camera, (b) two cameras, after [27]. ....	70
Figure 38: Transformations between coordinate systems for: (a) a single camera model, (b) a stereo-rig camera system, after [27].....	72
Figure 39. High speed DIC camera system.....	72
Figure 40. Stress versus strain curves from (a) tension, (b) compression and (c) torsion tests conducted over a wide range of strain rates on 2024-T351 aluminum. ....	75
Figure 41. Stress versus strain rate from tension, compression and torsion tests on 2024-T351 aluminum (a) tensile and compressive true stress values extracted at a true strain of 0.075, torsional shear stress values extracted at a shear strain of 0.13, (b) tensile and compressive true stress values extracted at a true strain of 0.15, torsional shear stress values extracted at a shear strain of 0.26. ....	76
Figure 42. Stress versus strain curves from (a) tension, (b) compression and (c) torsion tests conducted over a wide range of temperatures on 2024-T351 aluminum.....	77
Figure 43. Stress versus temperature from tension, compression and torsion tests on 2024-T351 aluminum, (a) tensile and compressive true stress values extracted at a true strain of 0.075, torsional shear stress values extracted at a shear strain of 0.13, (b) tensile and compressive true stress values extracted at a true strain of 0.15, torsional shear stress values extracted at a shear strain of 0.26. ....	78
Figure 44. True stress versus true strain curves from (a) tension and (b) compression tests conducted on specimens fabricated in several orientations of 2024-T351 aluminum plate stock. 79	79

Figure 45. Comparison of effective stress versus equivalent strain curves from tension, compression and torsion experiments. ....	80
Figure 46. Tension/compression effective stress ratio and torsion/compression effective stress ratio at two equivalent strains ( $\bar{\epsilon} = 0.15$ and $\bar{\epsilon} = 0.075$ ) .....	81
Figure 47. Comparison of yield function parameters for 12.7 mm thick 2024-T351 plate to those for 0.3 mm 2024-T3 sheet, (a) plane stress yield surfaces for 2024-T3(51) aluminum, (b) normalized yield stress versus specimen orientation angle.....	85
Figure 48. Finite element simulation geometry and setup: (a) tension simulation, (b) compression simulation and (c) torsion simulation. (Continued) .....	86
Figure 49. Cross-section finite element simulation results for: (a) a tension specimen, (b) a compression specimen, (c) a torsion specimen. Highlighted elements represent those used to extract effective stress and equivalent strain data for comparison to experiments. ....	90
Figure 50. Experimental and simulated tension stress strain curve comparison for two sets of yield criterion parameters, specimens oriented in: (a) rolled direction, (b) 45° to the rolled direction, (c) transverse to the rolled direction, (d) -45° to the rolled direction. ....	91
Figure 51. Experimental and simulated compression stress strain curve comparison for two sets of yield criterion parameters, specimens oriented in: (a) rolled direction, (b) 45° to the rolled direction, (c) transverse to the rolled direction, (d) -45° to the rolled direction, (e) plate thickness direction. (Continued).....	92
Figure 52. Experimental and simulated torsion stress strain curve comparison for two sets of yield criterion parameters. ....	93
Figure 53. Mesh used for impact simulations. ....	97
Figure 54. Experimental and numerical residual projectile velocity versus impact velocity for: (a) 3.175 mm 2024-T3 aluminum sheet targets, (b) 12.7 mm 2024-T351 aluminum plate targets. ...	98
Figure 55. Comparison of the plane stress von Mises yield function to (a) the anisotropic yield function for 2024-T3 aluminum sheet and (b) the anisotropic yield function for 2024-T351 aluminum plate. ....	100
Figure 56. Comparison of calculated strains to those measured with strain gages for (a) a 3.175 mm 2024-T3 aluminum sheet impact experiment, (b) a 12.7 mm 2024-T351 aluminum plate impact experiment.....	102
Figure 57. Comparison of calculated maximum principal strains (a) and displacements (b) to those measured using three dimensional DIC for a Ti-6Al-4V projectile impacting 3.175 mm thick 2024-T3 aluminum sheet at 205.1 m/s.....	104
Figure 58. Comparison of calculated maximum principal strains (a) and displacements (b) to those measured using three dimensional DIC for an A2 tool steel projectile impacting 12.7 mm thick 2024-T3 aluminum plate at 249.6 m/s. ....	106
Figure 59. Force versus displacement curves (a) and recovered specimens from restricted and unrestricted displacement dynamic punch experiments (2.39 mm punch radius): (b) 1.6 mm relative displacement, (c) 2.4 mm relative displacement, (d) unrestricted. ....	109
Figure 60. Force versus displacement curves (a) and recovered specimens from restricted and unrestricted displacement dynamic punch experiments (4.75 mm punch radius): (b) 2.4 mm relative displacement, (c) 3.9 mm relative displacement, (d) unrestricted. ....	110
Figure 61. Force versus displacement curve (a) and a specimen plug recovered from an unrestricted dynamic punch experiment (blunt punch): (b) rear view of plug, (c) front view (punch side) of plug, (d) plug resting on the punch. ....	110
Figure 62. Finite element model: (a) entire model assembly including the specimen, specimen adaptor fixtures and the sharp punch, (b) top view of the 2024-T351 aluminum disk specimen. ....	111
Figure 63. 2.39 mm radius punch simulation results: (a) comparison of experimental and simulated force versus displacement curves, (b) calculated stress state and equivalent plastic strain histories of an element in the region of initial crack formation. ....	113

Figure 64. 4.75 mm radius punch simulation results: (a) comparison of experimental and simulated force versus displacement curves, (b) calculated stress state and equivalent plastic strain histories of an element in the region of initial crack formation. ....	114
Figure 65. Blunt punch simulation results: (a) comparison of experimental and simulated force versus displacement curves, (b) calculated stress state and equivalent plastic strain histories of an element in the region of initial crack formation. ....	115
Figure 66. Dependence of equivalent plastic fracture strain on stress state in dynamic punch experiments: (a) stress triaxiality, $\sigma^*$ , (b) Lode parameter, $\mu$ , (c) product triaxiality, $\sigma_p^*$ . (Continued) .....	116
Figure 67. Finite element meshes for selected tension specimens: (a) plane stress, (b) axisymmetric, (c) plane strain. ....	119
Figure 68. Analysis procedure for a coupled experimental – numerical tension experiment on an axisymmetric notched specimen: (a) experimental maximum principal surface strain, (b) simulated maximum principal surface strain, (c) internal equivalent plastic strain. ....	120
Figure 69. Experimental and simulated data from an axisymmetric notched tension specimen. ....	121
Figure 70. Reduced history data from a combined tension-torsion experiment. ....	123
Figure 71. Fracture locus data for 2024-T351 aluminum, equivalent plastic fracture strain versus: (a) stress triaxiality, (b) Lode parameter, (c) product triaxiality. (Continued).....	125
Figure 72. Fracture locus for 2024-T351 aluminum in the triaxiality – Lode parameter stress space.....	127
Figure 73. Tension test data repeatability: $\dot{\epsilon} = 1 \times 10^{-4} \text{ s}^{-1}$ , room temperature, rolled direction. ...	132
Figure 74. Tension test data repeatability: $\dot{\epsilon} = 1 \times 10^{-2} \text{ s}^{-1}$ , room temperature, rolled direction. ...	133
Figure 75. Tension test data repeatability: $\dot{\epsilon} = 1.0 \text{ s}^{-1}$ , room temperature, rolled direction.....	133
Figure 76. Tension test data repeatability: $\dot{\epsilon} = 500.0 \text{ s}^{-1}$ , room temperature, rolled direction.....	134
Figure 77. Tension test data repeatability: $\dot{\epsilon} = 1850.0 \text{ s}^{-1}$ , room temperature, rolled direction....	134
Figure 78. Tension test data repeatability: $\dot{\epsilon} = 1.0 \text{ s}^{-1}$ , $T = -50 \text{ }^\circ\text{C}$ , rolled direction. ....	135
Figure 79. Tension test data repeatability: $\dot{\epsilon} = 1.0 \text{ s}^{-1}$ , $T = 150 \text{ }^\circ\text{C}$ , rolled direction. ....	135
Figure 80. Tension test data repeatability: $\dot{\epsilon} = 1.0 \text{ s}^{-1}$ , $T = 300 \text{ }^\circ\text{C}$ , rolled direction. ....	136
Figure 81. Tension test data repeatability: $\dot{\epsilon} = 1.0 \text{ s}^{-1}$ , $T = 450 \text{ }^\circ\text{C}$ , rolled direction. ....	136
Figure 82. Tension test data repeatability: $\dot{\epsilon} = 1.0 \text{ s}^{-1}$ , room temperature, transverse direction... ..	137
Figure 83. Tension test data repeatability: $\dot{\epsilon} = 1.0 \text{ s}^{-1}$ , room temperature, +/- 45° directions. ....	137
Figure 84. Compression test data repeatability: $\dot{\epsilon} = 1 \times 10^{-4} \text{ s}^{-1}$ , room temperature, rolled direction. ....	138
Figure 85. Compression test data repeatability: $\dot{\epsilon} = 1 \times 10^{-2} \text{ s}^{-1}$ , room temperature, rolled direction. ....	138
Figure 86. Compression test data repeatability: $\dot{\epsilon} = 1.0 \text{ s}^{-1}$ , room temperature, rolled direction. ....	139
Figure 87. Compression test data repeatability: $\dot{\epsilon} = 1400.0 \text{ s}^{-1}$ , room temperature, rolled direction. ....	139
Figure 88. Compression test data repeatability: $\dot{\epsilon} = 4600.0 \text{ s}^{-1}$ , room temperature, rolled direction. ....	140
Figure 89. Compression test data repeatability: $\dot{\epsilon} = 1.0 \text{ s}^{-1}$ , $T = -50 \text{ }^\circ\text{C}$ , rolled direction. ....	140
Figure 90. Compression test data repeatability: $\dot{\epsilon} = 1.0 \text{ s}^{-1}$ , $T = 150 \text{ }^\circ\text{C}$ , rolled direction. ....	141
Figure 91. Compression test data repeatability: $\dot{\epsilon} = 1.0 \text{ s}^{-1}$ , $T = 300 \text{ }^\circ\text{C}$ , rolled direction. ....	141
Figure 92. Compression test data repeatability: $\dot{\epsilon} = 1.0 \text{ s}^{-1}$ , $T = 450 \text{ }^\circ\text{C}$ , rolled direction. ....	142
Figure 93. Compression test data repeatability: $\dot{\epsilon} = 1.0 \text{ s}^{-1}$ , room temperature, transverse direction. ....	142

Figure 94. Compression test data repeatability: $\dot{\epsilon}=1.0 \text{ s}^{-1}$ , room temperature, +/- 45° direction.	143
Figure 95. Compression test data repeatability: $\dot{\epsilon}=1.0 \text{ s}^{-1}$ , room temperature, thickness direction.	143
Figure 96. Torsion test data repeatability: $\dot{\gamma}=1.732 \times 10^{-4} \text{ s}^{-1}$ , room temperature.	144
Figure 97. Torsion test data repeatability: $\dot{\gamma}=1.732 \times 10^{-2} \text{ s}^{-1}$ , room temperature.	144
Figure 98. Torsion test data repeatability: $\dot{\gamma}=1.732 \text{ s}^{-1}$ , room temperature.	145
Figure 99. Torsion test data repeatability: $\dot{\gamma}=925.0 \text{ s}^{-1}$ , room temperature.	145
Figure 100. Torsion test data repeatability: $\dot{\gamma}=5050.0 \text{ s}^{-1}$ , room temperature.	146
Figure 101. Torsion test data repeatability: $\dot{\gamma}=1.732 \text{ s}^{-1}$ , $T = -50 \text{ }^\circ\text{C}$ .	146
Figure 102. Torsion test data repeatability: $\dot{\gamma}=1.732 \text{ s}^{-1}$ , $T = 150 \text{ }^\circ\text{C}$ .	147
Figure 103. Torsion test data repeatability: $\dot{\gamma}=1.732 \text{ s}^{-1}$ , $T = 300 \text{ }^\circ\text{C}$ .	147
Figure 104. Torsion test data repeatability: $\dot{\gamma}=1.732 \text{ s}^{-1}$ , $T = 450 \text{ }^\circ\text{C}$ .	148
Figure 105. Mesh for plane stress tension specimen with a 1.984 mm radius notch.	149
Figure 106. Mesh for plane stress tension specimen with a 0.396 mm radius notch.	150
Figure 107. Mesh for axisymmetric, smooth tension specimen (section view).	150
Figure 108. Mesh for axisymmetric tension specimen with a 9.144 mm radius notch (section view).	151
Figure 109. Mesh for axisymmetric tension specimen with a 6.096 mm radius notch (section view).	151
Figure 110. Mesh for axisymmetric tension specimen with a 4.470 mm radius notch (section view).	152
Figure 111. Mesh for axisymmetric tension specimen with a 3.048 mm radius notch (section view).	152
Figure 112. Mesh for plane strain tension specimen with a smooth gage section.	153
Figure 113. Mesh for plane strain tension specimen with a 4.763 mm radius notch.	153
Figure 114. Comparison of specimen surface strains, plane stress specimen with smooth gage section: (a) DIC max. principal strain, (b) simulation max. principal strain, (c) DIC min. principal strain, (d) simulation min. principal strain.	155
Figure 115. Experimental and simulated data for a plane stress specimen with a smooth gage section.	155
Figure 116. Comparison of specimen surface strains, plane stress specimen with 4.763 mm radius notch: (a) DIC max. principal strain, (b) simulation max. principal strain, (c) DIC min. principal strain, (d) simulation min. principal strain.	156
Figure 117. Experimental and simulated data for a plane stress specimen with a 4.763 mm radius notch.	156
Figure 118. Comparison of specimen surface strains, plane stress specimen with 1.984 mm radius notch: (a) DIC max. principal strain, (b) simulation max. principal strain, (c) DIC min. principal strain, (d) simulation min. principal strain.	157
Figure 119. Experimental and simulated data for a plane stress specimen with a 1.984 mm radius notch.	157
Figure 120. Comparison of specimen surface strains, plane stress specimen with 0.396 mm radius notch: (a) DIC max. principal strain, (b) simulation max. principal strain, (c) DIC min. principal strain, (d) simulation min. principal strain.	158
Figure 121. Experimental and simulated data for a plane stress specimen with a 0.396 mm radius notch.	158

Figure 122. Comparison of specimen surface strains, axisymmetric specimen with a smooth gage section: (a) DIC max. principal strain, (b) simulation max. principal strain, (c) DIC min. principal strain, (d) simulation min. principal strain.....	159
Figure 123. Experimental and simulated data for an axisymmetric specimen with a smooth gage section.....	159
Figure 124. Comparison of specimen surface strains, axisymmetric specimen with a 14.503 mm radius notch: (a) DIC max. principal strain, (b) simulation max. principal strain, (c) DIC min. principal strain, (d) simulation min. principal strain.....	160
Figure 125. Experimental and simulated data for an axisymmetric specimen with a 14.503 mm radius notch.....	160
Figure 126. Comparison of specimen surface strains, axisymmetric specimen with a 9.144 mm radius notch: (a) DIC max. principal strain, (b) simulation max. principal strain, (c) DIC min. principal strain, (d) simulation min. principal strain.....	161
Figure 127. Experimental and simulated data for an axisymmetric specimen with a 9.144 mm radius notch.....	161
Figure 128. Comparison of specimen surface strains, axisymmetric specimen with a 6.096 mm radius notch: (a) DIC max. principal strain, (b) simulation max. principal strain, (c) DIC min. principal strain, (d) simulation min. principal strain.....	162
Figure 129. Experimental and simulated data for an axisymmetric specimen with a 6.096 mm radius notch.....	162
Figure 130. Comparison of specimen surface strains, axisymmetric specimen with a 4.470 mm radius notch: (a) DIC max. principal strain, (b) simulation max. principal strain, (c) DIC min. principal strain, (d) simulation min. principal strain.....	163
Figure 131. Experimental and simulated data for an axisymmetric specimen with a 4.470 mm radius notch.....	163
Figure 132. Comparison of specimen surface strains, axisymmetric specimen with a 3.048 mm radius notch: (a) DIC max. principal strain, (b) simulation max. principal strain, (c) DIC min. principal strain, (d) simulation min. principal strain.....	164
Figure 133. Experimental and simulated data for an axisymmetric specimen with a 3.048 mm radius notch.....	164
Figure 134. Comparison of specimen surface strains, plain strain specimen with a smooth gage section: (a) DIC max. principal strain, (b) simulation max. principal strain, (c) DIC min. principal strain, (d) simulation min. principal strain.....	165
Figure 135. Experimental and simulated data for a plane strain specimen with a smooth gage section.....	165
Figure 136. Comparison of specimen surface strains, plane strain specimen with 13.97 mm radius notch: (a) DIC max. principal strain, (b) simulation max. principal strain, (c) DIC min. principal strain, (d) simulation min. principal strain.....	166
Figure 137. Experimental and simulated data for a plane strain specimen with a 13.970 mm radius notch.....	166
Figure 138. Comparison of specimen surface strains, plane strain specimen with 4.763 mm radius notch: (a) DIC max. principal strain, (b) simulation max. principal strain, (c) DIC min. principal strain, (d) simulation min. principal strain.....	167
Figure 139. Experimental and simulated data for a plane strain specimen with a 4.763 mm radius notch.....	167
Figure 140. Surface strains on a combined tension – torsion specimen, $\frac{\sigma_x}{\tau_{xy}} = 0.868$ : (a) max. principal strain, (b) min. principal strain.....	168

Figure 141. Combined loading experimental data, $\frac{\sigma_x}{\tau_{xy}} = 0.868$ .....	169
Figure 142. Surface strains on a pure shear (torsion) specimen, $\frac{\sigma_x}{\tau_{xy}} = 0.0$ : (a) max. principal strain, (b) min. principal strain.....	169
Figure 143. Pure shear (torsion) experimental data, $\frac{\sigma_x}{\tau_{xy}} = 0.0$ .....	170
Figure 144. Surface strains on a combined compression – torsion specimen, $\frac{\sigma_x}{\tau_{xy}} = -0.868$ : (a) max. principal strain, (b) min. principal strain.....	170
Figure 145. Combined loading experimental data, $\frac{\sigma_x}{\tau_{xy}} = -0.868$ .....	171
Figure 146. Fracture locus for 2024-T351 aluminum, top view. ....	172
Figure 147. Fracture locus for 2024-T351 aluminum, 3D view #1. ....	173
Figure 148. Fracture locus for 2024-T351 aluminum, 3D view #2. ....	173
Figure 149. Fracture locus for 2024-T351 aluminum, side view #1.....	174
Figure 150. Fracture locus for 2024-T351 aluminum, side view #2.....	174

## Chapter 1: Introduction

As the field of computational mechanics has matured, many numerical codes have been developed that can accurately predict the mechanical response of complex physical phenomena. These include commercial codes such as LS-DYNA [1], ABAQUS [2], and AUTODYN [3] as well as government codes such as ALE3D [4] and CTH [5]. These codes have allowed analysts and researchers to gain valuable insight into their applications. The results from simulations, however, are heavily dependent on the material models used. These material models are usually application-specific. Simple, static applications that incur small strains can be modeled adequately with a simple linear elasticity model. If the application is complex and includes plastic deformation at high strain rates and elevated temperatures as well as fracture, more complex material models must be used in order to have any confidence in the numerical result.

The Johnson-Cook plasticity and fracture models [6,7] are phenomenological material models commonly used to simulate impact and penetration. The constitutive model defines the effective material flow stress as:

$$\bar{\sigma} = \left[ A + B(\bar{\epsilon}^p)^n \right] \left[ 1 + C \ln \left( \frac{\dot{\bar{\epsilon}}}{\dot{\bar{\epsilon}}_0} \right) \right] \left[ 1 - \left( \frac{T - T_r}{T_m - T_r} \right)^m \right] , \quad (1.1)$$

where,  $\bar{\epsilon}^p$  is the equivalent plastic strain,  $\dot{\bar{\epsilon}}_0$  is the reference strain rate (typically  $1.0 \text{ s}^{-1}$ ),  $T$  is the material temperature,  $T_r$  is the reference temperature (typically room temperature),  $T_m$  is the melt temperature, and  $A$ ,  $B$ ,  $n$ ,  $C$ , and  $m$  are model parameters. These parameters are typically determined from tension, compression or shear mechanical experiments over a wide range of strain rates and temperatures.

The fracture model defines a damage parameter for each element in a given simulation. This parameter ranges from zero, for pristine material, to unity for fractured material. The parameter is defined as:

$$D = \sum \frac{\Delta \bar{\epsilon}^p}{\bar{\epsilon}_f^p} , \quad (1.2)$$

or, the sum of the ratio of equivalent plastic strain increment ( $\Delta\bar{\epsilon}^p$ ) to the equivalent fracture strain ( $\bar{\epsilon}_f^p$ ) for each numerical integration cycle. Johnson and Cook model the equivalent plastic fracture strain as,

$$\bar{\epsilon}_f^p = \left[ D_1 + D_2 e^{-D_3 \sigma^*} \right] \left[ 1 + D_4 \ln \left( \frac{\dot{\bar{\epsilon}}}{\dot{\bar{\epsilon}}_0} \right) \right] \left[ 1 + D_5 \left( \frac{T - T_r}{T_m - T_r} \right) \right] \quad , \quad (1.3)$$

where,  $\sigma^*$  is a stress state parameter known as the triaxiality, and  $D_1, D_2, D_3, D_4$  and  $D_5$  are model parameters. These parameters are typically determined from mechanical experiments on notched and smooth axisymmetric specimens at several strain rates and temperatures.

Several other models have also been proposed for dynamic loading applications, including plasticity models introduced by Steinberg, Cochran and Guinan [8] and dislocation motion based plastic deformation models proposed by Zerilli and Armstrong [9] and Follansbee and Kocks [10]. Additionally, void nucleation and growth fracture models have been proposed by Gurson [11], Tvergaard [12] and Horstemeyer and Gokhale [13]. All of these models, whether phenomenological or physics-based, require experimental data for parameter calibration. Since results from numerical simulations are dependent on the material models, they are also dependent on the experimental data used to calibrate these models. Therefore, there is an ongoing need for high quality experimental data at the strain rates, temperatures and stress states present in the eventual application of interest.

### Significance of the Problem

The Federal Aviation Administration's (FAA) Uncontained Engine Debris Mitigation Program is interested in the behavior of 2024-T351 aluminum since it is a common component in aircraft structures. As illustrated in Figure 1, uncontained engine debris can pose a significant threat to the safety of passengers and crew aboard commercial transport aircraft. Figure 1 (a) shows damage to a DC-9 aircraft after a fire caused by uncontained engine debris [14], while Figure 1 (b) presents the damage to an aircraft from an uncontained turbine blade [15]. Recovered debris from a failed fan disk is presented in Figure 1 (c) [15]. A full-scale uncontained fan disk experiment is shown in Figure 1 (d) [14].

The Federal Aviation Regulation FAR/JAR 25.903(d)(1) addresses the safety hazards related to an engine rotor failure and states that design precautions must be implemented to minimize and

mitigate these hazards [15]. Frankenberger [15] illustrates that these precautions can be implemented in the following ways:

1. Minimizing the frequency of uncontained disc events.
2. Decreasing the hazard to safe flight by minimizing the quantity of and the energy of the fragments as well as precautions that cause fragment trajectories that are less harmful to the aircraft structure.
3. Mitigating the hazard to safe flight through structure designs that can safely contain uncontained disk debris.

Each aircraft engine in operation must be certified for use because of the significant threat this problem poses. The certification process involves full-scale experiments on real aircraft engines, such as the experiment shown in Figure 1 (d). These experiments are both difficult to conduct and extremely expensive. This, coupled with the maturity of the field of computational mechanics, provides motivation to supplement experimental data with numerical simulations.



Figure 1. The uncontained engine debris threat: (a) damage to a DC-9 aircraft from uncontained engine debris and subsequent fire, after [14], (b) damage to an aircraft from an uncontained turbine blade, after [15], (c) recovered debris from a fan disk failure event, after [15], (d) an uncontained fan blade experiment, after [14].

The results of uncontained engine debris failures can be catastrophic in loss of human life; therefore, the supplemental simulations used to design hazard mitigation must be accurate. The scenario is an impact and penetration one by nature, as engine debris fragments are ejected at high velocities radially from the centerline of the engine. The engine debris threat, shown in Figure 1 (c), is diverse in both geometry and impact velocity. Accurate simulations of these events must be able to capture the failure modes of impacted targets. Figure 2, adapted from Zukas, et al. [16] illustrates common impact failure modes. In order to capture these phenomena, material models that accurately describe the plastic deformation as well as the damage accumulation and fracture behavior of the target are necessary. Therefore, the availability of experimental data at the strain rates, temperatures and stress states present in the application is critical.

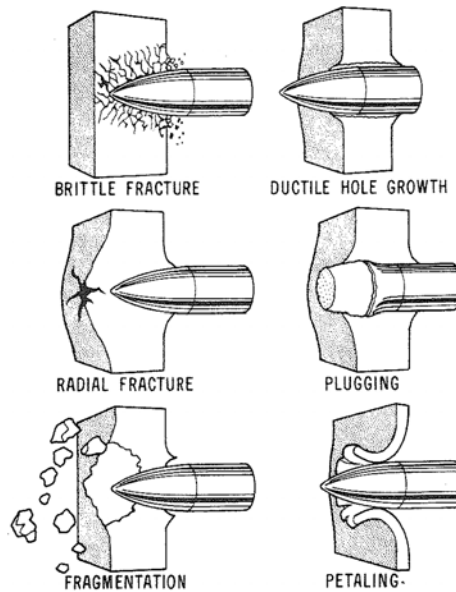


Figure 2. Failure modes of impacted targets, after [16].

The material models used to simulate uncontained engine debris events can also be used in simulations of several other applications. Military scenarios include response of structures to blast [17], vehicle and personnel armor design [18,19], explosive ordnance disposal (EOD) [20,21] and design of more lethal weapons such as shaped charge jets and explosively formed projectiles [22,23]. Industrial applications include metal forming [24] and automotive crash-worthiness [25]. In addition, the National Aeronautics and Space Administration (NASA) utilized numerical simulations of foam impacting the leading edge of the space shuttle wing in the Return to Flight program after the Columbia disaster [26]. As more engineering materials are

developed and numerical simulations of engineering applications are more commonly used, there will be an increasing need for accurate material models and hence, experimental data.

### Scope and Objectives of the Research

The objective of this research is to devise and execute an experimental program for the purposes of developing constitutive and ductile fracture models for 12.7 mm thick 2024-T351 aluminum plate. The plates studied in this research are produced by Kaiser Aluminum and the reported chemical composition is presented in Table 1. The compiled data from this experimental program is the most comprehensive collection of mechanical property data from a single stock of 2024 aluminum. Material models developed from these data will be used in numerical simulations supporting the FAA’s Uncontained Engine Debris Mitigation Program.

Table 1. Reported composition of 12.7 mm thick 2024-T351 aluminum plate.

Plate Stock		Chemistry									
Alloy / Treatment	Thickness (mm)	Si	Fe	Cu	Mn	Mg	Cr	Zn	Ti	V	Zr
2024-T351	12.70	0.08	0.22	4.47	0.59	1.37	0.01	0.18	0.02	0.01	0.01

The first phase of the experimental program is devised to determine the strain rate and temperature dependence on the plastic deformation behavior of the material. Tension, compression and shear (torsion) experiments at strain rates ranging from  $1.0 \times 10^{-4} \text{ s}^{-1}$  to  $5.0 \times 10^3 \text{ s}^{-1}$  and temperatures ranging from  $-50 \text{ }^\circ\text{C}$  to  $450 \text{ }^\circ\text{C}$  are conducted. Directional strength characteristics within the plate are also studied. Tension and compression experiments of specimens oriented in several different directions relative to the plate’s rolling axis are necessary to determine the anisotropic strength characteristics of the plate.

Another objective of this research is to explore the effect of anisotropic strength properties in a 2024 aluminum target panel impacted by a ballistic projectile. Answers to the following questions are sought:

- (a) Are there any experimental data that suggest anisotropic deformation in impacted 2024 aluminum target panels?
- (b) If so, can the anisotropic deformation be simulated numerically with an anisotropic plasticity model?
- (c) What is the variance between a simulation that employs an anisotropic yield function and one employing a von Mises yield function? How do the simulated impact versus residual velocity data generated using the two yield functions compare?

The results of this study will help numerical analysts studying the impact problem decide whether the results from the anisotropic model warrant the additional experimental effort required to determine anisotropic model parameters.

The second phase of the experimental program is proposed to study the ductile fracture behavior of the material. The program is designed specifically to study the effect of stress state on the equivalent plastic fracture strain of the material. The goal is to generate a fracture locus for 12.7 mm thick 2024-T351 aluminum from several different mechanical experiments. These experiments include tension tests on specimens with several different geometries, pure shear tests (torsion) and combined loading (tension-torsion or compression-torsion) tests. Three dimensional digital image correlation (DIC) [27] is used to measure the full-field displacements and calculate strains in many of these experiments. This measurement technique has a substantial advantage over traditional measurement techniques, such as the use of strain gages and extensometers, since deformation gradients and strains in localizations (such as necking and shear bands) can be resolved. These full-field surface strains can be directly compared to results from numerical simulations, making detailed critiques of the constitutive and fracture models more practical. For experiments with complex specimen geometries, a coupled experimental-numerical technique is used to determine the state of stress at the fracture initiation site. The technique consists of comparing results from a parallel numerical simulation to the experimental data. Simulation results are used to provide equivalent plastic fracture strain and stress state histories at the fracture initiation site.

Dynamic punch experiments are also used in the ductile fracture experimental program. These tests utilize the compression Kolsky or split Hopkinson bar (SHB) apparatus with varying punch geometry to alter the stress state in the specimen. A stop-ring is used to limit the punch displacement relative to the specimen to study the evolution of the specimen impact failure mode with displacement. The experimental-numerical technique described above is used to generate fracture locus data points for these experiments.

## Literature Review

### Plastic Deformation of 2024 Aluminum

Several authors have studied the strain rate sensitivity of 2024 aluminum. Li, et al. [28], presented the rate sensitivity of 2024 aluminum under uniaxial compression. They found that the alloy had minimal rate sensitivity at room temperature, a 3% to 8% increase in flow stress from  $10^{-3} \text{ s}^{-1}$  to  $3.5 \times 10^3 \text{ s}^{-1}$ . Hodowany, et al. [29], discussed the conversion of plastic work into heat and stored energy in 2024-T3 aluminum over a wide range of strain rates. Their work showed negligible strain rate sensitivity, in uniaxial compression, over the range of strain rates:  $10^{-3} \text{ s}^{-1}$  to  $3.0 \times 10^3 \text{ s}^{-1}$ . Johnson, et al. [30], presented data from torsion tests on 2024-T351 aluminum over a wide range of strain rates. A custom pneumatic torsional load frame was used to study the material over shear strain rates of  $8.0 \times 10^3 \text{ s}^{-1}$  to  $123 \text{ s}^{-1}$ . Johnson stated that the strain rate dependence of 2024-T351 aluminum is insignificant. Lesuer [31] presented high strain rate data from tension and compression experiments on specimens fabricated from 4 mm thick 2024-T3 aluminum plate. Data from compression experiments on specimens oriented in the rolled, transverse and thickness directions of the plate at a strain rate of  $4.0 \times 10^3 \text{ s}^{-1}$  was shown. Tension data at a strain rate of  $8.0 \times 10^3 \text{ s}^{-1}$  from specimens oriented in the rolled and transverse directions of the plate were also presented. Lesuer combined these data with data from other sources, including the torsion experiments conducted by Johnson, et al. [30], to cover a strain rate range of  $10^{-3} \text{ s}^{-1}$  to  $8.0 \times 10^3 \text{ s}^{-1}$ . Analyzing the compiled data set, Lesuer concluded that the material has minor strain rate dependence. There is, however, some uncertainty in this conclusion, since multiple data sets and hence multiple material stocks were tested in various loading modes (tension, compression and torsion).

Elevated temperature data from tensile experiments on 2024-T3 aluminum presented by Zhao and Lampman [32] demonstrated that as temperature increases, the ductility increases and the strength decreases. These phenomena arise due to dynamic recovery and recrystallization, which occur at high temperatures and reduce the room temperature restrictions on grain mobility, resulting in deformation at significantly lower stresses. Elevated temperature tension compression and shear data from the same stock of 2024 aluminum are unavailable in the current literature.

Anisotropic strength behavior in 2024-T3 aluminum has been reported by many authors. Barlat, et al. [33], reported strongly anisotropic behavior in 0.30 mm thick 2024-T3 sheet.

Tension specimens were fabricated in seven different directions relative to the rolled direction of the sheet (0°, 15°, 30°, 45°, 60°, 75° and 90°). These data show that the strength of the sheet decreased by as much as 15 % at angles larger than 45° to the rolled direction. Barlat, et al., also developed a widely used six-component yield function that can capture the typical anisotropic strength that exists in sheet metals. Gilmour, et al. published two papers on the anisotropic plastic behavior of 1.27 mm thick 2024-T3 aluminum [24,34]. In the first paper [24], experimental data were presented from tensile tests on specimens cut from the sheet in seven orientations, equivalent to those used by Barlat, et al. Additionally, the researchers conducted a hydraulic bulge test to acquire a biaxial effective stress versus equivalent strain curve. The tensile experiments showed similar strength reductions in the 45° and 90° orientations to those reported by Barlat, et al. The biaxial yield stress is identical to the rolled-direction tensile yield stress. The tensile stress strain curves show no evidence of directional dependence on strain hardening behavior. The second paper [34] focused on the in-plane shear behavior of 1.27 mm thick 2024-T3 aluminum sheet. Shear stress versus shear strain curves from samples oriented in the same seven orientations discussed above and tested in a custom designed shear fixture were presented. The data demonstrated that the in-plane shear strength is weaker in the 0° orientation than in the 45° direction. The shear strength in the 90° orientation was slightly stronger than the 0° orientation. The dependence of strain hardening on specimen orientation was also negligible in shear. The authors also reported shear yield stresses roughly half the magnitude of the yield stress in uniaxial tension. As discussed above, Lesuer presented high strain rate compression and tension experiments on specimens fabricated in various directions from 4 mm thick 2024-T3 aluminum plate [31]. Lesuer reported only small deviations between stress strain curves in three directions (0°, 90° and normal) in compression. In tension, he reported negligible variation between stress strain curves from specimens oriented 0° and 90° to the plate rolling direction. He concluded from these results that the plate can be considered isotropic. Some authors, however, have reported experimental results where the yield stresses are equivalent in the rolled and transverse directions, but still exhibit anisotropic behavior [35]. This information, coupled with the lack of additional in-plane experimental data, means that Lesuer's aluminum plate could indeed be anisotropic.

#### Effect of Anisotropic Behavior in Impacted Target Panels

Most research concerning anisotropic strength behavior of impacted targets has focused on composite structures. Hammond, et al. [36] experimentally studied the response of carbon fiber-

reinforced polymer targets subjected to normal impacts with steel spheres fired at 460 m/s. The researchers shot both quasi-isotropic and uni-directional lay-ups of the composite structure and found that the uni-directional layup showed anisotropic deformation behavior (favoring the direction perpendicular to the reinforcing fibers). Chen, Allahdadi and Carney [37] used the smoothed particle hydrodynamics numerical technique to simulate high velocity impact of steel cubes into graphite/epoxy composite laminates. An anisotropic elasto-plastic constitutive model was used to generate simulated damage profiles that agreed reasonably well with experiments. Rossikhin and Shitikova [38], motivated by the common occurrence of impact with composite structures, analytically studied low velocity impact of elastic rods into transversely isotropic target plates. Radchenko, et al. [39] used an anisotropic model implemented in a finite element code to investigate the effect of anisotropy of glass reinforced plastics under impact.

The effect of anisotropy in tantalum [40, 41] and zirconium [41] in Taylor cylinder impact experiments has been investigated. Kothari and Anand [40] presented constitutive equations for Tantalum that captures both initial and evolving anisotropy. They used their model to simulate Taylor impact experiments and found good agreement between the model-predicted deformed profiles and those measured experimentally. Plunket, et al. used an anisotropic elastic-viscoplastic constitutive model to simulate Taylor impact tests for both zirconium and tantalum. The authors reported very good agreement between the simulated and experimentally measured post-test deformation profiles. Both of these papers, however, focused on anisotropic behavior of the projectile, not an impacted target.

Grytten, et al. [42], conducted low velocity (3.5 – 15.8 m/s) impact experiments of a tethered, instrumented projectile with replaceable, hardened steel noses into 5083-H116 aluminum plates of varying thickness. The authors used a modified version of the Johnson Cook constitutive model for the target plates which includes an anisotropic yield function, among other upgrades, to simulate their experiments. The authors reported that the effect of anisotropy on the contact force versus time and the impact axis deflection profile in several locations was minimal.

Pereira, Revilock and Ruggeri [43] presented data from impact experiments on 6.35 and 12.7 mm thick 2024-T351 aluminum plate and 3.175 mm thick 2024-T3 sheet target panels. The authors used Ti-6Al-4V projectiles to impact the sheet target panels, while A2 tool steel projectiles were used for the plate targets. Quantitative data from strain gages and three dimensional DIC were acquired in the experiments. Numerical simulations of the 12.7 mm thick target panel impact cases using both a von Mises and an anisotropic yield function were presented by Nandwana [44]. Nandwana found little evidence of anisotropy in the simulated panel rear

surface strains. He did, however, find large variances between the projectile residual velocities predicted using the two yield functions.

### Ductile Fracture of 2024-T351 Aluminum

Most damage evolution and fracture models implemented for ductile metals are based on theories of microscopic void nucleation, growth and eventual coalescence. Dodd and Bai [45] provided an interesting overview and history of the theories. McClintock [46] developed a fracture criterion based on the growth of initially cylindrical holes for viscous and plastic materials. Among other findings, McClintock noted that the fracture strain is dependent on the entire state of stress rather than simply the maximum principal stress. He also concluded that the ductility is dependent on the stress and strain history. Rice and Tracey [47] developed a model to analyze the growth of a single spherical void in a rigid-plastic body. The authors found that the dilatational amplification factor of the void increases exponentially with the far-field mean stress, or  $\sigma_m = \frac{1}{3}\sigma_{kk}$ . Thus, volume increase of the void is enabled by the presence of large far-field mean stresses. Hancock and Mackenzie [48] made the assumption that the equivalent plastic fracture strain of a material is inversely proportional to the void volume growth rate. Therefore, the equivalent plastic fracture strain must decrease exponentially with increasing stress triaxiality, or:

$$\sigma^* = \frac{\sigma_m}{\bar{\sigma}} \quad , \quad (1.4)$$

and, the effective stress is defined as:

$$\bar{\sigma} = \left( \frac{3}{2} S_{ij} S_{ij} \right)^{\frac{1}{2}} \quad , \quad (1.5)$$

where,  $S_{ij} = \sigma_{ij} - \sigma_m \delta_{ij}$  is the deviatoric stress tensor. Hancock and Mackenzie [48] and Mackenzie, Hancock and Brown [49] described an experimental technique where the dependence of equivalent plastic fracture strain on stress triaxiality is determined using tensile tests on notched axisymmetric specimens and Bridgeman's analysis of the stress state at the necking localization of an axisymmetric specimen [50].

Many authors have utilized the findings of McClintock, Rice and Tracey and Hancock and Mackenzie. For example, the widely-used damage evolution and fracture model proposed by Johnson and Cook [7] defines the equivalent plastic fracture strain as an exponential function of

the stress triaxiality, see Equation 1.3. Several researchers have studied the effect of this stress state parameter on the effective plastic failure strain using a coupled experimental and numerical approach [51, 52, 53, 54, 55, 56, 57]. The approach consists of conducting both mechanical experiments and parallel numerical simulations on specimens of various geometries. As described above, the classic experiment for this purpose is a tensile test on an axisymmetric notched bar, however, Bau and Wierzbicki [53, 54] and Mohr and Henn [57] have used various specimen geometries and loading methods to explore a wider range of stress states. Experimentally measured data, such as a force versus displacement curve, is compared to the result from the simulation. If the simulated curve agrees with the experimental data, it is assumed that the simulation is adequately capturing the stresses and strains that exist in the specimen during the experiment. Thus, stresses and strains from the simulation can be used to develop a relationship between the equivalent plastic failure strain and the state of stress.

Using results from Bau and Wierzbicki [53, 54], Barsoum and Faleskog [58] concluded that the stress triaxiality parameter alone is insufficient to describe material fracture behavior over the entire range of potential stress states. Therefore, they studied the effect of the Lode parameter, another indicator of stress state, defined as,

$$\mu = -\frac{2\sigma_2 - \sigma_1 - \sigma_3}{\sigma_1 - \sigma_3} \quad , \quad (1.6)$$

where,  $\sigma_1 \geq \sigma_2 \geq \sigma_3$  are the principal stresses. Xue [59] formulated a new continuum damage plasticity model that implements both stress triaxiality and Lode parameter dependence on the equivalent plastic fracture strain. Carney, et al. [60] recently proposed a new parameter, denoted product triaxiality, based on the third stress invariant and is expressed as,

$$\sigma_p^* = \frac{\sigma_1 \sigma_2 \sigma_3}{\bar{\sigma}^3} = \frac{I_3}{\bar{\sigma}^3} \quad . \quad (1.7)$$

This work typically seeks a relationship between the equivalent plastic fracture strain and the stress state, or:

$$\bar{\varepsilon}_f^p = f(\sigma^*) \quad , \quad (1.8)$$

in the case of only stress triaxiality dependence. Using the conclusions of Xue [59], Barsoum and Faleskog [58] and Carney, et al. [60] the definition of the relationship can be extended to:

$$\bar{\varepsilon}_f^p = f(\sigma^*, \mu) \quad , \quad (1.9)$$

in the case of Lode parameter dependence, or alternatively:

$$\bar{\varepsilon}_f^p = f(\sigma^*, \sigma_p^*) \quad , \quad (1.10)$$

in the case of product triaxiality dependence.

### Dynamic Punch Experiments

The dynamic punch experiment is useful for studying impact events because the experiment is similar to the application. In a dynamic punch test, the specimen deforms plastically at high strain rates and is subject to stress states that are similar to those present in an impacted target. Data from these experiments, such as force versus displacement curves, can be used with the coupled experimental-numerical technique, described above, to determine the stress state history in the sample and the equivalent fracture strain at the onset of crack initiation. Therefore, the data can be used to calibrate continuum damage evolution and fracture models. The results of these experiments can also be used as an eventual means of validation for newly developed constitutive and fracture models.

Lee, et al. [61] and Grytten, et al. [62] used servohydraulic actuators to perform low strain rate punch experiments for the purposes of studying ductile fracture. Walters [63] studied the fracture of advanced high strength steels at intermediate strain rates (up to  $500 \text{ s}^{-1}$ ) using a drop weight test rig. Grytten, et al. [42] also studied dynamic perforation of aluminum plates using a tethered, instrumented, pneumatically-driven projectile.

The SHB apparatus has also been used for dynamic punch experiments by several authors [64, 65, 66]. Zurek [64] used a custom designed compression SHB fixture to conduct dynamic punch tests on pearlitic 4340 steel. The focus of the work was to examine adiabatic shear band instabilities in the material. Roessig and Mason [65] used a modified compression split Hopkinson bar apparatus to study adiabatic shear bands in plate specimens fabricated from 1018 steel, 6061-T6 aluminum and Ti-6Al-4V. The authors used an apparatus that consists of only the striker and incident bars that typically comprise a SHB apparatus. A clamped plate specimen is contacted by one end of the incident bar. A two-wave analysis is used to construct load versus displacement records for the experiments. The authors also conducted parallel numerical simulations of the experiments in a separate study [67]. Daboussi and Nemes [66] used the technique to study dynamic ductile fracture. The authors used dynamic punch experiments on a compression SHB apparatus to generate Johnson Cook constitutive and fracture model parameters for 6061-T6 aluminum Ti-6Al-4V and Nitronic 33. Only blunt punch geometries are used in the Hopkinson bar experimental work described above, so the stress states achievable in the specimens are limited.

Certain experimental techniques can be used to control the displacement of the punch into the specimen, which allows impact failure mode evolution to be studied. Common impact failure modes are shown in Figure 2. On impact, ductile metals typically fail in plugging, petaling, ductile hole growth or some combination of these modes. Meyers, et al. [68] used a stop-ring to limit the amount of shear strain imparted to a hat-shaped SHB specimen to study shear bands in pre-shocked copper. This technique can be implemented with the dynamic punch tests and recovered specimens can be examined at different stages in the failure process.

## Chapter 2: Methodology and Experimental Program

The experimental program devised to study both the plastic deformation and ductile fracture behavior of 2024-T351 aluminum is presented in this chapter. Tension, compression and torsion test series are presented in the plastic deformation experimental program. Methods used to analyze the effect of anisotropic strength behavior in panels under impact loads are also discussed. The experimental program to characterize the ductile fracture behavior consists of several test series that include plane stress, axisymmetric and plane strain tensile tests, combined loading tests and dynamic punch tests.

### Plastic Deformation of 2024-T351 Aluminum

The plastic deformation of 12.7 mm thick 2024-T351 aluminum plate is investigated. Goals are to determine: (1) if the effective stress – equivalent strain response of the material varies in tension, compression and shear loading, (2) the strain rate sensitivity of the stress-strain behavior, (3) the temperature sensitivity of stress-strain behavior, (4) the anisotropic strength behavior present in the plate due to crystallographic texture from processing and (5) if the Barlat anisotropic plasticity model [33] is suitable for capturing this anisotropic behavior in tension compression and shear.

Tension, compression and torsion specimens are fabricated from 12.70 mm thick 2024-T351 aluminum plate produced by Kaiser Aluminum. Tension specimens are flat dogbone samples. Compression specimens are cylinders with a length to diameter ratio of one. Torsion specimens are spools with a thin-walled tube gage section. All specimen geometries are consistent throughout the plastic deformation test program to eliminate geometric effects skewing the overall interpretation of the data. Figure 3 illustrates how the various test specimens are fabricated from the plate.

The plastic deformation experimental program is presented in Table 2. The program is designed to determine the plastic deformation behavior of the material at various strain rates and temperatures as well as in several orientations. Tests at and below equivalent strain rates of  $1.0 \text{ s}^{-1}$  are conducted using the axial (for tension and compression tests) or rotational (for torsion

tests) degree of freedom of an Instron bi-axial servohydraulic load frame, while a direct-tension [69], compression [70] or a stored-torque torsion split Hopkinson bar [71] are used to conduct experiments above  $1.0 \text{ s}^{-1}$ . Tension tests are conducted on specimens fabricated in the rolled direction ( $0^\circ$ ) of the aluminum plate at room temperature and nominal strain rates of  $1.0 \times 10^{-4} \text{ s}^{-1}$ ,  $1.0 \times 10^{-2} \text{ s}^{-1}$ ,  $1.0 \text{ s}^{-1}$ ,  $5.0 \times 10^2 \text{ s}^{-1}$  and  $1.8 \times 10^3 \text{ s}^{-1}$ . Tension experiments are also conducted on specimens aligned in the plate rolled direction at a strain rate of  $1.0 \text{ s}^{-1}$  at  $-50 \text{ }^\circ\text{C}$ ,  $150 \text{ }^\circ\text{C}$ ,  $300 \text{ }^\circ\text{C}$  and  $450 \text{ }^\circ\text{C}$ . Tension tests are conducted on specimens aligned in three additional plate directions ( $\pm 45^\circ$  and  $90^\circ$ ) at room temperature and a nominal strain rate of  $1.0 \text{ s}^{-1}$ .

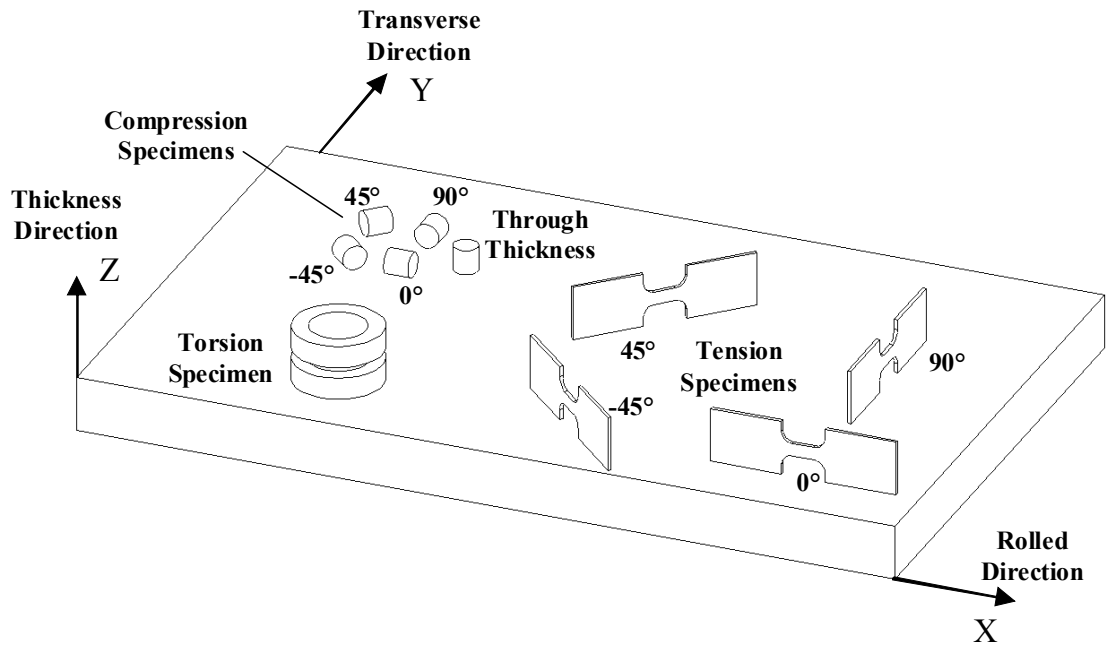


Figure 3. Tension, compression and torsion specimens fabricated from 12.7 mm thick 2024-T351 aluminum plate.

Compression tests are conducted on specimens fabricated in the rolled direction ( $0^\circ$ ) of the aluminum plate at room temperature and nominal strain rates of  $1.0 \times 10^{-4} \text{ s}^{-1}$ ,  $1.0 \times 10^{-2} \text{ s}^{-1}$ ,  $1.0 \text{ s}^{-1}$ ,  $1.5 \times 10^3 \text{ s}^{-1}$  and  $5.0 \times 10^3 \text{ s}^{-1}$ . Compression experiments are also conducted on specimens aligned in the rolled direction at a strain rate of  $1.0 \text{ s}^{-1}$  at  $-50 \text{ }^\circ\text{C}$ ,  $150 \text{ }^\circ\text{C}$ ,  $300 \text{ }^\circ\text{C}$  and  $450 \text{ }^\circ\text{C}$ . Compression tests are conducted on specimens aligned in four additional directions ( $\pm 45^\circ$ ,  $90^\circ$  and through the plate thickness).

Torsion tests are conducted at room temperature and equivalent strain rates of  $1.0 \times 10^{-4} \text{ s}^{-1}$ ,  $1.0 \times 10^{-2} \text{ s}^{-1}$ ,  $1.0 \text{ s}^{-1}$ ,  $5.0 \times 10^2 \text{ s}^{-1}$  and  $2.8 \times 10^3 \text{ s}^{-1}$ . Torsion experiments are also conducted at a strain rate of  $1.0 \text{ s}^{-1}$  at  $-50 \text{ }^\circ\text{C}$ ,  $150 \text{ }^\circ\text{C}$ ,  $300 \text{ }^\circ\text{C}$  and  $450 \text{ }^\circ\text{C}$ . All torsion specimens are fabricated

such that their axis of symmetry is parallel to the thickness direction of the plate, see Figure 3. Each experiment listed in Table 2 is conducted at least three times to assess the repeatability of the measurements.

Experimental data from the program, outlined in Table 2, is used to determine parameters for Barlat's anisotropic plasticity model [33]. This model, implemented in LS-DYNA, is used to simulate select tension, compression and torsion experiments and the results are compared to the test data.

Table 2. Plastic deformation experimental program.

Test #	Test Mode	Apparatus	Equivalent Strain Rate (1/s)	Temperature (°C)	Specimen Orientation	
1	Tension	Servohydraulic Load Frame	1.00E-04	RT	0°	
2			1.00E-02			
3			1.00E+00			
4		Tension SHB	5.00E+02			
5			1.80E+03			
6		Servohydraulic Load Frame	1.00E+00	-50		
7				150		
8				300		
9				450		
10				RT		45°
11						90°
12		-45°				
13	Compression	Servohydraulic Load Frame	1.00E-04	RT	0°	
14			1.00E-02			
15			1.00E+00			
16		Compression SHB	1.50E+03			
17			5.00E+03			
18		Servohydraulic Load Frame	1.00E+00	-50		
19				150		
20				300		
21				450		
22				RT		45°
23						90°
24		-45°				
25		Through Thickness				
26	Torsion	Servohydraulic Load Frame	1.00E-04	RT	Through Thickness	
27			1.00E-02			
28			1.00E+00			
29		Torsion SHB	5.00E+02			
30			2.80E+03			
31		Servohydraulic Load Frame	1.00E+00	-50		
32				150		
33				300		
34				450		

## Anisotropic 2024 Aluminum Sheet and Plate under Impact Loading

Pereira, Revilock and Ruggeri [43] provided the experimental data that is analyzed in Chapter 5. Their experiments are discussed in further detail in Chapter 3. The 12.7 mm thick target panels used in their research are fabricated from the same material stock characterized in the plastic deformation and ductile fracture experimental programs. Nandwana's simulations [44] are extended in the current research to include the impact cases with 3.175 mm 2024-T3 sheet target panels. This collection of information provides the basis for the analysis given in Chapter 5.

Results from numerical simulations of impact cases using both von Mises and anisotropic yield functions for 3.175 mm thick 2024-T3 and 12.7 mm thick 2024-T351 aluminum targets are compared to the experimental data. Simulated and experimental projectile residual velocities are compared. Data from strain gages mounted on the rear surface of the target panels are compared to simulated strains at the same locations. Target panel rear surface maximum principal strain and impact axis deflection data from three dimensional DIC measurements are also compared to the simulation results.

## Ductile Fracture of 2024-T351 Aluminum

The ductile fracture behavior of 12.7 mm thick 2024-T351 aluminum plate is investigated. The goals of this investigation are to: (1) construct a new fracture locus in stress space using both experimental data and, in some cases, parallel numerical simulations of specimens loaded in several stress states, (2) explore the dependence of equivalent plastic fracture strain on additional stress state parameters such as the Lode parameter and product triaxiality and (3) modify an existing compression SHB apparatus to conduct both restricted and unrestricted dynamic punch experiments for the purposes of studying dynamic ductile fracture and the impact failure mode evolution of a thin disk specimen.

### Low Rate Ductile Fracture behavior

The low rate ductile fracture behavior is investigated using three separate tensile test series, and a combined loading – pure shear test series. The first tensile test series is conducted on thin, flat, smooth and notched specimens. These experiments are summarized in Table 3. Specimen dimensions are provided in the table along with estimates for stress triaxiality ( $\sigma^*$ ), Lode parameter ( $\mu$ ) and product triaxiality ( $\sigma_p^*$ ). When loaded, the thin flat tensile specimens are in a

state of plane stress ( $\sigma_3 = 0.0$ ). Consequently, the product triaxiality term is zero for all thin specimens.

The second tensile test series is conducted on axisymmetric smooth and notched specimens. The specimens are presented with dimensions and estimated stress state parameter values in Table 4. This test series is the method typically used for calibrating ductile fracture models as presented by Hancock and Mackenzie [48]. Several researchers have used experiments like these to calibrate ductile fracture models [7, 21, 49, 51, 52, 53, 56]. When loaded in tension, these specimens undergo a stress state where two principal stresses are equal ( $\sigma_2 = \sigma_3$ ). This means that the Lode parameter value is 1.0 for all specimens listed in Table 4.

The third tensile test series consists of experiments on thick, smooth and notched specimens. Specimen geometries and anticipated stress state parameter values are presented in Table 5. These specimens are sufficiently thick (25.4 mm) to approach a state of plane strain in the center of the specimen.

All specimens are fabricated such that the direction of loading is parallel to the rolled direction of the plate. Estimations of the stress state for the axisymmetric specimens can be made using Bridgman's analysis of the stress state at the neck of a round tension specimen [50]. The plastic deformation in the specimen, however, leads to time-dependent specimen geometry and therefore, an evolving stress state. Because of this, the stress state parameter values and equivalent plastic strain histories are extracted from parallel numerical simulations. The stress state and equivalent plastic fracture strain are computed at the center of each specimen. The stress state parameter values listed in Table 3, Table 4 and Table 5 are averaged over the duration of the experiment.

The specimens listed in Table 3, Table 4 and Table 5 are designed to have similar stress triaxiality parameters yet different Lode and product triaxiality parameters. For example, the sharp notch plane stress specimen (test #4 in Table 3) has a similar stress triaxiality to two axisymmetric specimens (tests #6 and 7 in Table 4) and two plane strain specimens (tests #11 and 12 in Table 5). However, the Lode and product triaxiality parameters for these experiments are vastly different. If the stress triaxiality parameter alone is sufficient to describe the fracture locus, the equivalent plastic fracture strains for each of these experiments should be similar. In contrast, variance between the fracture strains for these experiments is an indication that additional stress state parameters are necessary to increase the fidelity of the fracture locus.

Combined loading experiments on thin-walled tube specimens provide a useful means of generating fracture strain data at a wide variety of stress states. Consider the thin-walled tube

specimen subjected to axial load ( $P$ ) and torque ( $T$ ) in Figure 4. The axial load can be either tensile or compressive. The gage section of the specimen is subjected to the following state of stress,

$$\sigma = \begin{bmatrix} \sigma_x & \tau_{xy} & 0 \\ \tau_{xy} & 0 & 0 \\ 0 & 0 & 0 \end{bmatrix} \quad . \quad (2.1)$$

The principal stresses are,

$$\sigma_1 = \frac{\sigma_x}{2} + \sqrt{\left(\frac{\sigma_x}{2}\right)^2 + \tau_{xy}^2} \quad , \quad \sigma_2 = 0 \quad , \quad \sigma_3 = \frac{\sigma_x}{2} - \sqrt{\left(\frac{\sigma_x}{2}\right)^2 + \tau_{xy}^2} \quad . \quad (2.2)$$

The stress triaxiality for this load condition is,

$$\sigma^* = \frac{\sigma_m}{\bar{\sigma}} = \frac{\sigma_x}{3(\sigma_x^2 + 3\tau_{xy}^2)^{\frac{1}{2}}} \quad , \quad (2.3)$$

and the Lode parameter can be found by substituting Equations 2.2 into the definition of the Lode parameter (Equation 1.6),

$$\mu = \frac{\sigma_x}{2\sqrt{\left(\frac{\sigma_x}{2}\right)^2 + \tau_{xy}^2}} \quad . \quad (2.4)$$

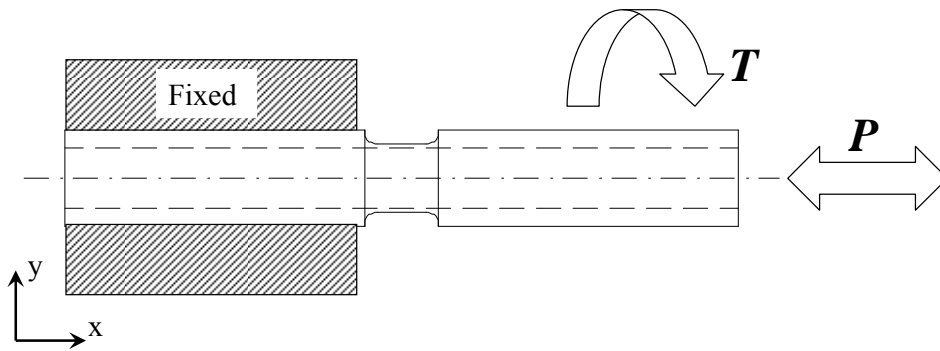


Figure 4. Combined axial and torsional loading of a thin walled tube specimen.

The stress triaxiality and Lode parameters are plotted versus the axial stress – shear stress ratio in Figure 5. When  $\frac{\sigma_x}{\tau_{xy}} > 0.0$ , the axial stress component is tensile. Conversely, when  $\frac{\sigma_x}{\tau_{xy}} < 0.0$ , the axial stress component is compressive. When  $\frac{\sigma_x}{\tau_{xy}} = 0.0$ , the specimen is subjected to pure shear loading. Figure 5 indicates that this relatively simple experiment can be used to investigate a wide range of potential stress states. Stress triaxialities within the range -0.333 (pure compression) to 0.333 (pure tension) are achievable. Likewise, the entire possible range of Lode parameters (-1.0 to 1.0) can be attained. There are, however, some practical restrictions on the stress states that can be achieved. It is more difficult to conduct these experiments in the compressive realm of stress state, since the thin-walled tube gage sections tend to buckle for  $\frac{\sigma_x}{\tau_{xy}} \ll 0.0$ . When buckling occurs, a more complex stress state than the one described in Equation 2.1 exists in the specimen gage and the previous analysis can not be relied upon to provide accurate records of the stress state. Shortening the specimen gage and increasing the wall thickness of the tube specimen can delay buckling, however, achieving stress states described at the far left of the scale of the plot in Figure 5 is unrealistic. Even with this limitation, the experiment is an extremely useful tool to characterize the fracture strain dependence on the state of stress.

This experiment owns two main advantages over other experiments typically used to characterize ductile fracture behavior. First, the axial stress to shear stress ratio can be maintained nearly constant by using load and torque control on a bi-axial servohydraulic load frame. This means that the stress state is nearly constant for the duration of the experiment and damage in the material accumulates at a constant rate. The geometry of tension specimens, such as those shown in Table 3, Table 4 and Table 5, evolve significantly from the initiation of loading to fracture. Therefore, the stress state also evolves significantly during this time. The second advantage is that the stress state is easily determined from the experimental force and torque records, using Equations 2.3 and 2.4. Thus, there is no need to conduct parallel numerical simulations.

Combined loading and pure shear experiments on thin-walled tube specimens for the purposes of characterizing fracture strain dependence on stress state are shown in Table 6. Tests #14 and 15 are conducted under combined tensile and torsional loading. Test #16 is a pure shear (torsion) experiment and Test #17 is a combined compression – torsion experiment. The

specimen used for the compression – torsion experiment (Test #17) has a different geometry than the others. The gage length is shortened and the wall thickness is increased to ensure that the specimen does not buckle. The ratio of axial stress to the shear stress in the specimen is held constant at 1.974 and 0.848 for tests #14 and 15, respectively. In the compressive experiment (test #17), an axial stress – shear stress ratio of -0.848 is targeted.

Chapter 3 presents additional detail on all experiments used to explore the ductile fracture behavior of 2024-T351 aluminum.

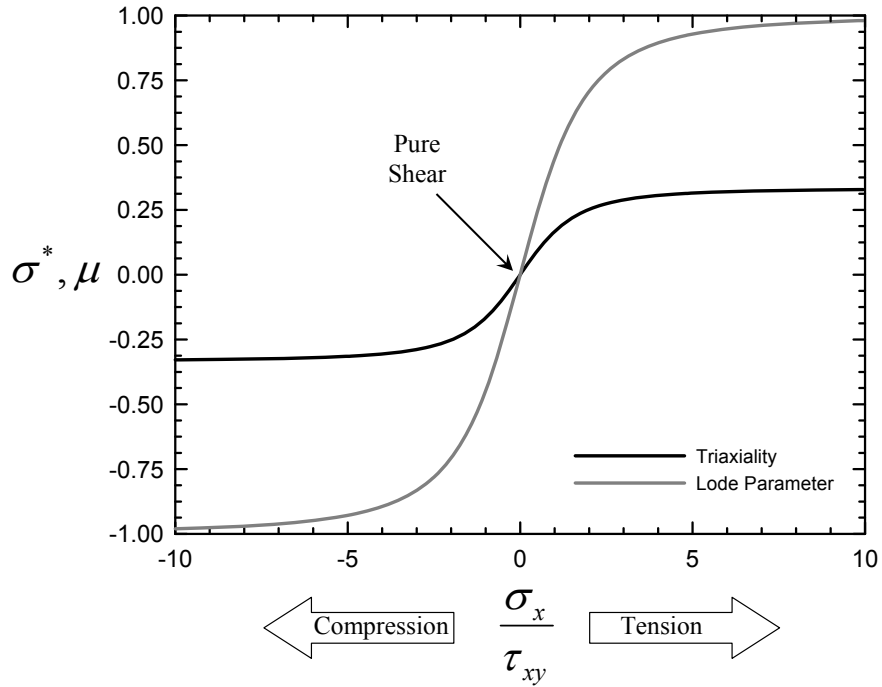


Figure 5. Stress triaxiality and Lode parameter vs axial stress to shear stress ratio for combined axial and torsional loading of a thin walled spool specimen.

Table 3. Ductile fracture experimental program: tensile tests conducted on plane stress test specimens.

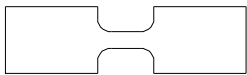
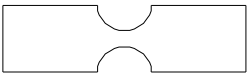
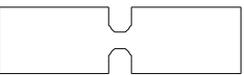
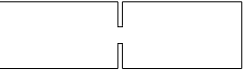
Test #	Geometry	Specimen Dimensions	$\sigma^*$	$\mu$	$\sigma_p^*$
1		Thin smooth specimen (plane stress) Gage Length: 5.080 mm Gage Width: 3.048 mm Thickness: 0.762 mm	0.333	1.000	0.000
2		Thin notched specimen (plane stress) Notch Radius: 4.763 mm Minimum Notch Width: 3.048 mm Thickness: 0.762 mm	0.431	0.660	0.000
3		Thin notched specimen (plane stress) Notch Radius: 1.984 mm Minimum Notch Width: 3.048 mm Thickness: 0.762 mm	0.490	0.415	0.000
4		Thin notched specimen (plane stress) Notch Radius: 0.396 mm Minimum Notch Width: 3.048 mm Thickness: 0.762 mm	0.579	-0.022	0.000

Table 4. Ductile fracture experimental program: tensile tests conducted on axisymmetric specimens.

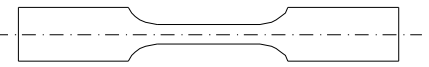
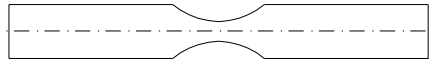
Test #	Geometry	Specimen Dimensions	$\sigma^*$	$\mu$	$\sigma_p^*$
5		Axisymmetric smooth specimen Gage Length: 24.130 mm Gage Diameter: 4.763 mm	0.333	1.000	0.000
6		Axisymmetric notched specimen Gage Radius: 14.503 mm Minumum Gage Diameter: 4.763 mm	0.524	1.000	0.048
7		Axisymmetric notched specimen Gage Radius: 9.144 mm Minumum Gage Diameter: 4.763 mm	0.607	1.000	0.097
8		Axisymmetric notched specimen Gage Radius: 6.096 mm Minumum Gage Diameter: 4.763 mm	0.675	1.000	0.164
9		Axisymmetric notched specimen Gage Radius: 4.470 mm Minumum Gage Diameter: 4.763 mm	0.763	1.000	0.265
10		Axisymmetric notched specimen Gage Radius: 3.048 mm Minumum Gage Diameter: 4.763 mm	0.855	1.000	0.438

Table 5. Ductile fracture experimental program: tensile tests conducted on plane strain specimens.

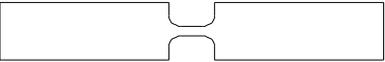
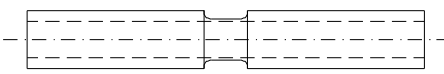
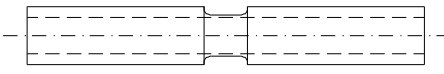
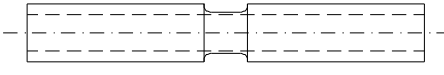
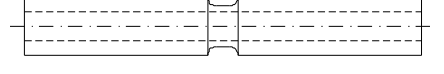
Test #	Geometry	Specimen Dimensions	$\sigma^*$	$\mu$	$\sigma_p^*$
11		Thick smooth specimen (plane strain) Gage Length: 5.080 mm Gage Width: 2.032 mm Thickness: 25.400 mm	0.564	0.085	0.003
12		Thick notched specimen (plane strain) Notch Radius: 13.970 mm Minimum Notch Width: 2.032 mm Thickness: 25.400 mm	0.606	0.121	0.038
13		Thick notched specimen (plane strain) Notch Radius: 4.763 mm Minimum Notch Width: 2.032 mm Thickness: 25.400 mm	0.730	0.061	0.155

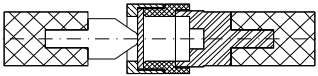
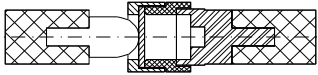
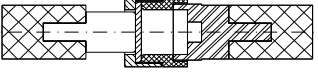
Table 6. Ductile fracture experimental program: pure shear (torsion) and combined loading (tension / torsion, compression / torsion) experiments conducted on thin walled tube specimens.

Test #	Geometry	Specimen Dimensions	$\sigma^*$	$\mu$	$\sigma_p^*$
14		Combined Tension/Torsion Specimen Gage Length: 6.35 mm Inside Diameter: 7.925 mm Outside Diameter: 9.144 mm	0.251	0.702	0.000
15		Combined Tension/Torsion Specimen Gage Length: 6.35 mm Inside Diameter: 7.925 mm Outside Diameter: 9.144 mm	0.147	0.390	0.000
16		Pure Shear Specimen Gage Length: 6.35 mm Inside Diameter: 7.925 mm Outside Diameter: 9.144 mm	0.000	0.000	0.000
17		Combined Compression/Torsion Specimen Gage Length: 3.175 mm Inside Diameter: 6.35 mm Outside Diameter: 9.144 mm	-0.147	-0.390	0.000

## Dynamic Punch Experiments for Ductile fracture

The dynamic punch experimental program is presented in Table 7. Three punch geometries, having tip radii of 2.39 mm, 4.75 mm and perfectly blunt, are used to alter the stress state in the disk specimen. The specimens are 1.473 mm thick, 14.73 mm diameter disks constrained outside of a 5.842 mm radius from its center by epoxy and adaptor fixtures. In addition to an unrestricted displacement experiment, two restricted displacement experiments are conducted for the 2.39 mm and 4.75 mm radius punches. Points of interest identified on the unrestricted displacement force versus displacement curve are used to design the restricted relative displacements. For example, drops in the force can be associated with strain localizations, crack formations or crack propagation. Only an unrestricted displacement experiment is conducted with the blunt punch. Additional details concerning the experimental techniques used in the dynamic punch experiments are found in Chapter 3.

Table 7. Ductile fracture experimental program: dynamic punch tests.

Test #	Geometry	Specimen/Punch Dimensions	Relative Displacement (mm)
1		Sharp Punch Radius	1.6
2		Punch Radius: 2.388 mm	2.4
3		Specimen Thickness: 1.473 mm	Unrestricted
4		Intermediate Punch Radius	2.4
5		Punch Radius: 4.750 mm	3.9
6		Specimen Thickness: 1.473 mm	Unrestricted
7		Blunt Punch Punch Radius: $\infty$ Specimen Thickness: 1.473 mm	Unrestricted

## Chapter 3: Experimental Techniques

This chapter presents the experimental techniques used to conduct the experiments outlined in both the plastic deformation and ductile fracture test series. The chapter is separated into techniques used for low strain rate experiments and those used for high strain rate experiments. A brief discussion of the three dimensional DIC technique for experimental mechanics and descriptions of the measurement systems used in this work are also presented.

### Low Strain Rate Experiments

Low strain rate experiments are conducted using the Instron 1321 bi-axial servohydraulic load frame shown in Figure 6. The machine's actuator can move axially with stroke limits of +/- 63 mm and rotate with angle limits of +/- 45°. Multiple experiments can be conducted with this load frame because of these two degrees of freedom. These experiments include uniaxial tension and compression, pure shear (torsion) and combinations of both tension-shear and compression-shear. The load frame can be equipped with two load cells, depending on the amount of load/torque expected in the experiment. The Lebow 6467-107 cell has a maximum load capacity of 88.964 kN and a torque capacity of 1,130 N-m and is used for experiments that require large loads or torques. An Interface 1216CEW-2K load cell is used for experiments requiring loads less than 8.896 kN and torques less than 113 N-m. The machine is controlled with an MTS FlexTest SE controller equipped with multi-purpose testware, a suite of software which allows the user to independently control both the axial and torsional channels of the load frame. The FlexTest SE is also used for digital data acquisition through MTS 493.25 Digital Universal Conditioners with maximum sample rates of 100 KHz and 22-24 bit resolution.

Multiple grips are used for specimen attachment and loading, depending on the test conducted. MTS 647.02B-22 axial-torsional hydraulic wedge grips, see Figure 6 (a), are used to conduct the low rate experiments outlined in the ductile fracture test series. These experiments are found in Table 3, Table 4, Table 5, and Table 6. Flat and V-notch wedges are available to grip flat (for tests listed in Table 3 and Table 5) and round specimens (for tests in Table 4 and

Table 6), respectively. Inconel 718 push/pull rods, see Figure 6 (b), are used to conduct the low rate tension and compression experiments outlined in Table 2. Separate adaptors are used with the push/pull rods for compression and tension experiments. The tension adaptors are fabricated from Inconel 718 and are shown in Figure 7 (b) and (c). The compression adaptors are comprised of Inconel 615 and are visible in Figure 6 (b) and Figure 15. Custom MAR-246 torsion fixtures, see Figure 18 (e), are used for the low strain rate torsion experiments in Table 2.

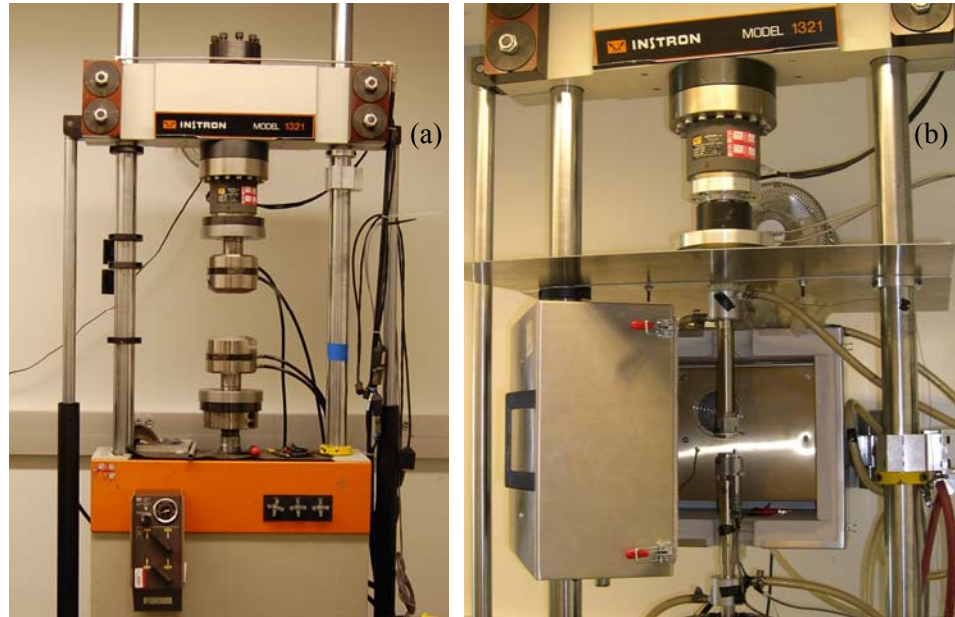


Figure 6. Instron 1321 bi-axial servohydraulic load frame: (a) equipped with the Lebow cell and hydraulic wedge grips, (b) equipped with the Interface cell and Inconel 718 push rods.

### Low Rate Tension Experiments

Low strain rate tension tests are conducted on several test specimen geometries for the various purposes outlined in Chapter 2. These include:

1. The smooth, flat, thin specimens used to study the plastic deformation behavior of 2024-T351, see Table 2. These specimens are used to study both the rate dependence and temperature dependence of plastic deformation.
2. The plane stress specimens tested to study the ductile fracture behavior of the material, see Table 3.
3. The axisymmetric specimens used to study ductile fracture, see Table 4.
4. The plane strain specimens used to study ductile fracture, see Table 5.

The specimen geometry used to study the plastic deformation behavior is presented in Figure 7 (a). Inconel 718 grip fixtures, shown in Figure 7 (b) and (c), are used to attach the samples to the load frame. An Epsilon 3442 miniature axial extensometer with a 4.0 mm initial gage length, see Figure 7 (c), is used for all tensile plastic deformation experiments at temperatures equal to and below 150 °C. The experiments are conducted by imposing a constant downward axial actuator velocity, resulting in a constant strain rate. The experiment actuator velocities for the three low strain rate experiments are:

1. Strain rate:  $1.0\text{E-}04 \text{ s}^{-1}$ , actuator velocity:  $5.08\text{E-}04 \text{ mm/s}$ .
2. Strain rate:  $1.0\text{E-}02 \text{ s}^{-1}$ , actuator velocity:  $5.08\text{E-}02 \text{ mm/s}$ .
3. Strain rate:  $1.0 \text{ s}^{-1}$ , actuator velocity:  $5.08 \text{ mm/s}$ .

Axial load is measured with the Interface load cell and the extension of the specimen gage is measured with the extensometer. Sample data from a servohydraulic tension experiment are shown in Figure 8. The histories of engineering stress and strain are presented in Figure 8 (a). The black trace is engineering stress and corresponds to the vertical axis on the left. Strain traces are represented by the gray traces and correspond to the vertical axis on the right. Two strain traces are presented, one calculated from the extensometer record (solid trace) and one from the LVDT record on the Instron frame (dashed trace). The extensometer trace is more accurate, since the compliance in the machine and the pull rods is eliminated. A nominal strain rate of  $0.893 \text{ s}^{-1}$  is calculated from the extensometer record. Engineering (black trace) and true (gray trace) stress strain curves are presented in Figure 8 (b). True stress and true strain are calculated using the following well-known formulas:

$$\varepsilon = \ln(1 + \varepsilon_E) \quad , \quad (3.1)$$

$$\sigma = \sigma_E(1 + \varepsilon_E) \quad , \quad (3.2)$$

where,  $\varepsilon$  and  $\sigma$  are true strain and stress, respectively and  $\varepsilon_E$  and  $\sigma_E$  are engineering strain and stress. These formulas assume volume constancy and that the deformation takes place uniformly within the specimen. These assumptions are no longer valid at the onset of the necking localization, therefore, care must be taken when interpreting the true stress versus true strain response at large strains.

Additional measurements are made for the plane stress ductile fracture tension test series. The test series is summarized and nominal specimen dimensions are given in Table 3. Select experiments are instrumented with Vishay Micro-Measurements CEA-06-032WT-120 bi-axial strain gage rosettes. The rosettes are bonded to the flat, notched specimens at the center of the specimen's minimum cross-sectional area. A plane stress specimen with a 0.396 mm notch

radius on is shown instrumented with the rosette in Figure 9 (a). Surface displacements and strains are measured using a commercially available three dimensional DIC system. Maximum and minimum principal strains on a specimen with a 0.396 mm radius notch are presented in Figure 10 (a) and (b), respectively. History data for the 0.396 mm notch radius specimen are presented in Figure 9 (b). The black trace represents the load sustained by the specimen while the solid and dashed gray traces are the longitudinal and transverse surface strains at the center of the notch, measured with the rosette. The markers indicate the maximum and minimum principal strains at the same location on the opposite surface of the specimen measured using DIC. It is clear in Figure 9 (b) that the two measurement techniques agree generally well. DIC and rosette strain measurements agree for the other plane stress specimen geometries as well. Fracture onset is identified by a drop in the force history. The data in Figure 9 (b) and Figure 10 is used to generate a fracture locus data point for 2024-T351 aluminum. More detail regarding the use of these data for fracture locus construction is found in Chapter 7 and Appendix C.

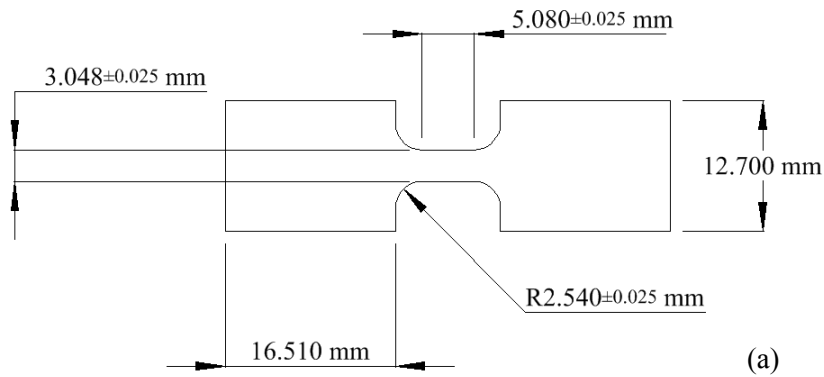


Figure 7. (a) Tension test specimen dimensions (0.762 mm thick), (b) specimen clamped in Inconel 718 attachment fixture, (c) Epsilon 3442 axial extensometer attached to specimen. (Continued)

Figure 7 continued

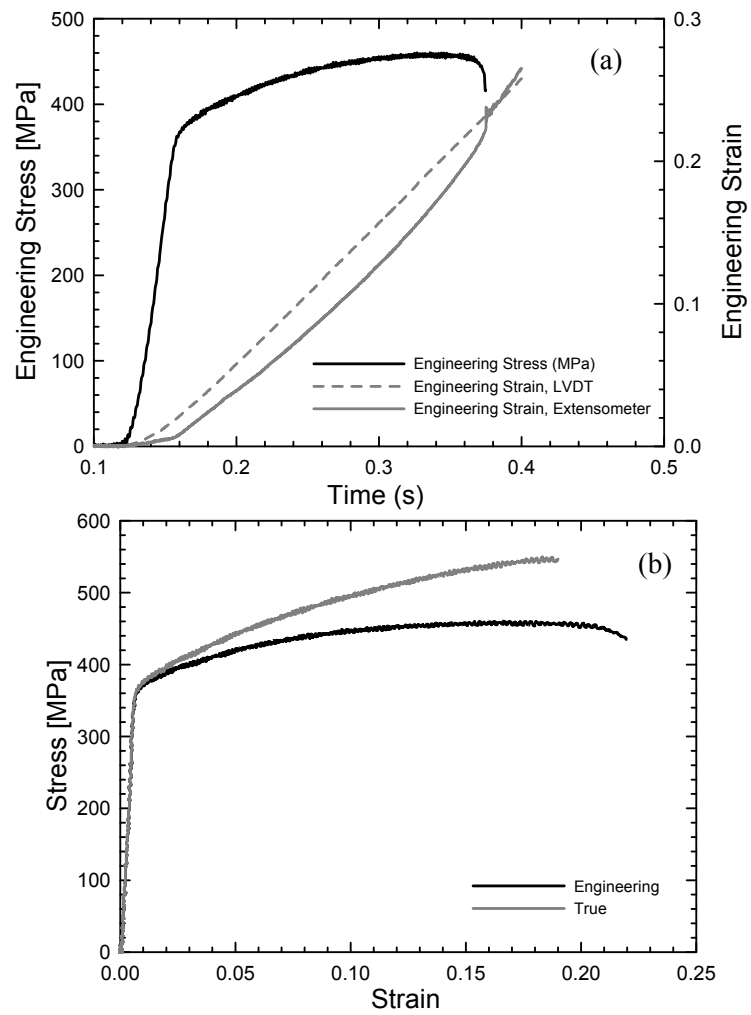
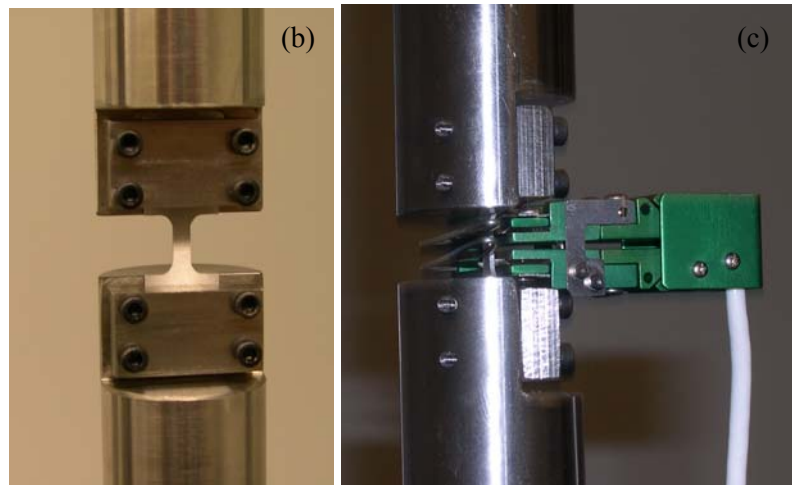


Figure 8. Sample data from a servohydraulic tension experiment: (a) engineering stress and engineering strain history data, (b) engineering and true stress strain curves.

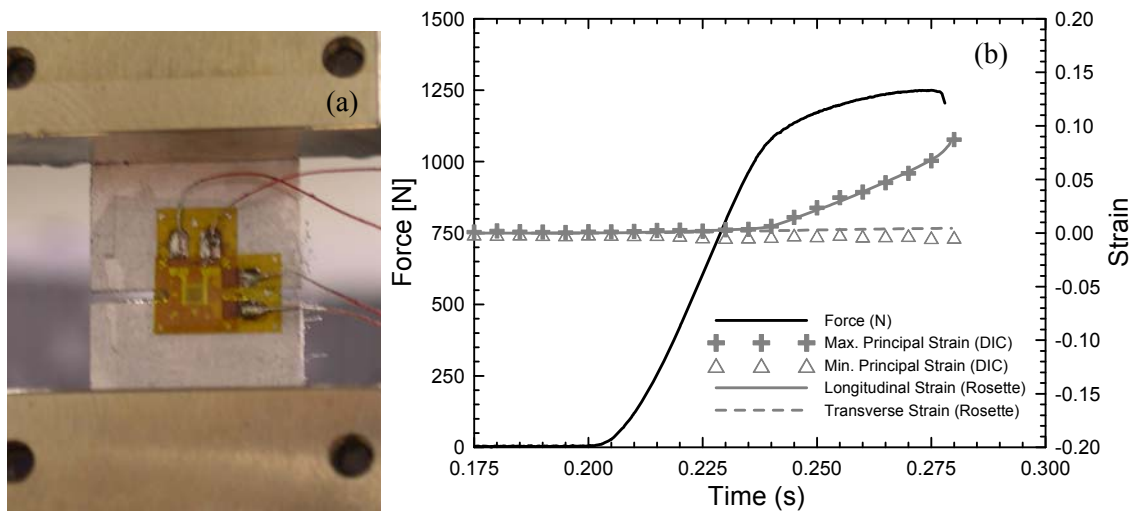


Figure 9. Plane stress notched specimen tension experiment: (a) specimen instrumented with a biaxial strain gage rosette, (b) experimental data.

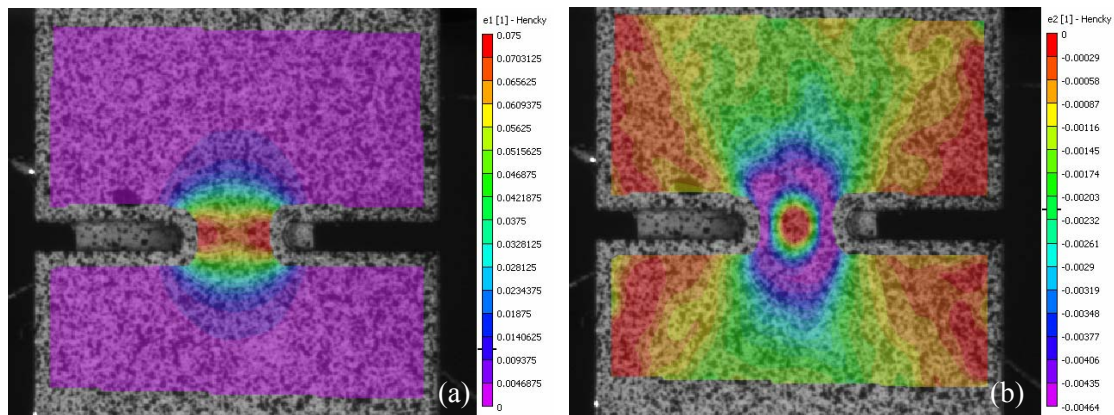


Figure 10. Maximum principal (a) and minimum principal (b) strains on the surface of a notched, plane stress tension specimen.

The axisymmetric tension test series is summarized and specimen dimensions are presented in Table 4. One specimen has a smooth gage section while five others are notched with radii ranging from 14.503 mm to 3.048 mm. The plane strain tension test series is summarized in Table 5. One smooth specimen and two notched samples, with notch radii of 13.97 mm and 4.763 mm, are tested. The experimental setup and data acquisition are identical for both the axisymmetric and plane strain test series. The experimental setup for a notched plane strain test specimen is shown in Figure 11. The specimens are gripped using the hydraulic wedge grips and the specimen is loaded with a constant axial actuator velocity to achieve a nominal strain rate of  $1.0 \times 10^{-2} \text{ s}^{-1}$ . Actuator velocities of 0.2413 mm/s and 0.0508 mm/s are used for the axisymmetric and plane strain specimens, respectively.

Force is measured using the Lebow load cell and specimen surface strains are measured with 3D DIC. For these experiments, the 3D DIC technique is critical, since the specimen geometries contain three dimensional features. These features are illustrated in Figure 12. Figure 12 (a) shows the surface of an axisymmetric tension specimen with a notch radius of 6.096 mm while Figure 12 (b) shows the surface of a plane strain specimen with a notch radius of 13.970 mm. The surface Z-coordinate (depth or out-of-plane coordinate) is shown in both plots in Figure 12. Specimen surface strain distributions just prior to fracture are presented in Figure 13. Maximum and minimum principal strains on an axisymmetric specimen with a 6.096 mm notch radius are shown in Figure 13 (a) and (b), respectively. Maximum and minimum principal strains on a wide specimen with a 13.970 mm notch radius are shown in Figure 13 (c) and (d), respectively. Experimental data from a test on an axisymmetric specimen with a 6.096 mm radius notch are shown in Figure 14. History data of the force and the maximum and minimum principal surface strains at the center of the minimum specimen cross section, measured using DIC, are shown in Figure 14 (a). The drop in the load indicates specimen fracture. Force versus displacement curves are shown in Figure 14 (b). One curve is generated using the LVDT record from the Instron frame, while the second curve uses a DIC extensometer. In the latter case, the relative displacements of two points straddling the minimum notch width of the specimen are compared to their initial distance apart, or the initial gage length of the DIC extensometer. The DIC extensometer trace is more accurate than that from the Instron LVDT because compliance in the machine and the grips are eliminated. The initial gage lengths of the DIC extensometers vary for the different specimen geometries tested and are summarized in Table 8.

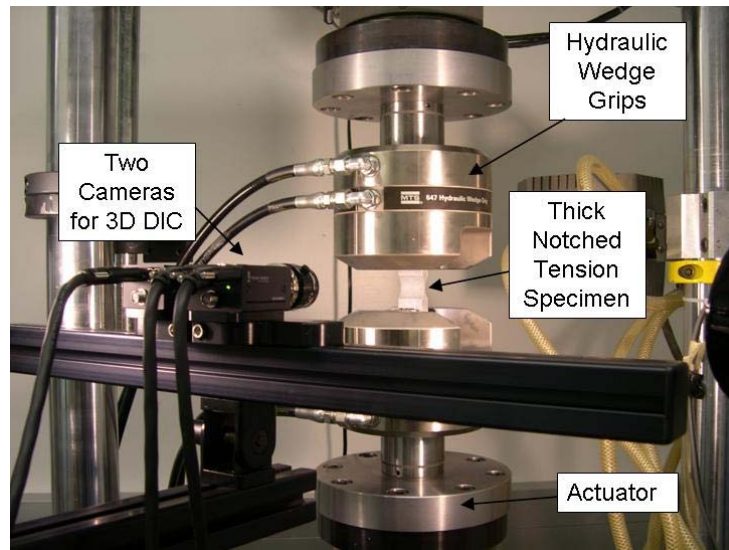


Figure 11. Experimental setup for axisymmetric and plane strain tensile tests.

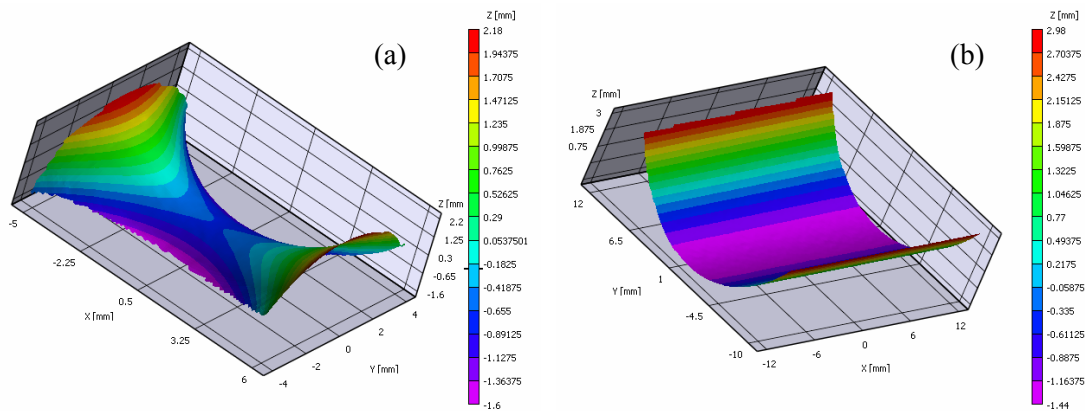


Figure 12. Three dimensional surface features of (a) a notched axisymmetric tension specimen and (b) a notched plane strain tension specimen.

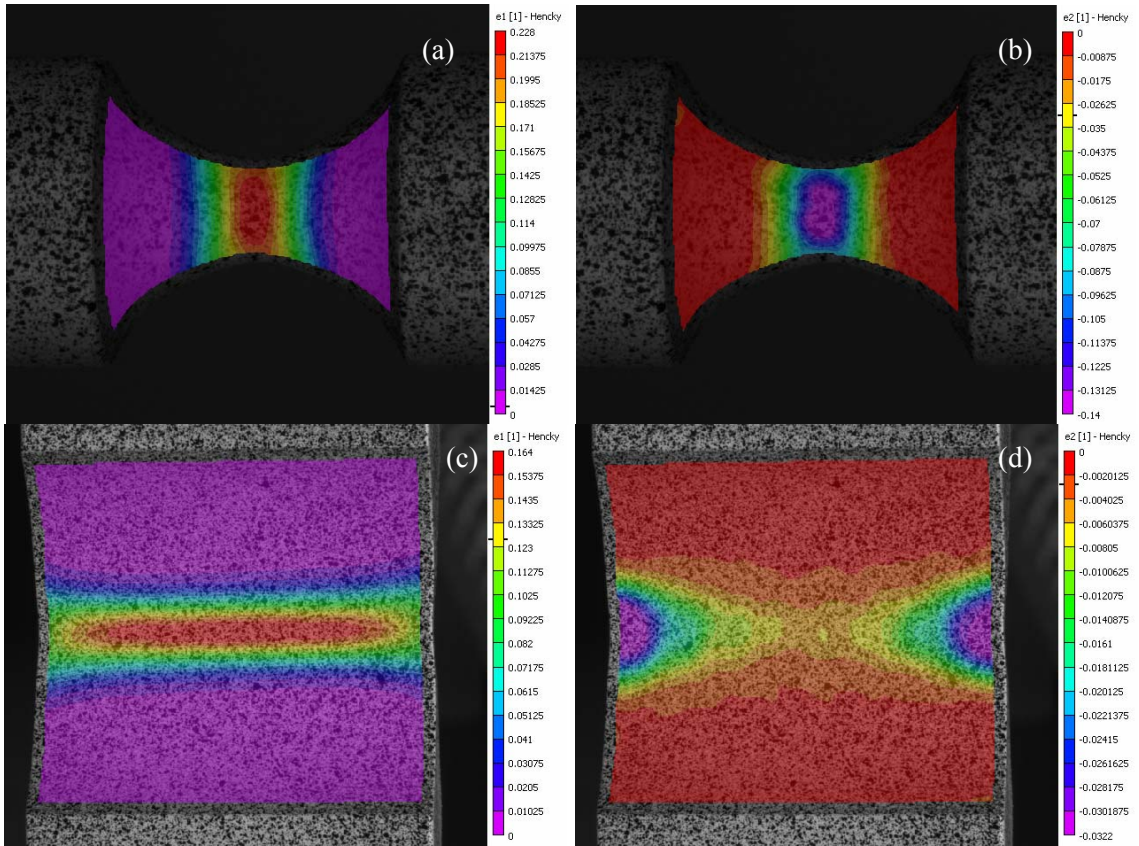


Figure 13. Tension specimen surface strains just prior to fracture: maximum (a) and minimum (b) principal strains of a notched axisymmetric specimen, maximum (c) and minimum (d) principal strains of a notched plane strain specimen.

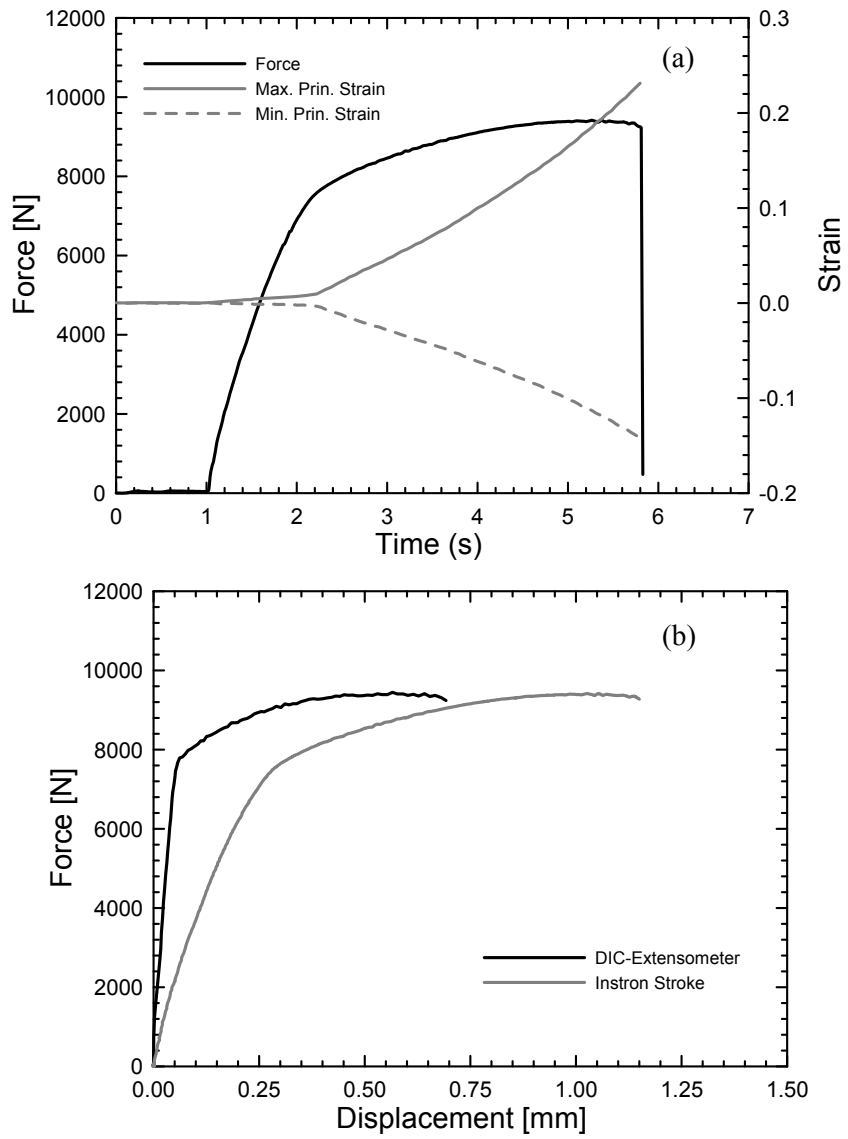
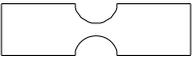
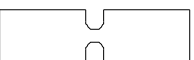
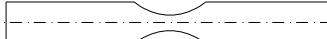
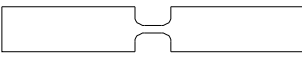
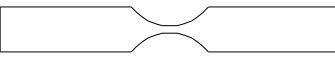
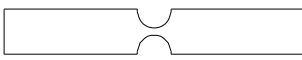


Figure 14. Sample data from a tension test on a notched axisymmetric specimen: (a) force and strain history data, (b) force versus displacement data.

Table 8. DIC extensometer gage lengths used for all tension specimen geometries.

Test #	Geometry	Specimen Dimensions	DIC Extensometer Gage Length (mm)
<b>Thin (Plane Stress)</b>			
1		Thin smooth specimen (plane stress) Gage Length: 5.080 mm Gage Width: 3.048 mm Thickness: 0.762 mm	12.7
2		Thin notched specimen (plane stress) Notch Radius: 4.763 mm Minimum Notch Width: 3.048 mm Thickness: 0.762 mm	11.3
3		Thin notched specimen (plane stress) Notch Radius: 1.984 mm Minimum Notch Width: 3.048 mm Thickness: 0.762 mm	6.6
4		Thin notched specimen (plane stress) Notch Radius: 0.396 mm Minimum Notch Width: 3.048 mm Thickness: 0.762 mm	3.8
<b>Axisymmetric</b>			
5		Axisymmetric smooth specimen Gage Length: 24.130 mm Gage Diameter: 4.763 mm	22.3
6		Axisymmetric notched specimen Gage Radius: 14.503 mm Minimum Gage Diameter: 4.763 mm	17.9
7		Axisymmetric notched specimen Gage Radius: 9.144 mm Minimum Gage Diameter: 4.763 mm	13.5
8		Axisymmetric notched specimen Gage Radius: 6.096 mm Minimum Gage Diameter: 4.763 mm	10.2
9		Axisymmetric notched specimen Gage Radius: 4.470 mm Minimum Gage Diameter: 4.763 mm	7.7
10		Axisymmetric notched specimen Gage Radius: 3.048 mm Minimum Gage Diameter: 4.763 mm	5.0
<b>Wide (Plane Strain)</b>			
11		Thick smooth specimen (plane strain) Gage Length: 5.080 mm Gage Width: 2.032 mm Thickness: 25.400 mm	7.9
12		Thick notched specimen (plane strain) Notch Radius: 13.970 mm Minimum Notch Width: 2.032 mm Thickness: 25.400 mm	19.5
13		Thick notched specimen (plane strain) Notch Radius: 4.763 mm Minimum Notch Width: 2.032 mm Thickness: 25.400 mm	8.0

## Low Rate Compression Experiments

Uniaxial compression experiments are conducted on 3.048 mm long, 3.048 mm diameter cylinders at three nominal strain rates on the Instron load frame. The specimen is placed between Inconel 718 push rods and custom designed Inconel 625 compression platens. Contact surfaces with the upper and lower platens are lubricated with molybdenum disulfide grease, see Figure 15 (a), to minimize friction and “barreling” deformation behavior at large plastic strains. Load is applied by imposing an upward constant actuator velocity. Actuator velocities for the three low strain rate experiments are listed below:

1. Strain rate:  $1.0\text{E-}04 \text{ s}^{-1}$ , actuator velocity:  $3.048\text{E-}04 \text{ mm/s}$ .
2. Strain rate:  $1.0\text{E-}02 \text{ s}^{-1}$ , actuator velocity:  $3.048\text{E-}02 \text{ mm/s}$ .
3. Strain rate:  $1.0 \text{ s}^{-1}$ , actuator velocity:  $3.048 \text{ mm/s}$ .

Specimens tested at and below  $150 \text{ }^{\circ}\text{C}$  are instrumented with Vishay Micro-Measurements EA-06-015LA-120 strain gages, see Figure 15 (a). A custom-designed, secondary LVDT fixture is used to measure the decrease in specimen length during the experiment. The fixture is shown in Figure 15 (b) and consists of an LVDT collar that attaches to the upper platen/pushrod and a zeroing fixture which attaches to the lower platen/pushrod. The LVDT collar accommodates a Lucas-Schaevitz 050 HCA LVDT. When the actuator moves upward, the screw in the zeroing fixture pushes the LVDT probe upward. This device provides more accurate specimen displacement data than the Instron’s integrated LVDT because it is located closer to the specimen and a significant amount of compliance in the load frame and push rods is eliminated from the measurement.

Sample data from a servohydraulic, uniaxial compression experiment at a nominal strain rate of  $1.0 \text{ s}^{-1}$  are presented in Figure 16. Figure 16 (a) shows engineering stress and strain history data, while Figure 16 (b) shows engineering and true stress versus strain curves. Three strain traces are plotted in Figure 16 (a). The first trace is calculated using the secondary LVDT displacement record and the second trace is from the strain gage mounted on the surface of the specimen. The final strain trace is a composite strain history that utilizes the strain gage record at low strains (pre-yield) and the strain calculated from the secondary LVDT record for large strains (post-yield). The stress strain curves in Figure 16 (b) use the composite strain.

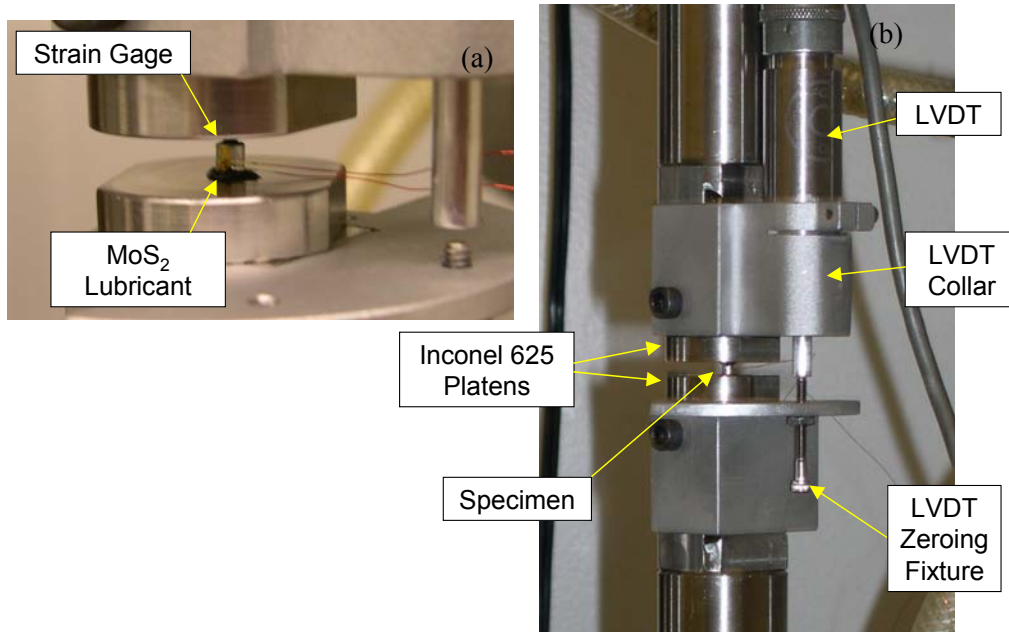


Figure 15. Low strain rate compression experimental setup: (a) specimen placed between inconel 615 platens, (b) push-rod and platen setup with secondary LVDT fixture.

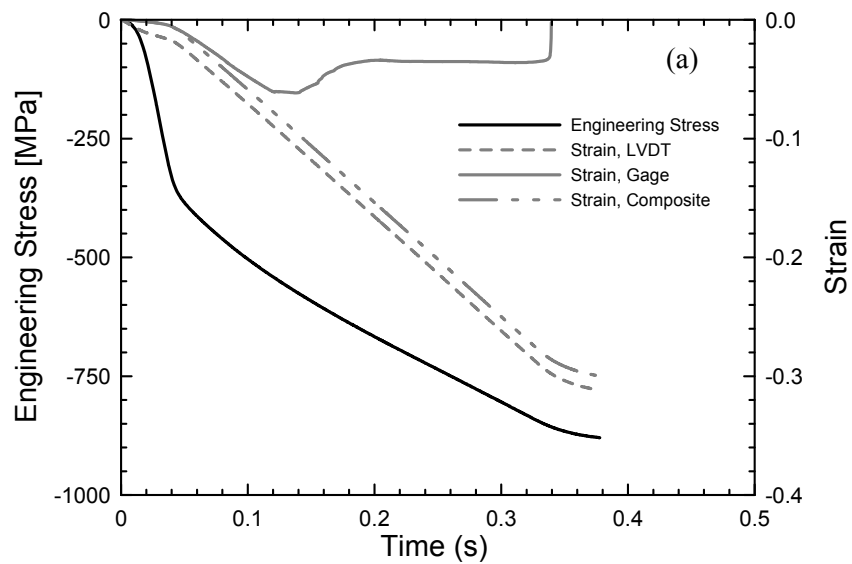
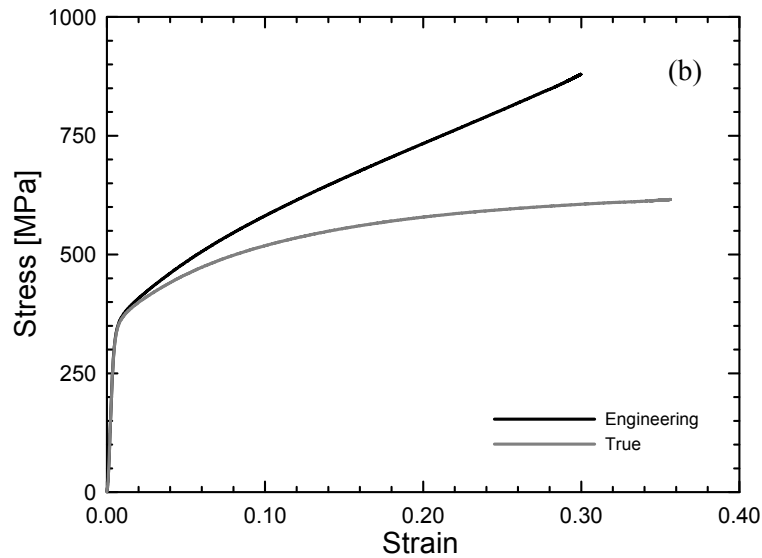


Figure 16. Sample data from a servohydraulic compression experiment: (a) engineering stress and engineering strain history data, (b) engineering and true stress strain curves. (Continued)

Figure 16 continued



### Low Rate Torsion and Combined Loading Experiments

Low strain rate torsion experiments are conducted on the Instron 1321 load frame to characterize both the plastic deformation and fracture behavior of 2024-T351 aluminum under pure shear. Thin-walled tube specimens, see Figure 17, are loaded using the load frame's rotational degree of freedom. The specimens are shaped like spools and fabricated such that the longitudinal axis of the specimen is parallel with the thickness direction of the plate, see Figure 3. The plate stock provides obvious limitations on the geometry of the specimen; the most restricting is that the length of the specimen is limited to the thickness of the plate (12.7 mm). Short spool specimens are difficult to grip, so adaptor fixtures are fabricated to fit the MAR-246 torsion grips. The spool specimen is epoxied into upper and lower 6061-T6 aluminum adaptors, see Figure 18 (a) and (b). Split pins are inserted through the adaptors into the spool flanges to reinforce the epoxy bonds between the adaptors and the specimen. The specimen assembly is shown in Figure 18 (c). The hex-shaped ends of the adaptors are inserted into the torsion rods and Inconel set screws are used to grip the specimen, see Figure 18 (e).

The experiments are conducted by imposing a constant actuator rotational velocity predetermined to achieve the desired equivalent strain rates. Load control is used on the axial channel to ensure that the axial stresses in the specimen are zero. Actuator rotational velocities for the three low rate experiments are:

1. Strain rate:  $1.0\text{E-}04 \text{ s}^{-1}$ , actuator rotational velocity:  $3.781\text{E-}03 \text{ }^\circ/\text{s}$ .

2. Strain rate:  $1.0\text{E-}02 \text{ s}^{-1}$ , actuator rotational velocity:  $3.781\text{E-}01 \text{ }^\circ/\text{s}$ .
3. Strain rate:  $1.0 \text{ s}^{-1}$ , actuator rotational velocity:  $37.81 \text{ }^\circ/\text{s}$ .

The reaction torque is measured with the Interface load cell, while a custom angle of twist measurement device or “torsional extensometer” provides an accurate measurement of the twist angle in the specimen gage. This device, which consists of an upper collar that houses an LVDT and a lower collar that releases the LVDT probe as the actuator rotates, is shown in Figure 18 (d). The LVDT (Lucas-Schaevitz 050 HCA) provides a record of arc-length which can be converted to angle of twist using the distance from the LVDT probe to the center of the spool specimen.

The angle of twist is,  $\theta = \frac{s}{r}$ , where  $s$  is the arc-length and  $r$  is the radius. This angle of twist measurement is more accurate than the record from the Instron’s integrated RVDT, since it eliminates compliances in the machine and grip fixtures.

Shear stress and shear strain are calculated using the formulas:

$$\tau = \frac{T r_m}{J} \quad , \quad \text{and} \quad (3.3)$$

$$\gamma = \frac{\theta r_m}{L_s} \quad , \quad (3.4)$$

where  $T$  is the torque,  $r_m$  is the mean gage radius,  $J$  is the polar moment of inertia and  $L_s$  is the gage length. Sample data from an experiment with an equivalent strain rate of  $1.0\text{E-}2 \text{ s}^{-1}$  are presented in Figure 19. History data of the shear stress and shear strain are presented in Figure 19 (a). Two shear strain traces are presented in the plot, one calculated from the Instron RVDT record and one calculated using the torsional extensometer device described above. The compliance in the machine clearly influences the RVDT measurement, as the shear strain accumulates too rapidly in the beginning of the experiment. Figure 19 (b) presents both shear stress versus shear strain and effective stress versus equivalent strain. Effective stress is defined by Equation 1.5 and the equivalent strain is defined as,

$$d\bar{\varepsilon} = \left( \frac{2}{3} d\varepsilon'_{ij} d\varepsilon'_{ij} \right)^{1/2} \quad , \quad (3.5)$$

where,  $d\varepsilon'_{ij}$  is the deviatoric strain tensor increment, or  $d\varepsilon'_{ij} = d\varepsilon_{ij} - \frac{1}{3} d\varepsilon_{kk} \delta_{ij}$ .

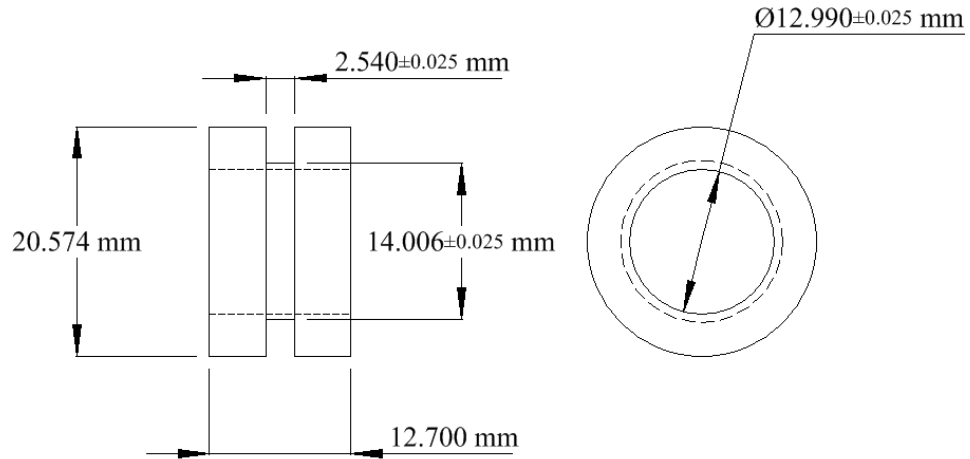


Figure 17. Spool-shaped torsion specimen.

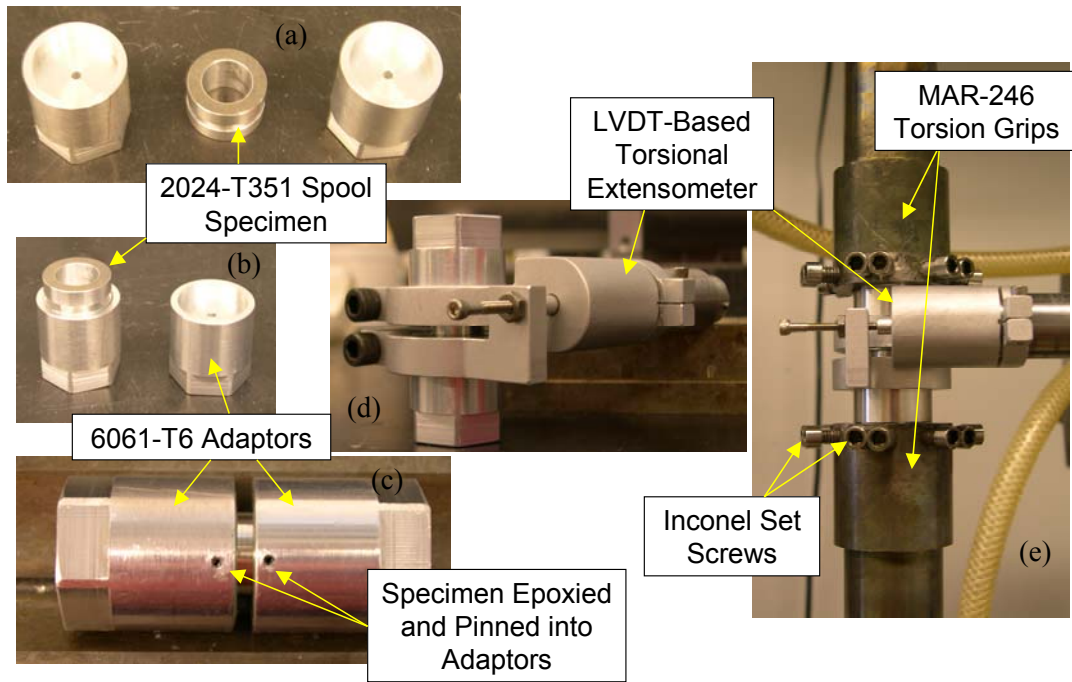


Figure 18. Torsion specimen and adaptors (a)-(b), specimen-adaptor assembly (c), instrumentation (d) and grip fixtures (e).

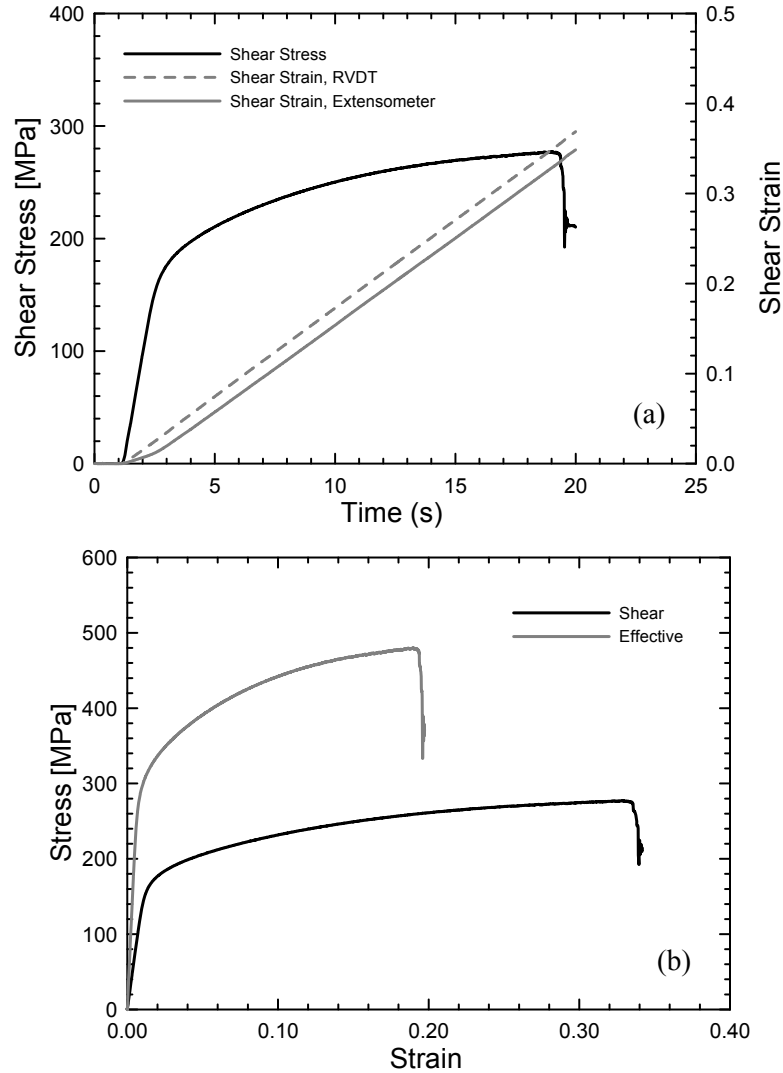


Figure 19. Sample data from a servohydraulic torsion experiment: (a) shear stress and shear strain history data, (b) shear and effective stress strain curves.

Combined loading experiments are conducted using both the axial and rotational degrees of freedom on the Instron load frame. The dimensions of the thin-walled tube specimens used in the experiments are listed in Table 6. The specimens are fabricated from the 12.7 mm thick plate such that the axis of symmetry is parallel to the rolled axis of the plate. Specimen flanges are attached to the load frame using hydraulic wedge grips. Axial load control and torque control are used for the combined loading experiments (tests 14, 15 and 17 in Table 6). The load and torque are both increased linearly with time such that the axial stress – shear stress ratio,  $\frac{\sigma_x}{\tau_{xy}}$ , is nearly

constant for the duration of the experiment. The pure shear experiment (test 16 in Table 6) is conducted using constant rotational velocity actuator motion coupled with axial load control set

to zero. Torques and axial loads are measured using the Interface load cell for tests 14, 15 and 16, while the Lebow cell is used for test 17.

In addition to the axial stroke and rotation measurements from the LVDT and RVDT integrated into the Instron frame, DIC is used to capture surface displacement and strain data for each of these experiments. Surface strain plots for a combined loading specimen with  $\frac{\sigma_x}{\tau_{xy}} = 1.974$  are shown in Figure 20. Maximum principal strains are shown in Figure 20 (a), while minimum principal strains are shown in Figure 20 (b). The white axes overlaid on the strain contours indicate the directions of the principal strains. The maximum principal strain directions are generally more vertical while the minimum principal strain directions tend to be horizontal. The images clearly indicate a band of high strains in the center of the specimen gage. These images emphasize the usefulness of full-field strain information from the DIC technique. If the history of the load frame's actuator motion from the LVDT and RVDT were used to compute strain, it would be assumed that the strains were evenly distributed throughout the gage section of the specimen. This is clearly not the case, as shown in Figure 20. The result would be an average strain of significantly lower magnitude than those found the high-strain region. Even an axial-torsional extensometer would be subject to these errors.

Sample data for an experiment with  $\frac{\sigma_x}{\tau_{xy}} = 1.974$  are presented in Figure 21. Force versus displacement, torque versus rotation and strain versus time are presented in Figure 21 (a), (b) and (c), respectively. In Figure 21 (a) and (b), the black traces indicate the curves generated from the MTS stroke and rotation records, while the gray traces represent data extracted from the DIC measurements. Maximum and minimum principal strains at the eventual specimen fracture region are presented in Figure 21 (c). These data can be used to generate a fracture locus data point. The procedure used to do this is presented in detail in Chapter 7.

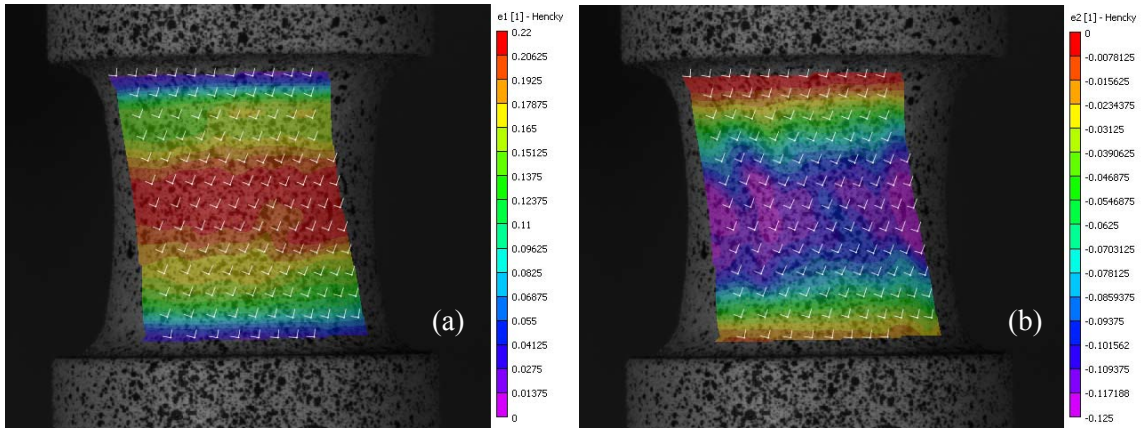


Figure 20. Surface strains on a combined loading specimen: (a) maximum principal strain, (b) minimum principal strain.

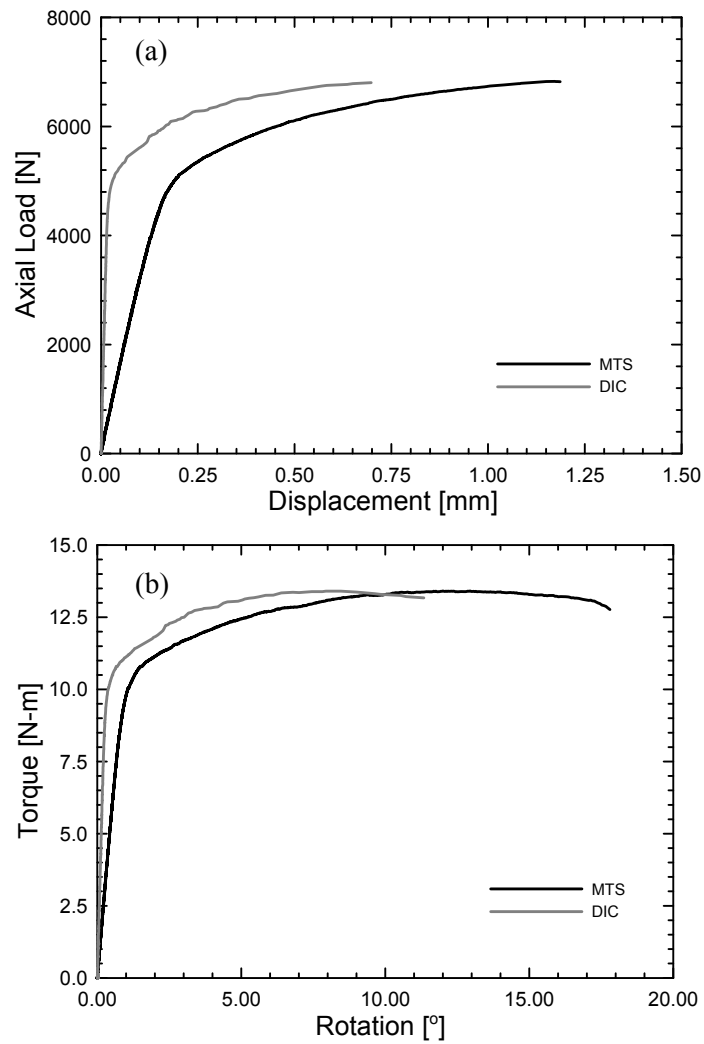
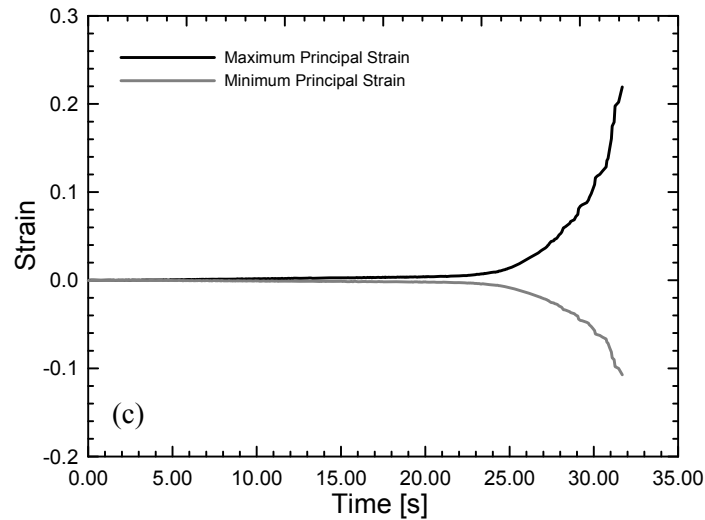


Figure 21. Experimental data from a combined loading experiment: (a) axial force versus displacement, (b) torque versus rotation, (c) strain versus time. (Continued)

Figure 21 continued



### Elevated and Low Temperature Experiments

Elevated and low temperature experiments are conducted to determine the stress versus strain dependence on temperature. Tension, compression and torsion experiments are conducted at five temperatures: -50 °C, Room temperature, 150 °C, 300 °C, and 450 °C. Two furnaces and a cryogenic chamber are used to reach the temperatures listed. An ATS 3620 convection furnace is used for experiments at 150 °C. A Research, Inc., E4-2 IR furnace is used for the 300 °C and 450 °C tests. These furnaces are shown in Figure 22 (a). In the picture, the front door of the ATS 3620 furnace is removed. The full 3620 furnace is shown in Figure 6 (b). Two cooling sleeves, one on the upper push/pull rod and the other on the lower push/pull rod, contain flowing water to remove a significant portion of the heat conducted into the grips. This is necessary, especially for the upper grip, because the excess heat (if unmitigated) could negatively influence the load and torque measurements and potentially damage the cell. The cryogenic chamber is shown in Figure 22 (b). Copper tubing supplies liquid nitrogen to the chamber to achieve the desired temperature. All of the mechanical fixtures used in these experiments are fabricated from high-temperature alloy steels. The push/pull rods are comprised of Inconel 718 while the torsion rods are fabricated from MAR-246. The tension grips are fabricated from Inconel 718 and compression platens are fabricated from Inconel 625. Two sets of fasteners used to attach specimens to the tension and torsion grips are comprised of A286 superalloy and Inconel 718, respectively.

Omega type K thermocouples are used to monitor and regulate the specimen temperature in each experiment. In each type of experiment, tension, compression and shear, multiple

thermocouples are used to monitor the temperature at several different locations to identify possible temperature gradients in the furnaces or cryogenic chamber. Tension, compression and torsion specimens, instrumented with thermocouples, are presented in Figure 23. A tension specimen, instrumented with two thermocouples on the specimen gage, is shown in Figure 23 (a). The thermocouples are attached to the specimen using Omega CC high temperature cement. The tension setup also uses two additional thermocouples, one clamped to the fixture above the specimen and one clamped below the specimen. A compression test is shown instrumented with three thermocouples in Figure 23 (b). One thermocouple is attached directly to the specimen surface using Omega CC cement, see the inlay photo. Two additional thermocouples are clamped to the upper and lower compression platens. A low-temperature torsion experiment is shown in Figure 23 (c). A thermocouple is attached to the outside wall of the tubular specimen gage with Omega CC cement. Additional thermocouples are attached to the upper and lower grips with cement.

The thermocouple on the test specimen is used with a Micristar 828-B10 controller to regulate temperature in the E4-2 IR furnace experiments. The ATS 3620 furnace has an in-built type K thermocouple that provides feedback to an ATS AB900 temperature control system. The chamber temperature for the low temperature experiments is controlled manually. A four-channel Omega HH309 thermocouple data-logger is used to record time histories of the various thermocouples shown in Figure 23. In general, the test temperature was reached without incident and temperature gradients were minimal.

Mechanically, the experiments were conducted using the same methods described in this chapter. Instrumentation used for experiments at the two highest temperatures (300 °C and 450 °C) is limited. These temperatures exceed the upper-level operational limit of the Epsilon 3442 extensometer, the Lucas-Schaevitz 050 HCA LVDT and the strain gages used in the mechanical experiments. The test section of the E4-2 furnace is also too small to accommodate the extensometer and LVDT fixtures.

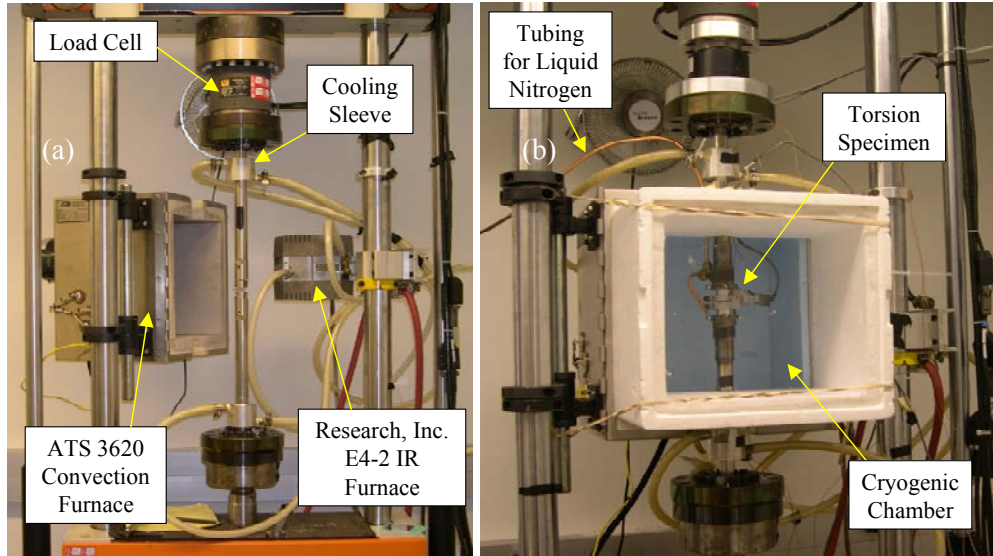


Figure 22. Instron 1321 load frame equipped for (a) elevated temperature testing and (b) low temperature testing.

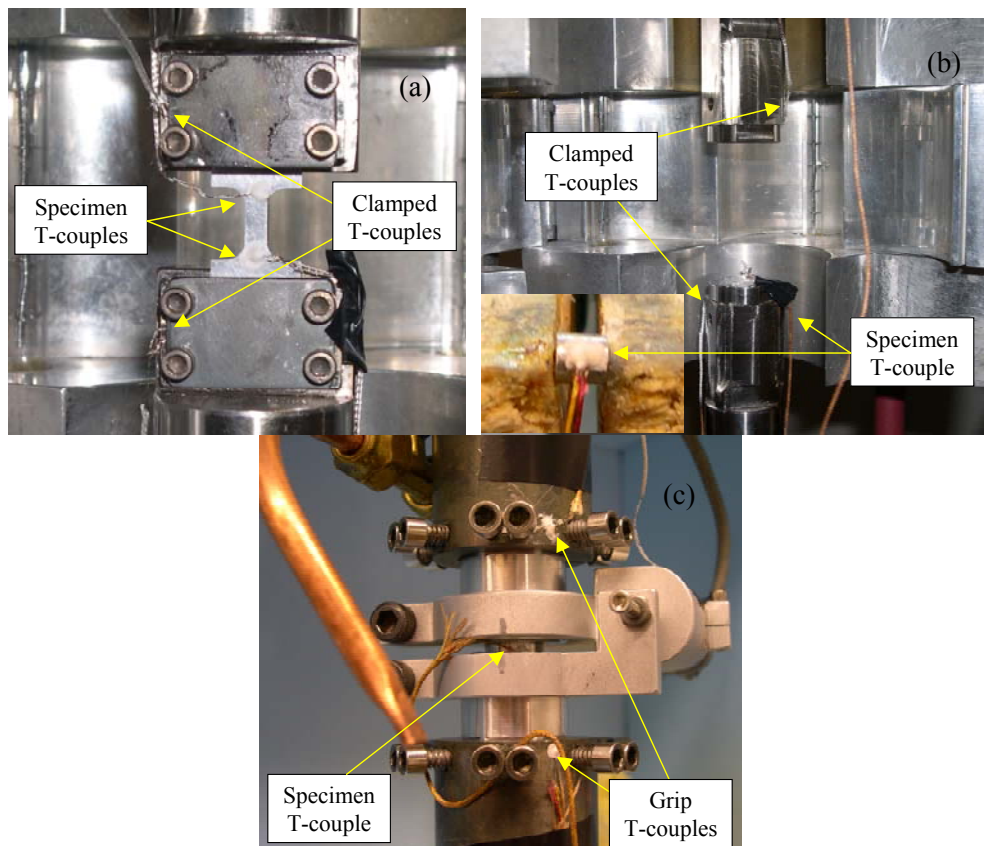


Figure 23. Elevated or low temperature experiments instrumented with thermocouples: (a) tension, (b) compression, (c) torsion.

## High Strain Rate Experiments

High strain rate experiments are conducted on 2024-T351 aluminum to characterize the material's strain rate sensitivity. The split Hopkinson bar (SHB) or Kolsky bar apparatus is commonly used for this purpose. The SHB concept can be adapted for compression, tension, torsion and other custom mechanical experiments at high strain rates. The available strain rate range of the technique depends on the mode of loading and on the dimensions of the actual apparatus, however, the range of  $500 \text{ s}^{-1}$  to  $5000 \text{ s}^{-1}$  is common for most SHB installations. This work employs three separate SHB setups: compression, tension and torsion. It is uncommon for high strain rate data from the same material stock to be available in compression, tension and shear. This section describes the compression, tension and torsion SHB experiments and also discusses a modification made to the compression bar apparatus to conduct dynamic punch experiments for the purposes of studying dynamic ductile fracture.

### Compression SHB Experiments

The compression SHB apparatus is the most common method of testing material strength properties at high strain rates. Gray [70] provides a comprehensive overview of the experimental technique which includes: the history, implementation, calibration and data reduction methods. The apparatus, sketched in Figure 24 (a), consists of three round bars: an incident, transmitter and striker bar. A specimen, typically a small cylinder, is placed between the incident and transmitter bars. The interfaces between the specimen and the incident and transmitter bars are lubricated to minimize friction and keep the stress state uniaxial. A dynamic load pulse is generated by firing a striker bar into the end of the incident bar with a gas gun. The result is a square, elastic, compressive strain pulse ( $\varepsilon_i$ ) that travels from the impact point towards the specimen. The amplitude of this strain pulse is proportional to the velocity of the striker bar,  $v$ :

$$\varepsilon_i = \frac{v}{2c_b}, \quad (3.6)$$

where,  $c_b$  is the axial wave speed in an axisymmetric rod, or  $c_b = \sqrt{\frac{E}{\rho}}$ , where  $E$  and  $\rho$  are the elastic modulus and density of the bar, respectively. The duration of this strain pulse is twice the time required for an elastic wave to traverse the length of the striker bar. When the incident pulse reaches the specimen, the specimen undergoes plastic deformation as part of the incident pulse goes through to the transmitter bar ( $\varepsilon_t$ ) and part of the wave reflects back into the incident bar as a tensile pulse ( $\varepsilon_r$ ). The engineering stress in the specimen is proportional to the transmitted pulse,

$$\sigma(t) = \frac{EA\varepsilon_i(t)}{A_s} \quad , \quad (3.7)$$

where,  $A$  is the cross sectional area of the transmitter bar and  $A_s$  is the initial cross sectional area of the specimen. The strain rate in the specimen is proportional to the reflected pulse,

$$\dot{\varepsilon}(t) = \frac{\dot{u}_1(t) - \dot{u}_2(t)}{L_s} = \frac{2c_b \varepsilon_r(t)}{L_s} \quad , \quad (3.8)$$

where,  $\dot{u}_1$  and  $\dot{u}_2$  are the velocities of the ends of the incident and transmitter bars, respectively, and  $L_s$  is the length of the specimen. The engineering strain in the specimen is computed by integrating the strain rate history,

$$\varepsilon(t) = \frac{u_1(t) - u_2(t)}{L_s} = \int_0^t \dot{\varepsilon}(t) dt \quad . \quad (3.9)$$

The previous analysis is known as a 1-wave analysis and assumes that the specimen is in dynamic force equilibrium. This means that the force at the incident bar – specimen interface ( $F_1$ ) must be equal to the force at the transmitter bar – specimen interface ( $F_2$ ). This assumption is not always true, especially shortly after loading of the specimen begins. At the beginning of loading, the specimen undergoes an initial “ringing-up” phase, where the load waves propagate back and forth in the specimen itself. During this phase, dynamic force equilibrium is not achieved ( $F_1 \neq F_2$ ). Dynamic force equilibrium can be monitored by conducting a 2-wave analysis. The 1-wave analysis simply uses the force at the specimen-transmitter bar interface to calculate the stress history in the specimen, or:

$$F_2 = AE\varepsilon_i \quad . \quad (3.10)$$

The force at the specimen-incident bar interface is,

$$F_1 = AE(\varepsilon_i + \varepsilon_r) \quad . \quad (3.11)$$

The dynamic equilibrium assumption made in the 1-wave analysis requires that,

$$\varepsilon_i = \varepsilon_i + \varepsilon_r \quad . \quad (3.12)$$

A second stress history can be determined using  $F_1$  instead of  $F_2$ . The 2-wave stress history can be written as,

$$\sigma(t) = \frac{EA[\varepsilon_i(t) + \varepsilon_r(t)]}{A_s} \quad . \quad (3.11)$$

A photograph of the actual apparatus used in the experiments is found in Figure 24 (b). The bars are comprised of 12.7 mm diameter Ti-6Al-4V. The incident and transmitter bars are 1886

mm long. The 616 mm long striker bar generates a 245  $\mu$ s long square strain pulse on impact with the incident bar. The strain pulses in the incident and transmitter bars are measured using two full Wheatstone bridges, each constructed with four Micro-Measurements ED-DY-125AC-10C strain gages (1000  $\Omega$ ) positioned in the center of each bar. The positions are shown schematically as Gage A and Gage B, respectively in Figure 24 (a). The bridges are powered with 15.0 V excitation using two separate HP 3611A power supplies. The output signals are conditioned with Tektronix ADA400A differential preamplifiers with a low-pass filter upper bandwidth of 100 KHz. The signals are recorded using a four channel, 350 MHz, 8-bit Tektronix TDS5034B digital phosphor oscilloscope at a rate of 2.5E6 samples per second. Compression SHB experiments are conducted on 3.048 mm long, 3.048 mm diameter specimens which is the same geometry used in the low rate compression experiments. Molybdenum disulfide grease is used to lubricate the contact surfaces of the specimen with the incident and transmitter bars.

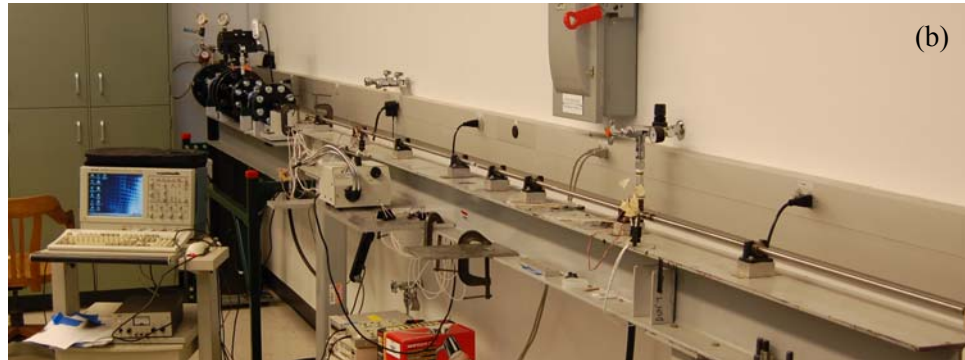
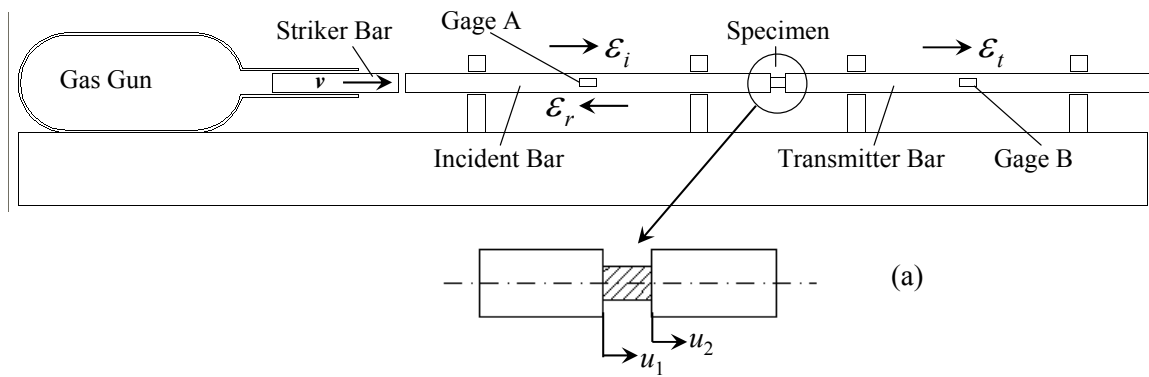


Figure 24. Compression split Hopkinson bar: (a) schematic representation of a typical compression SHB apparatus, (b) compression SHB used in this research.

Sample data from a compression SHB experiment on a specimen fabricated from 2024-T351 aluminum are presented in Figure 25. Wave data are presented in Figure 25 (a). The black trace

is the strain history in the incident bar. Both the incident ( $\epsilon_i$ ) and reflected ( $\epsilon_r$ ) strain pulses are measured with gage A in Figure 24 (a). The gray trace is the strain history in the transmitter bar measured using gage B in Figure 24 (a). This record provides the transmitted strain pulse ( $\epsilon_t$ ). Reduced time history data of engineering stress, strain rate and engineering strain are shown in Figure 25 (b). The engineering stress (black trace) is proportional to the transmitted pulse, according to Equation 3.7. The strain rate history is proportional to the reflected pulse (see Equation 3.8) and is not constant for the duration of the experiment. The strain rate decreases from  $\sim 2000 \text{ s}^{-1}$  to  $\sim 1000 \text{ s}^{-1}$  as the experiment progresses. An average strain rate of  $1476.44 \text{ s}^{-1}$  is calculated for this particular experiment. The strain history is displayed as the dashed trace. Three force versus displacement curves are shown in Figure 25 (c). Engineering stress-strain curves calculated using the 1-wave and 2-wave analyses discussed above are represented by the solid black and dashed black traces, respectively. For strains larger than 0.045, dynamic force equilibrium is achieved. The gray trace represents the true stress versus true strain curve of the specimen assuming volume constancy calculated using the 1-wave analysis.

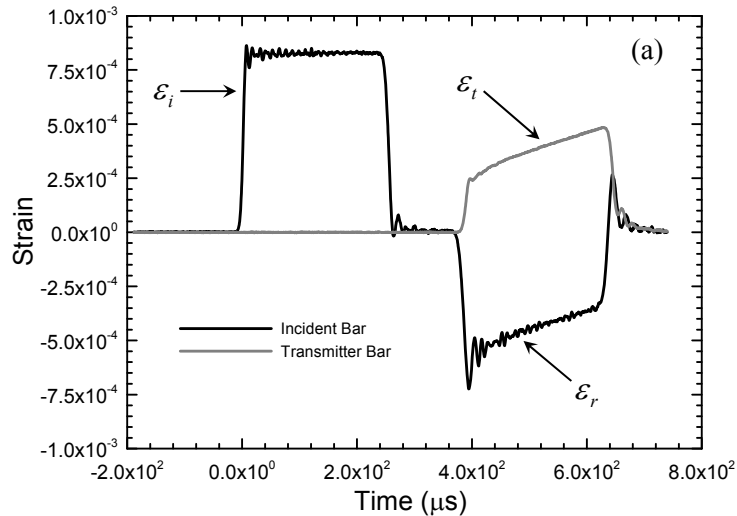
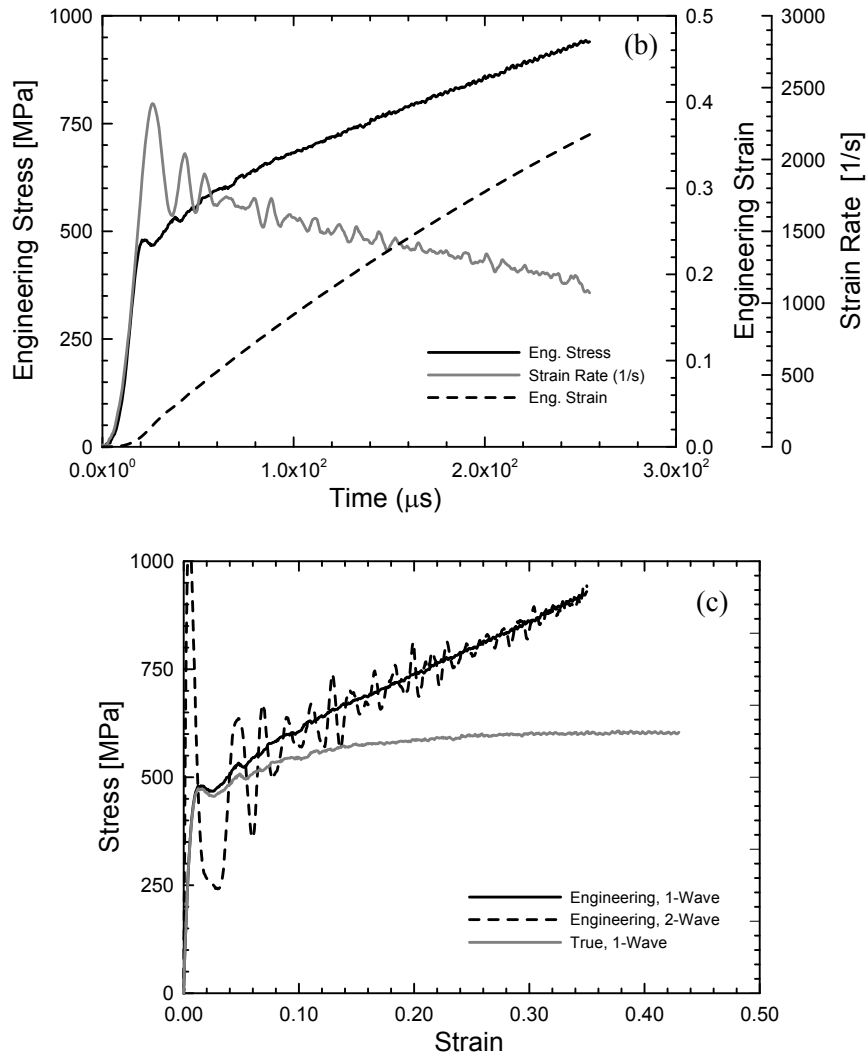


Figure 25. Sample data from a compression SHB experiment on 2024-T351 aluminum: (a) wave data, (b) reduced history data, (c) stress strain data. (Continued)

Figure 25 continued



### Dynamic Punch Experiments

Punch experiments are conducted to study the dynamic ductile fracture behavior of 2024-T351 aluminum. The compression SHB apparatus, described in the previous section, is modified for the experiments. A hardened (HRC 47) 4340 steel punch is threaded into the end of the incident bar, see Figure 26 (a). Three punch geometries are used, two with tip radii of 2.39 mm and 4.75 mm and one blunt. A 1.473 mm thick, 14.732 mm diameter 2024-T351 aluminum disk specimen is glued between two Ti-6Al-4V specimen adaptors. The specimen assembly is glued to a Ti-6Al-4V bar adaptor that is threaded into the transmitter bar. Impedance matching is implemented to minimize undesirable wave reflections at the punch-incident bar interface and the

specimen assembly-transmitter bar interface. The punch displacement relative to the specimen can be unrestricted or restricted to a pre-determined magnitude to investigate the failure mode evolution of the specimen. Two additional components are proposed to the setup to conduct restricted displacement dynamic punch experiments, see Figure 26 (b). A VASCOMAX C-350 stop-ring is used to restrict the relative displacement of the punch into the specimen. A 7075-T6 aluminum adaptor is also added to protect the end of the incident bar from deformation after the stop ring is engaged. This technique has been utilized previously by researchers to limit the amount of shear strain imparted into a dynamic shear experiment on a hat-shaped specimen [68].

The analysis for this experiment is similar to that presented for standard compression SHB testing. In this case, the contact force between the specimen and the transmitter bar is proportional to the transmitted strain pulse ( $\varepsilon_t$ ):

$$F_2(t) = AE\varepsilon_t(t) \quad . \quad (3.12)$$

The relative velocity between the punch and the specimen is proportional to the reflected strain pulse ( $\varepsilon_r$ ):

$$\dot{u}(t) = \dot{u}_1(t) - \dot{u}_2(t) = 2c_b \varepsilon_r(t) \quad . \quad (3.13)$$

The relative displacement between the punch and the specimen is calculated by integrating the velocity history:

$$u(t) = u_1(t) - u_2(t) = \int_0^t \dot{u}(t) dt \quad . \quad (3.14)$$

Therefore, a dynamic force versus displacement curve can easily be constructed. Dynamic force equilibrium can be monitored using the two wave analysis described in the previous section. This analysis uses the contact force between the punch and the disk specimen, or:

$$F_1(t) = AE[\varepsilon_i(t) + \varepsilon_r(t)] \quad . \quad (3.15)$$

A high speed, three dimensional DIC system is used to acquire an independent measurement of the relative displacement between the punch and specimen. The system, shown in Figure 39, consists of two Photron SA1.1 high speed cameras and a commercially available DIC software package. Typical frame rates for these experiments are 105,000 to 135,000 fps.

Results from an unrestricted test using the 2.39 mm radius punch are presented in Figure 27. Figure 27 (a) presents wave records from the incident bar (black trace) and the transmitter bar (gray trace). Figure 27 (b) shows reduced data from the same experiment. The solid trace is the contact force history between the punch and the specimen. The dashed trace is the history of the relative velocity between the punch and specimen. The relative velocity is nearly constant at 22.5

m/s for the duration of the experiment. Two relative displacement traces are also presented in Figure 27 (b). The first (distinguished with diamonds) is integrated from the velocity record, while the second is measured using the DIC technique. The independent relative displacement measurements agree to within 1.6% at a peak relative displacement of roughly 5.5 mm. Force versus displacement data are shown in Figure 27 (c). The solid trace is generated using the 1-wave analysis (computed using the transmitted wave,  $\epsilon_t$ ), while the dashed trace is computed using the 2-wave analysis (calculated using the sum of the incident and reflected waves,  $\epsilon_i + \epsilon_r$ ). Figure 27 (c) shows that dynamic force equilibrium is achieved at a displacement of roughly 0.6 mm.

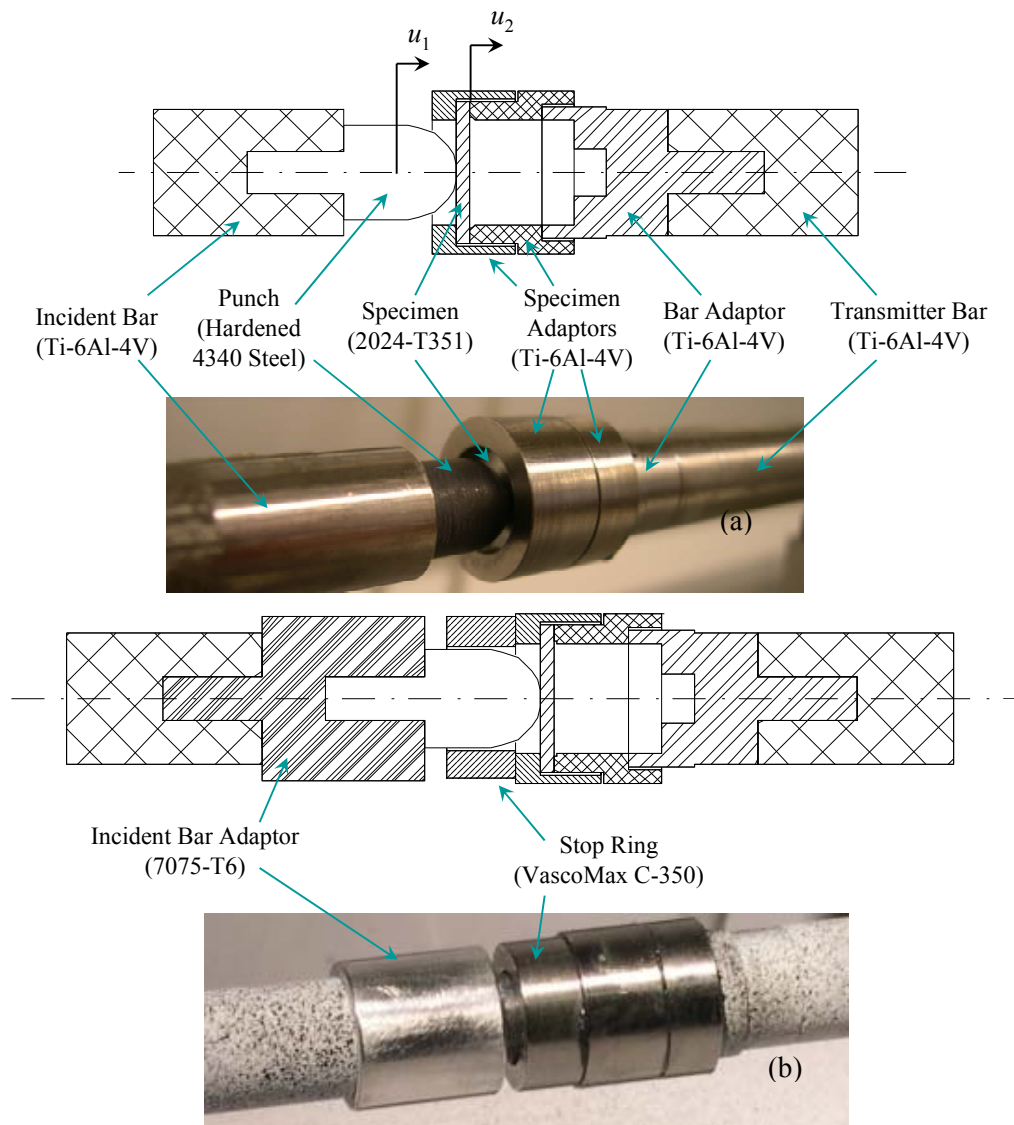


Figure 26. Experimental setup for dynamic punch testing on a compression SHB apparatus, (a) configured for unrestricted displacement, (b) configured for restricted displacement.

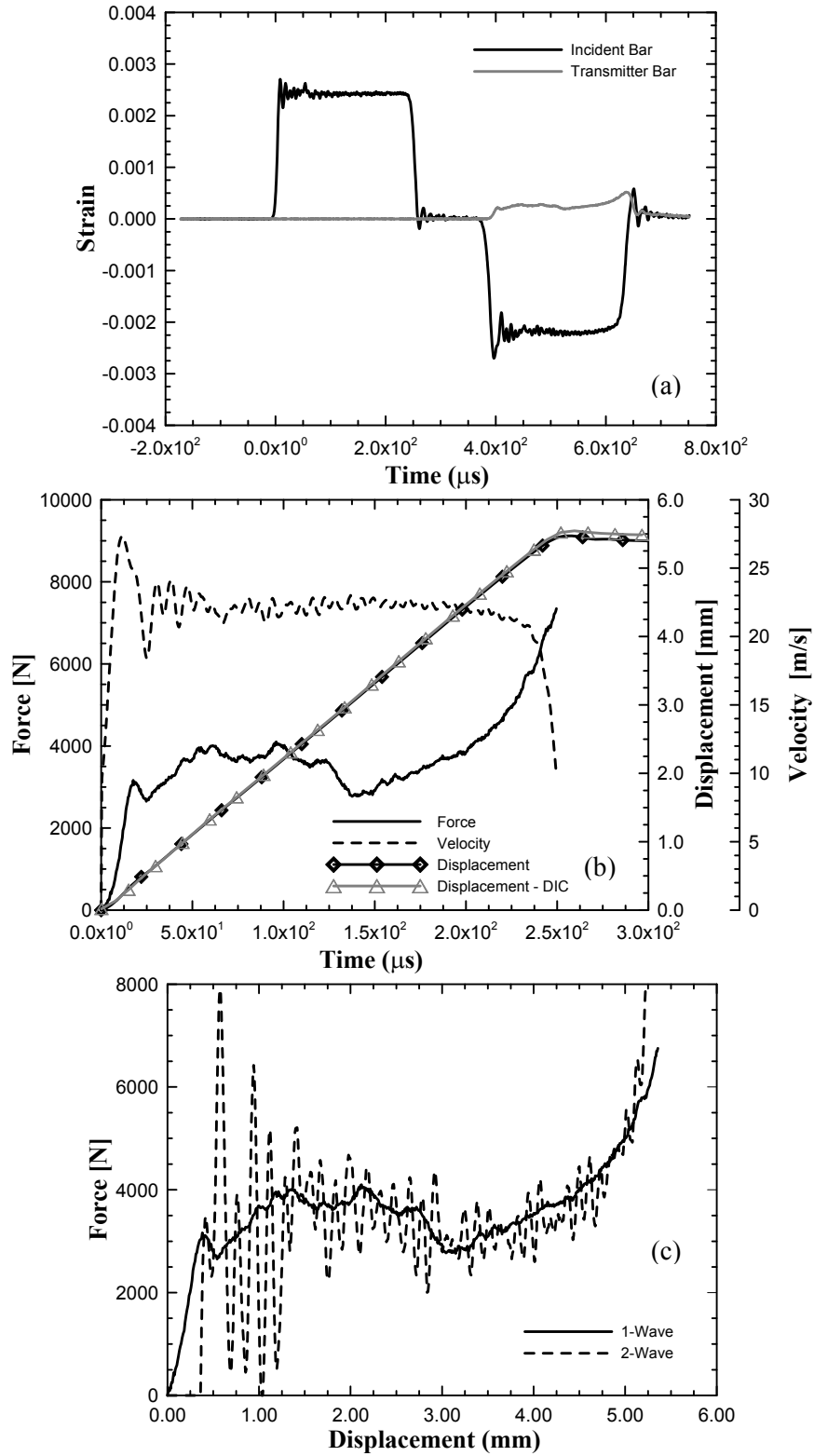


Figure 27. Experimental results from an unrestricted punch test (2.39 mm punch radius): (a) split Hopkinson bar wave data, (b) reduced history data including transmitted force, relative velocity and relative displacement, (c) 1-wave and 2-wave force vs displacement data.

## Tension SHB Experiments

The SHB apparatus can also be used to characterize a material's strain rate sensitivity under tensile loading. The apparatus is similar to the compression SHB, the obvious difference is that a tensile load pulse must be generated instead of a compression one. This has been successfully accomplished using several different techniques. The first technique consists of firing a striker tube in the opposite direction of the specimen into a flanged incident bar [70].

A second technique uses a "top hat"-shaped specimen geometry [70]. The "brim" of the specimen rests on the surface of a transmitter tube. The incident bar is a solid bar which contacts the surface of the specimen that rests inside the transmitter tube. The load pulse is generated using the same technique for the compression bar – a striker bar impacting the end of the incident bar. The specimen geometry and the configuration of the incident bar and transmitter tube ensure that the sample is loaded in tension. Drawbacks to this technique include complex specimen geometry and, more importantly, the specimen gage lies inside the transmitter bar which eliminates the option of using optical strain measurement techniques directly on the surface of the specimen.

A third technique uses a standard compression bar apparatus with a collar that fits over the tension specimen and contacts the incident and transmitter bars [72]. In this technique, a compressive load pulse is generated in the transmitter bar. When the pulse reaches the specimen, it is transferred through the collar into the incident bar, protecting the tension specimen from compressive load. When the pulse reaches the free end of the incident bar, the wave reflects as a tensile pulse. The tensile pulse then loads the specimen, since the collar can only support compressive loading. This technique suffers from the same problem as the previously described technique: the specimen is obscured from view by the collar, negating the possible use of optical measurement techniques. It is also difficult to ensure that the initial compressive load does not pre-load the specimen.

This research uses a direct-tension SHB apparatus [69] for dynamic tension experiments. A sketch of the apparatus is shown in Figure 28. The tensile load pulse is generated by attaching a pulley fixture to the end of the incident bar. A mechanical clamp is used to grip the incident bar and load is applied to the clamped section of the bar using a cable and a hydraulic cylinder. The section of the incident bar between the clamp and the pulley carries a static tensile load,  $P$ . The remainder of the incident bar (to the right of the clamp) is unloaded. A pin in the clamp is broken

using a second hydraulic cylinder and an elastic tensile pulse ( $\varepsilon_i$ ) propagates down the incident bar from the clamp toward the specimen. The amplitude of the strain pulse is,

$$\varepsilon_i = \frac{P}{2EA} \quad , \quad (3.16)$$

where,  $E$  and  $A$  are the elastic modulus and cross sectional area of the incident bar, respectively. The experiment then becomes similar to the previously described compression SHB experiment. As the specimen is deformed plastically, part of the load pulse is transmitted through to the transmitter bar ( $\varepsilon_t$ ) and part is reflected back into the incident bar as a compressive wave ( $\varepsilon_r$ ). The transmitted pulse is proportional to the engineering stress in the specimen while the reflected pulse is proportional to the strain rate. The disadvantage of the stored-load wave generation technique is that the reflected pulse is not as easily resolved as it is for the compression SHB. The inertia of the pulley system attached to the end of the incident bar would obscure the reflected pulse if the strain gages were mounted at the center of the incident bar. Two gages, identified as gage A and gage B in Figure 28, are mounted on the incident bar to resolve this issue. The motion of the end of the incident bar, which can be found using the method of characteristics, is:

$$\dot{u}_1(t) = \frac{1}{\rho A c_b} [F_A(t-t_A) + F_A(t-t_A+2t_B) - F_B(t+t_B)] \quad , \quad (3.17)$$

where,  $F_A(t)$ , and  $F_B(t)$  are the force histories in the incident bar measured by gage A and gage B, respectively.  $t_A$  and  $t_B$  are the durations required for an elastic wave to propagate from the specimen to gages A and B, respectively. The motion of the end of the transmitter bar is:

$$\dot{u}_2(t) = \frac{1}{\rho A c_b} [F_C(t+t_C)] \quad (3.18)$$

where,  $F_C(t)$  is the force history in the transmitter bar measured by gage C and  $t_C$  is the duration required for an elastic wave to propagate from the specimen to gage C. The strain rate for this experiment with a specimen gage length,  $L_s$ , is:

$$\dot{\varepsilon}(t) = \frac{\dot{u}_1(t) - \dot{u}_2(t)}{L_s} = \frac{1}{\rho A c_b L_s} [F_A(t-t_A) + F_A(t-t_A+2t_B) - F_B(t+t_B) - F_C(t+t_C)] \quad . \quad (3.19)$$

The engineering strain is simply the time integral of the strain rate, see Equation 3.9. The engineering stress in the specimen is:

$$\sigma(t) = \frac{EA\varepsilon_i(t)}{A_s} = \frac{F_C(t+t_C)}{A_s} \quad , \quad (3.20)$$

where,  $A_s$  is the initial cross-sectional area of the tension specimen.

The tension SHB apparatus used for this research is shown in Figure 29. The incident and transmitter bars are comprised of 12.7 mm diameter 7075-T6 aluminum rods. The clamped section of the incident bar is 1562 mm long which stores a 630  $\mu$ s load pulse. The free section of the incident bar is 1984 mm long and the transmitter bar is 1729 mm long. The force pulses in the incident and transmitter bars are measured using three full Wheatstone bridges, each constructed with four active Micro-Measurements ED-DY-075AM-10C strain gages (1000  $\Omega$ ) positioned at the locations shown schematically as gage A, gage B, and gage C in Figure 28. The bridge excitation, signal conditioning and data acquisition are identical to those used for the compression SHB apparatus. 2024-T351 aluminum specimens with dimensions identical to those in Figure 7 (a) are epoxied into adaptors that are bonded between the incident and transmitter bars, see Figure 30. Figure 30 (a) shows the specimen instrumented with a Micro-Measurements EA-06-062AQ-350 strain gage. Figure 30 (b) shows a side-view of the specimen-adaptor joint. The specimen flanges are bonded in slits in two adaptors with Emerson and Cuming TRA-BOND 2106T two part epoxy. The adaptors are then bonded to the incident and transmitter bars, respectively. A fractured specimen is shown in Figure 30 (c).

Sample data from a tension SHB experiment on a 2024-T351 aluminum specimen are presented in Figure 31. Wave data are presented in Figure 31 (a). The solid black trace is the force history in the incident bar recorded by gage A ( $F_A$ ) while the dashed, black trace is the force history in the incident bar recorded by gage B ( $F_B$ ). The gray trace is the force history in the transmitter bar measured using gage C ( $F_C$ ). A measure of dynamic force equilibrium in the specimen is attained by comparing the force histories measured by gages B and C. Gages B and C are positioned on the incident and transmitter bars such that they are equidistant from specimen. Since the bars are comprised of the same material, the elastic waves travel at the same velocity. Therefore, after the load pulse reaches the specimen, gage B gives a time history of force at the joint between the incident bar and the specimen. Likewise, gage C gives a time history of the joint between the specimen and the transmitter bar. After a brief rise time, the forces measured by gages B and C equilibrate at  $\sim 470$   $\mu$ s in Figure 31 (a), showing dynamic force equilibrium in the specimen. Reduced time history data of engineering stress, strain rate and engineering strain are shown in Figure 31 (b). The engineering stress (black trace) is proportional to the transmitted pulse, according to Equation 3.20. The strain rate history, calculated with Equation 3.19, is nearly constant at 505.401  $\text{s}^{-1}$  for the duration of the experiment. The strain history integrated from the strain rate is displayed as the black, dashed trace, while an independent measurement from a strain gage mounted directly on the specimen is represented by

the gray, dashed trace. These two independent strain measurements agree up to a strain level of 0.03, when the strain gage on the specimen fails. Engineering and true stress versus strain curves are shown in Figure 31 (c). The engineering stress-strain curve is calculated using Equations 3.19, 3.9 and 3.20 and is represented by the solid black trace. The gray trace represents the true stress versus true strain curve of the specimen assuming volume constancy.

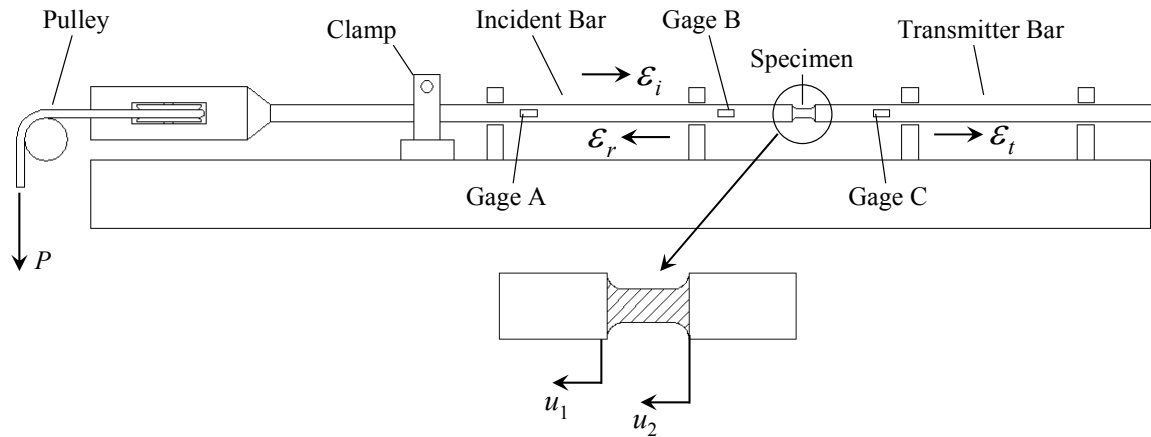


Figure 28. Sketch of a direct-tension SHB apparatus.

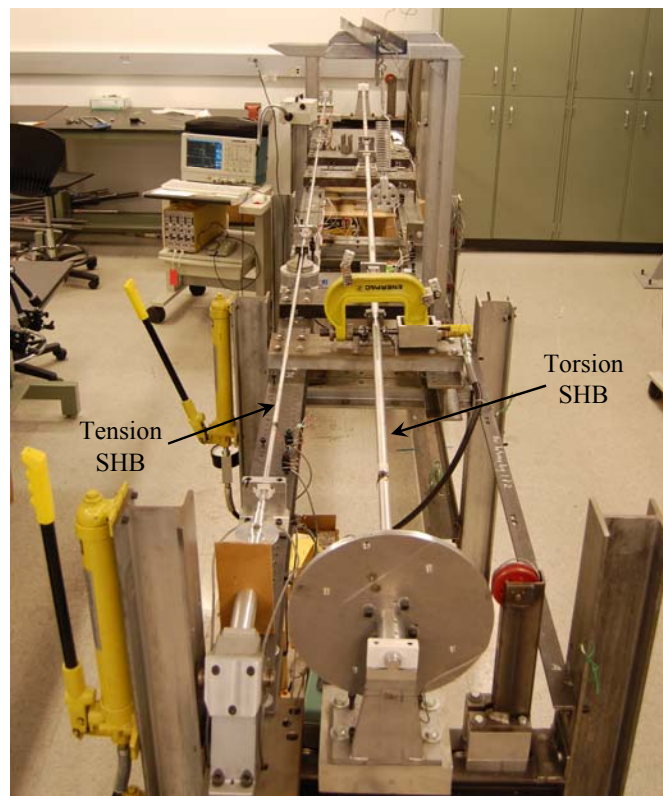


Figure 29. A direct-tension SHB apparatus and a stored-torque torsion SHB apparatus.

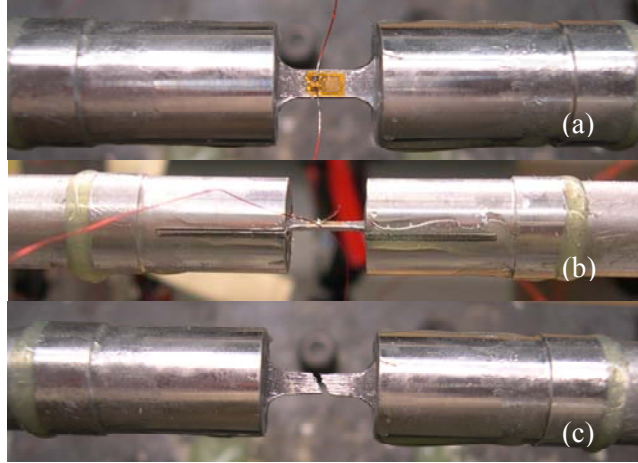


Figure 30. Specimen attachment for a tension SHB experiment: (a) top view of a specimen instrumented with a strain gage, (b) side view of the specimen, (c) post-test photo.

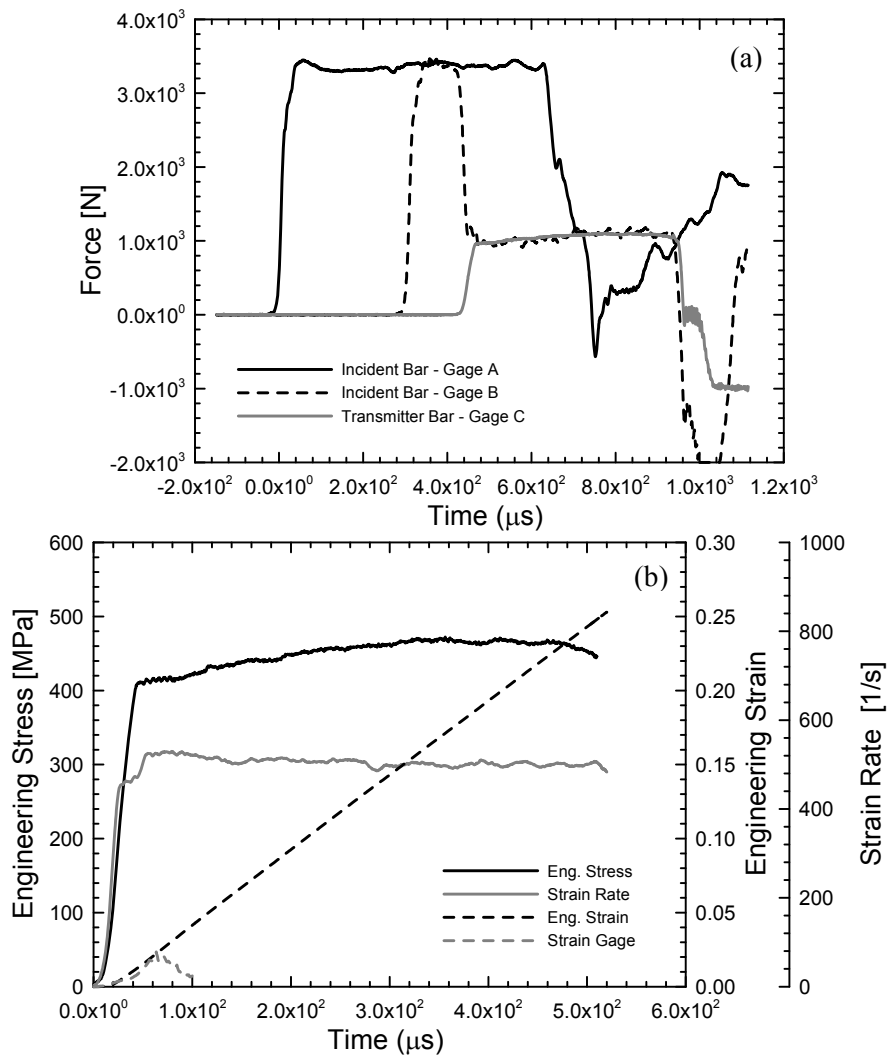
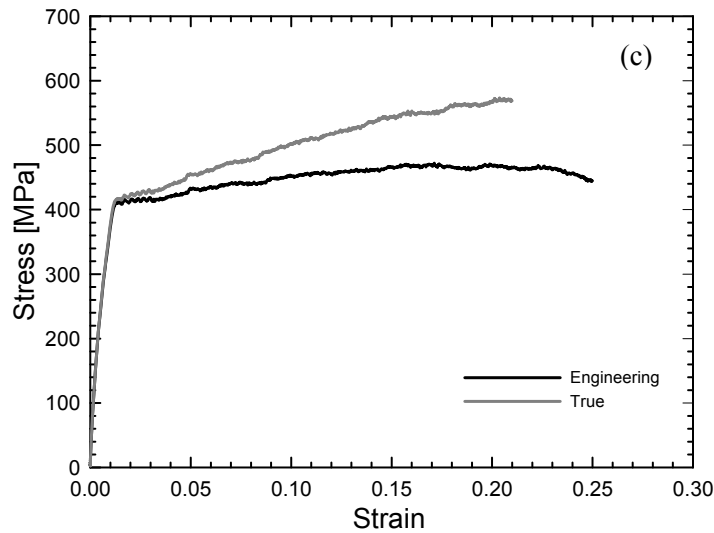


Figure 31. Sample data from a tension SHB experiment on 2024-T351 aluminum: (a) wave data, (b) reduced history data, (c) stress strain data. (Continued)

Figure 31 continued



### Torsion SHB Experiments

A torsion SHB apparatus can be used to characterize the strain rate sensitivity of a material under shear loading. The apparatus is similar to both the tension SHB and compression SHB except a torsional load pulse is generated instead of a tensile or compressive one. Two load-generating techniques have been utilized for this purpose. The first technique uses two explosive charges in contact with two tabs that protrude symmetrically from the incident bar [71]. The charges are detonated simultaneously to provide a symmetric torque load pulse to the incident bar through the tabs. The advantage to this technique is short rise times, however, the use of explosives provide several disadvantages. An obvious disadvantage is the safety measures which must be implemented whenever explosives are used in a laboratory setting. Second, the detonation of the two charges must be near-simultaneous to ensure a pure torsion load pulse is generated. If the charges do not fire simultaneously, a bending wave, which travels faster than shear waves, will be generated. Pulse smoothers are typically used to filter out high-frequency components of the loading wave. Another disadvantage is the shape of the pulse profile. The load pulse amplitudes are typically not constant, leading to variable strain rates in the specimen throughout the test duration. Also, explosively generated load pulses are relatively short, providing practical limits on the maximum attainable shear strains in the specimen.

This research uses a stored-torque SHB [71] to characterize the rate sensitivity of 2024-T351 aluminum in shear. A sketch of the apparatus is presented in Figure 32. The load pulse

generation technique is similar to the one employed by the direct-tension SHB described above. The torsional load pulse is generated by attaching a torque wheel fixture to the end of the incident bar. A mechanical clamp is used to grip the incident bar and a pure torque is applied to the wheel through a couple using a cable and a hydraulic cylinder. The section of the incident bar between the clamp and the pulley carries a static torque,  $T$ . The remainder of the incident bar (to the right of the clamp) is unloaded. A pin in the clamp is broken using a second hydraulic cylinder and an elastic shear pulse ( $\gamma_i$ ) propagates down the incident bar from the clamp toward the specimen. The amplitude of the shear strain pulse on the surface of the bar is,

$$\gamma_i = \frac{T r_b}{2GJ} \quad , \quad (3.21)$$

where,  $r_b$  is the radius of the bar and  $G$  and  $J$  are the shear modulus and polar moment of inertia of the incident bar, respectively. The experiment then becomes similar to the previously described SHB experiments. As the specimen is deformed plastically, part of the load pulse is transmitted through to the transmitter bar ( $\gamma_t$ ) and part is reflected back into the incident bar as a torsional wave with opposite direction of the incident pulse ( $\gamma_r$ ). The transmitted pulse is proportional to the shear stress in the specimen while the reflected pulse is proportional to the strain rate. This technique suffers from the same disadvantage that the direct-tension bar does: the inertia of the torque wheel attached to the end of the incident bar would obscure the reflected pulse if the strain gages were mounted at the center of the incident bar. The issue is resolved in the same fashion as for the tension bar: two gages, identified as gage A and gage B in Figure 32 are mounted on the incident bar. The rotational velocity of the end of the incident bar, determined using the method of characteristics, is:

$$\dot{\theta}_1(t) = \frac{1}{\rho J c_T} [T_A(t-t_A) + T_A(t-t_A+2t_B) - T_B(t+t_B)] \quad , \quad (3.22)$$

where,  $c_T = \sqrt{\frac{G}{\rho}}$  is the transverse elastic wave speed,  $T_A(t)$ , and  $T_B(t)$  are the torque histories in the incident bar measured by gage A and gage B, respectively.  $t_A$  and  $t_B$  are the durations required for a transverse elastic wave to propagate from the specimen to gages A and B, respectively. The motion of the end of the transmitter bar is:

$$\dot{\theta}_2(t) = \frac{1}{\rho J c_T} [T_C(t+t_C)] \quad , \quad (3.23)$$

where,  $T_C(t)$  is the torque history in the transmitter bar measured by gage C and  $t_C$  is the duration required for an elastic wave to propagate from the specimen to gage C. The shear strain rate for this experiment is:

$$\dot{\gamma}(t) = \frac{r_m [\dot{\theta}_1(t) - \dot{\theta}_2(t)]}{L_s} = \frac{r_m}{\rho J C_T L_s} [T_A(t - t_A) + T_A(t - t_A + 2t_B) - T_B(t + t_B) - T_C(t + t_C)] , \quad (3.24)$$

where,  $r_m$  is the mean gage radius and  $L_s$  is the gage length of the thin-walled tube specimen. The shear strain is the time integral of the strain rate, or:

$$\gamma(t) = \frac{r_m [\theta_1(t) - \theta_2(t)]}{L_s} = \int_0^t \dot{\gamma}(t) dt . \quad (3.25)$$

The shear stress in the specimen is:

$$\tau(t) = \frac{G J r_m \gamma(t)}{r_b J_s} = \frac{r_m T_C(t + t_C)}{J_s} , \quad (3.26)$$

where,  $J_s$  is the polar moment of inertia of the torsion specimen.

The torsion SHB apparatus used for this research is shown in Figure 29. The incident and transmitter bars are comprised of 22.225 mm diameter 7075-T6 aluminum rods. The clamped section of the incident bar is 1227 mm long and stores an 810  $\mu$ s torsional loading pulse. The free section of the incident bar is 2283 mm long and the transmitter bar is 2026 mm long. The torque pulses in the incident and transmitter bars are measured using three full Wheatstone bridges, each constructed with four active Micro-Measurements 1000  $\Omega$  strain gages positioned at the locations shown schematically as gage A, gage B, and gage C in Figure 32. The bridges are powered with 20.0 V excitation using three separate HP 3611A power supplies. The signal conditioning and data acquisition are identical to those used for the compression and tension bars. Spool specimens are fabricated from 2024-T351 aluminum, see Figure 33 (a). The dimensions are similar to those used in the low rate torsion experiments. The flanges of the specimens have larger outside diameters diameter to match the impedance of the Hopkinson bars. The flanges are bonded directly to the incident and transmitter bars with Emerson and Cuming TRA-BOND 2106T two part epoxy, see Figure 33 (b). A post-test photograph of a fractured spool specimen is shown in Figure 33 (c).

Sample data from a torsion SHB experiment on a 2024-T351 aluminum specimen are presented in Figure 34. Wave data are presented in Figure 34 (a). The solid black trace is the torque history in the incident bar recorded by gage A ( $T_A$ ) while the dashed, black trace is the torque history in the incident bar recorded by gage B ( $T_B$ ). The gray trace is the torque history in the transmitter bar measured using gage C ( $T_C$ ). A measure of dynamic torque equilibrium in the

specimen is attained by comparing the torque histories measured by gages B and C. Gages B and C are positioned on the incident and transmitter bars such that they are equidistant from specimen. Since the bars are comprised of the same material, the elastic waves travel at the same velocity. Therefore, after the load pulse reaches the specimen, gage B records a time history of torque at the joint between the incident bar and the specimen. Likewise, gage C provides a torque history at the joint between the specimen and the transmitter bar. After a brief rise time, the torques measured by gages B and C equilibrate at  $\sim 730 \mu\text{s}$  in Figure 34 (a), showing dynamic torque equilibrium in the specimen. Reduced time history data of shear stress, shear strain rate and shear strain are shown in Figure 34 (b). The shear stress (black trace) is proportional to the transmitted pulse, according to Equation 3.26. The shear strain rate history, calculated with Equation 3.24, ranges from  $1030 \text{ s}^{-1}$  early in the loading to  $860 \text{ s}^{-1}$  just prior to specimen failure. The average shear strain rate is  $912.324 \text{ s}^{-1}$  for the duration of the experiment. The strain history integrated from the strain rate is displayed as the black, dashed trace. Shear stress versus shear strain and effective stress versus equivalent strain curves are shown in Figure 34 (c). The shear stress-shear strain curve is calculated using Equations 3.24, 3.25 and 3.26 and is represented by the solid, black trace. The gray trace represents the effective stress versus equivalent strain curve calculated using Equations 1.5 and 3.5.

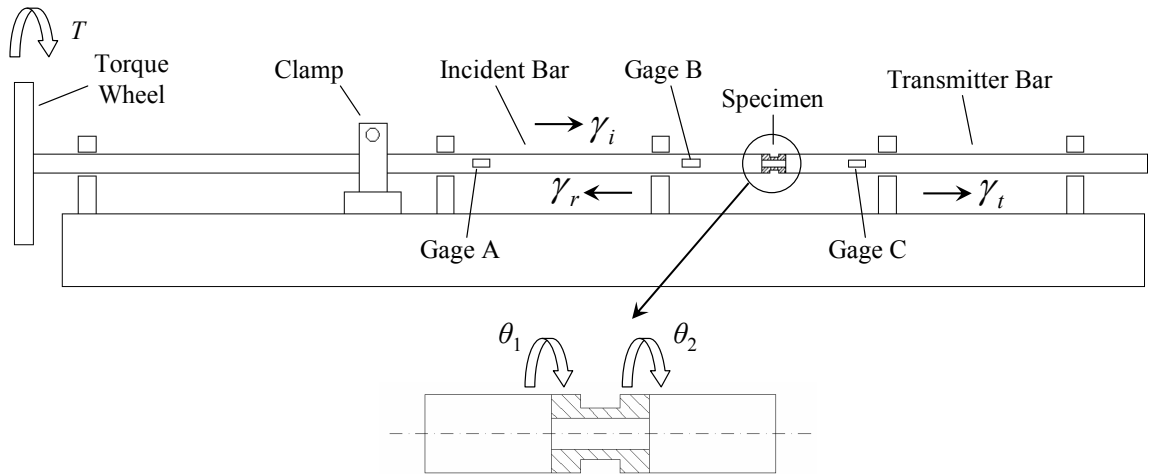


Figure 32. Sketch of a stored-torque SHB apparatus.

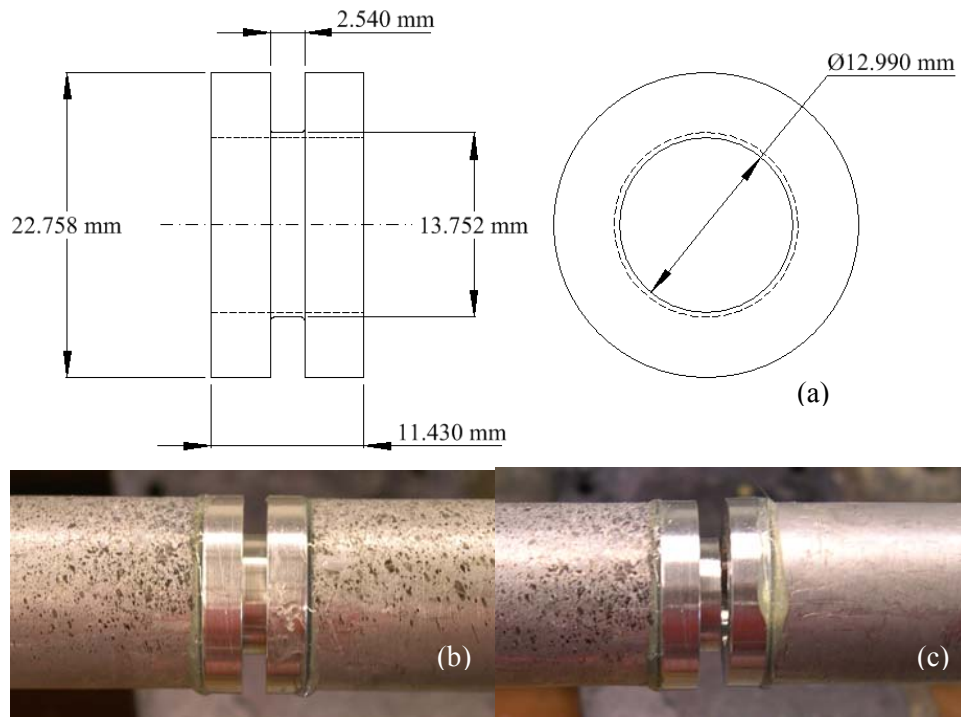


Figure 33. Spool-shaped, thin-walled tube specimen for torsion SHB experiments: (a) drawing, (b) specimen epoxied between incident and transmitter bars, (c) post test photograph.

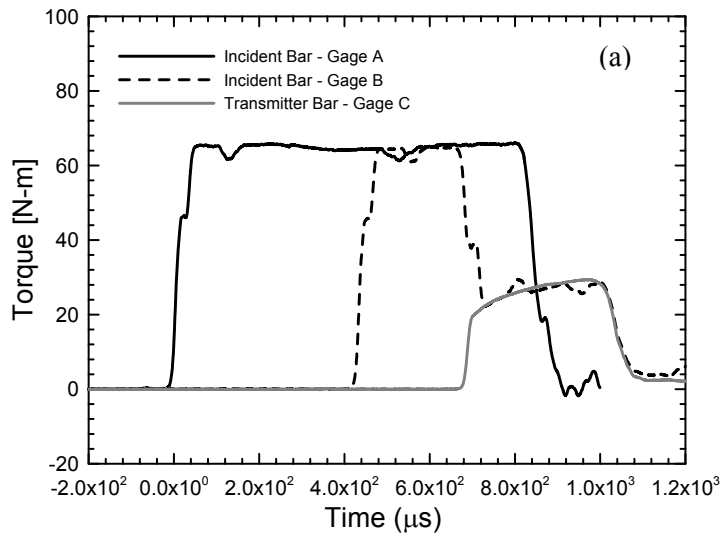
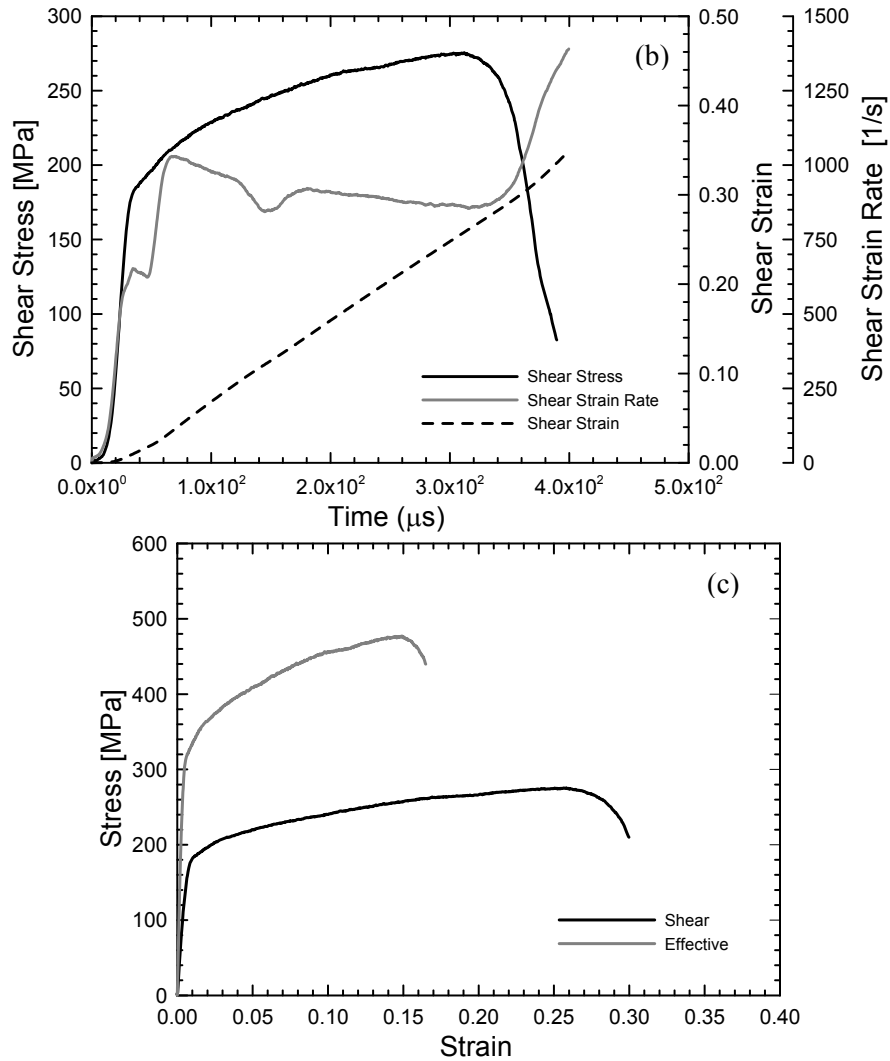


Figure 34. Sample data from a torsion SHB experiment on 2024-T351 aluminum: (a) wave data, (b) reduced history data, (c) stress strain data. (Continued)

Figure 34 continued



### Impact Experiments Conducted by NASA Researchers

Investigators at NASA Glenn Research Center have conducted normal impact experiments in support of the FAA's uncontained engine debris mitigation project [43]. The research presented in Chapter 5 compares numerical simulations of impact experiments to data generated in these experiments. The experimental techniques used by the NASA researchers are briefly described in this section.

Square (381 mm by 381 mm) target panels, see Figure 35 (a), fabricated from either 3.175 mm thick 2024-T3 aluminum sheet or 12.7 mm thick 2024-T351 aluminum plate are constrained in a heavy steel fixture with a 254 mm diameter circular aperture by a 330 mm bolt circle. The

rear surfaces of select target panels are instrumented with five strain gages as shown in Figure 35 (b). One gage is centered at the impact location of the panel oriented in the rolled direction of the plate. Three additional strain gages, also oriented in the rolled direction, are positioned in 25.4 mm increments from the target panel center. The final gage is oriented in the transverse direction of the plate 50.8 mm from the target panel center. Strain measurements for the 3.175 mm sheet targets and the 12.7 mm plate targets are shown in Figure 56 (a) and (b), respectively.

Cylindrical, titanium alloy (Ti-6Al-4V) projectiles, see Figure 36, are used to impact the 3.175 mm thick target panels. The projectiles are 7.78 mm long, 12.7 mm diameter cylinders with a nearly blunt impact face (nose radius of 69.85 mm) that transitions with a 0.794 mm fillet radius. The titanium alloy projectiles have a nominal mass of 9.9 gm. A2 tool steel projectiles (HRC 60) are used to impact the 12.7 mm thick target panels. The tool steel projectiles are 28.575 mm long. All other dimensions are identical to those in Figure 36 (a) giving a nominal projectile mass of 28.0 gm.

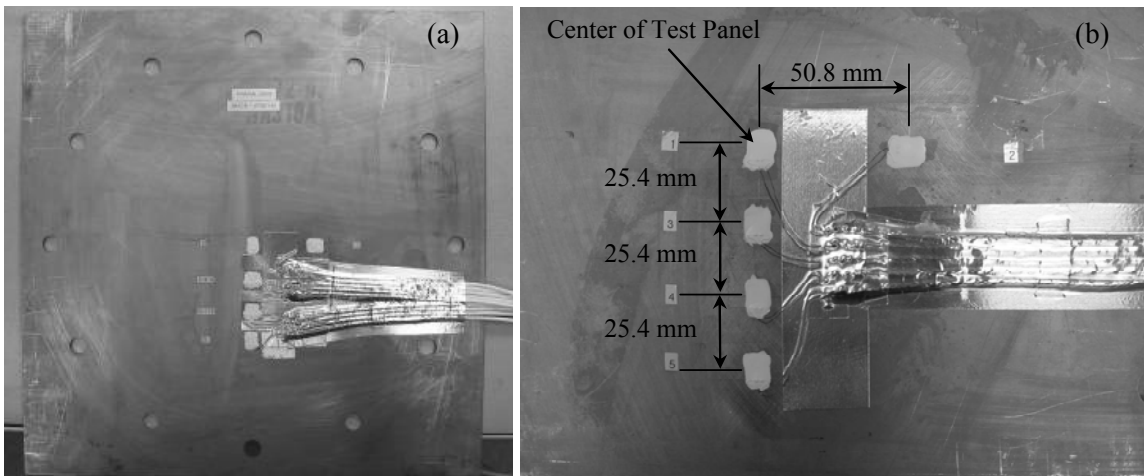


Figure 35. 2024 aluminum target panel, (a) showing the through holes for the 330 mm bolt circle constraint, (b) close-up view of the target panel instrumented with five strain gages, after [43].

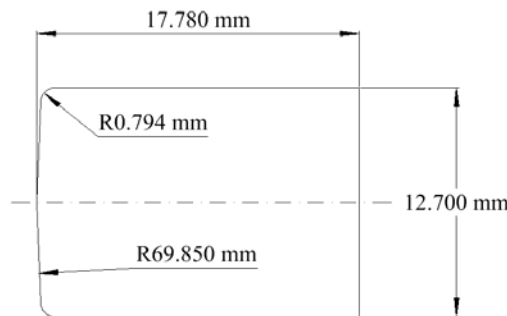


Figure 36. Cylindrical Ti-6Al-4V projectile used to impact the 3.175 mm target panels.

Seven high speed digital cameras are used for each experiment. A calibrated pair of high speed cameras, oriented above and orthogonal to the projectile trajectory, is used with a commercially available point-tracking software system to measure both the impact velocity and orientation of the projectile. In general, the angle between the projectile axis and the plate normal is less than  $4.0^\circ$  for the Ti-6Al-4V projectiles and less than  $2.0^\circ$  for the A2 tool steel projectiles. Typical frame rates for these cameras are 20,000 frames per second. Two additional high speed cameras aft of the target plate provide orthogonal views (top and side) normal to the projectile path. If perforation occurs, data from these cameras are used to measure projectile residual velocity. Calibration tests, with the target panel removed, indicate that the velocities measured with these two cameras are within 1% of those measured with the point tracking system. Frame rates of 12,500 and 8,000 frames per second were used for the side and top view cameras, respectively. For select experiments, two more high speed cameras, located outside of the vacuum chamber for their protection, are focused on the rear surface of the target panel through viewports. Footage from these cameras is used with a commercially available, three dimensional digital image correlation (DIC) software package [27] to measure full-field displacements and calculate strains on the rear surface of the panel. Frame rates for these cameras range from 150,000 frames per second at 128 pixels by 160 pixels resolution to 180,000 frames per second at 128 pixels by 128 pixels resolution. The optics are configured such that the square resolution case (128 pixels by 128 pixels) cover a 101.6 mm by 101.6 mm approximate field of view centered at the impact point of the projectile. Maximum principal strain and displacement data measured with DIC are presented for the 3.175 mm and 12.7 mm thick target panels in Figure 57 and Figure 58, respectively. Finally, a single high speed camera, offset from the projectile trajectory and aimed at the front of the target panel, is used to capture a qualitative view of each impact.

### Digital Image Correlation (DIC)

Three dimensional digital image correlation is used to measure specimen surface displacements and strains for the majority of the experiments in the ductile fracture test program. A brief discussion of the experimental technique is presented here as well as the camera system hardware used for both low and high rate tests. The details of image correlation for experimental mechanics applications are presented thoroughly by Sutton, Orteu and Schreier [27] and by Sutton, McNeil and Schreier [73].

Consider a two dimensional DIC system. In this system, a single digital camera is used to image a flat specimen that is parallel to the camera's sensor. If the specimen surface remains flat and maintains a constant working distance from the camera, the data provided by the single camera is sufficient to determine the deformation in the specimen. The main challenge of DIC for this purpose is to identify points in the reference frame (no deformation in the specimen) in a later frame where significant deformation has accumulated. Each image is comprised of pixels and each pixel has a gray value associated with it. One pixel in the reference frame cannot be uniquely identified in the deformed frame, since there are typically many pixels in deformed image that have exactly the same gray value as the pixel of interest in the reference image. In order to compensate for this, the region around the point of interest in the reference frame is included in the tracking algorithm. This region is typically referred to as a subset or a square  $N$  by  $N$  pixel box centered at the point of interest in the reference frame. Each pixel in the subset contains a gray value, so now there is significantly more information for a tracking algorithm to use. A non-repetitive, high contrast pattern is applied to the specimen surface to ensure that each subset has pixel gray value matrices distinctive enough to be identified by the tracking algorithm. This speckle pattern is typically applied using black spray paint spatter on a white spray paint base-coat, or vice versa. The tracking algorithm works by minimizing a sum of the squared differences functions (SSD function) between the facet in the reference image and the facet in the deformed image. The SSD correlation function is written as [73]:

$$C(\bar{x}, \bar{u}) = \sum [G(\bar{x} + \bar{u}) - F(\bar{x})]^2, \quad (3.27)$$

where,  $G$  and  $F$  are gray values matrices of the deformed and undeformed images, respectively.  $\bar{x}$  is a two element vector which specifies the center pixel location of the subset in the reference image and  $\bar{u}$  is a two element vector specifying the horizontal and vertical displacements from the center of the subset in the reference image to the center of the potential subset in the deformed image. The tracking algorithm searches in the deformed image for a vector,  $\bar{u}$ , which minimizes  $C(\bar{x}, \bar{u})$ .

The tracking algorithm described above only works well if the subset in the deformed image remains square. In many engineering applications, complex deformations arise and the subset shapes evolve significantly in the successive images. To account for this, shape functions are used to model the deformed shape of the subset. When shape functions are used to describe the deformed subset shapes, Equation 3.27 becomes:

$$C(\bar{x}, \bar{u}) = \sum [G(\xi(\bar{x} + \bar{u}, \bar{p}) - F(\bar{x}))]^2, \quad (3.27)$$

where,  $\zeta$  is the subset shape function vector that has a parameter vector  $\bar{p}$ . B-spline shape functions are often used for this purpose. When all of subsets in the reference frame are identified in the deformed image, displacement information is available at the center of each subset. Strain tensors can then be computed according to their continuum mechanics definitions. Malvern provides a good reference for the strain tensor definitions [74].

The experiments conducted in the ductile fracture test series require the use of three dimensional DIC because many of the specimens have three dimensional surface features. Three dimensional objects cannot be resolved with only one camera, therefore, two cameras must be used. This is concept is explained by the sketch in Figure 37. In the figure, the light gray trapezoids represent a mathematical model for the camera sensor. If only one camera is used, C in Figure 37 (a), a feature at point Q and point R will both be imaged on the camera's sensor at point p. Consequently, there is no way to differentiate between these two points using only one camera. If information from a second camera is added, C' in Figure 37 (b), the difference between Q and R can be determined. The points Q and R are imaged at point q' and r', respectively, in the second camera's sensor. This is known as stereo-triangulation and it is only possible if the rays from the each camera are known in the same coordinate system. Therefore, the two camera stereo-rig must be calibrated in the same world coordinate system.

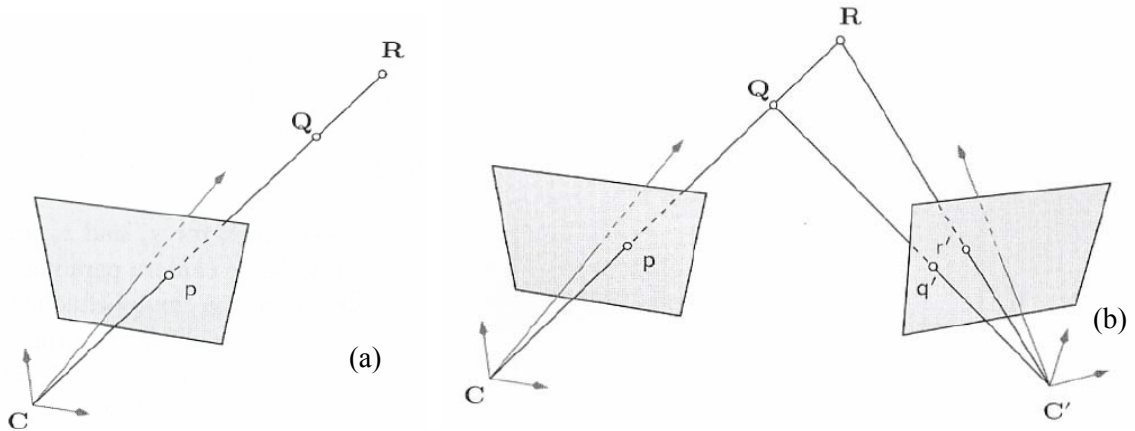


Figure 37. Sketch illustrating that two cameras are necessary to resolve three dimensional features: (a) one camera, (b) two cameras, after [27].

The calibration process establishes transformations between the common world coordinate system and the sensor plane coordinate system for each camera. This consists of three separate transformations for each camera, see Figure 38 (a). The first is a transformation between the three dimensional world ( $R_w$ ) and the three dimensional camera coordinate system ( $R_c$ ). The second is a transformation between the 3D camera system and the 2D image plane coordinate

system which is located at the center of the camera sensor plane ( $R_r$ ). Finally, a transformation is made between image plane coordinate system and the sensor coordinate system ( $R_s$ ) where the 2D sensor-plane spatial position is transformed into pixel coordinates. In the calibration process, several camera parameters are sought. These include four intrinsic parameters which are functions of the camera focal length and the length-to-pixel conversion for the sensor plane and six extrinsic parameters that include three components of a translation vector and three rotations required to go from  $R_w$  to  $R_c$ . Each camera is calibrated independently by capturing images of a calibration grid. For each calibration image captured, a system of equations relating the sensor position of the calibration grid points to the camera parameters is formed. The solution of these equations provide the camera parameters discussed above and the basis to transform camera sensor coordinates to world coordinates. After calibration, the transformations between both  $R_c$  to  $R_w$  and  $R_c'$  to  $R_w$  in Figure 38 (b) are known.

Two systems are used in this research. A low rate system is used for the ductile fracture tension test series and the combined loading test series. This system consists of two Point Gray Research GRAS-20S4M-C cameras with 1624 pixel by 1224 pixel resolution. The cameras are equipped with Schneider 35 mm lenses and acquire images at a maximum rate of nineteen images per second. The low rate cameras are visible in Figure 11. Sample data from the low rate camera system is shown in Figure 10, Figure 12, Figure 13, Figure 20 and in several Figures found in Appendix C and D.

A high rate system is used to for the dynamic punch experiments. This system consists of two Photron SA1.1 cameras with 1024 pixel by 1024 pixels at full resolution. 90 mm Tamron lenses are used with the Photrons. Frame rates of 125,000 fps are achievable at a reduced resolution of 256 pixels by 128 pixels. These settings are typical for the dynamic punch experiments conducted in this research. The high speed camera system is shown on a custom designed vertical mount fixture in Figure 39.

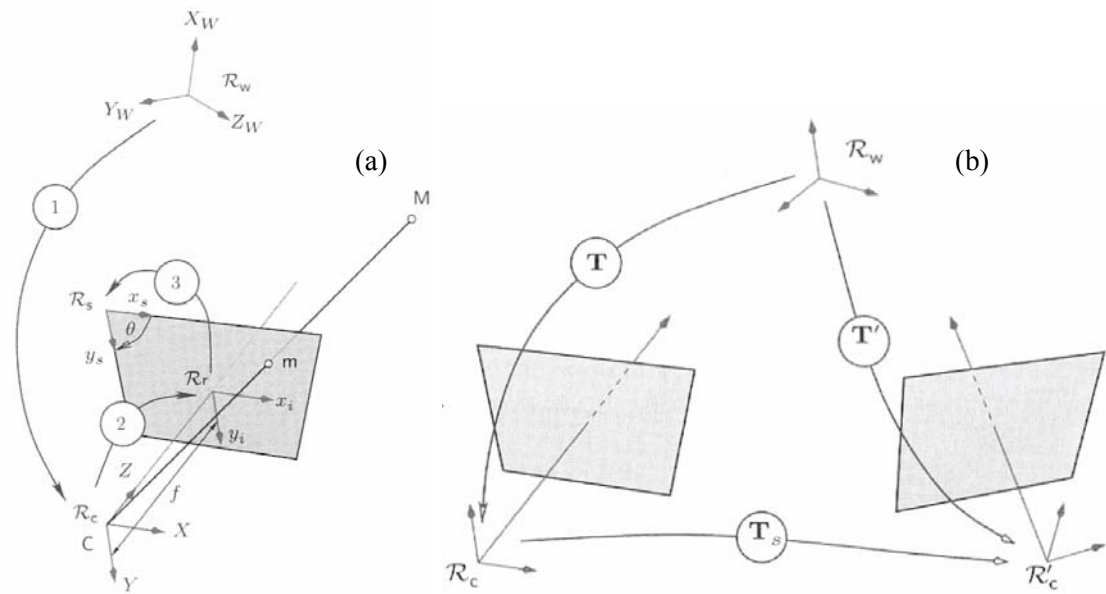


Figure 38: Transformations between coordinate systems for: (a) a single camera model, (b) a stereo-rig camera system, after [27].

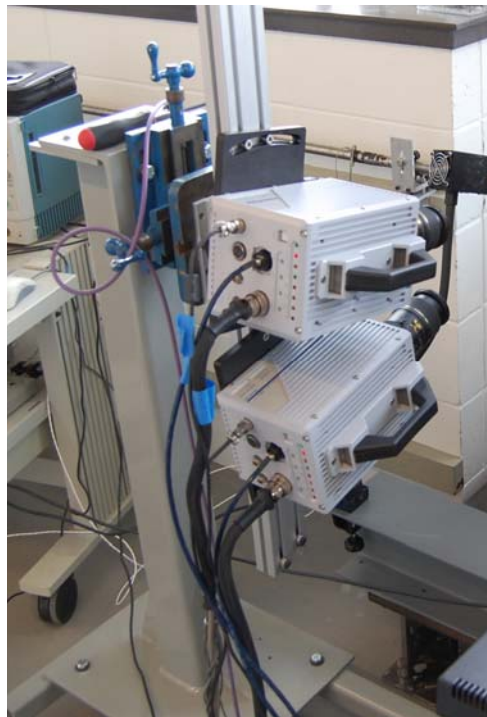


Figure 39. High speed DIC camera system.

## Chapter 4: Experimental Characterization and Anisotropic Modeling of the Plastic Deformation of 2024-T351 Aluminum in Tension, Compression and Shear

This chapter presents the data generated from the plastic deformation characterization test program shown in Table 2. The data presented are results of the low rate tension (on thin smooth specimens), compression and torsion experiments as well as the compression, tension and torsion SHB tests described in Chapter 3. Numerical simulations of select experiments using an anisotropic plasticity model are also presented and compared to the experimental data. Barlat's anisotropic yield function [33] is used to model tension, compression and torsion experiments on specimens oriented in several different directions in the plate.

### Experimental Data

Stress strain curves from tension, compression and torsion tests conducted at room temperature over a wide range of strain rates are presented in Figure 40. True stress versus true strain curves from tension and compression tests are shown in Figure 40 (a) and Figure 40 (b), respectively. All tension and compression stress strain curves in Figure 40 are determined from experiments on specimens oriented in the plate's rolled direction ( $0^\circ$ ). Shear stress versus shear strain curves from torsion tests are shown in Figure 40 (c). Figure 40 illustrates that the material is nearly strain rate insensitive in tension, compression and torsion over the strain rate ranges tested.

Stress data from tension, compression and torsion experiments are plotted versus the logarithm of strain rate in Figure 41. For tension and compression experiments, true stress values extracted at two true strains ( $\varepsilon = 0.075$  and  $\varepsilon = 0.15$ ), are plotted versus the strain rate ( $\dot{\varepsilon}$ ) in Figure 41 (a), and Figure 41 (b), respectively. For torsion experiments, shear stress values extracted at two shear strains ( $\gamma = 0.13$  and  $\gamma = 0.26$ ) are plotted versus the shear strain rate ( $\dot{\gamma}$ ) in Figure 41 (a), and Figure 41 (b), respectively. Figure 41 illustrates that the material has slightly positive strain rate sensitivity in compression and negligible rate sensitivity in both tension and torsion. The repeatability of the experimental results is also on display in Figure 41. In general, the servohydraulic test results are more repeatable than the SHB test results. Appendix

A presents data repeatability for each test conducted in this experimental program. A strain rate insensitive constitutive model could adequately describe the stress strain behavior of 2024-T351 aluminum considering the data set presented in Figure 40 and Figure 41.

Stress strain curves from tension, compression and torsion experiments conducted at an equivalent strain rate of  $1.0 \text{ s}^{-1}$  over a wide range of temperatures are presented in Figure 42. True stress versus true strain curves from tension and compression experiments are presented in Figure 42 (a) and Figure 42 (b), respectively. All tension and compression stress strain curves presented in Figure 42 are determined from tests on specimens oriented in the plate's rolled direction ( $0^\circ$ ). Shear stress versus shear strain curves from torsion experiments are presented in Figure 42 (c). The strength of 2024-T351 aluminum decreases monotonically with increasing temperature in tension, compression and torsion. The strain hardening behavior of the material changes significantly between  $150 \text{ }^\circ\text{C}$  and  $300 \text{ }^\circ\text{C}$ . At  $150 \text{ }^\circ\text{C}$  and below, the material exhibits strain hardening which could be well represented by a power law strain hardening model. Above  $300 \text{ }^\circ\text{C}$ , the material exhibits near elastic-perfectly plastic behavior. The data at  $300 \text{ }^\circ\text{C}$  shows softening behavior with increasing strain. This phenomenon is exacerbated by the necking localization in the tension data, but is also present in the compression and torsion data as well. The rapid onset of the necking localization in tension at  $300 \text{ }^\circ\text{C}$  limits the usefulness of the corresponding true stress true strain curve in Figure 42 (b). Since the cross-sectional area of the specimen was not measured during the experiment, the curve is only valid to a true strain of roughly 0.10. Other researchers have observed this softening behavior and state it is due to dynamic recovery and recrystallization, where dislocations are destroyed by increasing strain and new strain-free grains are created during the deformation process [32],[75]. Dynamic recovery is noted to have a more prominent softening effect on FCC materials (aluminum is FCC) than BCC and HCP materials. Also, recrystallization typically only occurs in FCC materials [75].

Stress data from tension, compression and torsion experiments are plotted versus temperature in Figure 43. For tension and compression experiments, true stress values extracted at two true strains ( $\epsilon = 0.075$  and  $\epsilon = 0.15$ ) are plotted versus temperature in Figure 43 (a) and Figure 43 (b), respectively. For torsion experiments, shear stress values extracted at two shear strains ( $\gamma = 0.13$  and  $\gamma = 0.26$ ) are plotted versus temperature in in Figure 43 (a) and Figure 43 (b), respectively. In general, the compressive stress of 2024-T351 aluminum is greater than the tensile and shear stress at all of the temperatures tested. Repeatability of the temperature test series data is displayed in Figure 43. Stress strain curves from each experiment conducted in the temperature test series are presented in Appendix A.

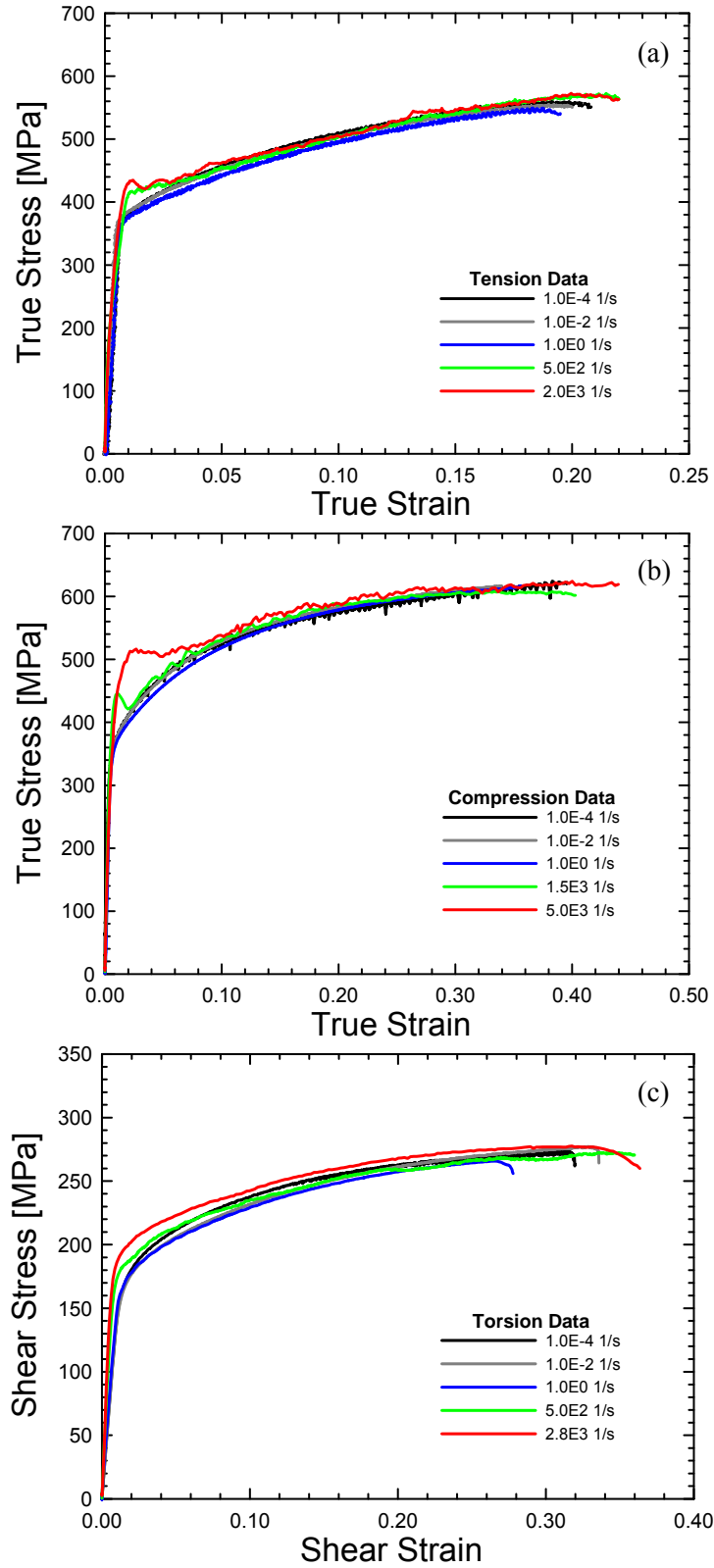


Figure 40. Stress versus strain curves from (a) tension, (b) compression and (c) torsion tests conducted over a wide range of strain rates on 2024-T351 aluminum.

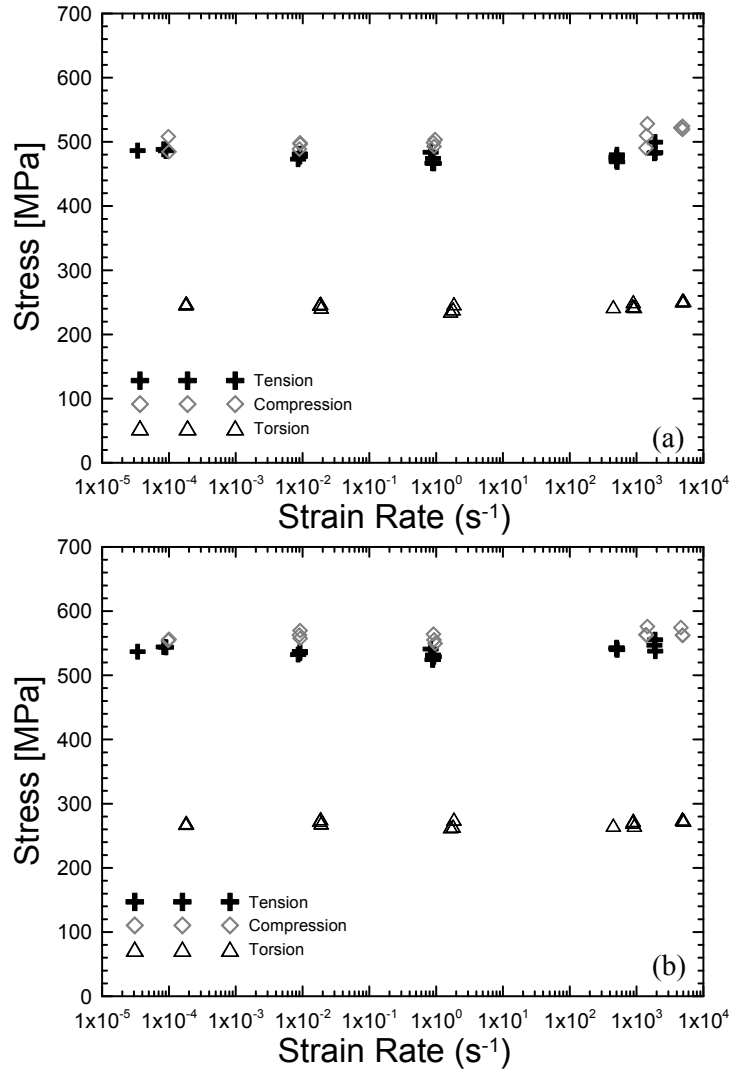


Figure 41. Stress versus strain rate from tension, compression and torsion tests on 2024-T351 aluminum (a) tensile and compressive true stress values extracted at a true strain of 0.075, torsional shear stress values extracted at a shear strain of 0.13, (b) tensile and compressive true stress values extracted at a true strain of 0.15, torsional shear stress values extracted at a shear strain of 0.26.

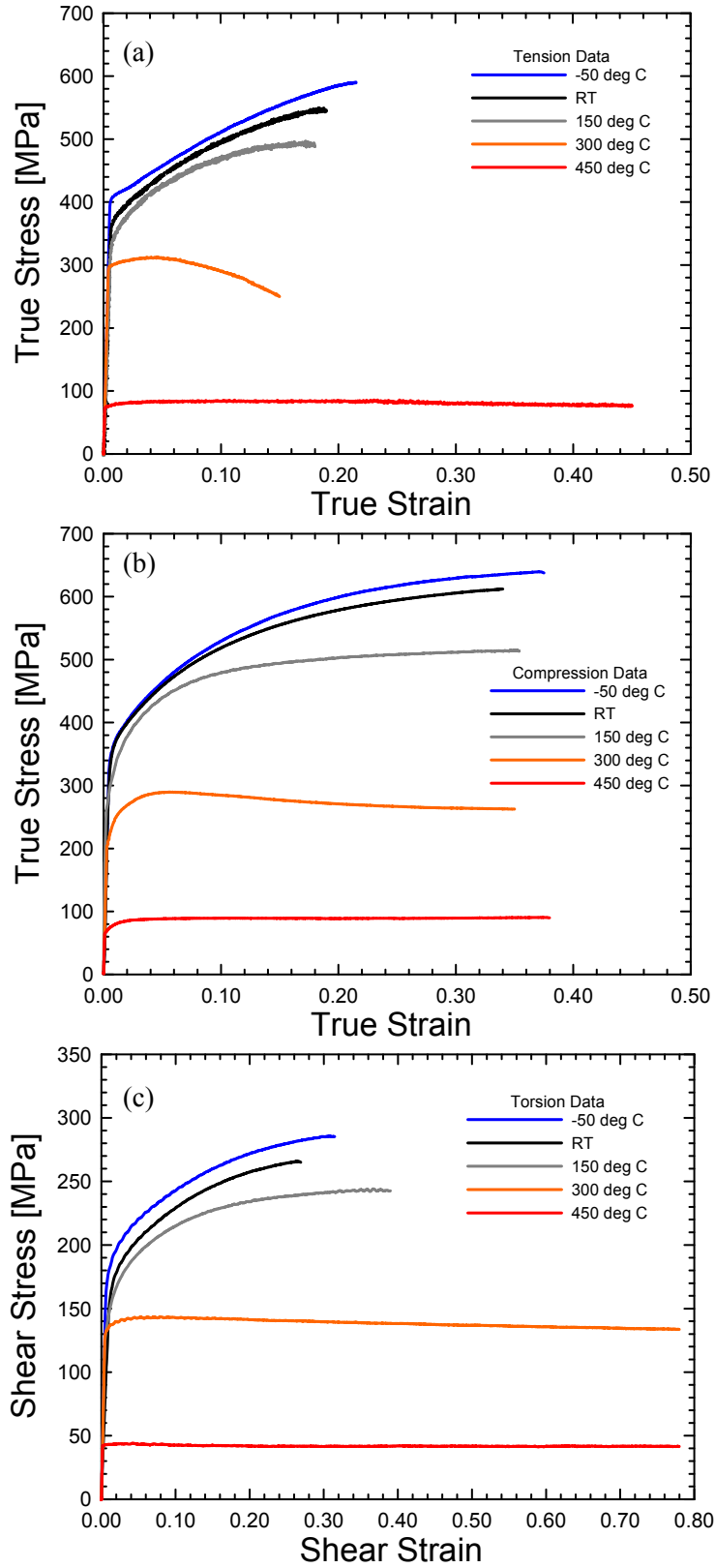


Figure 42. Stress versus strain curves from (a) tension, (b) compression and (c) torsion tests conducted over a wide range of temperatures on 2024-T351 aluminum.

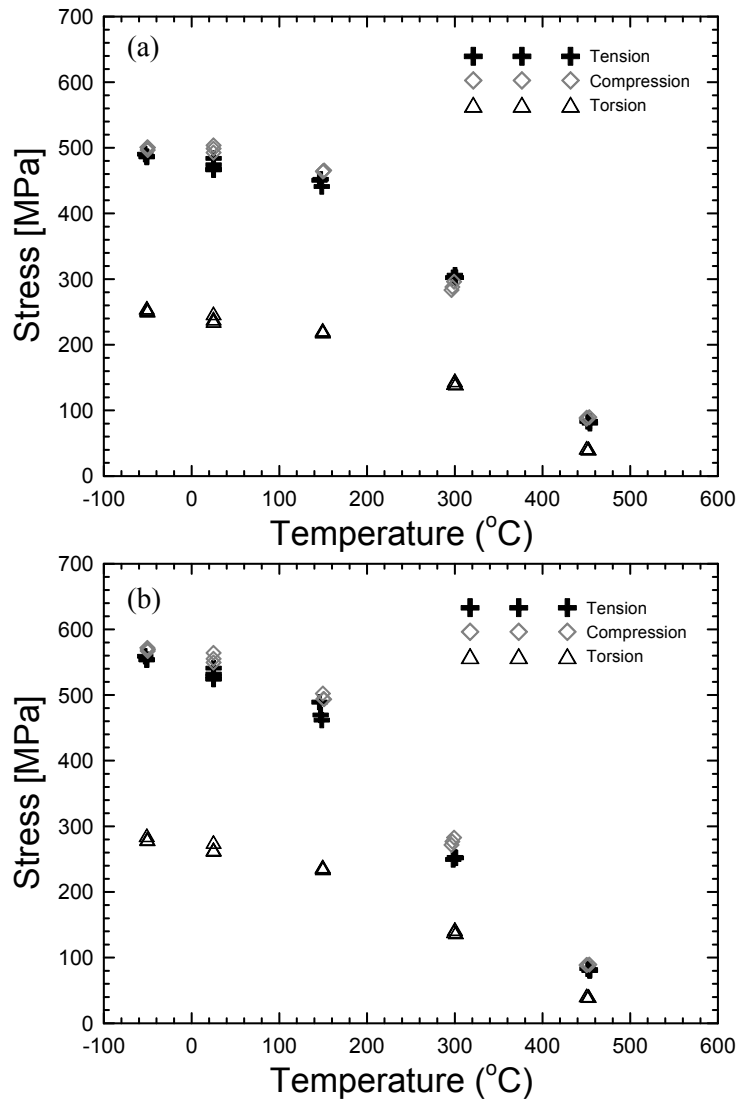


Figure 43. Stress versus temperature from tension, compression and torsion tests on 2024-T351 aluminum, (a) tensile and compressive true stress values extracted at a true strain of 0.075, torsional shear stress values extracted at a shear strain of 0.13, (b) tensile and compressive true stress values extracted at a true strain of 0.15, torsional shear stress values extracted at a shear strain of 0.26.

True stress versus true strain curves from tension and compression experiments conducted on specimens fabricated in the orientations illustrated in Figure 3 are presented in Figure 44 (a) and (b), respectively. The data in Figure 44 are from experiments conducted at room temperature and an equivalent strain rate of  $1.0 \text{ s}^{-1}$ . In compression, the stress strain curves are similar in the  $0^\circ$ ,  $90^\circ$ , and thickness directions. This finding agrees with Lesuer's [31], however, drawing the conclusion that the plate is isotropic would be incorrect as shown by the  $\pm 45^\circ$  data. The material is weaker in these directions and clearly, the plate is anisotropic. Similar results are found in

tension. The  $0^\circ$  and  $90^\circ$  strengths are nearly identical, however, the  $\pm 45^\circ$  directions are weaker. In both tension and compression, the  $45^\circ$  stress is identical to the  $-45^\circ$  stress, showing that the X-Z plane is a symmetry plane. This is evidence that the plate is orthotropic (has three symmetry planes), which is common for rolled aluminum material [33].

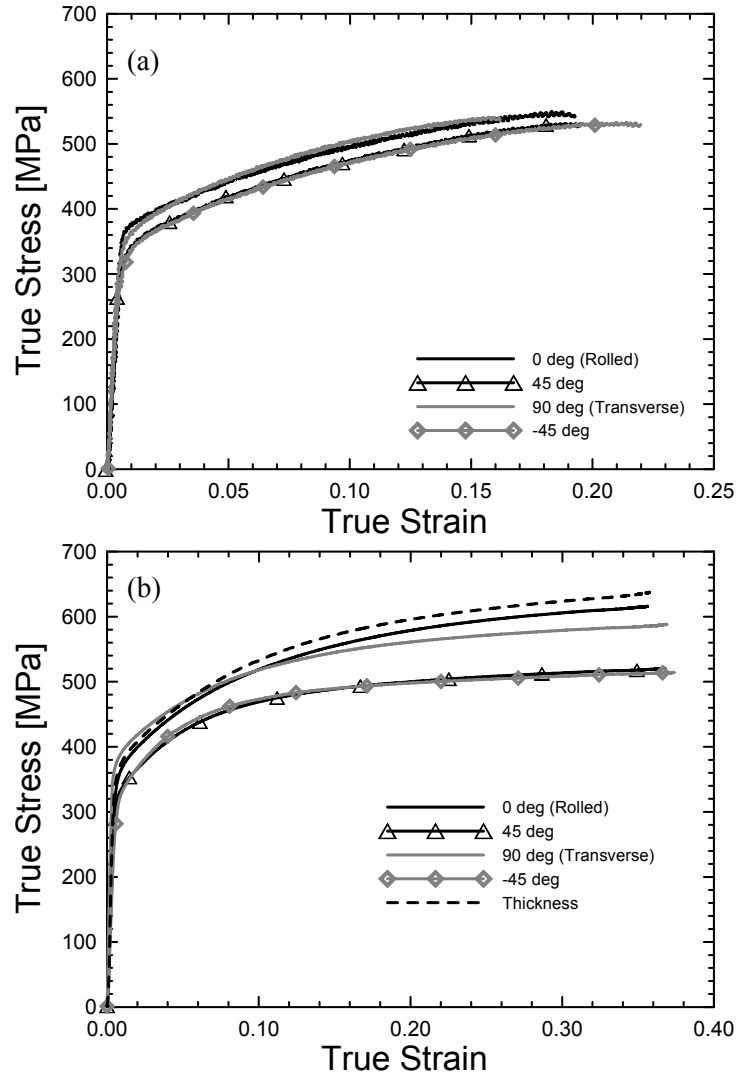


Figure 44. True stress versus true strain curves from (a) tension and (b) compression tests conducted on specimens fabricated in several orientations of 2024-T351 aluminum plate stock.

Effective stress versus equivalent strain curves from select tension, compression and torsion experiments are shown in Figure 45. The effective stress is defined by Equation 1.5 while the equivalent strain is defined by Equation 3.5. The tension compression and torsion test data in Figure 45 are from experiments conducted at an equivalent strain rate of  $1.0 \text{ s}^{-1}$  at room temperature. The tension and compression specimens are aligned in the plate's rolled direction,

while the torsion specimens are aligned in the plate's thickness direction, see Figure 3. The comparison in Figure 45 shows that simple  $J_2$  flow theory cannot adequately describe the material behavior.  $J_2$  flow theory uses one universal effective stress versus equivalent plastic strain curve. The theory can only model materials whose effective stress strain curve in shear coincides with those in compression and tension. This is clearly not the case for 12.7 mm thick 2024-T351 aluminum since the shear data lies well below both the tensile and compressive data. Figure 45 shows that the material has roughly the same yield point in tension and compression, however, the compression curve exhibits more strain hardening.

The torsional effective stress versus effective strain curve lies well below all of the compression and tension curves, regardless of orientation. This is evidence that the low equivalent stress from the torsion experiments cannot be due to anisotropy and specimen orientation alone.

Averaged ratios of tensile effective stress to compressive effective stress and torsional effective stress to compressive effective stress at all five temperatures studied are presented in Figure 46. The figure shows that the torsion-to-compression stress ratio maintains at nearly the same level over the entire temperature range. This illustrates that the effective stress representation from  $J_2$  flow theory will be inadequate to describe the material behavior at all temperatures. Interestingly, this characteristic is maintained at elevated temperatures even after the material has significantly evolved and transitioned to near elastic-perfectly plastic behavior. Figure 46 also shows that the tensile stress is roughly 95% of the compressive stress for all temperatures except 300 °C, where the tensile necking localization affects the data.

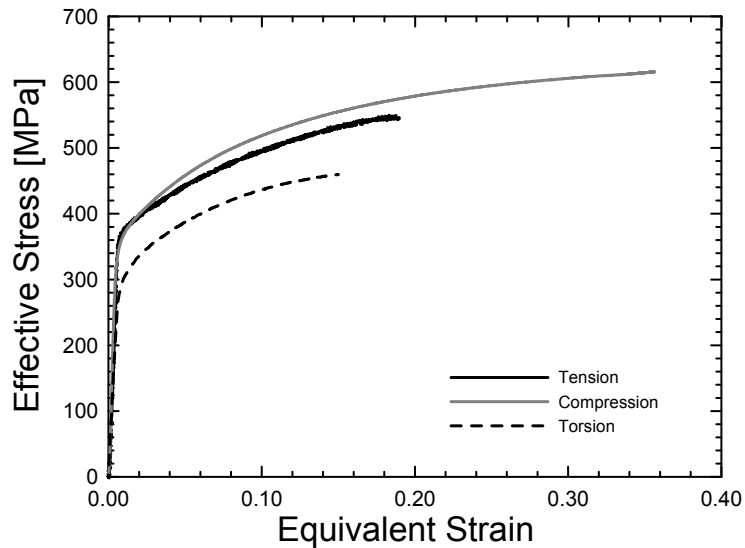


Figure 45. Comparison of effective stress versus equivalent strain curves from tension, compression and torsion experiments.

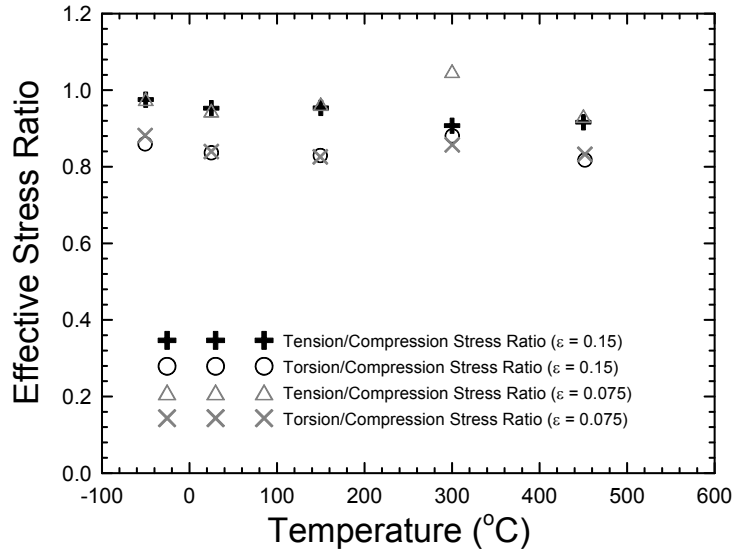


Figure 46. Tension/compression effective stress ratio and torsion/compression effective stress ratio at two equivalent strains ( $\bar{\epsilon} = 0.15$  and  $\bar{\epsilon} = 0.075$ )

### Constitutive Modeling and Parameter Determination

Barlat's anisotropic plasticity model [33] is used to model select experiments from the test matrix in Table 2, using the commercial finite element code LS-DYNA. This section attempts to determine if Barlat's anisotropic constitutive model can capture the tension compression and shear deformation behavior as well as the directional strength characteristics shown in the previous section. Anisotropic plasticity is considered, while strain rate and temperature dependence are neglected. The Barlat yield function is an extension of the Hosford phenomenological yield function, or,

$$f = |S_1 - S_2|^m + |S_2 - S_3|^m + |S_3 - S_1|^m - 2\bar{\sigma}^m = 0 \quad , \quad (4.1)$$

where,  $S_1$ ,  $S_2$ , and  $S_3$  are the deviatoric principal stresses, and  $m$  is a model parameter. For  $m = 2$  or  $m = 4$ , Equation 3 reduces to the von Mises yield criterion. For  $m = 1$  or  $m = \infty$ , Equation 3 reduces to the Tresca yield function. Barlat rewrites Equation 4.1 in the following form,

$$f = (3J_2)^{m/2} \left\{ \left[ 2 \cos\left(\frac{2\theta + \pi}{6}\right) \right]^m + \left[ 2 \cos\left(\frac{2\theta - 3\pi}{6}\right) \right]^m + \left[ -2 \cos\left(\frac{2\theta + 5\pi}{6}\right) \right]^m \right\} - 2\bar{\sigma}^m = 0 \quad , \quad (4.2)$$

where,

$$\theta = \cos^{-1} \left( \frac{J_3}{J_2^{3/2}} \right) \quad , \quad (4.3)$$

and  $J_2$  and  $J_3$  are the second and third deviatoric stress invariants, respectively. The model uses the Bishop and Hill representation of the deviatoric stress tensor, or,

$$[S] = \begin{bmatrix} S_x & S_{xy} & S_{zx} \\ S_{xy} & S_y & S_{yz} \\ S_{zx} & S_{yz} & S_z \end{bmatrix} = \begin{bmatrix} \frac{C-B}{3} & H & G \\ H & \frac{A-C}{3} & F \\ G & F & \frac{B-A}{3} \end{bmatrix} \quad . \quad (4.4)$$

$A, B, C, F, G,$  and  $H$  are functions of the Cauchy stress tensor, or  $A = \sigma_y - \sigma_z$ ,  $B = \sigma_z - \sigma_x$ ,  $C = \sigma_x - \sigma_y$ ,  $F = \sigma_{yz}$ ,  $G = \sigma_{zx}$ ,  $H = \sigma_{xy}$ . Anisotropy is introduced by replacing  $A, B, C, F, G$  and  $H$  in Equation 4.4 with  $aA, bB, cC, fF, gG,$  and  $hH$ , respectively, where  $a, b, c, f, g$  and  $h$  are yield function parameters. Therefore the deviatoric stress tensor becomes

$$[S] = \begin{bmatrix} \frac{cC-bB}{3} & hH & gG \\ hH & \frac{aA-cC}{3} & fF \\ gG & fF & \frac{bB-aA}{3} \end{bmatrix} \quad . \quad (4.5)$$

The second and third deviatoric stress invariants for the representation in equation 4.5 are

$$J_2 = \frac{(fF)^2 + (gG)^2 + (hH)^2}{3} + \frac{(aA-cC)^2 + (cC-bB)^2 + (bB-aA)^2}{54} \quad , \quad (4.6)$$

and,

$$J_3 = \frac{(cC-bB)(aA-cC)(bB-aA)}{54} + fghFGH - \frac{(cC-bB)(fF)^2 + (aA-cC)(gG)^2 + (bB-aA)(hH)^2}{6} \quad . \quad (4.7)$$

In classic incremental plasticity theory, the yield function is also a plastic potential function. Therefore, the instantaneous rate of plastic deformation can be related to the yield function and the current state of stress as

$$\dot{\epsilon}_{ij}^p = \dot{\lambda} \frac{\partial f}{\partial \sigma_{ij}} \quad , \quad (4.8)$$

where  $\dot{\lambda}$  is a scalar function which depends on the hardening model used. Equation 4.2 is utilized in Equation 4.8 for this particular constitutive model. Isotropic hardening is assumed and a universal stress strain curve determined from a compression experiment on a specimen oriented in the rolled direction of the plate defines the strain hardening behavior.

The yield function has a total of seven parameters that must be determined from experimental data ( $m, a, b, c, f, g$  and  $h$ ). A value of 8 is used for the  $m$  parameter since Barlat claims that this value leads to a particularly good representation of FCC materials [33]. According to Banabic, et al. [35], the six remaining anisotropy parameters can be found in multiple ways. Ideally, three uniaxial tests in the directions of the plate orthotropic axes (X, Y and Z in Figure 3) are used to determine  $a, b$  and  $c$ , while three properly oriented shear tests are used to find  $f, g$  and  $h$ .

Tension and compression data in the  $0^\circ, \pm 45^\circ$  and  $90^\circ$  orientations are available from the current experimental program. Compression data in the thickness direction, or the Z direction in Figure 3, are also available. Finally, torsion data, providing information about the shear strength in the X-Y plane, are also available. Figure 44 and Figure 45 illustrate there is variance between the tension and compression hardening response of the material. The constitutive model described above cannot account for this variance, so it is necessary to calibrate the yield function parameters from either tension or compression data. Compression data is used to find the  $a, b$  and  $c$  parameters because of the availability of test data in the thickness direction of the plate (Z-direction in Figure 3). Because of this decision, errors in the simulated tensile response of the material are expected. The  $a, b$  and  $c$  parameters are found using uniaxial compressive yield stresses determined experimentally from specimens aligned in the direction of the orthotropic axes (X, Y, Z). Substituting these three yield stresses into Equation 4.2, using Equations 4.3, 4.6 and 4.7, produces a set of coupled non-linear equations for  $a, b$  and  $c$  which can be solved numerically. The  $h$  parameter is found using the determined  $a, b$  and  $c$  parameters and the uniaxial compressive yield stress of a specimen oriented  $45^\circ$  to the rolled direction. The stress transformation equations are used to substitute the  $45^\circ$  yield stress into Equation 4.2 giving a single equation for  $h$ . Finally, the parameters  $f$  and  $g$  are determined using the torsion data. The torsion specimen orientation gives rise to a pure shear stress state that is a combination of  $\sigma_{zx}$  and  $\sigma_{yz}$ . A simplifying assumption is made in order to find both  $f$  and  $g$  from the torsional yield stress. It is assumed that the shear yield stresses in ZX and YZ directions are equivalent, which also means that  $f = g$ . Ideally, these parameters would be determined using two shear yield stresses determined by independent experiments, however, this assumption was deemed

reasonable in light of the available data. The yield function parameters, determined for 12.7 mm thick 2024-T351 aluminum plate, are presented in Table 9. Also included in the table are parameters determined by Barlat, et al. for 0.3 mm thick 2024-T3 aluminum sheet [33].

Table 9. Parameters for the anisotropic yield function for 12.7 mm thick 2024-T351 aluminum plate and 0.3 mm thick 2024-T3 aluminum sheet.

Material	$m$	$a$	$b$	$c$	$f$	$g$	$h$
2024-T351 Plate	8	0.9853	1.0452	0.9533	1.1835	1.1835	1.1475
2024-T3 Sheet	8	1.3780	1.0440	0.9550	1.0000	1.0000	1.2100

The two sets of parameters for 2024-T3(51) aluminum found in Table 9 are compared in Figure 47. Figure 47 (a) is a comparison of the plane stress yield surface for the two sets of parameters. The plot is generated assuming that  $\sigma_z = \sigma_{yz} = \sigma_{zx} = 0$ . The dashed trace in Figure 47 (a) represents Barlat's parameters for 0.3 mm 2024-T3 sheet while the solid trace represents 12.7 mm thick 2024-T351 plate. The normalized yield stress plotted versus specimen orientation angle is compared with compression experimental data in Figure 47 (b). The dashed line is generated using the 2024-T3 sheet parameters while the solid trace is generated with the 2024-T351 plate parameters. The variance between the two sets of parameters is obvious in both Figure 47 (a) and Figure 47 (b). The most striking variation is the underestimation of the plate strength in the transverse direction, Y direction in Figure 47 (a), and a specimen orientation angle of 90° in Figure 47 (b). This comparison clearly shows the variance in mechanical properties of 0.3 mm 2024-T3 aluminum sheet and 12.7 mm thick 2024-T351 aluminum plate. The significant difference in thickness leads to a drastic difference in the anisotropic strength behavior of the two aluminum products. The thicker plate is less anisotropic than the sheet stock, however, it still must be considered anisotropic due to the  $\pm 45^\circ$  strength behavior. This also illustrates the importance of characterizing the actual material to be used in the application. Using the 0.3 mm thick 2024-T3 yield function parameters to simulate 12.7 mm thick 2024-T351, and vice-versa, could yield considerable errors.

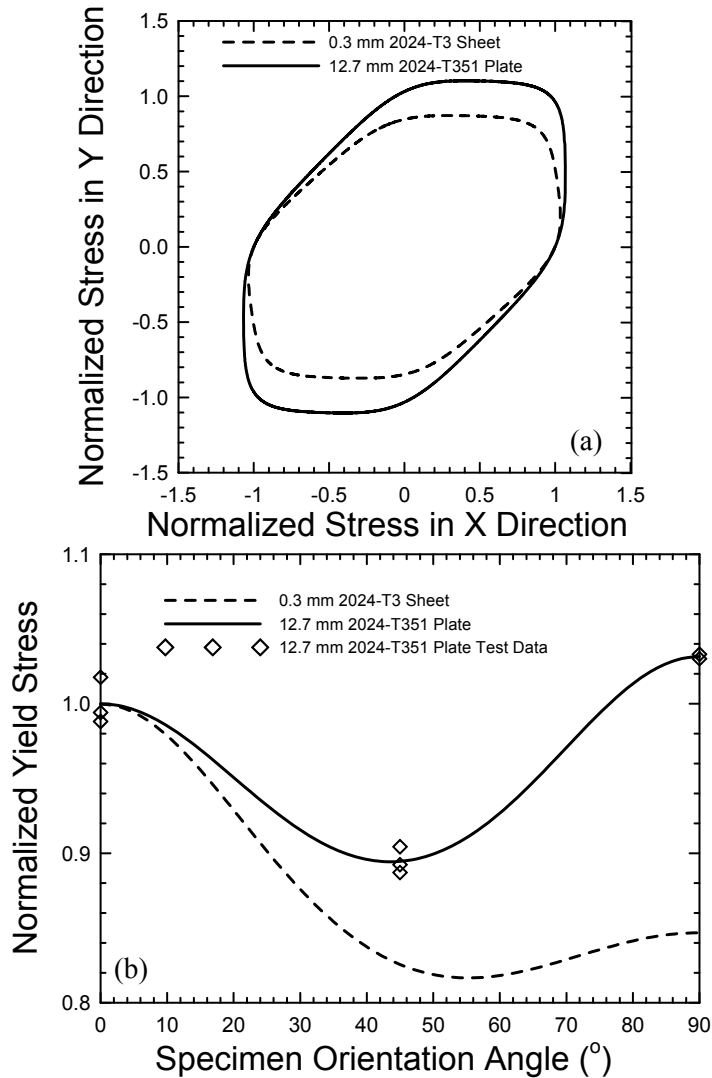


Figure 47. Comparison of yield function parameters for 12.7 mm thick 2024-T351 plate to those for 0.3 mm 2024-T3 sheet, (a) plane stress yield surfaces for 2024-T3(51) aluminum, (b) normalized yield stress versus specimen orientation angle.

### Finite Element Simulations and Results

Select experiments from those listed in Table 2 are simulated using the finite element code LS-DYNA and the constitutive model described in the previous section. Compression simulations include those conducted in the five specimen orientations ( $0^\circ$ ,  $\pm 45^\circ$ ,  $90^\circ$ , and through thickness). Tension simulations include those conducted in four specimen orientations ( $0^\circ$ ,  $\pm 45^\circ$ , and  $90^\circ$ ). Torsion simulations of a specimen oriented in the manner illustrated in Figure 3 are also analyzed. Strain rate and temperature effects are not considered in these simulations and the

results are compared to the experimental data collected at room temperature and a strain rate of  $1.0 \text{ s}^{-1}$ .

Three dimensional, eight-node, constant stress, solid elements are used in all simulations. The simulation geometry and setup are illustrated in Figure 48. Figure 48 (a) presents the tension simulation mesh and setup. There are ten elements through the thickness of the tensile specimen. In the specimen gage section, these elements have an aspect ratio of 1.0. Load is applied to the specimen by constraining one end and applying a displacement history,  $u(t)$  at constant velocity to the other, closely mimicking the actual mechanical experiment. Figure 48 (b) presents the compression simulation mesh and setup. There are twenty elements across both the length and diameter of the compression specimen. A translating, rigid platen with displacement history,  $u(t)$ , is used to compress the specimen against a constrained, rigid platen. Friction between the specimen and the platens is considered in the simulation, using a static friction coefficient of 0.01 and a dynamic friction coefficient of 0.008. These friction coefficients are determined iteratively by comparing the “barreling” deformation profiles of simulated specimens to average measurements from the test specimens. Molybdenum disulfide lubricant is used at the specimen and platen interfaces, so “barreling” is minimal, thus leading to relatively small friction coefficients. Figure 48 (c) presents the torsion simulation mesh and setup. There are five elements through the gage thickness of the spool specimen. In the specimen gage section, these elements have an aspect ratio of nearly 1.0. Torque is applied to the specimen by constraining one end and applying a rotation history,  $\theta(t)$  at constant rotational velocity to the other.

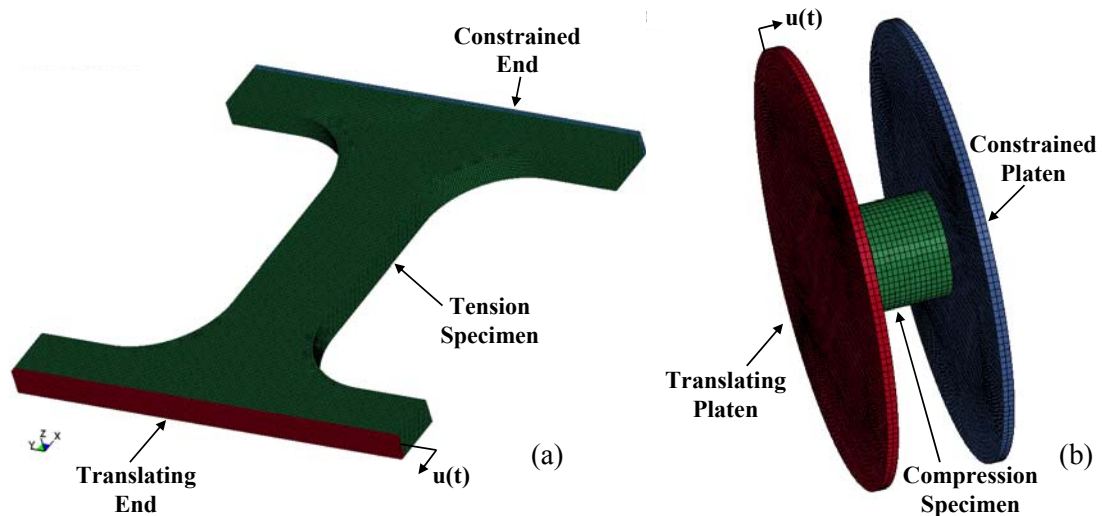
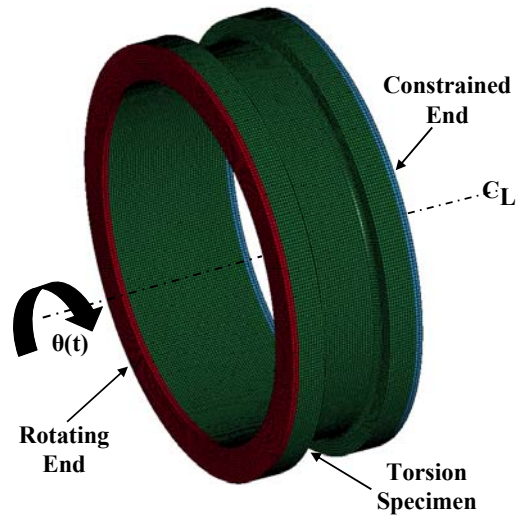


Figure 48. Finite element simulation geometry and setup: (a) tension simulation, (b) compression simulation and (c) torsion simulation. (Continued)

Figure 48 continued



Simulations are conducted with both sets of yield function parameters in Table 9. The results of these simulations are compared to actual test data. Stress versus strain curves are extracted from the simulation results using two methods:

(1) *Replicating the experiment.*

- a. For tension simulations, strain is measured using a “numerical extensometer” that parallels the actual extensometer record from the experiment. The history of the length between two nodes on the surface of the specimen in the gage section is recorded. The initial length between these two nodal points is nearly identical to the gage length of the extensometer used for the experiments (4.0 mm). Force is extracted across a cross-section plane normal to the direction of loading. This record parallels that of the force recorded by the load cell in the actual experiment.
- b. For compression simulations, strains are measured using a “numerical LVDT” record, which tracks the length between the moving compression platen and the stationary platen. This directly parallels the LVDT measurement from the fixture described in Chapter 3. The contact force between the specimen and the stationary platen provides a direct comparison to the experimental load cell record.
- c. In torsion simulations, shear strains are calculated from an extracted angle of twist record. These shear strains are compared to experimental data recorded using the torsional extensometer described in Chapter 3. Simulated torque is extracted across a

cross-section plane normal to the axis of symmetry of the spool specimen. This provides parallel data to that recorded by the torque cell in the actual experiment.

- (2) *Extracting the history of the stress and strain directly from the center element of the gage section.* These center elements are highlighted in Figure 49 for each simulation mode. A cross-section of the tension specimen is shown in Figure 49 (a). Figure 49 (b) shows the cross-section of the compression specimen. Figure 49 (c) is a cross section of the torsion specimen. Equivalent plastic strain contours are shown in all three images. For tension and compression simulations, effective stress and equivalent strain are extracted. For torsion simulations, shear stress and shear strain are extracted.

Tension, compression and torsion simulation results are compared to experimental data in Figure 50, Figure 51 and Figure 52, respectively. In each plot, the black trace represents the experimental data, while gray traces represent the simulation results using the yield function parameters for both 2024-T3 sheet and 2024-T351 plate found in Table 9. In each case, curve 1 is the stress strain curve extracted using method described in (1) above. Likewise, curve 2 is the stress strain curve extracted using method (2). In all cases, the stress strain curves found using method 1 and method 2 coincide.

Figure 50 (a), (b), (c) and (d) present simulated and experimental data from tension specimens oriented in the rolled direction,  $45^\circ$  to the rolled direction, the transverse direction and  $-45^\circ$  to the rolled direction, respectively. Both parameter sets give nearly identical results for rolled direction simulations, see Figure 50 (a). The simulations overestimate the strength of the material in tension. This is due to the strain hardening variance in tension and compression illustrated in Figure 45. Since the model cannot capture this variance, and the model is tuned using compression data, the tensile strength is overestimated in the simulation. The variance between the two sets of parameters is clear in the three off-axis directions:  $45^\circ$ , see Figure 50 (b),  $90^\circ$ , see Figure 50 (c), and  $-45^\circ$ , see Figure 50 (d). In each case, the 2024-T3 sheet constants significantly underestimate the strength of the material. The parameters determined for 2024-T351 plate yield simulation results very similar to the experimental data for the  $\pm 45^\circ$  directions. The plate parameters overestimate the strength of the material in the transverse direction, again, due to the fact that the model was tuned using compression data. In general, the 2024-T351 model captures the directional tensile strength of the material more closely than the 2024-T3 model.

Figure 51 (a), (b), (c), (d) and (e) present simulated and experimental data from compression specimens oriented in the rolled, 45° to the rolled, transverse, -45° to the rolled and the plate normal directions, respectively. Both parameters sets give nearly identical results which closely match the experimental curve for the rolled direction, see Figure 51 (a). This is expected, since the yield surface parameters were determined from compression data and the strain hardening behavior was determined from rolled direction compression data. The variance between the two sets of parameters is clear in the four off-axis directions: 45°, see Figure 51 (b), 90°, see Figure 51 (c), -45°, see Figure 51 (d) and the normal direction, see Figure 51 (e). In each case, the 2024-T3 sheet constants significantly underestimate the strength of the material. The parameters determined for 2024-T351 plate produce simulation results that capture the compressive yield strengths in all directions well. Variance between the simulated stress strain curves and the experimental ones in the off-axis directions are due to the strain hardening model. This plasticity model uses a single effective stress versus equivalent plastic strain curve to describe strain hardening in all directions. Therefore, if the strain hardening is directionally dependent, as is the case with the current material of interest, the model will generate errors. These errors are evident in the gradual divergence of the simulated stress strain curves from the experimental curves in Figure 51 (b), (c), (d) and (e). In the in-plane directions ( $\pm 45^\circ$  and  $90^\circ$ ), the model overestimates the strength of the material for large strains. In the normal direction, the model underestimates the strength of the material for large strains. In general, the 2024-T351 plate parameters capture the directional compressive response of the material more accurately than the 2024-T3 sheet parameters.

Torsion simulation results are compared to experimental data in Figure 52. The simulation using 2024-T3 sheet parameters overestimates the strength of the material, while the current parameters underestimate the strength. The 2024-T351 plate parameters capture the torsional yield point well, however, the simulated stress strain curve diverges below the experimental curve due to the implemented model's inability to capture variances in strain hardening with stress-state. The 2024-T351 parameters capture the torsional response of the material better than the 2024-T3 parameters.

The 2024-T351 parameters capture the directional response of 2024-T351 aluminum well in compression and tension and shear. The accuracy could be increased by incorporating directional and stress-state dependent strain hardening dependence into the material model. The 2024-T3 model parameters result in considerable errors for this particular material stock. This underscores the importance of characterizing the actual material to be used in the application of interest.

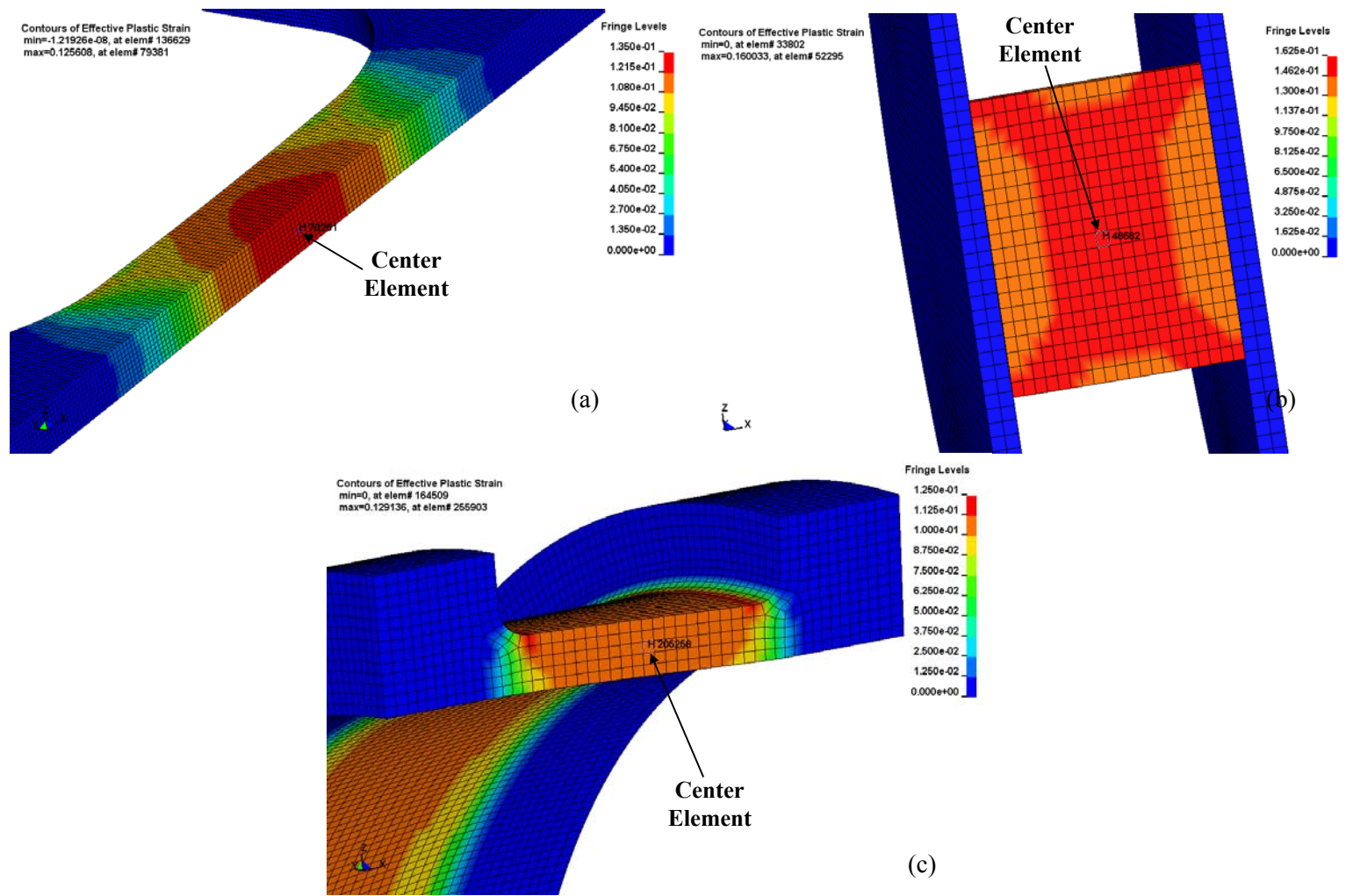


Figure 49. Cross-section finite element simulation results for: (a) a tension specimen, (b) a compression specimen, (c) a torsion specimen. Highlighted elements represent those used to extract effective stress and equivalent strain data for comparison to experiments.

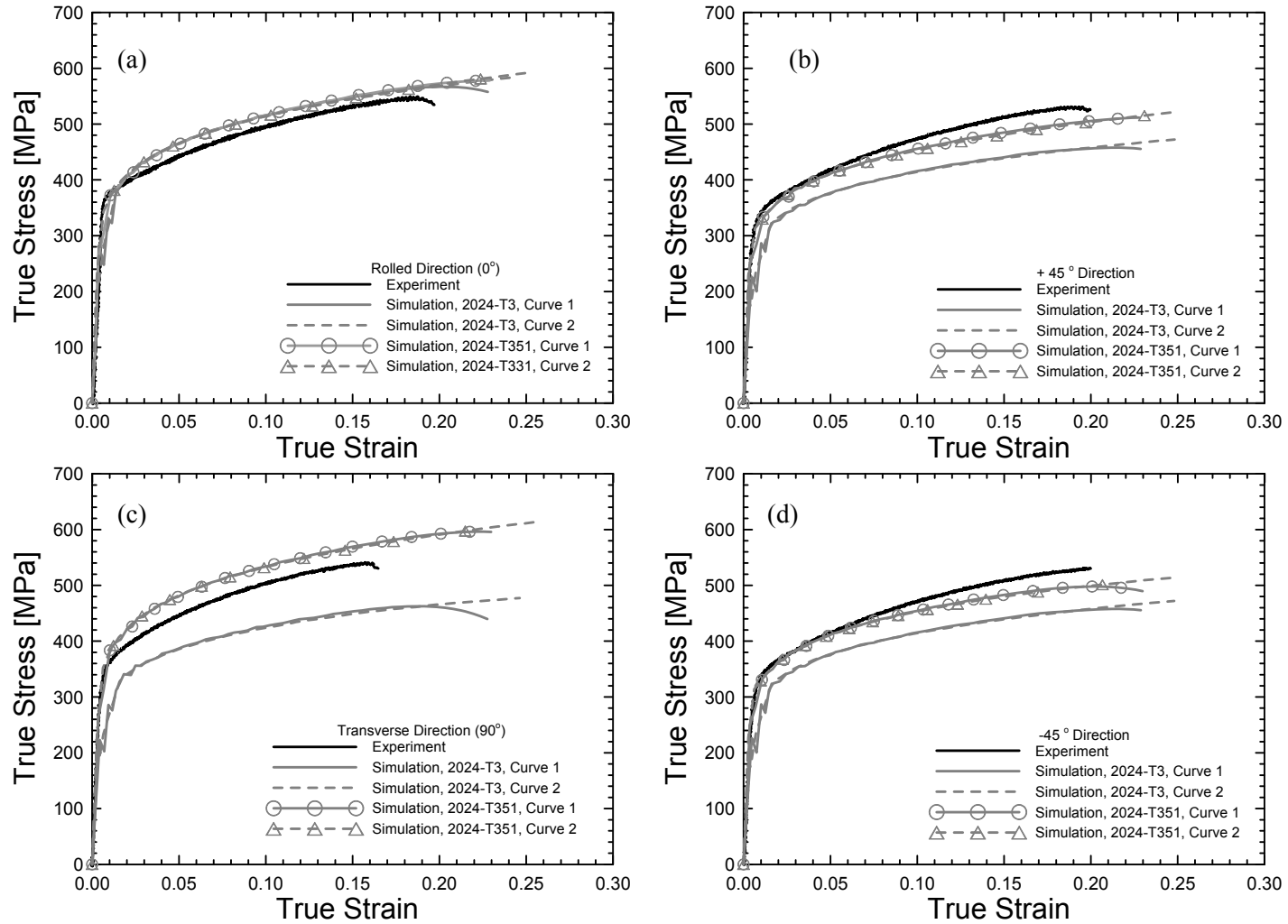


Figure 50. Experimental and simulated tension stress strain curve comparison for two sets of yield criterion parameters, specimens oriented in: (a) rolled direction, (b) 45° to the rolled direction, (c) transverse to the rolled direction, (d) -45° to the rolled direction.

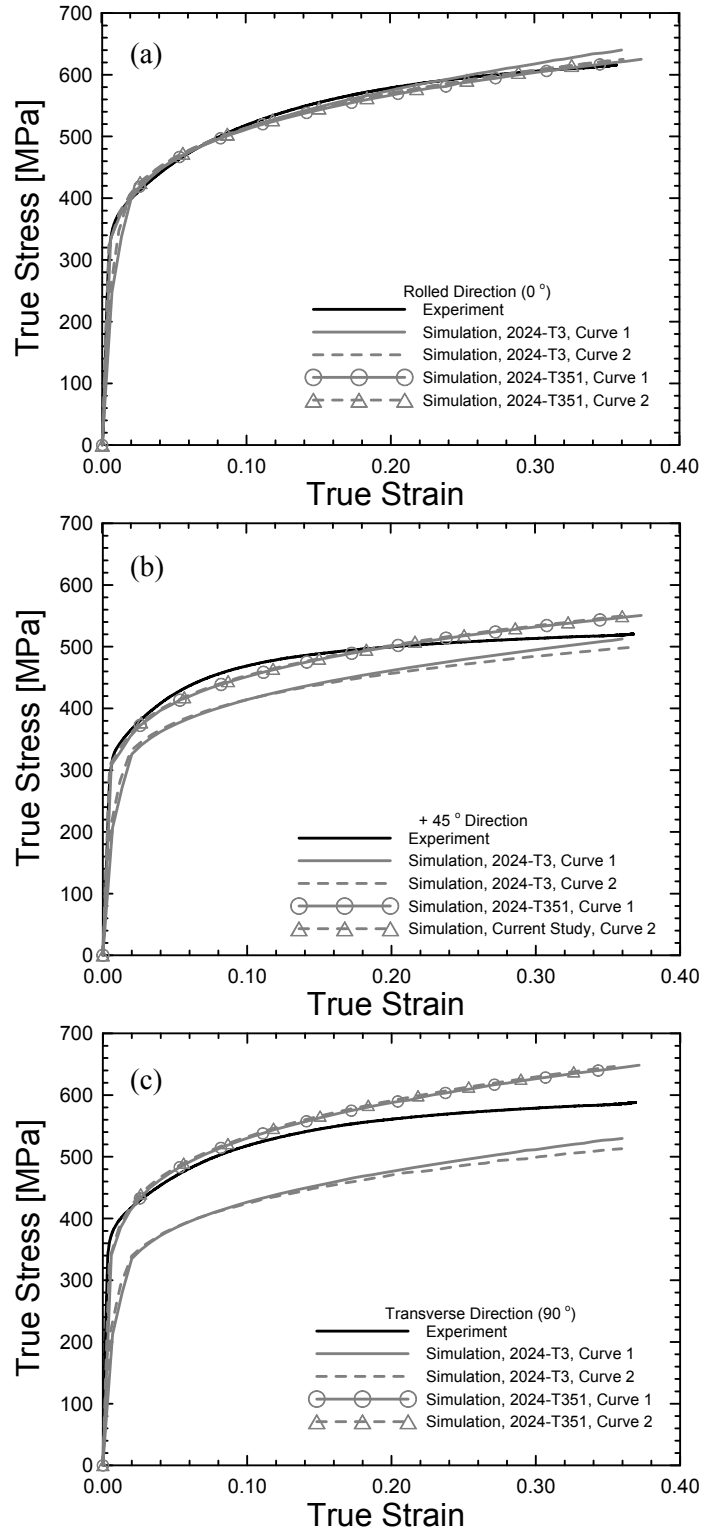


Figure 51. Experimental and simulated compression stress strain curve comparison for two sets of yield criterion parameters, specimens oriented in: (a) rolled direction, (b) 45° to the rolled direction, (c) transverse to the rolled direction, (d) -45° to the rolled direction, (e) plate thickness direction. (Continued)

Figure 51 continued

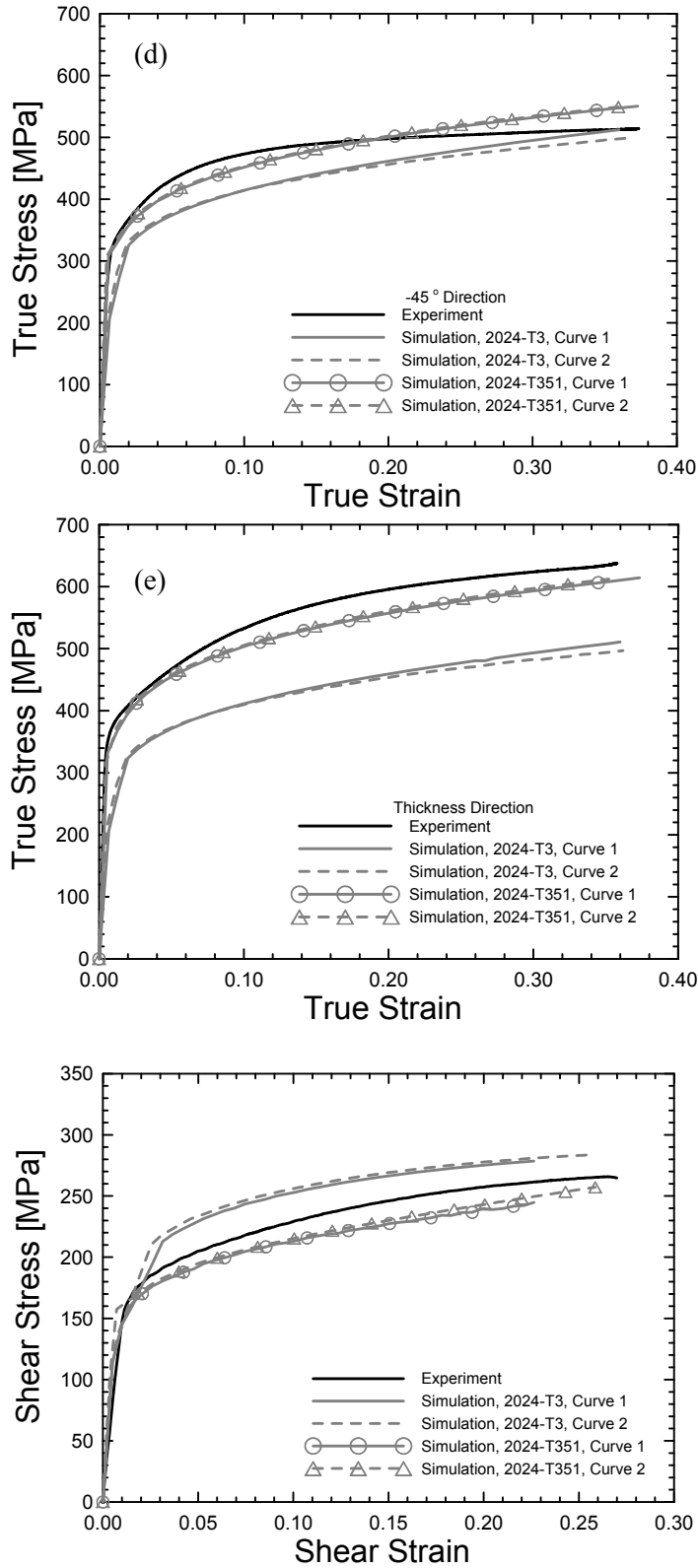


Figure 52. Experimental and simulated torsion stress strain curve comparison for two sets of yield criterion parameters.

## Chapter 5: The Effect of Anisotropic Strength Properties on Ballistic Impact and Penetration of 2024 Aluminum Sheet and Plate

The experimental data presented in the previous chapter shows that there is significant anisotropic behavior in 12.7 mm thick 2024-T351 aluminum. Another finding of the work shown in Chapter 4 is that Barlat's anisotropic yield function implemented in LS-DYNA can satisfactorily capture this behavior in tension, compression and shear. This chapter explores the effect of anisotropic strength behavior in a target panel under ballistic impact loading. Experimental data from the impact experiments described in Chapter 3 are analyzed and compared to numerical simulations using two plasticity models: one which incorporates a von Mises yield function and one which utilizes the anisotropic yield function described in the previous chapter.

Residual velocity versus impact velocity data for all of the impact experiments are presented in Figure 54. The data for the 3.175 mm target panels, see Figure 54 (a), show a well-defined shape to the residual velocity versus impact velocity behavior and a clear ballistic limit velocity of 215 m/s. The 12.7 mm target panel data, see Figure 54 (b), shows significant spread and no clear ballistic limit velocity. The data shows two potential branches for the residual velocity curve, the first starting at a ballistic limit velocity of roughly 238 m/s, and the second starting at a ballistic limit velocity of roughly 253 m/s. The researchers who conducted the experiments report no clear qualitative or quantitative evidence why this may be the case from the available experimental data [43].

LS-DYNA [1] is used to simulate selected impact experiments with two yield functions for the target, see Table 10. Runs 1-8 are simulations of the titanium alloy projectile impacting the 3.175 mm target panel, while runs 9-16 consider impact of the tool steel projectile with the 12.7 mm thick target at various impact velocities. For each target panel, the anisotropic yield function is used for the target in the first four simulations (runs 1-4 and 9-12). A von Mises yield function is used to reproduce the same impact cases (runs 5-8 and 13-16).

In this work, a conscious decision is made to keep the material models as simple as possible for both the von Mises and anisotropic descriptions. Because of this, it is easier to conclude that

the variances in the global results of the simulations are due to the contrasting yield functions and not additional nuances in the models. The von Mises yield function is expressed as

$$f = \frac{1}{2} S_{ij} S_{ij} - \frac{1}{3} \bar{\sigma}^2 = J_2 - \frac{1}{3} \bar{\sigma}^2 = 0 \quad , \quad (5.1)$$

where;  $S_{ij}$  are the components of the deviatoric stress tensor,  $\bar{\sigma}$  is the effective stress, and  $J_2$  is the second invariant of the deviatoric stress tensor. A simplified version of the Johnson Cook model [6] is used to describe the strain hardening behavior of the target panel for the von Mises yield function case. In the simplified version of the model, temperature effects are not considered and the damage evolution and fracture model is dormant [1]. Thus, the effective stress in the material is described by the relation

$$\bar{\sigma} = \sqrt{\frac{3}{2} S_{ij} S_{ij}} = \left[ A + B (\bar{\epsilon}^p)^n \right] \left[ 1 + C \ln(\dot{\epsilon}^*) \right] \quad , \quad (5.2)$$

where;  $A$ ,  $B$ ,  $n$  are strain hardening model parameters,  $C$  is a strain rate sensitivity parameter,  $\bar{\epsilon}^p$  is the equivalent plastic strain and  $\dot{\epsilon}^*$  is the normalized strain rate. Strain rate effects in the target are not considered by setting the  $C$  parameter to zero. This is done for both practical and physical considerations, since rate sensitivity is not used for the anisotropic model and since the material is known to be relatively strain rate insensitive up to  $5000 \text{ s}^{-1}$ , as discussed in Chapter 4. Identical hardening parameters for this model are used for both 2024-T3 sheet and 2024-T351 plate, see Table 11. The parameters were determined from compression tests on specimens fabricated in the rolled direction of a 12.7 mm thick 2024-T351 aluminum plate.

Barlat's six component anisotropic yield function [33] is used for the contrasting case. This yield function is presented and described in Chapter 4. Anisotropic yield function parameters used for the 2024-T351 plate and 2024-T3 sheet target panels are presented in Table 9. As shown in the previous chapter, the two sets of yield function parameters have significantly different directional strength properties. Thus, it is anticipated that the 2024-T3 sheet target panels will exhibit more drastic directional effects. The anisotropic yield function uses a universal effective stress versus equivalent plastic strain curve that is identical to the parameterized one used for the von Mises case.

A simple failure criterion for the target panel materials, based on maximum principal strain, is used for all the simulations in Table 10. Elements erode when the maximum principal strain reaches a magnitude of 0.281. The simplified Johnson Cook model is used for both projectile materials. Model parameters for Ti-6Al-4V [76] and A2 tool steel [21] are also presented in Table 11.

Table 10. Run list of impact simulations.

Run #	Target Thickness (mm)	Target Yield Function	Projectile		
			Material	Length (mm)	Impact Velocity (m/s)
1	3.175	Anisotropic	Ti-6Al-4V	17.780	205.1
2					215.5
3					220.1
4					238.4
5		von Mises			205.1
6					215.5
7					220.1
8					238.4
9	12.700	Anisotropic	A2 Tool Steel	28.575	239.6
10					249.6
11					256.9
12					292.9
13		von Mises			239.6
14					249.6
15					256.9
16					292.9

Table 11. Simplified Johnson Cook model parameters and other physical properties for various materials in the impact simulations.

Material	$A$ (MPa)	$B$ (MPa)	$n$	$C$	$\rho$ (gm/cc)	$E$ (GPa)	$\nu$
2024-T3(51) Aluminum	225.528	516.142	0.2446	0.000	2.78	73.1	0.33
Ti-6Al-4V	862.000	331.000	0.3400	0.012	4.43	114.0	0.33
A2 Tool Steel	999.739	1785.300	0.1401	0.000	7.86	203.0	0.30

A close-up view of the impact location finite element mesh is presented in Figure 53. Three dimensional, eight-node, constant stress, solid elements are used in all simulations. The mesh in the target panel is constructed such that there are five elements through the thickness of the 3.175 mm panel and twenty elements through the thickness of the 12.7 mm panel. Target material nodes lying outside of a 127 mm radius from the center of the panel are constrained, simulating the 254 mm diameter aperture in the experimental clamp fixture. The projectile is given an initial velocity corresponding to the impact velocity column in Table 10.

Simulated residual projectile velocities for the 3.175 mm and 12.7 mm thick target panels are presented with the experimentally measured data in Figure 54 (a) and (b), respectively. For both target panels, there are clear differences between the results generated using the two yield functions.

The anisotropic yield function data compares relatively well with the experimental data, for the 3.175 mm target panel impact cases, while the von Mises data shows no projectile perforation for all of the impact cases considered. The anisotropic model underestimates projectile residual velocity at low impact velocities (215.5 m/s), yet overestimates residual velocity at high impact velocities (238.4 m/s).

The anisotropic model predicts higher residual velocities than the von Mises model for each of the 12.7 mm target panel impact cases. The spread in the experimental data makes it difficult to comment on the accuracy of the simulated residual projectile velocities. The anisotropic model tends to better match the first potential branch in the residual velocity curve, while the von Mises model shows potential to capture the second branch more accurately.

The point of this work is not to show that the simulations have matched the experimental results with minimal errors, especially since relatively simplistic constitutive models and failure criteria are used. The data in Figure 54 illustrates the main point of this chapter by showing that the yield function used in the constitutive model does in fact play a large role in the overall results of impact simulations of both 2024-T3 sheet and 2024-T351 plate.

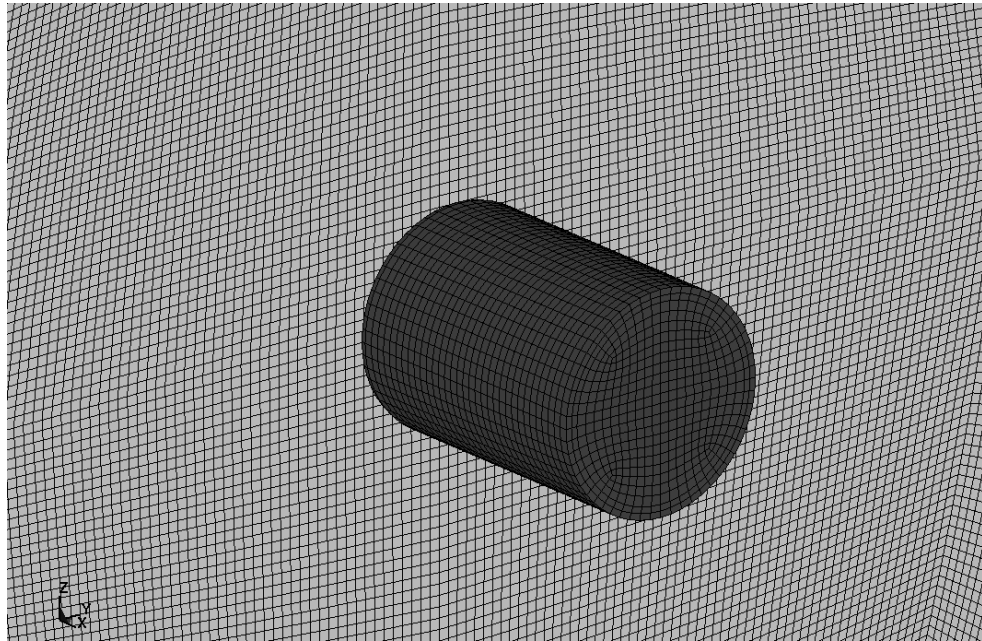


Figure 53. Mesh used for impact simulations.

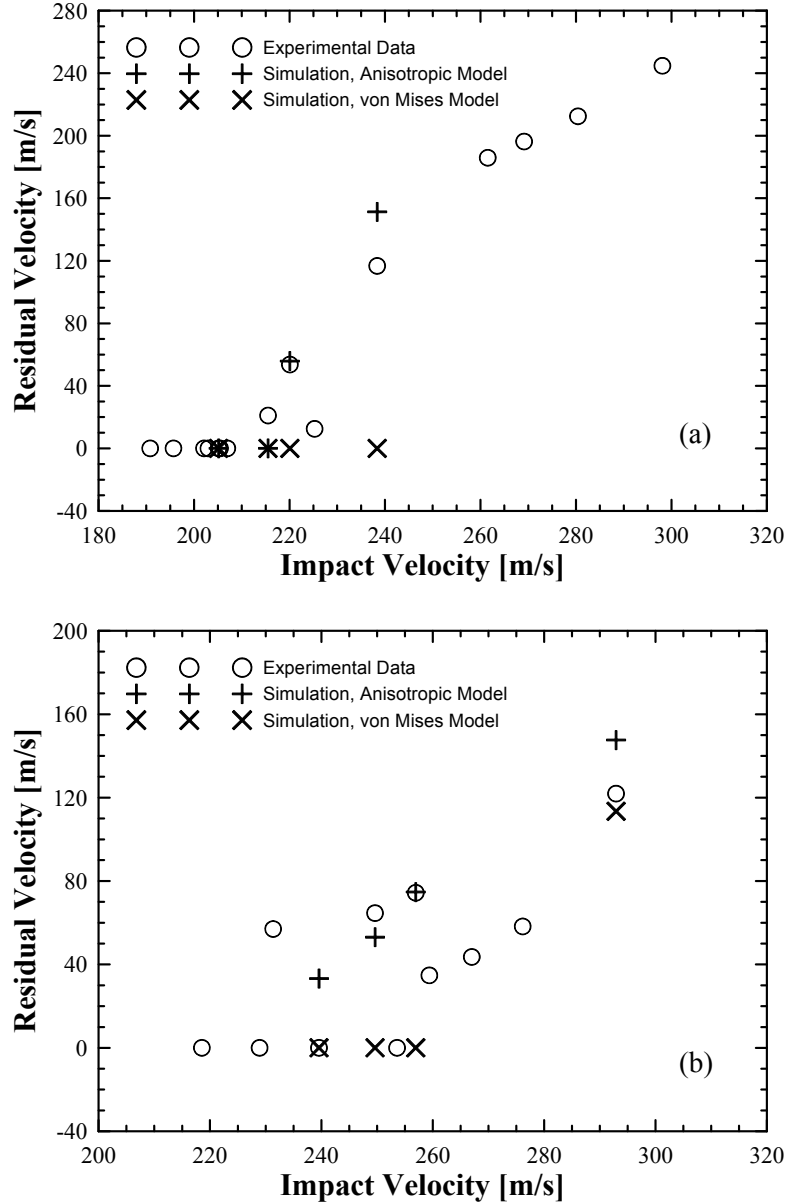


Figure 54. Experimental and numerical residual projectile velocity versus impact velocity for: (a) 3.175 mm 2024-T3 aluminum sheet targets, (b) 12.7 mm 2024-T351 aluminum plate targets.

The fact that the anisotropic yield function simulations predict higher projectile residual velocities than those using the von Mises yield function is explained by inspecting the yield functions. Figure 55 (a) and (b) present comparisons of the plane stress von Mises yield function to the anisotropic plane stress yield function for 2024-T3 aluminum sheet and 2024-T351 aluminum plate, respectively. Both plots present the normalized stress in the Y direction ( $\sigma_y/\bar{\sigma}$ ) plotted versus the normalized stress in the X direction ( $\sigma_x/\bar{\sigma}$ ). For each trace in both plots, the material is assumed to be in a state of plane stress ( $\sigma_z = \sigma_{yz} = \sigma_{zx} = 0$ ). The plots

contain two curves representing the same yield function with different values for the normalized in-plane shear stress ( $\sigma_{xy}/\bar{\sigma}$ ). The solid traces represent  $\sigma_{xy}/\bar{\sigma} = 0.0$  (no shear), while the dashed traces represent  $\sigma_{xy}/\bar{\sigma} = 0.35$ . The difference between the von Mises yield function and the anisotropic yield function for 2024-T3 sheet is clearly evident in Figure 55 (a). For  $\sigma_{xy}/\bar{\sigma} = 0.0$ , there are significant differences between these two functions, most notably when stresses are concentrated in the transverse (Y) direction. When  $\sigma_{xy}/\bar{\sigma} = 0.35$ , the difference is exacerbated, illustrating that the anisotropic model is more sensitive to shear stresses than the von Mises model. The difference between the anisotropic yield function for 2024-T351 plate and the von Mises yield function is shown in Figure 55 (b). For  $\sigma_{xy}/\bar{\sigma} = 0.0$ , the anisotropic function for the plate material is similar to the von Mises function. In fact, the anisotropic function predicts slightly higher yield stresses than the von Mises function for uniaxial tension and compression in the transverse (Y) direction. The anisotropic function for the plate is also more sensitive to shear stresses. This is clear because the anisotropic trace is entirely enclosed by the von Mises yield function when  $\sigma_{xy}/\bar{\sigma} = 0.35$ .

Figure 55 illustrates that the anisotropic model, in general, is weaker than the von Mises model for both 2024-T3 sheet and 2024-T351 plate, especially when shear stresses are present. This is important for the application of interest, since normal impact of a blunt projectile with a flat target panel typically leads to highly localized shear stresses around the circumference of the eventual plug. The target material yields more quickly and plastic strains accumulate more rapidly when the anisotropic yield function is used in contrast to the von Mises yield function. This leads to the discrepancy in projectile residual velocity predicted by the two models, shown in Figure 54. This discrepancy is larger for the 3.175 mm thick 2024-T3 sheet impact cases than for the 12.7 mm thick 2024-T351 plate, as none of the projectiles perforated the 3.175 mm target in the von Mises simulations. This is intuitive when considering the yield functions plotted in Figure 55 because there is a larger variance between the anisotropic and the von Mises yield functions for the 3.175 mm sheet than there is for the 12.7 mm plate.

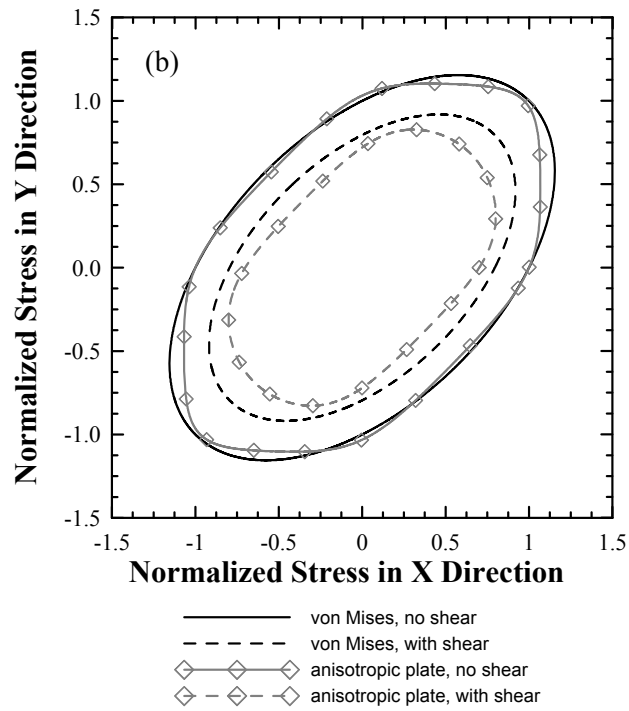
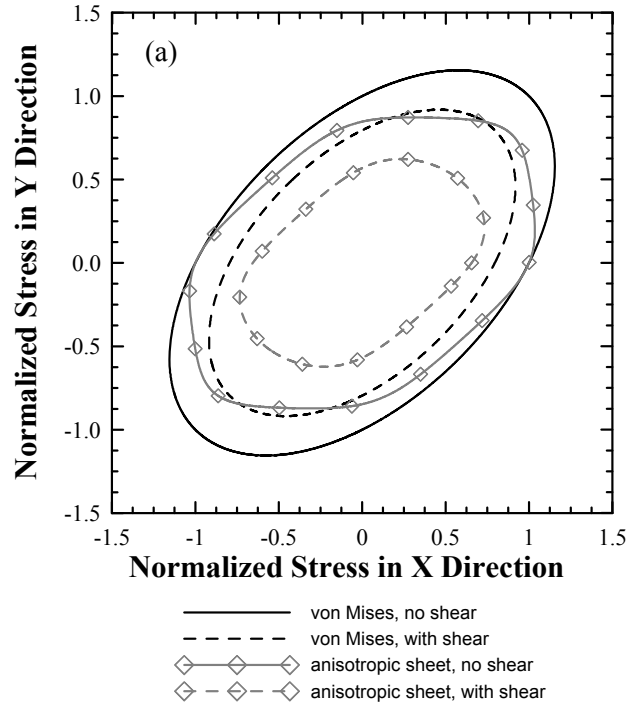


Figure 55. Comparison of the plane stress von Mises yield function to (a) the anisotropic yield function for 2024-T3 aluminum sheet and (b) the anisotropic yield function for 2024-T351 aluminum plate.

Target panel rear surface strains histories calculated in the simulations are compared to strain gage data in Figure 56 for two impact cases. Each plot in Figure 56 contains five traces. Two of the traces are experimental data measured from strain gages located 50.8 mm from the impact point and oriented in the rolled and transverse directions of the target panel. The longitudinal and transverse strain gages are numbered 4 and 2, respectively, in Figure 35 (b). Three simulated strain histories are also shown in each plot. The first two are from the anisotropic simulation, run #1 for Figure 56 (a) and run #11 for Figure 56 (b), one oriented in the panel's rolled direction and one oriented in the panel's transverse direction. The final trace is from the isotropic simulation; run #5 for Figure 56 (a) and run #15 for Figure 56 (b); and is denoted rolled/transverse since the transverse strains are indistinguishable from the rolled direction strains in this case due symmetry of the yield function.

Figure 56 (a) presents strain gage data and simulated strains for a Ti-6Al-4V projectile impacting a 3.175 mm thick target panel at 205.1 m/s. The projectile does not perforate the target panel for this impact case in the experiment and in both anisotropic and isotropic simulations. The simulated strain histories match the experimental strains of the target panel well. The initial amplitudes of the experimental strains are larger than those of the simulated traces, however, the overall form of the strain response is good except for a noticeable phase lag in the curves at later times. It is difficult to distinguish variances between the strain histories in the rolled and transverse directions in both the experimental data and the simulated data. According to the simulation, there is very limited plastic deformation (the maximum accumulated equivalent plastic strains,  $\bar{\epsilon}^P$ , are roughly 1.5E-4) 50.8 mm from the impact location. Thus, there is limited variance in the strain history response in the two directions.

Figure 56 (b) presents strain gage and simulated strain data for an A2 tool steel projectile impacting a 12.7 mm thick target panel at 256.9 m/s. The projectile perforates the target panel with a residual velocity of 74.4 m/s (measured experimentally) and 74.7 m/s (extracted from the anisotropic simulation). The projectile did not perforate the panel in the isotropic simulation. Like the previous case, the experimental strain histories are rather well-predicted in both the anisotropic and isotropic simulations and there is a noticeable phase error in the predicted curves at later times. In this case, it is even more difficult to identify variances in the strain histories oriented in the rolled and transverse directions. Simulation results for this case show that no plastic strains have accumulated 50.8 mm from the impact location in both the rolled and transverse directions of the panel.

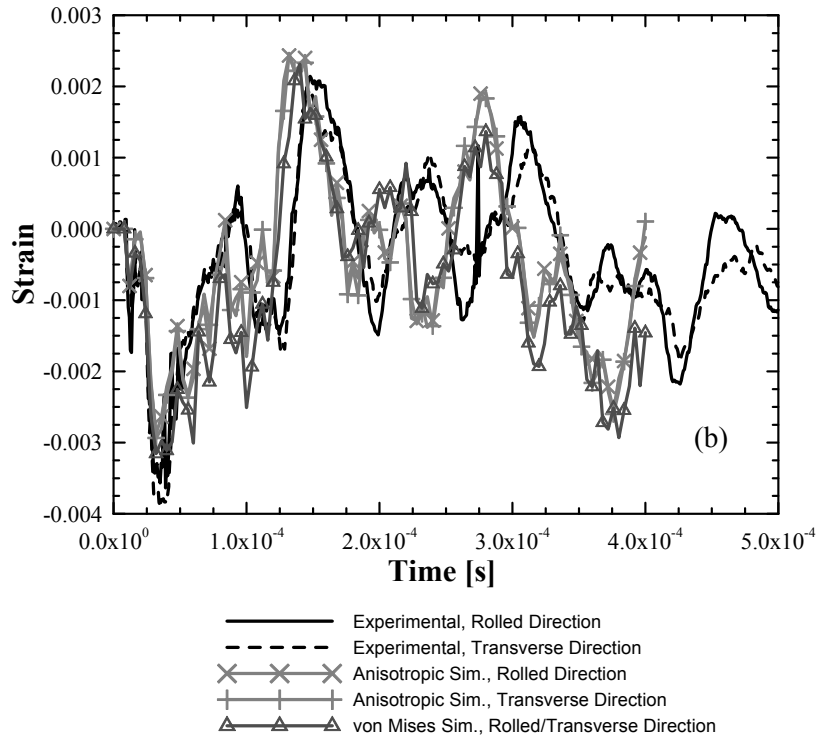
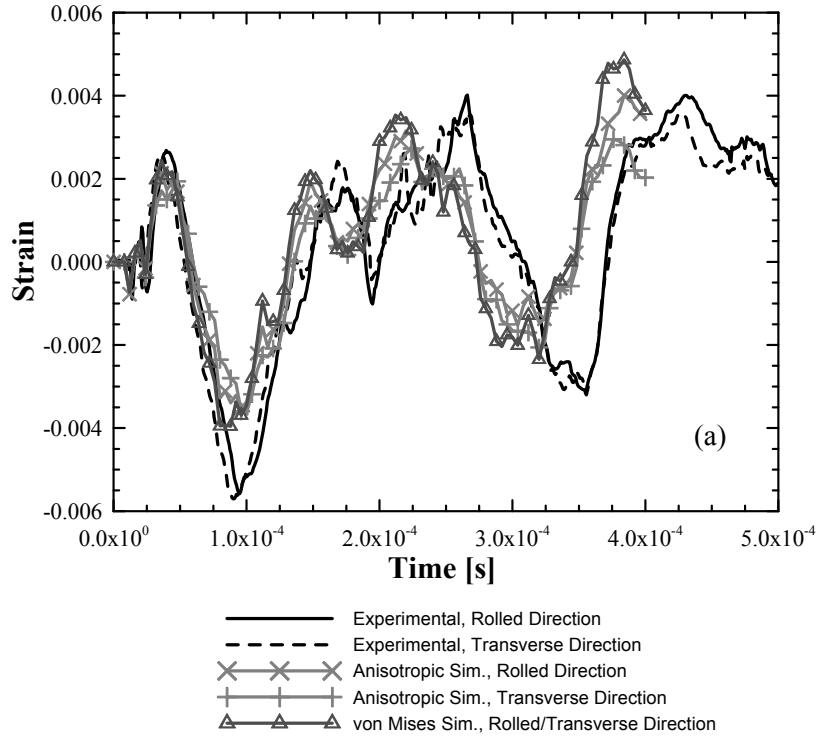


Figure 56. Comparison of calculated strains to those measured with strain gages for (a) a 3.175 mm 2024-T3 aluminum sheet impact experiment, (b) a 12.7 mm 2024-T351 aluminum plate impact experiment.

The strain gage data presented in Figure 56 is measured 50.8 mm from the point of impact, at a position where plastic strain accumulation is negligible and there is essentially no evidence of anisotropic behavior. The DIC data, however, gives access to full-field displacement and strain data in a roughly 100 mm by 100 mm field of view centered at the impact point. DIC data is extracted 15 mm from the impact point and compared to simulation data, at the same location, in Figure 57 and Figure 58.

Figure 57 presents maximum principal strain (a) and displacement (b) data for a titanium alloy projectile impacting a 3.175 mm 2024-T3 target panel at 205.1 m/s. For this impact case, the projectile did not perforate the target panel experimentally and in both the anisotropic and von Mises simulations. The first experimental trace in Figure 57 (a) is the maximum principal strain history 15 mm from the impact point on the rolled axis of the target panel. The second experimental trace is the maximum principal strain history 15 mm from the impact point on the transverse axis of the panel. The fact that the maximum principal strain on the transverse axis is generally less than that on the rolled axis is experimental evidence of anisotropic deformation in the plate. 15 mm from the impact point, the maximum principal strains are circumferential in direction. Thus, for the point on the rolled axis, the maximum principal strain direction is oriented in the transverse direction. Likewise, the maximum principal strain for the point on the transverse axis is oriented in the rolled direction of the panel. Since the 3.175 mm thick sheet is significantly weaker in the transverse direction than it is in the rolled direction, see Figure 55 (a), the maximum principal strain at the point that lies on the rolled axis accumulates more rapidly than its counterpart. The numerical simulation using the anisotropic yield function also exhibits this behavior, see the two solid traces in Figure 57 (a). The dashed trace in Figure 57 (a) is a result from the numerical simulation which employs the von Mises yield function. The results from this simulation are axisymmetric, thus the strains and displacements are identical 15 mm from the impact point, regardless of in-plane angle.

Experimental and calculated rear surface target displacement histories 15 mm from the impact point are presented in Figure 57 (b). The experimental displacement data is additional evidence of anisotropic behavior, since the displacements on the rolled axis are generally larger than those on the transverse axis. These results are predicted rather well by the anisotropic numerical simulation, see the solid traces in Figure 57 (b). The displacement history from the von Mises simulation is represented by the dashed trace and lies below both the experimental and anisotropic numerical traces because the von Mises yield function overestimates the strength of the target, see Figure 55 (a).

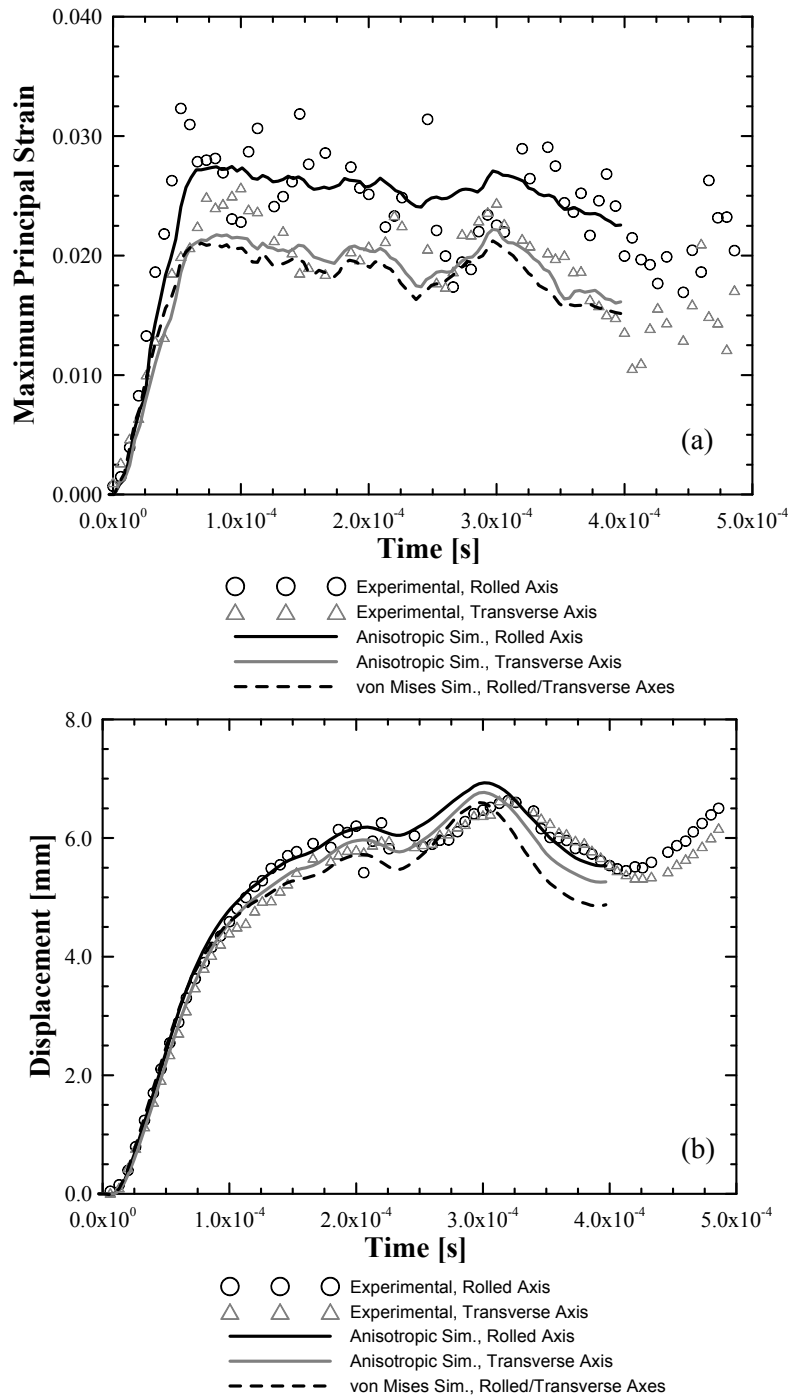


Figure 57. Comparison of calculated maximum principal strains (a) and displacements (b) to those measured using three dimensional DIC for a Ti-6Al-4V projectile impacting 3.175 mm thick 2024-T3 aluminum sheet at 205.1 m/s.

Figure 58 presents maximum principal strain (a) and displacement (b) data for an A2 tool steel projectile impacting a 12.7 mm thick 2024-T351 target panel at 249.6 m/s. In this impact

case, the projectile perforates the target panel with a measured residual velocity of 64.6 m/s. The simulation employing the anisotropic yield function predicts target perforation with a projectile residual velocity of 53.0 m/s while the von Mises simulation predicts no perforation. The experimental maximum principal strain data in Figure 58 (a) shows no evidence of directional deformation behavior since the strain response on the rolled and transverse axes are nearly identical. The anisotropic simulation, represented by solid traces in Figure 58 (a), predicts similar behavior by showing negligible variance between the data extracted from the two axes. The anisotropic simulation generally overestimates the maximum principal strain on the rear panel surface. The dashed trace in Figure 58 (a) represents the maximum principal strain history from the von Mises simulation which is a significant overestimation compared to the experimental data.

Experimental and calculated rear surface target displacement histories are presented in Figure 58 (b). The experimental displacement data shows little evidence of anisotropic behavior, especially for the first 100 microseconds after impact. The anisotropic simulation also shows little variance between the displacement histories on the rolled and transverse axes, as the two solid traces in Figure 58 (b) are nearly indistinguishable. Both the anisotropic simulation and the von Mises simulations over-predict the panel displacement. The anisotropic simulation data, however, agrees more closely with the experimental data. It is shown in Figure 55 (b) that the shear strength of 2024-T351 plate is overestimated by the von Mises yield function. Because of this, the panel is perforated in the anisotropic simulation, but it is not in the von Mises simulation. The larger strains and displacements from the simulations evident in Figure 58 are due to the fact that the target panel absorbs more kinetic energy from the projectile than it does experimentally. The anisotropic simulation predicts a residual projectile velocity of 53.0 m/s and the projectile is completely brought to rest in the von Mises simulation. Both simulations predict projectile residual velocities significantly lower than that measured experimentally (64.6 m/s). The difference in kinetic energy is absorbed by the target panels leading to higher simulated strains and displacements.

The experimental and numerical data suggest that the anisotropy of the 12.7 mm thick plate target does not have a significant effect on the global deformation behavior. There is a large difference, however, between the projectile residual velocities from the anisotropic and von Mises simulations. In all cases, the projectile residual velocities predicted by the anisotropic model were higher than those predicted by the von Mises model, see Figure 54 (b). It is concluded that this is due to the fact that the anisotropic yield function is weaker under shear loads than the von

Mises function, as illustrated in Figure 55 (b). This is intuitive when considering the application since normal impact of a projectile with a flat target panel gives rise to concentrated shear stresses located around the circumference of the eventual plug.

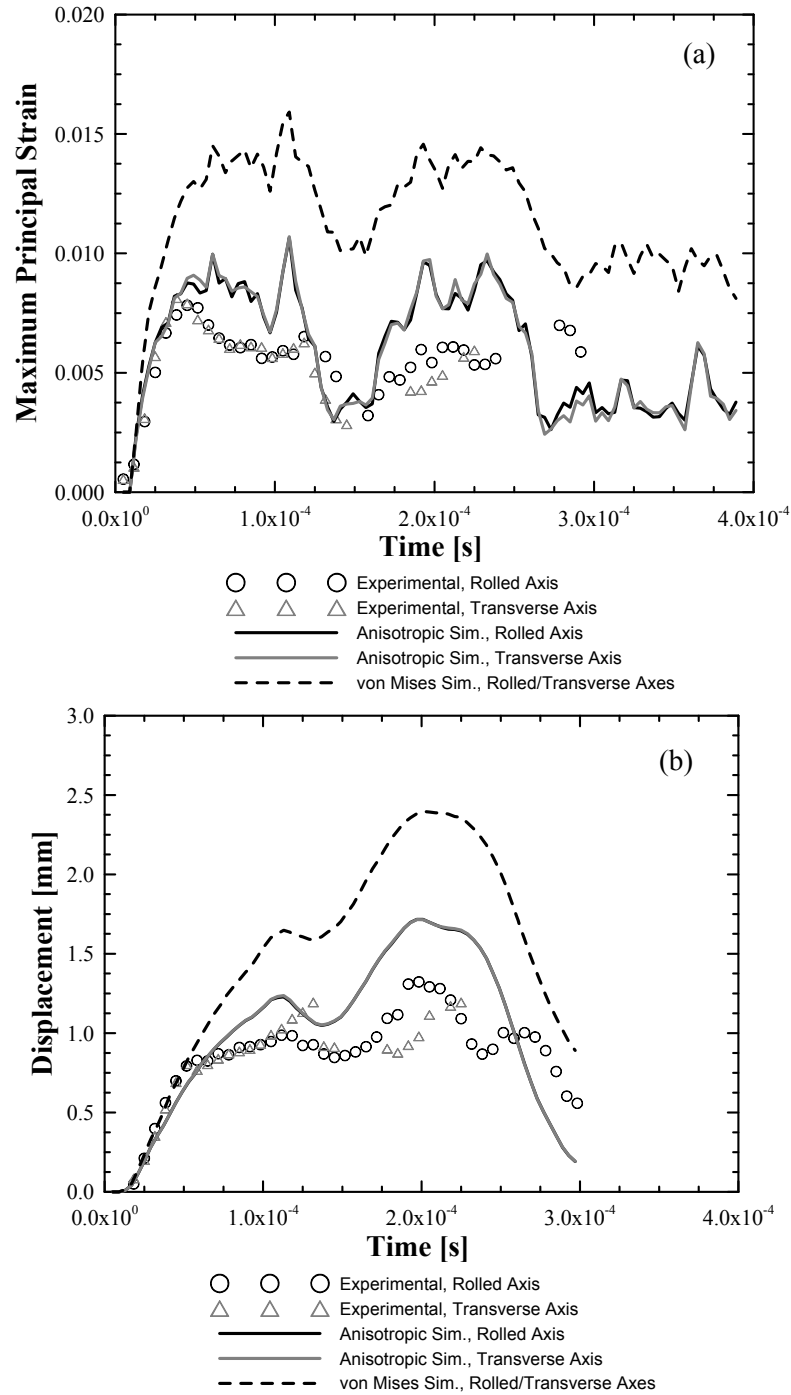


Figure 58. Comparison of calculated maximum principal strains (a) and displacements (b) to those measured using three dimensional DIC for an A2 tool steel projectile impacting 12.7 mm thick 2024-T3 aluminum plate at 249.6 m/s.

## Chapter 6: Dynamic Ductile Fracture of 2024-T351 Aluminum in Punch Experiments

Results from the dynamic punch experiments described in Chapter 3 are presented here. The dynamic ductile fracture behavior of 2024-T351 aluminum is investigated using the dynamic punch experiments listed in Table 7. The failure mode evolution of the disk specimens is studied by examining recovered specimens from restricted and unrestricted displacement punch experiments. Results from numerical simulations of the experiments are compared to the test data. Simulation results are used to monitor the specimen's stress state and equivalent plastic strain histories at the region of initial crack formation. Average triaxiality, product triaxiality and Lode parameter values are computed for each experiment. These parameters combined with the equivalent strain at the instant of crack formation are used to provide data for the fracture locus discussed in Chapter 7.

### Failure Mode Evolution of Disk Specimens under Dynamic Punch Loads

Results from three experiments, conducted with the 2.39 mm radius punch, are presented in Figure 59. Force versus displacement curves from restricted and unrestricted experiments are shown in Figure 59 (a). The solid black trace represents data from an unrestricted displacement experiment while the dashed and gray traces represent data from experiments restricted to 1.6 mm and 2.4 mm of relative displacement, respectively. Photographs of recovered specimens after 1.6 mm, 2.4 mm and unrestricted displacements are presented in Figure 59 (b), (c) and (d). After 1.6 mm of relative displacement, see Figure 59 (b), a fully-formed circumferential crack is evident and radial cracks are beginning to form petals. At 2.4 mm of relative displacement, see Figure 59 (c), the circumferential crack has grown as a plug roughly the diameter of the punch tip begins to form. The radial cracks have extended and the petals are further developed. A combined plugging and petaling failure mode is evident in the photo of the specimen recovered from the unrestricted test, see Figure 59 (d). The plug is surrounded by a ring comprised of eight petals.

Results from experiments, conducted using the 4.75 mm radius punch, are presented in Figure 60. Figure 60 (a) presents force versus displacement curves from three experiments (one

unrestricted and two restricted to 2.4 mm and 3.9 mm displacement). Photographs of recovered specimens are presented in Figure 60 (b), (c) and (d). Figure 60 (b) shows a circumferential crack, which is not entirely enclosed, formed in the specimen after 2.4 mm of relative displacement. Figure 60 (c) presents the specimen recovered after 3.9 mm of relative displacement. A plug has nearly been ejected and small petals have formed from the development of radial cracks. The 4.75 mm radius punch also induces a combined plugging and petaling failure mode in the specimen, see Figure 60 (d). Seven petals have formed around the plug, two are still attached to the plug and five are separate.

Figure 61 presents results from an unrestricted displacement test conducted with the blunt punch. Figure 61 (a) shows the load versus displacement curve. Figure 61 (b) and (c) present photos of the rear and punch sides of the specimen plug, respectively. A lip conforming to the fillet radius of the blunt punch is evident in Figure 61 (c). Figure 61 (d) is a photo of the specimen plug resting on the blunt punch showing that the plug diameter is nearly identical to the punch diameter.

The failure mode evolution of the disk specimen under loading from the 2.39 mm punch can be investigated by comparing the force versus displacement curves and the photos of the recovered specimen in Figure 59. The force versus displacement curves in Figure 59 (a) are not perfectly repeatable, however, they show similar trends. In all three experiments, there is a phase of increasing force with increasing displacement as the specimen is deformed plastically. A drop in the force at 1.0 to 1.3 mm of relative displacement (evident in both the unrestricted and 2.4 mm restricted displacement curves) coupled with the photograph in Figure 59 (b) provide evidence that the initial circumferential crack forms at just over 1.0 mm of relative displacement. It is difficult to identify this drop in 1.6 mm restricted displacement curve because the load increases rapidly when the stop ring engages. The unrestricted curve in Figure 59 (a) shows a decrease in force from 2.0 mm to 3.0 mm of relative displacement. This information combined with the photos in Figure 59 (c) and (d) provide evidence that the radial crack formation propagation (petal formation) is the reason for this decrease. The contact force between the specimen and punch increases from 2800 N at 3.0 mm displacement to 7500 N at 5.4 mm displacement. This, coupled with the photo in Figure 59 (d), indicates that the increase in load is due to the punch forcing the outer edge of the petal ring into the supporting adaptor.

A similar analysis can be made for the 4.75 mm punch test results in Figure 60. Similar to the 2.39 mm force versus displacement curves, each curve in Figure 60 (a) has a phase of increasing force with increasing displacement as the specimen is deformed plastically. There is a

drop in the load at a relative displacement of roughly 1.75 mm. This drop is most evident in the 3.9 mm restricted displacement curve and more gradual for the unrestricted curve. This information, coupled with the post test photograph in Figure 60 (b), is evidence that the circumferential crack initially forms at roughly 1.75 to 2.0 mm of relative displacement. It is difficult to identify the load drop in the 2.4 mm restricted displacement test because the stop ring engages and the load rapidly increases. As the radial cracks, evident in Figure 60 (c), form and propagate, the transmitted load decreases further. At ~2.7 mm of relative displacement, the load increases as the punch pinches the specimen material into the adaptor support. The petals are sheared out at the support leading to the drop in load seen at 3.6 mm of relative displacement.

The specimen failure mode when loaded with the blunt punch is simply plugging instead of combined plugging/petaling. As punch displacement increases, the force increases as the specimen is plastically deformed, primarily in shear, in a region confined to the punch circumference. At ~1.0 mm displacement, the force drops indicating crack initiation and the plug is eventually ejected.

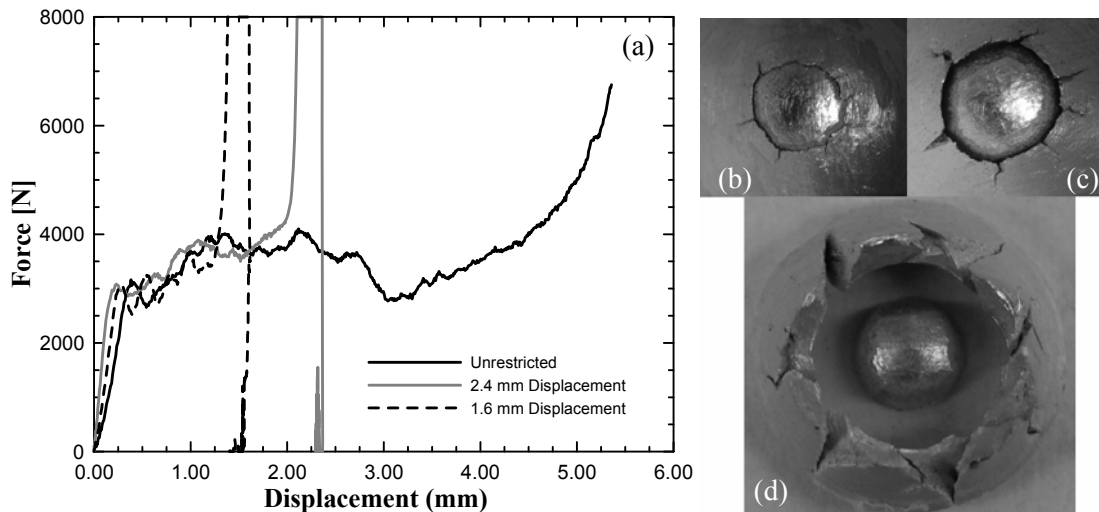


Figure 59. Force versus displacement curves (a) and recovered specimens from restricted and unrestricted displacement dynamic punch experiments (2.39 mm punch radius): (b) 1.6 mm relative displacement, (c) 2.4 mm relative displacement, (d) unrestricted.

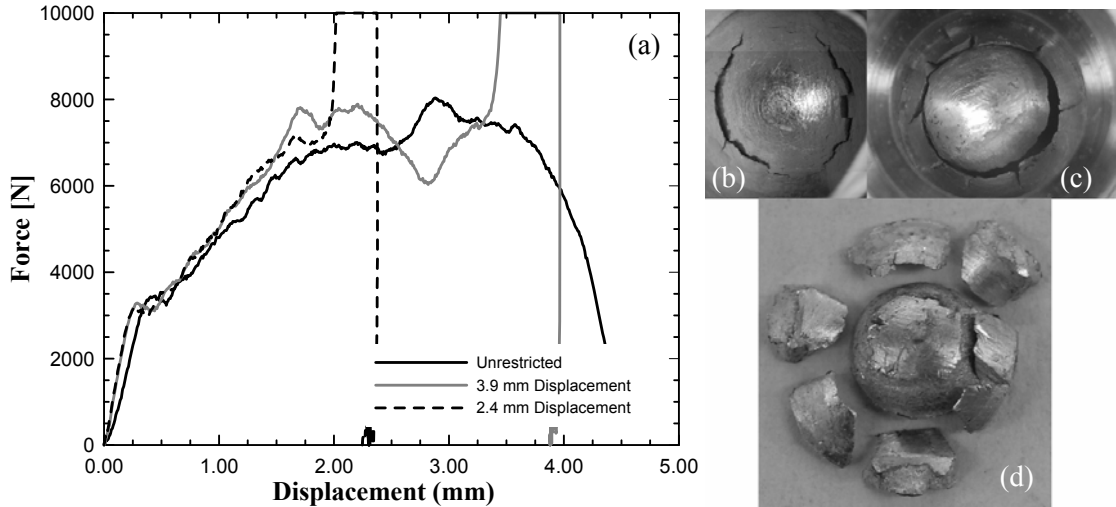


Figure 60. Force versus displacement curves (a) and recovered specimens from restricted and unrestricted displacement dynamic punch experiments (4.75 mm punch radius): (b) 2.4 mm relative displacement, (c) 3.9 mm relative displacement, (d) unrestricted.

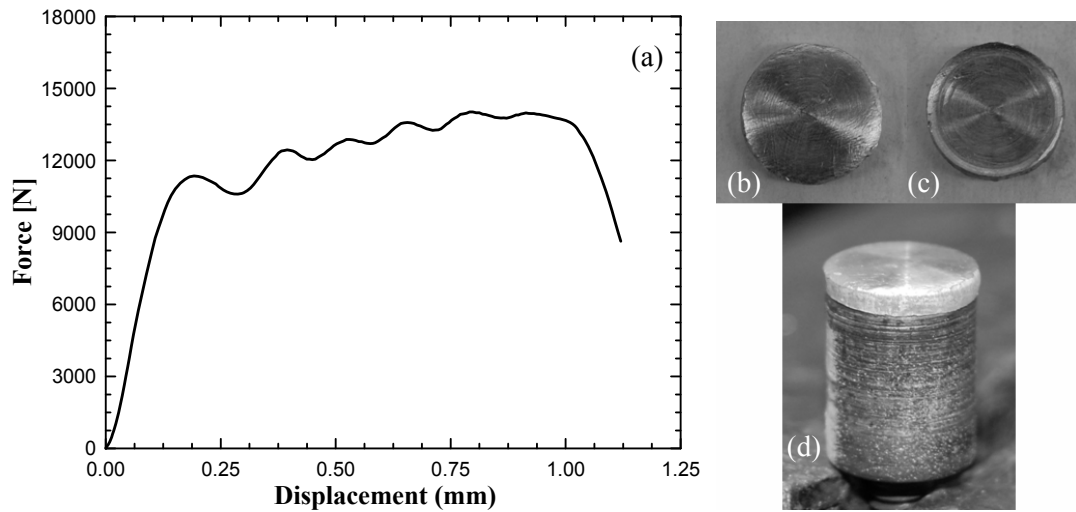


Figure 61. Force versus displacement curve (a) and a specimen plug recovered from an unrestricted dynamic punch experiment (blunt punch): (b) rear view of plug, (c) front view (punch side) of plug, (d) plug resting on the punch.

### Finite Element Simulations and Results

Numerical simulations of the experiments described above are conducted using LS-DYNA [1] to determine the stress state and plastic strain histories in the crack formation region of the disk specimens. The finite element model is presented in Figure 62. Figure 62 (a) shows the 2.39 mm radius punch and a sectioned view of the specimen assembly consisting of two specimen adaptors and the disk specimen itself. Figure 62 (b) presents a normal view of the mesh for the disk specimen. Three dimensional, eight-node, constant stress, solid elements are used in all

simulations. The mesh for the 2024-T351 disk specimen is constructed such that there are twenty elements through the thickness and that the aspect ratios of the elements in the region contacted by the punch are nearly 1.0. Specimen material surface nodes outside of a 5.842 mm radius from the center of the disk specimen are bound to the left and right adaptor fixtures, simulating the epoxy bond between the parts in the experiment. The adaptor fixture at the left of Figure 62 (a) is fixed at its base and the punch motion is prescribed to simulate a constant relative velocity of 20.0 m/s.

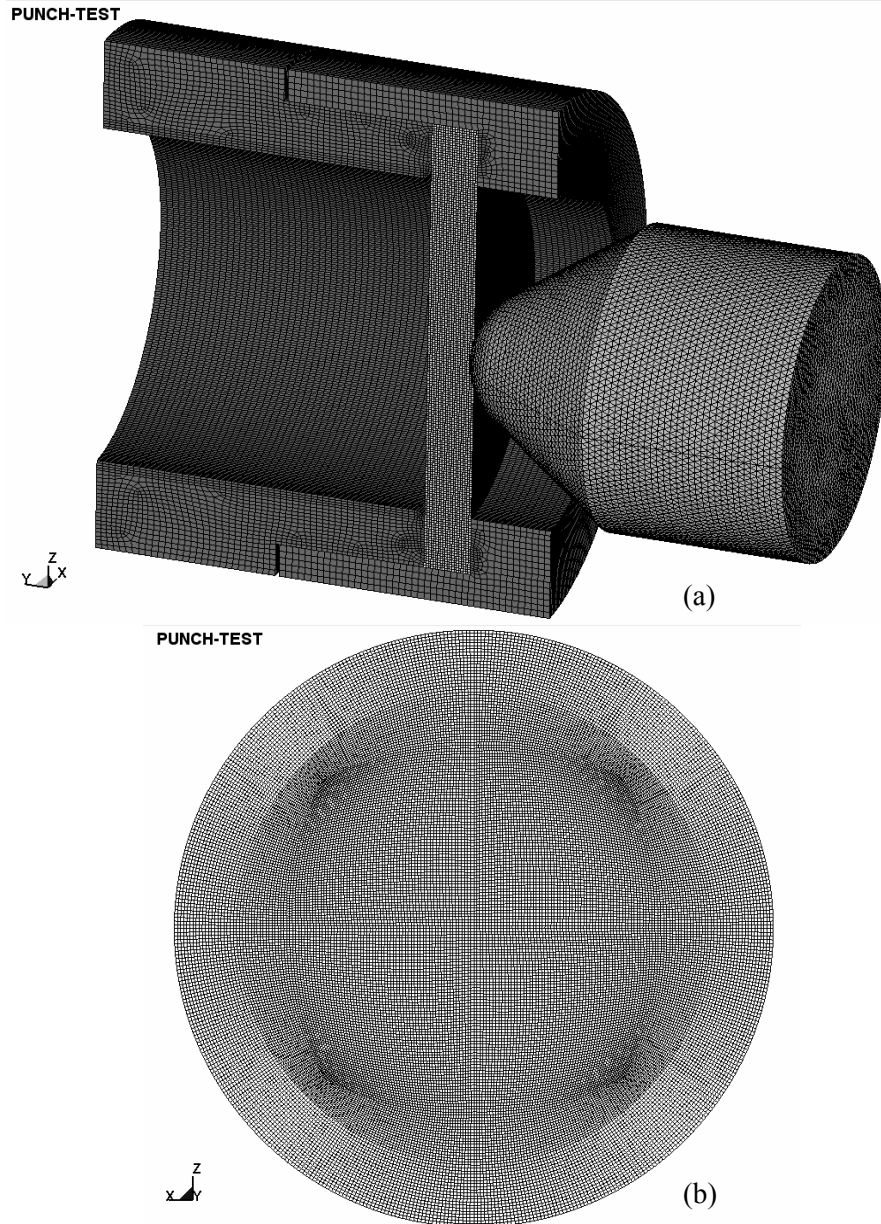


Figure 62. Finite element model: (a) entire model assembly including the specimen, specimen adaptor fixtures and the sharp punch, (b) top view of the 2024-T351 aluminum disk specimen.

The hardened 4340 steel punch is assumed to be rigid in the simulations, while the Ti-6Al-4V adaptors are modeled with a linear elastic constitutive model. The 2024-T351 disk specimen is modeled with the same representation of the simplified Johnson Cook constitutive model [6] used for the von Mises yield function impact simulations in Chapter 5. Constitutive model parameters for 2024-T351 aluminum used in the simulations are found in Table 11. No fracture criterion is specified for the 2024-T251 disk specimen. This approach was taken to ensure that the simulated specimen would not form cracks at relative punch displacements less than those determined experimentally.

Results from the 2.39 mm radius punch test simulation are presented in Figure 63. Simulated and experimental force versus displacement curves are compared in Figure 63 (a). For displacements less than 1.25 mm, the simulated and experimental traces agree rather well, especially for the unrestricted data. The experimental curves show that the load decreases and diverge from the simulated trace at  $\sim 1.25$  mm of displacement. In the previous section, this load drop and divergence is attributed to the initial circumferential crack formation that forms on the rear surface of the specimen, see Figure 59 (b). In contrast, strain hardening in the specimen causes the simulated trace to increase monotonically with increasing displacement. The load drop is not captured in the simulated trace since a fracture criterion is not used in the simulation. If failure process initiates when the load drops, the data comparison in Figure 63 (a) can be used to identify the displacement at which the circumferential crack initially forms. This information can be used with the simulated stress state and plastic strain histories in Figure 63 (b) to relate the equivalent plastic failure strain to the stress state parameters discussed previously. The stress triaxiality, Lode parameter, product triaxiality and equivalent plastic strain histories of an element at the position where the circumferential crack initially forms on the rear of the specimen are presented in Figure 63 (b). The location of initial crack formation is measured on recovered specimens from restricted displacement experiments. When loaded with the 2.39 mm radius punch, the disk specimen forms a circumferential crack on its rear surface 1.18 mm from the center. The triaxiality at this location increases to 0.625 20  $\mu$ sec after loading. The Lode parameter evolves significantly through the duration of loading. It increases initially to 0.5 and then becomes negative after 15  $\mu$ sec with a minimum value of -0.78 at  $\sim 25$   $\mu$ sec and eventually levels off at -0.425. The product triaxiality term is slightly negative and nearly constant at a magnitude close to zero.

Simulation results are presented for the 4.75 mm radius punch in Figure 64. The simulated force versus displacement curve for the 4.75 mm radius punch agrees well with the experimental

data, see Figure 64 (a). The divergence of the experimental traces from the simulated trace at  $\sim 1.69$  mm of displacement indicates the formation of the circumferential crack evident in Figure 60 (b). The simulated stress state and equivalent plastic strain histories for the 4.75 mm punch are shown in Figure 64 (b). These data are extracted from an element 5.69 mm from the center of the disk specimen which is the location measured from the recovered restricted displacement specimen where the circumferential crack initially forms. For this case, the triaxiality is generally lower and the Lode parameter is generally higher than those present in the specimen loaded by the 2.39 mm punch. The product triaxiality is nearly zero for the entire simulation. In general, the stress state parameters for specimen loaded with the 4.75 mm punch vary more widely than those for the specimen loaded with the 2.39 mm punch.

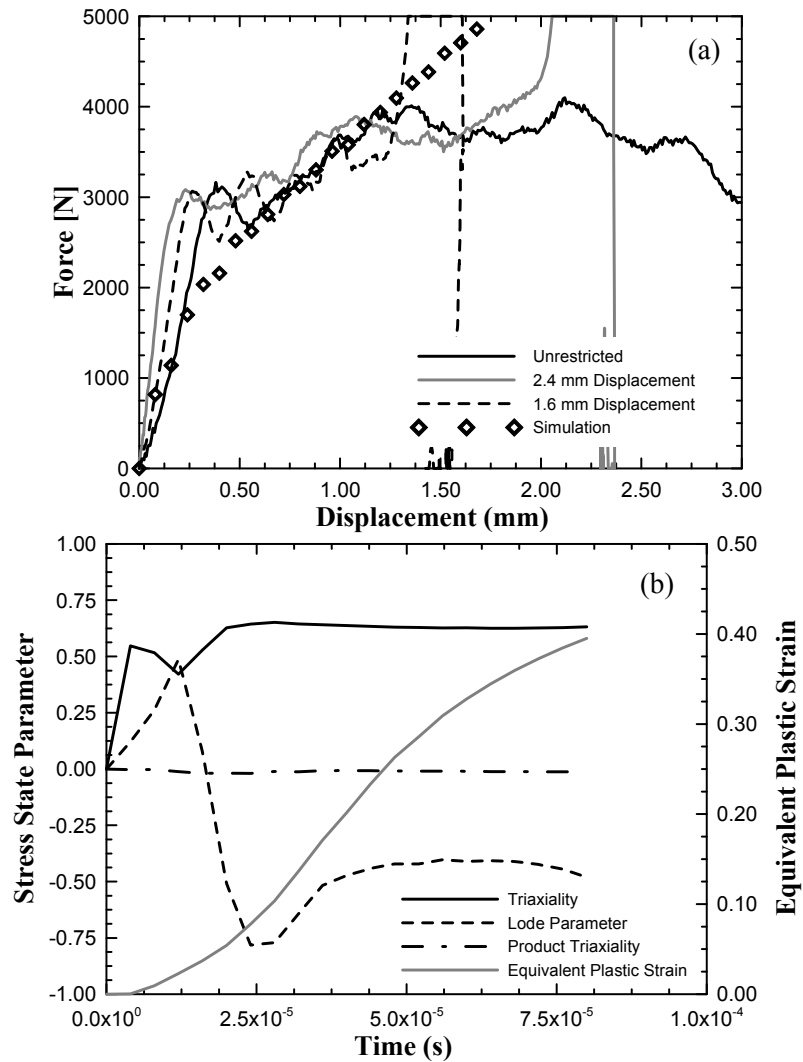


Figure 63. 2.39 mm radius punch simulation results: (a) comparison of experimental and simulated force versus displacement curves, (b) calculated stress state and equivalent plastic strain histories of an element in the region of initial crack formation.

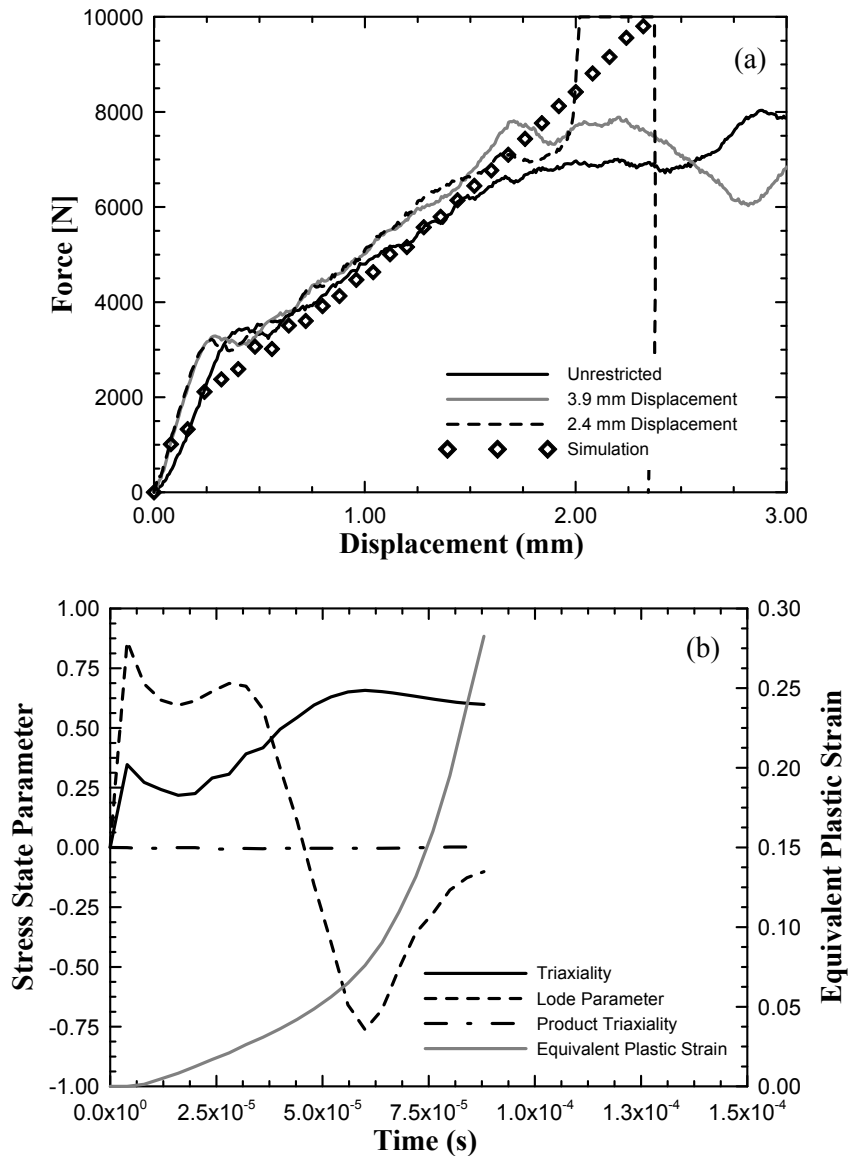


Figure 64. 4.75 mm radius punch simulation results: (a) comparison of experimental and simulated force versus displacement curves, (b) calculated stress state and equivalent plastic strain histories of an element in the region of initial crack formation.

The simulated force versus displacement curve agrees well with the experimental data for the blunt punch, see Figure 65 (a). The load drop in the experimental trace at  $\sim 1.02$  mm displacement indicates the onset of fracture in the disk specimen. The simulated stress state and equivalent plastic strain histories for the blunt punch are shown in Figure 65 (b). These data are extracted from an element 4.75 mm from the center of the disk specimen which is nearly identical to the radius of the blunt punch cross-section and the location where the specimen plug forms, see Figure 61 (d). 8  $\mu$ sec after the start of loading, the stress triaxiality is nearly constant at 0.6. The

Lode parameter settles at a value of  $-0.25$   $16 \mu\text{sec}$  after load. The product triaxiality for this case is nearly zero for the duration of the simulation.

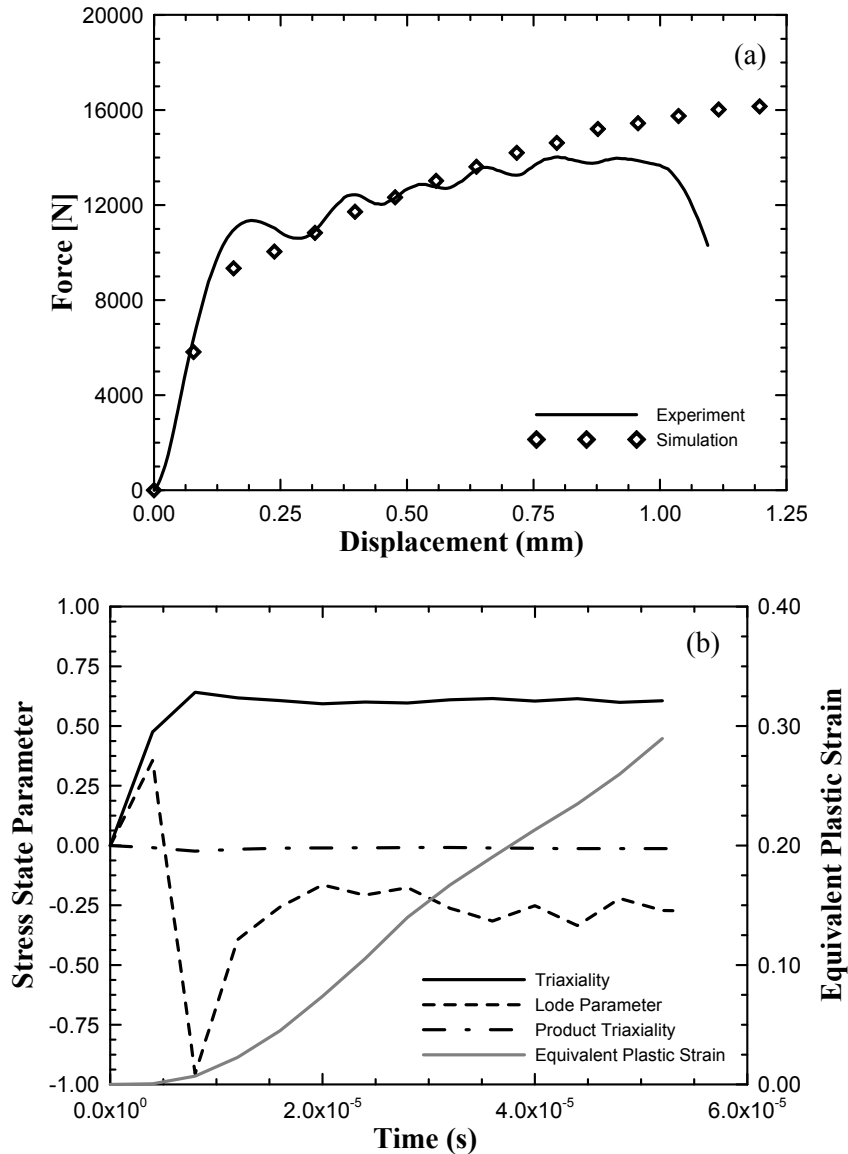


Figure 65. Blunt punch simulation results: (a) comparison of experimental and simulated force versus displacement curves, (b) calculated stress state and equivalent plastic strain histories of an element in the region of initial crack formation.

The data in Figure 63, Figure 64 and Figure 65 are used to determine a relationship between the equivalent plastic fracture strain and the stress state for these punch experiments. Figure 66 (a), (b) and (c) present the equivalent plastic fracture strain versus stress triaxiality, Lode parameter and product triaxiality, respectively. Evolution of the stress state parameters in time is

undesirable from the standpoint of using these data to generate equivalent plastic fracture strain versus stress state data. Because the stress state varies, damage in the specimen accumulates at varying rates. Since the stress state parameters evolve significantly as plastic strains accumulate for all of the punch experiments, the stress state parameter values presented in Figure 66 are averages from the beginning of load to the crack initiation. The stress triaxiality ranges from 0.478, for the 4.75 mm radius punch, to 0.6, for the 2.39 mm radius punch. Lode parameters range from -0.323, for the 2.39 mm radius punch, to 0.110, for the 4.75 mm radius punch. The variation in product triaxiality is minimal ranging from -0.012, for the blunt punch, to -0.003, for the 4.75 mm radius punch. The material is most ductile when loaded with the 2.39 mm radius punch and exhibits the least ductility when loaded by the 4.75 mm radius punch. The data shows an increase in ductility with increasing triaxiality, which is contrary to the findings of Hancock and Mackenzie [48] but consistent with other experimental studies [53],[58]. The ductility decreases with increasing Lode parameter. There is little variation in the product triaxiality parameter making it difficult to draw conclusions about its influence on ductility for the punch experiments considered here.

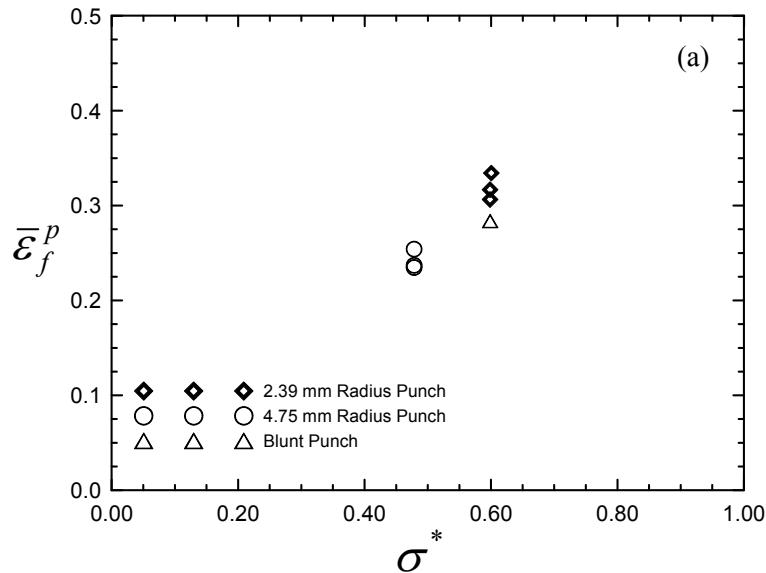
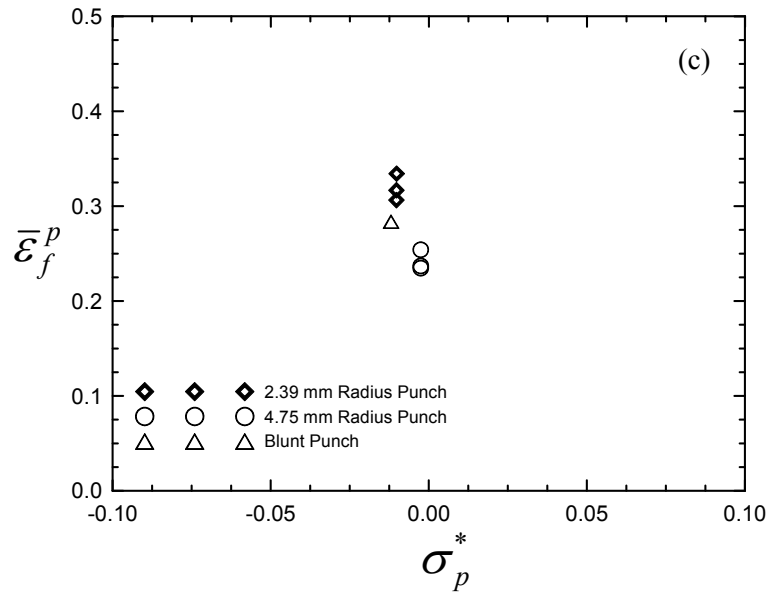
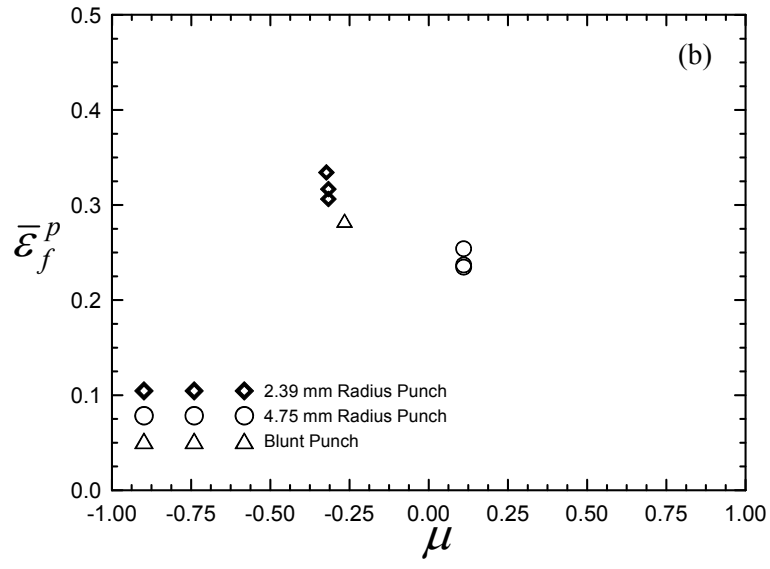


Figure 66. Dependence of equivalent plastic fracture strain on stress state in dynamic punch experiments: (a) stress triaxiality,  $\sigma^*$ , (b) Lode parameter,  $\mu$ , (c) product triaxiality,  $\sigma_p^*$ .

(Continued)

Figure 66 continued



## Chapter 7: Fracture Locus Construction for 2024-T351 Aluminum

Results of the ductile fracture test program are presented and consolidated in this chapter. Experimental data from the tests summarized in Tables 3, 4, 5, 6 and 7 are used to construct a new fracture locus for 12.7 mm thick 2024-T351 aluminum plate. The experiments include tension tests on specimens with various geometries, pure shear (torsion) tests, combined loading (tension – torsion and compression – torsion) and the dynamic punch experiments discussed in Chapter 6. The experimental techniques used for each of these experiments are discussed in Chapter 3.

### Tension Experiments

The tension test data is used with a coupled experimental – numerical technique to generate data points for the fracture locus. The results of numerical simulations of the experiments are compared to experimental data to determine the stress state history and the equivalent plastic strain history of the specimen at the region where fracture initiates. Numerical simulations are conducted using LS-DYNA. Meshed specimen geometries are presented in Figure 67. The mesh for the plane stress specimen with a notch radius of 4.763 mm is shown in Figure 67 (a). The mesh of the axisymmetric specimen with a notch radius of 14.503 mm is presented in Figure 67 (b). The plane strain specimen with a notch radius of 13.970 mm is presented in Figure 67 (c). The simulations are constructed similar to the tension simulations discussed in Chapter 4, one end is fixed while a constant velocity displacement history is applied to the other. Three dimensional, eight-node, constant stress, solid elements are used in all simulations. The plane stress specimens are meshed so that there are ten elements through the thickness and forty elements across the minimum gage section width. Axisymmetric specimen meshes contain forty elements across the diameter of the minimum notch cross-section. Plane strain specimens are meshed to contain ten elements across the minimum gage section width and 125 elements across the gage thickness. Care is taken to keep the aspect ratios of the elements close to one in the gage section region of all specimen meshes. Meshes for all specimen geometries not shown in Figure 67 are presented in Appendix B. The simplified Johnson Cook constitutive model, described in Chapter 5, is used with the model parameters in Table 11 to represent the 2024-T351 specimens. No fracture criterion is used in these simulations to ensure that the simulated specimen does not fracture prematurely.

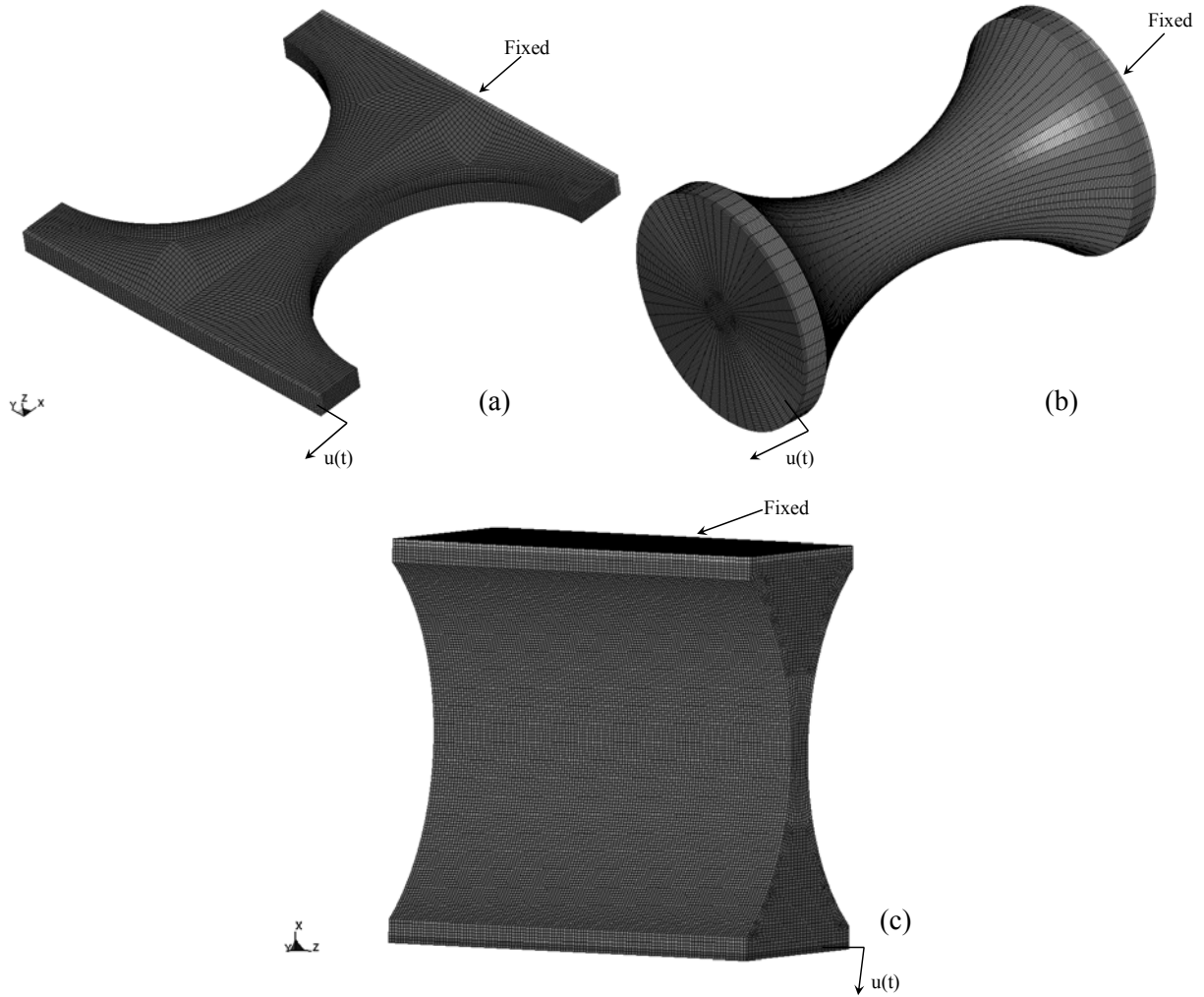


Figure 67. Finite element meshes for selected tension specimens: (a) plane stress, (b) axisymmetric, (c) plane strain.

The analysis procedure for these experiments is illustrated for an axisymmetric specimen with a 14.503 mm radius notch in Figure 68. The procedure consists of comparing the maximum principal strains on the surface of the specimen measured using 3D DIC, see Figure 68 (a), to the simulated maximum principal surface strains, see Figure 68 (b). The surface strains are extracted at the point where they are the largest which corresponds to the minimum notch cross-section for all tension specimen geometries. The simulated specimen is sectioned and the internal center element is used to extract equivalent plastic strain and stress state histories, see Figure 68 (c). The onset of specimen fracture is accompanied by a drop in the experimental load measurement. At this point, the maximum principal surface strain at fracture (measured with DIC) is recorded. When the simulated maximum principal surface strains reach this value, the current equivalent plastic strain at the center of the specimen is

extracted as the equivalent plastic fracture strain ( $\bar{\epsilon}_f^p$ ). Since the stress state at the center of the specimen evolved throughout the duration of the experiment, average values of the stress state parameters ( $\sigma^*$ ,  $\mu$  and  $\sigma_p^*$ ) are computed from the beginning of loading to the onset of fracture.

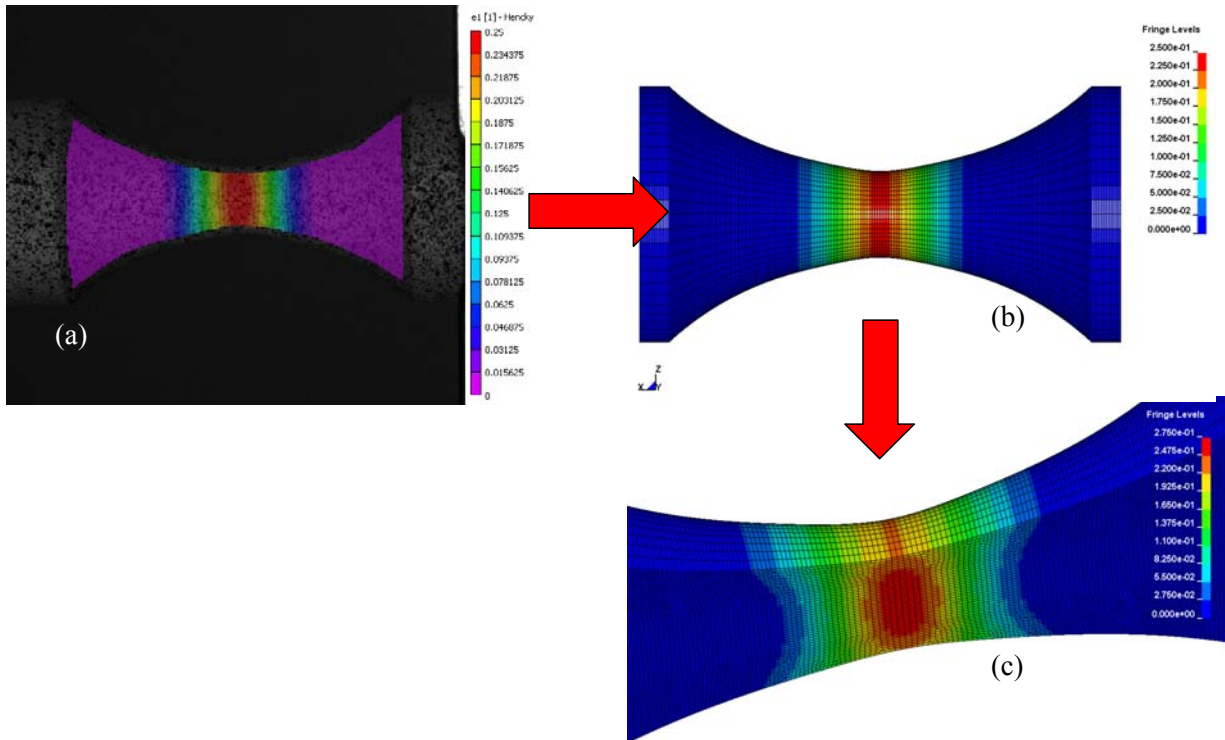


Figure 68. Analysis procedure for a coupled experimental – numerical tension experiment on an axisymmetric notched specimen: (a) experimental maximum principal surface strain, (b) simulated maximum principal surface strain, (c) internal equivalent plastic strain.

Experimental and simulated data from a tension test on an axisymmetric specimen with a 14.503 mm notch are presented in Figure 69. Load, strain and three stress state parameters are plotted versus specimen displacement. The solid and dashed light gray traces are the experimental and simulated load carried by the specimen, respectively. These traces correspond to the vertical axis on the left of the plot. The simulated load history is extracted from a cross-section plane normal to the direction of loading. The simulated load slightly overestimates the force measured experimentally. In general, the experimental and simulated force versus displacement curves agree well. The solid and dashed black traces represent experimental and numerical maximum principal surface strains, respectively, at a point on the minimum notch diameter. The black trace distinguished with diamonds is the simulated equivalent plastic strain of an internal element located on the specimen axis of symmetry and at the minimum cross section diameter.

Data is also extracted from this internal element to calculate the stress triaxiality, Lode parameter and product triaxiality. These parameters are plotted versus the vertical axis on the far right. The triaxiality and product triaxiality evolve throughout the duration of the experiment, while the Lode parameter is constant at 1.0, since  $\sigma_2 = \sigma_3$ , due to symmetry of the specimen geometry and loading. The vertical gray line at a displacement value  $\sim 1.0$  mm identifies specimen fracture. At this displacement, the experimental and simulated surface strains agree at a value of 0.25. Thus, an equivalent plastic fracture strain of 0.295 is extracted for this particular experiment. The stress state parameters extracted for the fracture locus are averaged from load initiation to the onset of fracture.

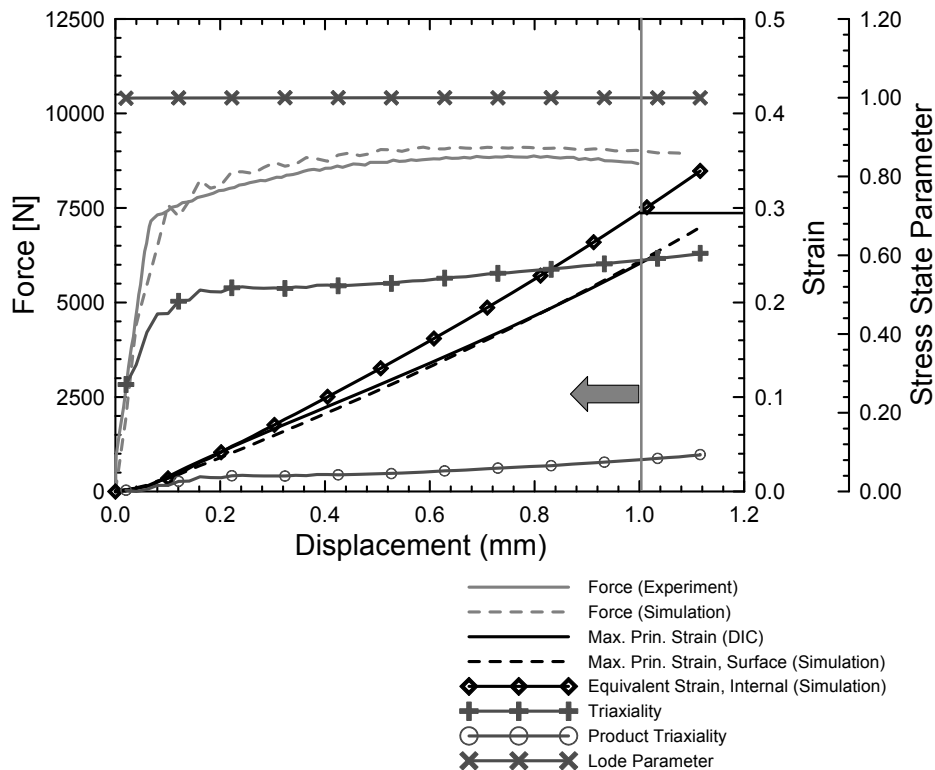


Figure 69. Experimental and simulated data from an axisymmetric notched tension specimen.

Experimental data and results from numerical simulations of the other tension specimen geometries are presented in Appendix C. For the plane stress specimens, the simulated force versus displacement curves matched the experimental curves well, however, the simulated maximum principal surface strains overestimate those measured with DIC. The axisymmetric notched specimen simulation results matched both the force versus displacement and maximum principal surface strain experimental data well. The plane strain specimen simulations overestimate the force endured by the specimen for all three geometries. It is postulated that this may be due to the fact that the von Mises yield function used in the

simulations overestimates the strength of the material, as described in Chapter 5. The simulated maximum principal surface strains for the plane strain specimens match the experimental strains well.

### Combined Loading Experiments

Combined tension – torsion loading and compression – torsion loading of 2024-T351 aluminum thin walled tube specimens are also conducted to generate data points for the fracture locus. The combined loading experimental program is described in Chapter 2 and the specifics of the experiments are described in Chapter 3. Combined loading experiments are desirable for the purpose of constructing a fracture locus for two reasons. First, the experiment can be controlled such that the stress state history remains nearly constant for the duration of the experiment. Second, the thin-walled tube specimen geometry is simple enough that there is no need to conduct parallel numerical simulations to determine the stress state and equivalent plastic strain histories. If the specimen does not buckle, the stress triaxiality and Lode parameter in the gage section can be computed directly from experimental load and torque measurements using Equations 2.3 and 2.4, respectively. Surface strain data from DIC measurements can be used to determine equivalent plastic failure strain. The tube specimen is thin, therefore, it is assumed that stress and strain gradients through the thickness of the gage section are minimal. The nature of torsional loading requires that the maximum strains in the specimen must exist on the surface, see Equation 3.4.

Reduced history data for a tension – torsion experiment with  $\frac{\sigma_x}{\tau_{xy}} = 1.974$  is presented in Figure 70.

The light gray traces are stresses and correspond to the left axis. The solid light gray trace is axial stress while the dashed light gray trace is the shear stress. Stress state parameters can be calculated from these stress components using the analysis discussed in Chapter 2. Three stress state parameters (triaxiality, Lode parameter and product triaxiality) are also plotted on the far right axis of Figure 70. The stress state parameter histories illustrate one of the advantages that combined loading experiments provide. Most tests used to calibrate damage and fracture models use mechanical experiments in which the stress state history evolves significantly over time and damage is accumulated at different stress states over the duration of the experiment. The stress state parameters for the combined loading experiment, see Figure 70, are nearly constant for the duration of the experiment. Maximum and minimum principal DIC strain histories of a point in the region of eventual fracture are also plotted in Figure 70. These are the black traces and they correspond to the strain axis. It is assumed that the material is incompressible which demands the following constraint in terms of the logarithmic principal strains [77]:

$$\varepsilon_1 + \varepsilon_2 + \varepsilon_3 = 0 \quad . \quad (7.1)$$

The equivalent plastic failure strain ( $\bar{\epsilon}_f^p$ ) is computed using the strain data in Figure 70 and Equations 7.1 and 3.5. All the information necessary to generate a point on a fracture locus is provided experimentally: (1) histories of the state of stress and (2) histories of the surface strains. Reduced history data for the other combined loading cases listed in Table 6 are found in Appendix D.

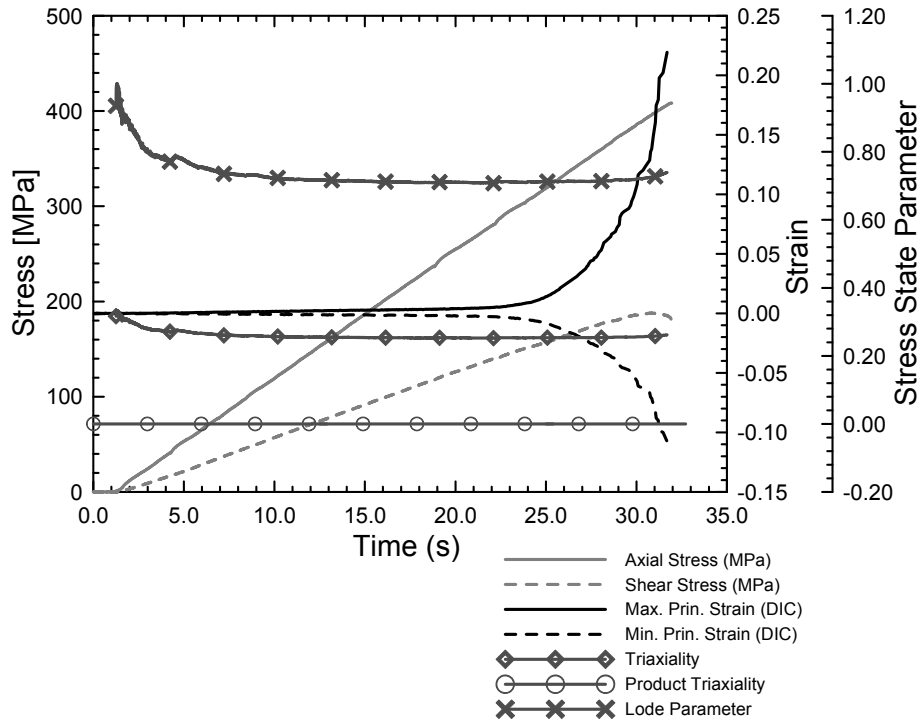


Figure 70. Reduced history data from a combined tension-torsion experiment.

### Fracture Locus Data and Discussion

Fracture locus data for 2024-T351 aluminum are presented in Figure 71. Each plot in Figure 71 is constructed using data from plane stress, axisymmetric and plane strain tension tests, combined loading and pure shear tests and the dynamic punch tests discussed in Chapter 6. Plane stress tension test data are represented by black diamonds while axisymmetric and plane strain tension data are represented by the red boxes and blue triangles, respectively. Combined loading and pure shear experiments are represented by the green circles. The punch experiments are represented by the orange plus signs. At least three experiments are conducted for all of the data points in Figure 71, except for the blunt punch experiment. The fracture strain data in Figure 71 are average values of all of the experiments. Standard deviation of the fracture strain data are indicated with error bars. In general, the experiments were repeatable. The lowest standard deviations are owned by tension tests on both plane strain and notched axisymmetric

specimens. There is significant data spread for the smooth axisymmetric tensile data and the combined compression – torsion experiment.

Equivalent plastic fracture strain is plotted versus stress triaxiality ( $\sigma^*$ ) in Figure 71 (a). The data shows that stress triaxiality alone cannot adequately capture ductile fracture of 2024-T351 aluminum under the stress states considered in this experimental program. This is clearly evident when comparing the axisymmetric, plane strain and plane stress tensile data. The plane stress, plane strain and axisymmetric test series all produce data at triaxiality values within the range:  $0.564 \leq \sigma^* \leq 0.607$ . If stress triaxiality alone is sufficient to describe the fracture behavior, the equivalent plastic fracture strains for each of these experiments would be similar. These four experiments have vastly different average equivalent plastic failure strains, ranging from 0.104 for the plane stress specimen to 0.290 for the notched axisymmetric specimen. The plot in Figure 71 (a) shows two branches in the triaxiality – equivalent plastic fracture strain space. The axisymmetric tension data provides an upper branch, while the plane stress tension data provides a lower one. Interestingly, the plane strain tension data seem to provide a bridge between the two branches. The punch experiments also lie on these branches. The 4.75 mm radius punch data exists near the plane stress branch, while the 2.39 mm radius and blunt punch data are close to the axisymmetric branch. As the triaxiality decreases from 0.3 to 0.0, the combined tension – torsion and pure shear data show a trend of decreasing fracture strains which has been observed by other researchers [53]. The combined compression – torsion tests provides the largest fracture strain data point and the lowest triaxiality magnitude. This agrees with earlier work in the field of ductile fracture which contends that the fracture strain must increase with decreasing triaxiality [48,49].

Equivalent plastic fracture strain is plotted versus the Lode parameter ( $\mu$ ) in Figure 71 (b). Fracture behavior trends are evident in this plot. For  $0.1 > \mu < 1.0$ , the equivalent plastic fracture strains hold relatively steady at a magnitude of  $\sim 0.225$ . Data from several different types of experiments, including tension tests on plane stress and plane strain specimens, combined tension – torsion tests and the 4.75 mm radius punch tests, contribute to this trend. As the Lode parameter decreases from 0.15 to -0.02, the fracture strain decreases precipitously to 0.10. Data from the blunt and sharp radius punch tests and the combined compression – torsion test indicate that the fracture strain increases rapidly as the Lode parameter decreases from -0.02 to -0.41.

The dependence of equivalent plastic fracture strain on the product triaxiality parameter ( $\sigma_p^*$ ) is presented in Figure 71 (c). It is difficult to identify trends in the fracture strain – product triaxiality space, since relatively few of the experiments provide non-zero product triaxiality values. Only the tension tests on axisymmetric and plane strain specimens provide product triaxiality magnitudes that are

significantly different than zero. The plane stress and combined loading experiments do not provide useful data in the product triaxiality space because the third stress invariant is always zero. The punch tests yield product triaxialities that are slightly negative, yet, still nearly zero. Consequently, the product triaxiality parameter does not stand out as a candidate to significantly enhance the fracture locus. The product triaxiality may eventually play a role in the fidelity of ductile fracture modeling, however, considering the limitations of the current data, it is difficult to draw conclusions about its effect on the fracture behavior of 2024-T351 aluminum. The data presented in Figure 71 covers the following ranges in stress parameter space:

$$\begin{aligned}
 -0.157 &\leq \sigma^* \leq 0.855, \\
 -0.420 &\leq \mu \leq 1.000, \\
 -0.012 &\leq \sigma_p^* \leq 0.438.
 \end{aligned}$$

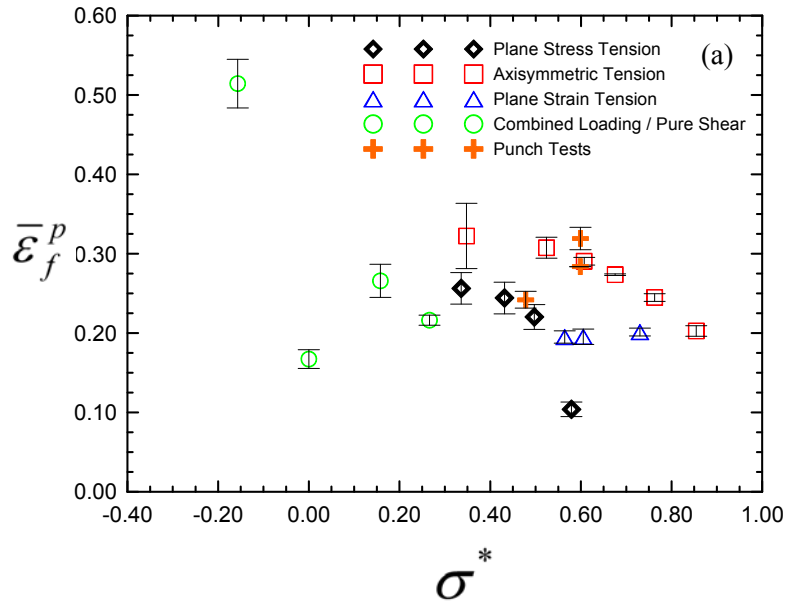
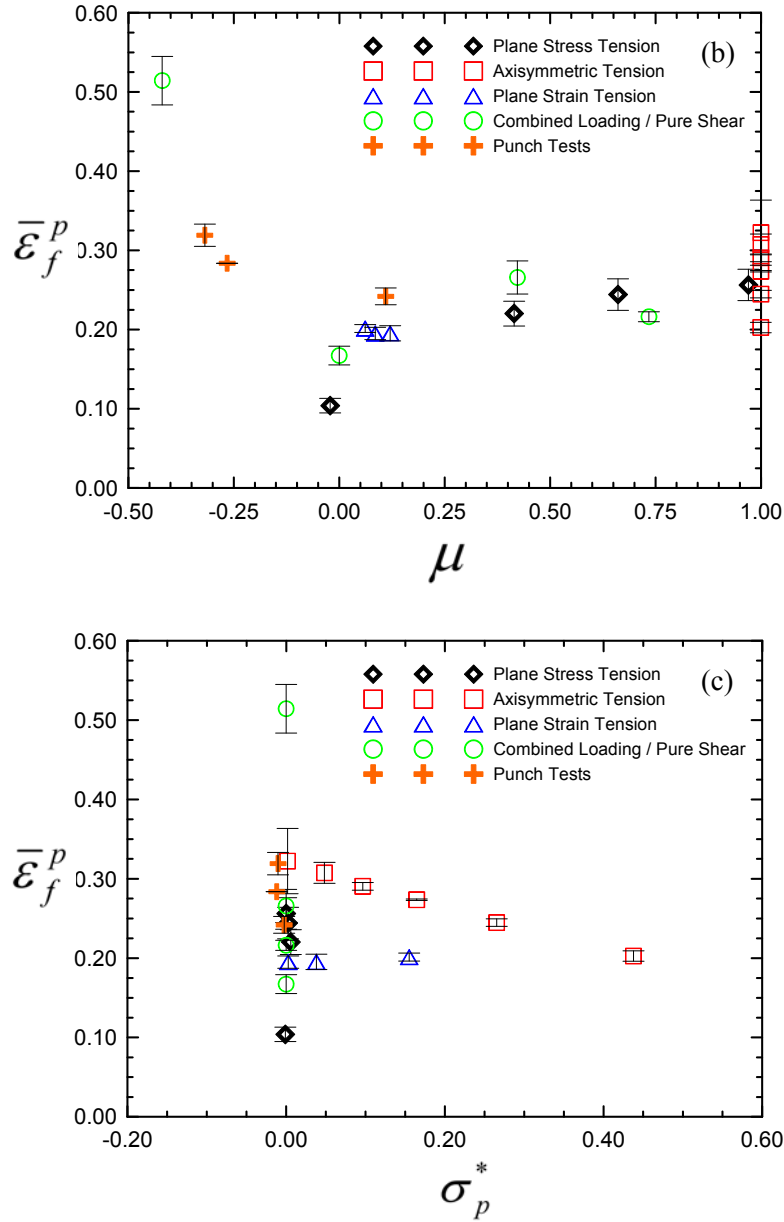


Figure 71. Fracture locus data for 2024-T351 aluminum, equivalent plastic fracture strain versus: (a) stress triaxiality, (b) Lode parameter, (c) product triaxiality. (Continued)

Figure 71 continued



A three dimensional plot of the fracture locus in stress triaxiality and Lode parameter stress space is presented in Figure 72. Experimental data are represented by the black circles, while the surface plot is generated over  $-0.157 < \sigma^* < 0.855$  and  $-0.420 < \mu < 1.0$  with a biharmonic spline interpolation algorithm [78]. Additional views of the fracture locus are shown in Appendix E. The surface passes through all of the experimental data, however, care must be taken when utilizing the surface fit. Although the data points shown in Figure 72 represent eighty-four total experiments of twenty different loading conditions, the data is rather sparse in some regions of stress parameter space.

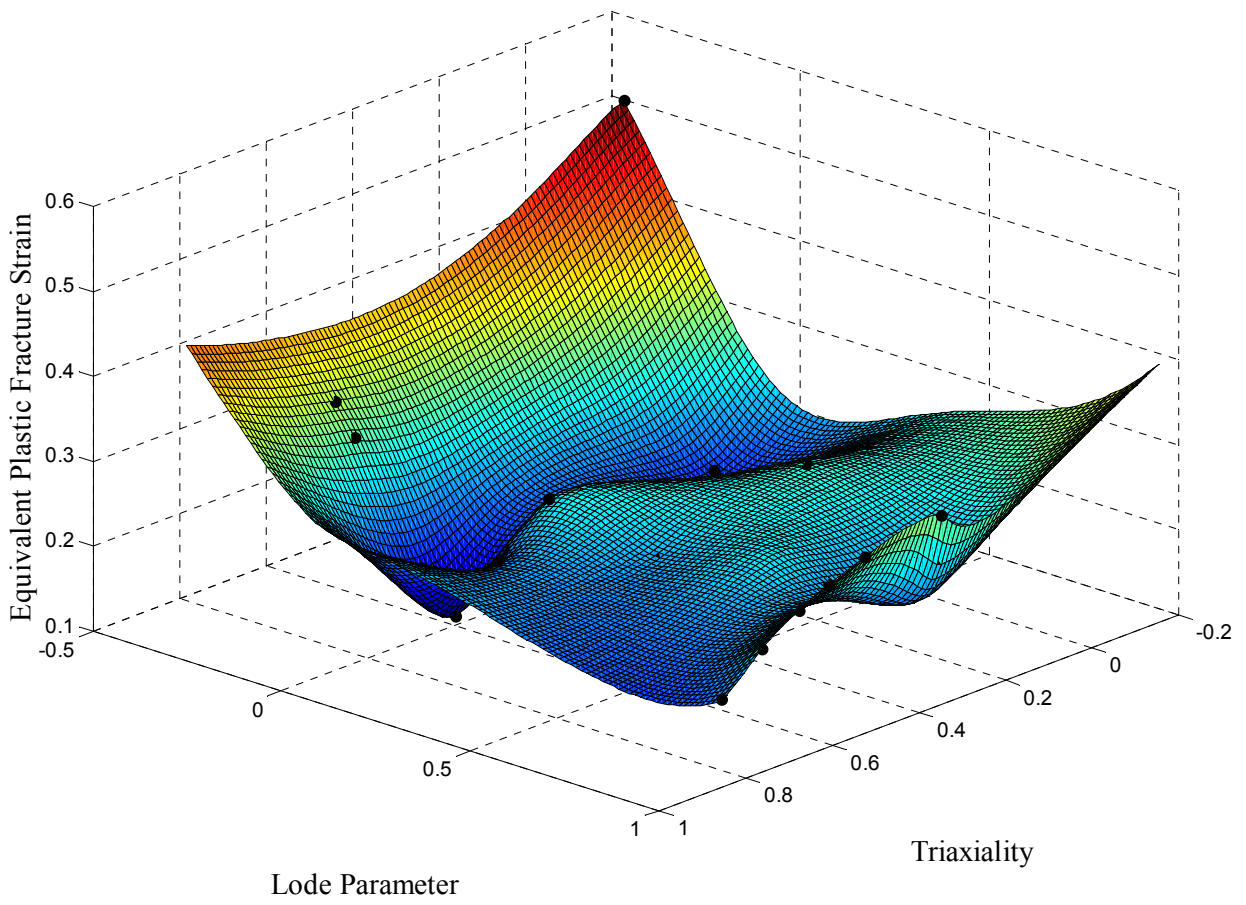


Figure 72. Fracture locus for 2024-T351 aluminum in the triaxiality – Lode parameter stress space.

## Chapter 8: Summary and Conclusions

The findings of the plastic deformation and ductile fracture experimental programs are summarized here. Summaries are included for: (a) the investigation of the plastic deformation behavior of 2024-T351 aluminum presented in Chapter 4, (b) the effect of anisotropic behavior in impacted target panels discussed in Chapter 5, (c) the use of the dynamic punch experiment for ductile fracture characterization (Chapter 6) and (d) the fracture locus developed for 2024-T351 aluminum in Chapter 7.

### Plastic Deformation of 2024-T351 Aluminum

Chapter 4 presents a comprehensive data set from an experimental program devised to determine the strain rate and temperature dependence and the anisotropic strength characteristics of 12.7 mm thick 2024-T351 aluminum. Tension tests over a wide range of strain rates ( $1.0\text{E-}4\text{ s}^{-1}$  to  $1.8\text{E}3\text{ s}^{-1}$ ) and temperatures ( $-50\text{ }^{\circ}\text{C}$  to  $450\text{ }^{\circ}\text{C}$ ) are conducted. Tension tests are also conducted on specimens oriented in four different directions relative to the plate's rolling direction. Compression tests over a wide range of strain rates ( $1.0\text{E-}4\text{ s}^{-1}$  to  $5.0\text{E}3\text{ s}^{-1}$ ) and temperatures ( $-50\text{ }^{\circ}\text{C}$  to  $450\text{ }^{\circ}\text{C}$ ) are conducted. Compression tests are also conducted on specimens oriented in five different directions relative to the plate's rolling direction. Torsion tests over a wide range of strain rates ( $1.0\text{E-}4\text{ s}^{-1}$  to  $2.8\text{E}3\text{ s}^{-1}$ ) and temperatures ( $-50\text{ }^{\circ}\text{C}$  to  $450\text{ }^{\circ}\text{C}$ ) are also conducted. The results show insignificant strain rate effect on the flow stress of the material in tension, compression and shear up to strain rates of about  $5000\text{ s}^{-1}$ .  $J_2$  plasticity theory is not suitable for modeling the plastic deformation of the material since effective stress versus equivalent strain curves from tension, compression and shear tests do not coincide. The material becomes weaker and more ductile with increasing temperature. The strain hardening response of the material decreases significantly at  $300\text{ }^{\circ}\text{C}$ , providing evidence of dynamic recovery and recrystallization. Tension, compression and shear effective stress versus equivalent strain curves do not coincide at any temperature, in fact, the ratio of tensile strength to compressive strength and the ratio of shear strength to compressive strength are less than unity and nearly constant for all test temperatures. Experimental results from tension and compression specimens, machined in five different orientations relative to the plate rolling direction, show that 2024-T351 aluminum plate has anisotropic properties with regard to plastic deformation.

A six-component anisotropic plasticity model is used to simulate the directional tension, compression and shear experiments using the finite element code, LS-DYNA. Published yield function parameters for 2024-T3 aluminum sheet fail to adequately capture the behavior of 2024-T351 plate. A new set of parameters are determined for 2024-T351 aluminum plate using uniaxial compression data from specimens machined in five orientations within the plate and the torsion data. Simulations of select tension, compression and torsion experiments match the experimental data well when using the 2024-T351 plate yield function parameters.

#### Anisotropic Target Panels under Ballistic Impact Loads

Numerical simulations of titanium alloy and tool steel projectiles impacting 3.175 mm thick 2024-T3 sheet and 12.7 mm thick 2024-T351 plate targets at velocities ranging from 205.1 to 292.9 m/s are compared to published experimental data. Available experimental data includes: projectile impact velocity and residual velocity and target panel rear surface strains and displacements from both strain gages and three dimensional DIC. Rear surface target strains measured with strain gages 50.8 mm from the impact point were almost entirely in the elastic range and showed no evidence of anisotropic plasticity behavior for both the 3.175 mm and 12.7 mm target panels. Rear surface strains and displacements, measured using three dimensional DIC 15 mm from the impact point, show experimental evidence of anisotropic deformation behavior in impact cases involving the 3.175 mm thick 2024-T3 target panels, but not the 12.7 mm thick 2024-T351 panels.

Two constitutive models, one using a von Mises yield function and another using an anisotropic yield function, are used to describe the target panels in the numerical simulations. The same failure criterion and mesh density are used for both constitutive models in an effort to determine the effect of using an anisotropic yield function for these specific impact cases. The residual projectile velocities predicted by the two yield functions are considerably different for both the 3.175 mm thick sheet and 12.7 mm thick plate targets. Analysis of the two yield functions show that the anisotropic one gives a generally weaker description of the material and is more sensitive to shear stress than the von Mises function. The material yields quicker and plastic strains accumulate more rapidly in the simulations using the anisotropic yield function. The fracture criterion is also met more rapidly and this leads to perforation and significantly higher projectile residual velocities. Simulated rear surface strains 50.8 mm from the impact point on the target plate agree reasonably well with experimental strains measured with strain gages and they confirm that negligible plastic strains accumulate far from the loading. Therefore, there is little variance in the measured and simulated strains in the rolled and transverse directions of the target panels. Calculated maximum principal strains and displacements 15 mm from the impact location agree well with those

measured using three dimensional DIC for both target materials. Anisotropic deformation behavior is evident in simulations of the 3.175 mm thick 2024-T3 sheet targets, however, it is not in simulations of the 12.7 mm thick 2024-T351 targets.

The yield function used in numerical simulations of impact events should be carefully matched to the target panel. Many constitutive models that are commonly used for impact events, such as the Johnson Cook [6] and Zerilli Armstrong [9] models, employ a von Mises yield function. This simplification could lead to errors in plastic strain accumulation and projectile residual velocity, even for relatively simple materials such as 2024 aluminum sheet and plate. Initial target panel anisotropy and the material's response under shear stress should be considered, the latter especially, since shear stresses are prevalent in the plugging failure mode of normal impact events.

#### Dynamic Punch Experiments for Ductile Fracture

Dynamic punch experiments are used to study dynamic ductile fracture of 2024-T351 aluminum. Circular thin disk specimens are tested using a modified compression SHB apparatus. The punch-specimen contact force, relative velocity and relative displacement histories are determined using standard SHB data reduction techniques. 1-wave, 2-wave SHB analysis shows dynamic force equilibrium is attained. DIC measurements of relative displacement between the punch and specimen adaptor agree with those calculated from the elastic waves to within 1.6% at peak displacement. Stop-rings are used to limit the amount of relative displacement between the punch and specimen. Recovered specimens from restricted displacement experiments coupled with force-displacement curves provide insight into the petaling/plugging failure mode evolution of the disk specimen.

Numerical simulations of the experiments are also presented. The simulated force versus displacement curves agree well with the experiments for all three punches used. A coupled experimental-numerical technique is used to determine the dependence of equivalent fracture strain on the state of stress in the region of initial crack formation. Equivalent plastic fracture strains in the initial crack formation region range from 0.235 to 0.334. Average stress triaxiality in the same region ranges from 0.48 to 0.60. Average Lode parameter values range from -0.32 to 0.11. There is minimal variation in the product triaxiality term (-0.012 to -0.0025) for the three punch geometries. In addition to studying the dependence of ductility on stress state, these data can be used to validate constitutive and fracture models.

## Construction of a Fracture Locus for 2024-T351 Aluminum

A fracture locus for 2024-T351 aluminum is constructed using several different types of mechanical experiments. These tests include tension tests on several different specimen geometries, combined loading and pure shear experiments and the dynamic punch experiments summarized above. Tension tests are conducted on plane stress, axisymmetric and plane strain specimens for a total of thirteen different sample geometries. The plane stress tension test series is conducted on thin specimens, one with a straight gage section and three fabricated with different notch radii. Tension tests are also conducted on axisymmetric specimens, one with a straight gage section and five others with different notch radii. The plane strain tension test series is conducted on thick specimens, one with a smooth gage section and two more with different notch radii. Fracture locus data points are determined from the tension tests using a coupled experimental-numerical technique. Specimen surface strains, measured experimentally with 3D DIC are compared to those from numerical simulations. The simulated data are used to extract the stress state history and the equivalent plastic strain at the fracture initiation site. Combined tension – torsion, compression – torsion and pure shear experiments are also conducted. Stress state histories in the thin-walled tube specimens are determined from load and torque cell measurements while surface strains are measured with 3D DIC. Fracture locus data points are determined solely from experimentally measured data.

The dependence of equivalent plastic fracture strain on three stress state variables is determined. Stress triaxiality ( $\sigma^*$ ), the Lode parameter ( $\mu$ ) and the product triaxiality ( $\sigma_p^*$ ) are considered. The experimental program covers the following ranges for the stress state parameters:

$$\begin{aligned} -0.157 &\leq \sigma^* \leq 0.855, \\ -0.420 &\leq \mu \leq 1.000, \\ -0.012 &\leq \sigma_p^* \leq 0.438. \end{aligned}$$

The data shows that the triaxiality parameter alone is insufficient to describe the ductile fracture behavior of 2024-T351. Tests conducted with similar stress triaxiality, yet different Lode parameters and product triaxiality, have significantly different equivalent plastic fracture strains. Considering the current data set, the Lode parameter is more useful than the product triaxiality to increase the fidelity of fracture strain dependence. This is primarily due to the fact that many of the tests in the experimental program are in a state of plane stress, thus, the product triaxiality term is zero. A three dimensional surface plot of equivalent plastic fracture strain is presented in the stress triaxiality – Lode parameter stress space. A surface is generated using a biharmonic spline fit to the fracture locus data.

## Appendix A: Repeatability of the Experimental Data Recorded in the Plastic Deformation Test Series

The repeatability of the test data from each of the experiments discussed and presented in Chapter 4 is presented here. Tension, compression and torsion data are shown at the various strain rates, temperatures and specimen orientations considered. All tension and compression plots present true stress versus true strain curves. Shear stress versus shear strain is shown for the torsion data.

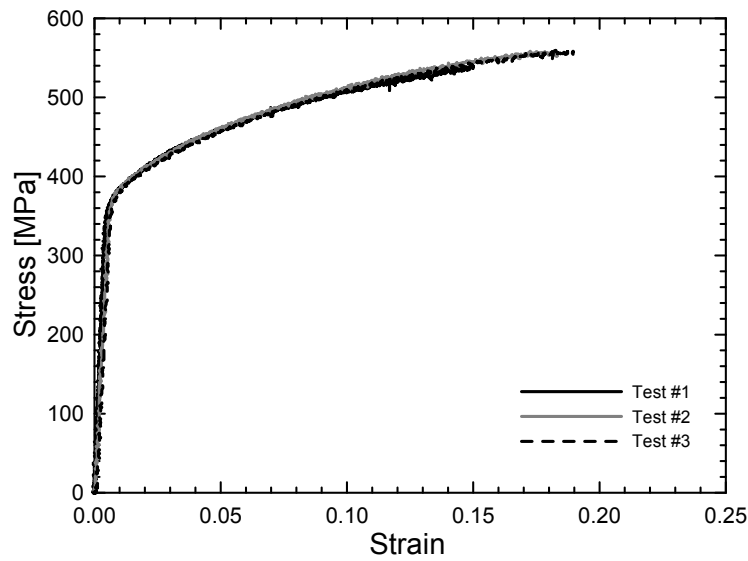


Figure 73. Tension test data repeatability:  $\dot{\epsilon} = 1 \times 10^{-4} \text{ s}^{-1}$ , room temperature, rolled direction.

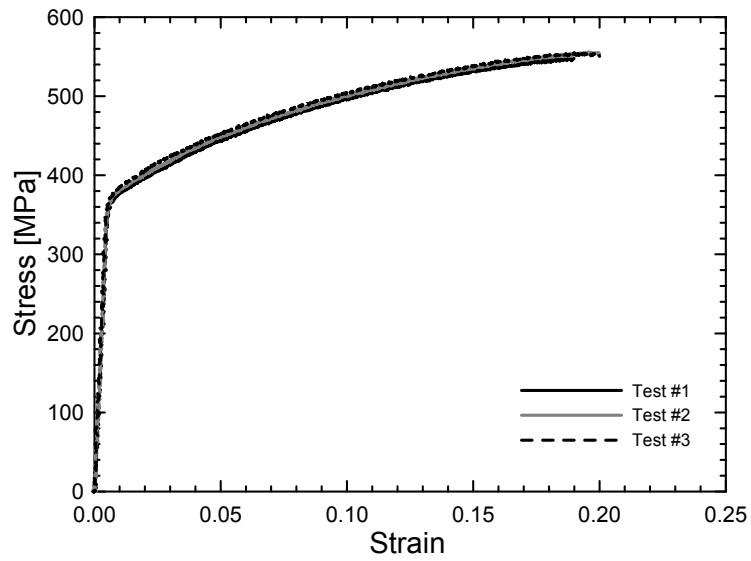


Figure 74. Tension test data repeatability:  $\dot{\epsilon}=1 \times 10^{-2} \text{ s}^{-1}$ , room temperature, rolled direction.

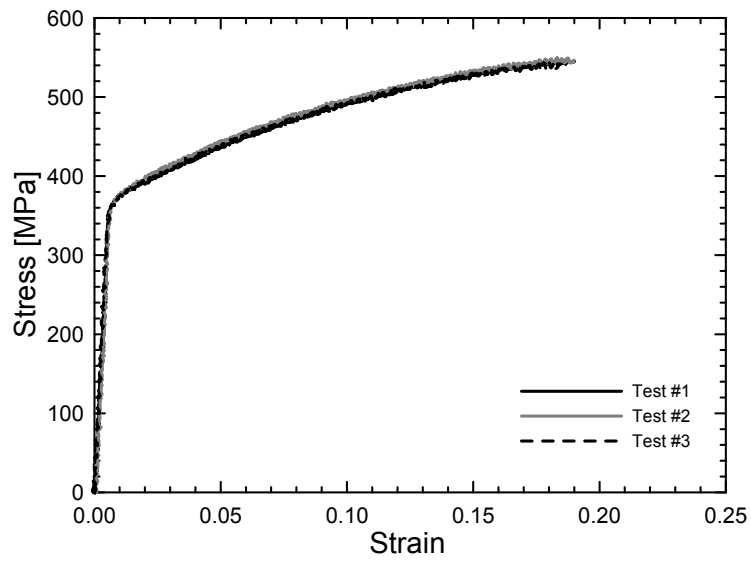


Figure 75. Tension test data repeatability:  $\dot{\epsilon}=1.0 \text{ s}^{-1}$ , room temperature, rolled direction.

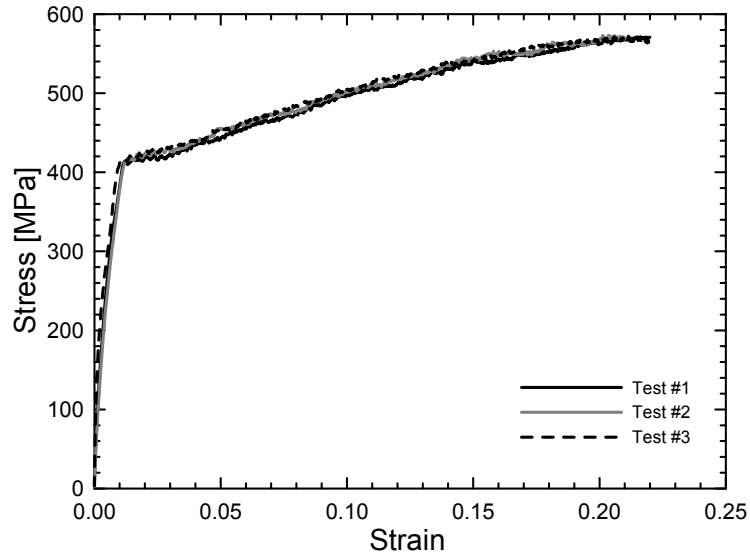


Figure 76. Tension test data repeatability:  $\dot{\epsilon} = 500.0 \text{ s}^{-1}$ , room temperature, rolled direction.

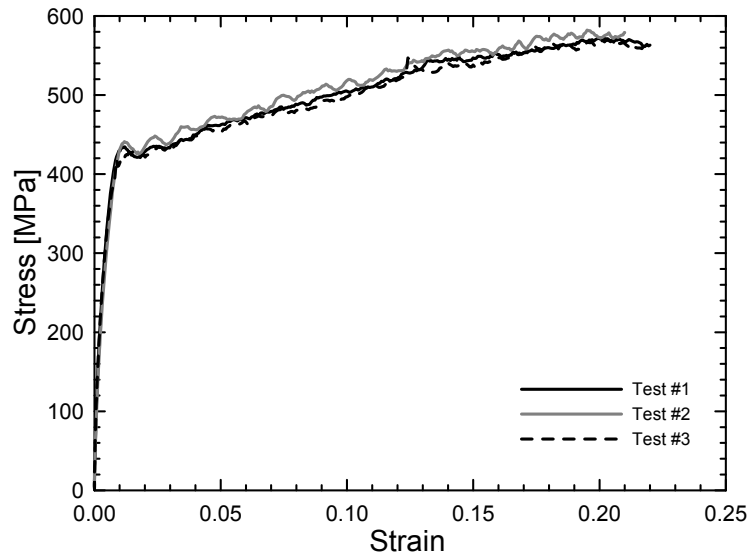


Figure 77. Tension test data repeatability:  $\dot{\epsilon} = 1850.0 \text{ s}^{-1}$ , room temperature, rolled direction.

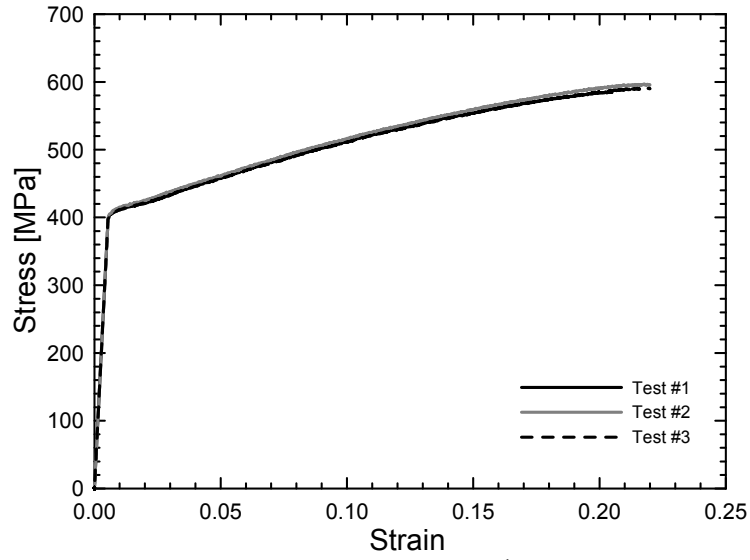


Figure 78. Tension test data repeatability:  $\dot{\epsilon} = 1.0 \text{ s}^{-1}$ ,  $T = -50 \text{ }^\circ\text{C}$ , rolled direction.

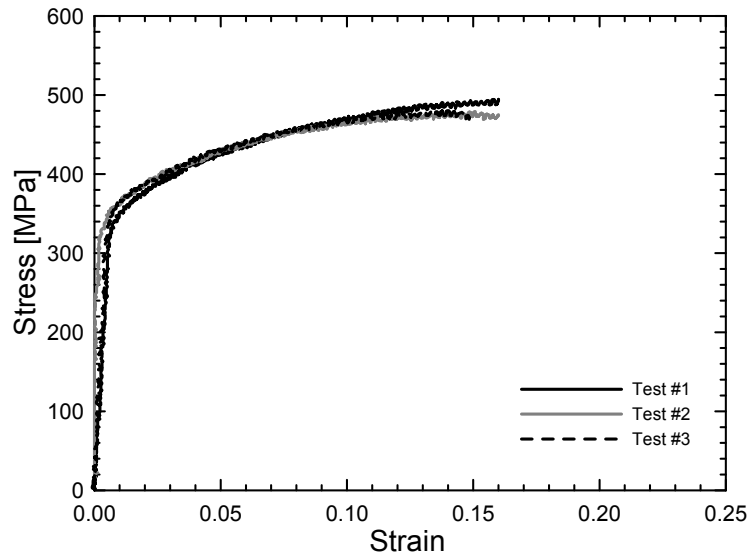


Figure 79. Tension test data repeatability:  $\dot{\epsilon} = 1.0 \text{ s}^{-1}$ ,  $T = 150 \text{ }^\circ\text{C}$ , rolled direction.

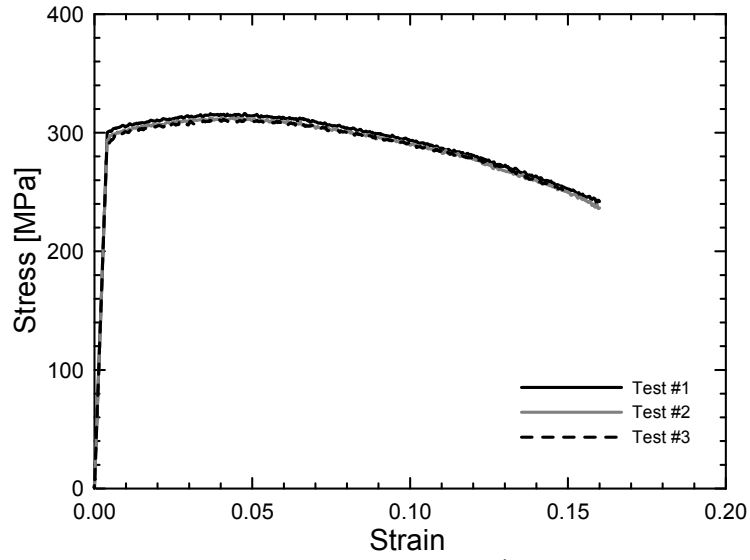


Figure 80. Tension test data repeatability:  $\dot{\epsilon} = 1.0 \text{ s}^{-1}$ ,  $T = 300 \text{ }^\circ\text{C}$ , rolled direction.

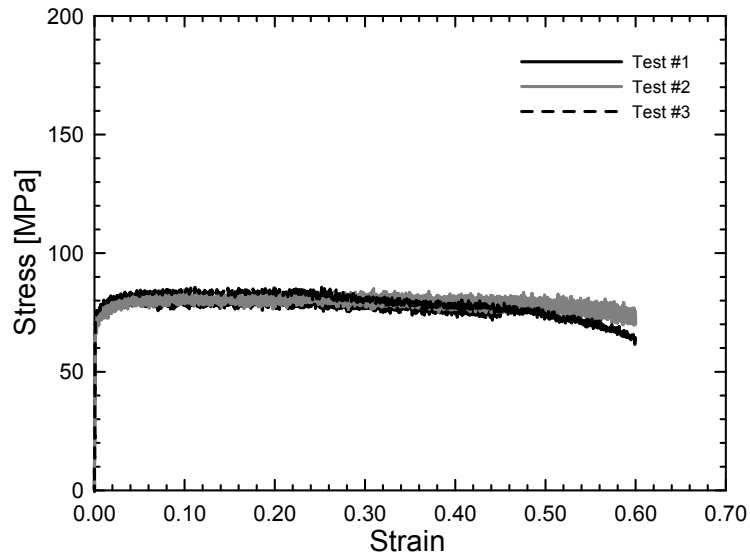


Figure 81. Tension test data repeatability:  $\dot{\epsilon} = 1.0 \text{ s}^{-1}$ ,  $T = 450 \text{ }^\circ\text{C}$ , rolled direction.

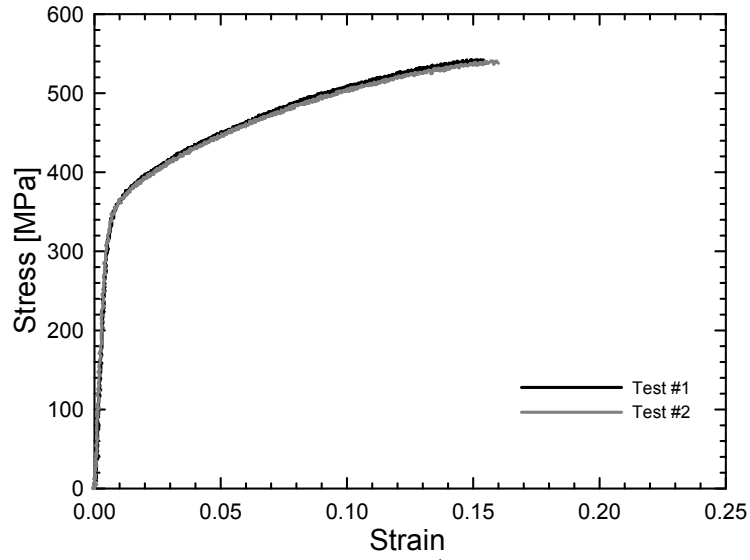


Figure 82. Tension test data repeatability:  $\dot{\epsilon} = 1.0 \text{ s}^{-1}$ , room temperature, transverse direction.

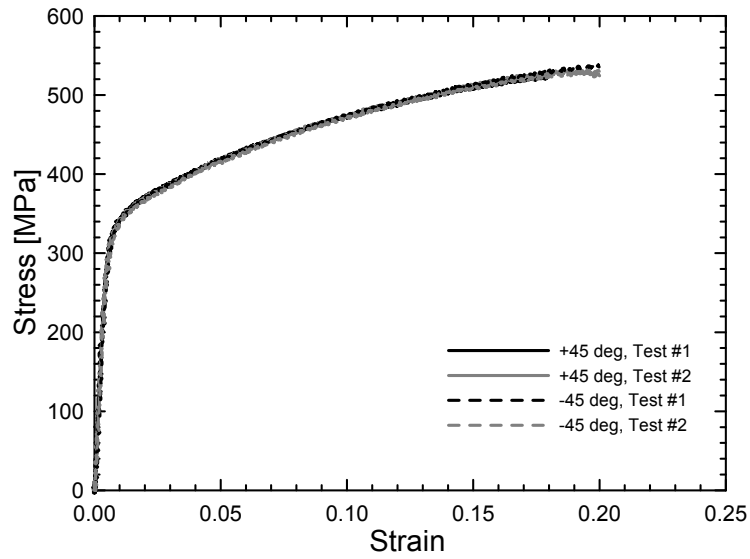


Figure 83. Tension test data repeatability:  $\dot{\epsilon} = 1.0 \text{ s}^{-1}$ , room temperature, +/- 45° directions.

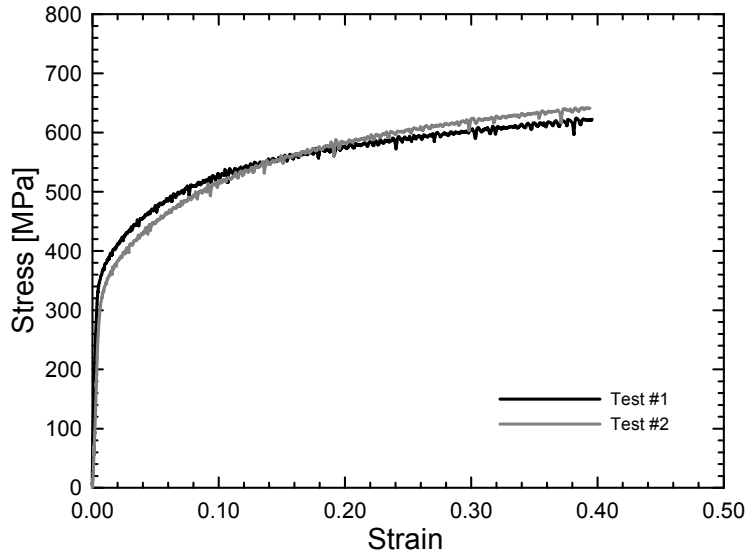


Figure 84. Compression test data repeatability:  $\dot{\epsilon} = 1 \times 10^{-4} \text{ s}^{-1}$ , room temperature, rolled direction.

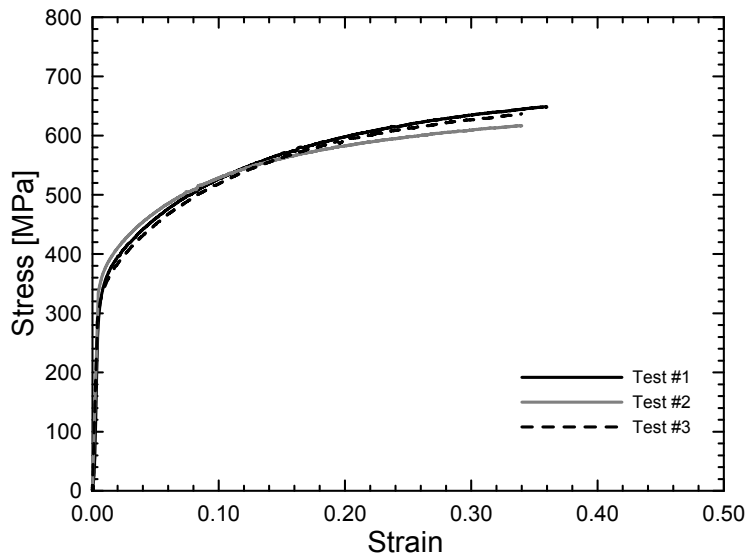


Figure 85. Compression test data repeatability:  $\dot{\epsilon} = 1 \times 10^{-2} \text{ s}^{-1}$ , room temperature, rolled direction.

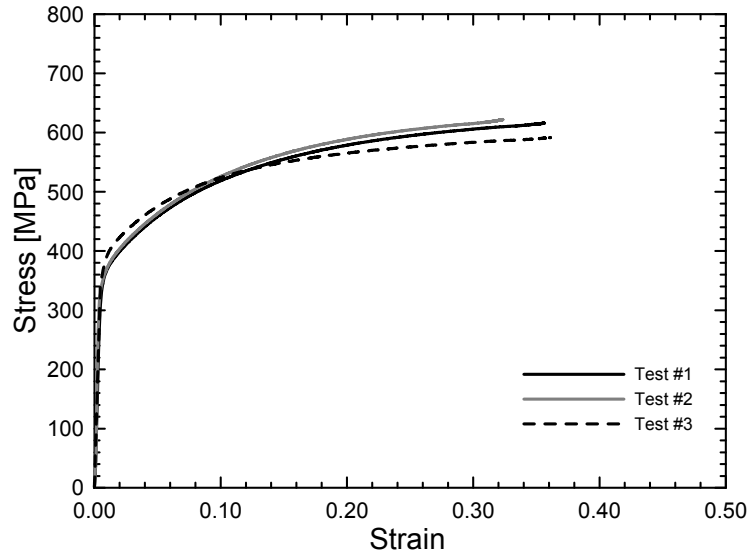


Figure 86. Compression test data repeatability:  $\dot{\epsilon} = 1.0 \text{ s}^{-1}$ , room temperature, rolled direction.

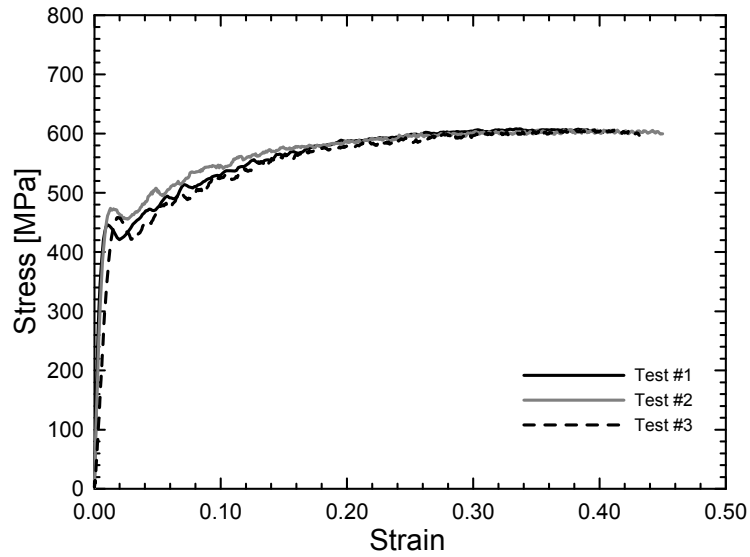


Figure 87. Compression test data repeatability:  $\dot{\epsilon} = 1400.0 \text{ s}^{-1}$ , room temperature, rolled direction.

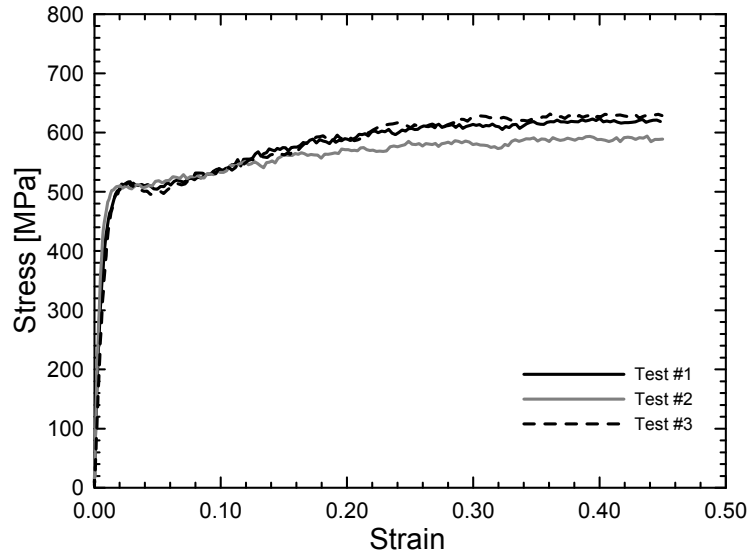


Figure 88. Compression test data repeatability:  $\dot{\epsilon} = 4600.0 \text{ s}^{-1}$ , room temperature, rolled direction.

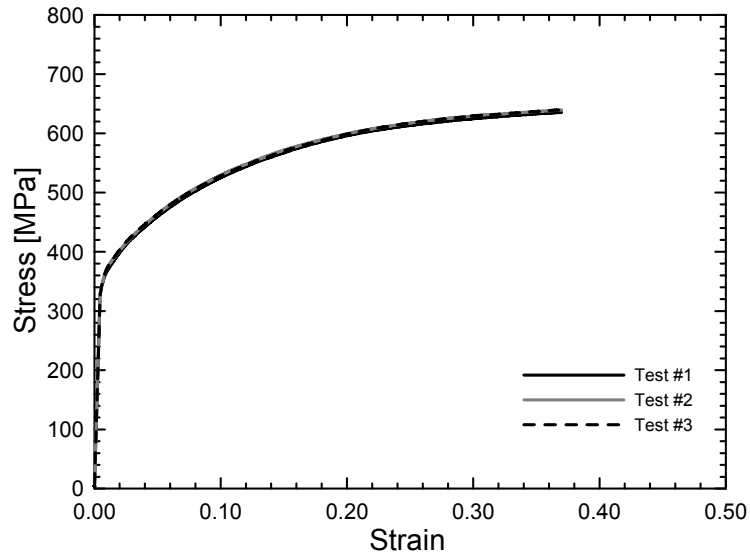


Figure 89. Compression test data repeatability:  $\dot{\epsilon} = 1.0 \text{ s}^{-1}$ ,  $T = -50 \text{ }^\circ\text{C}$ , rolled direction.

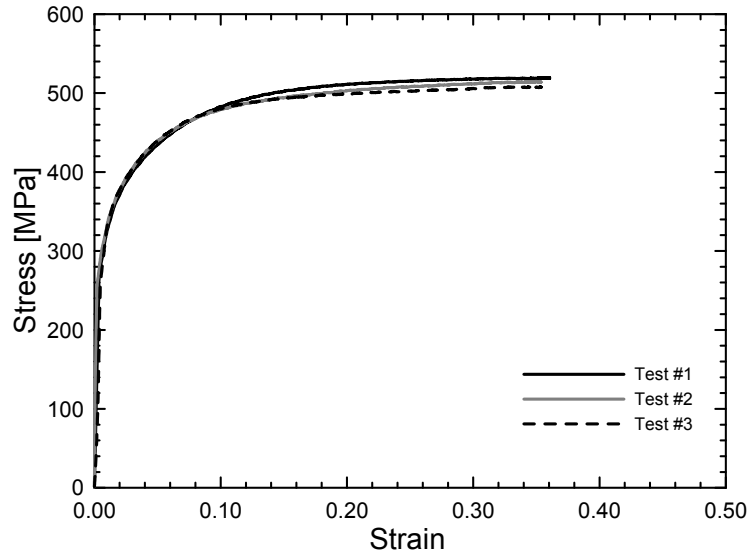


Figure 90. Compression test data repeatability:  $\dot{\epsilon} = 1.0 \text{ s}^{-1}$ ,  $T = 150 \text{ }^{\circ}\text{C}$ , rolled direction.

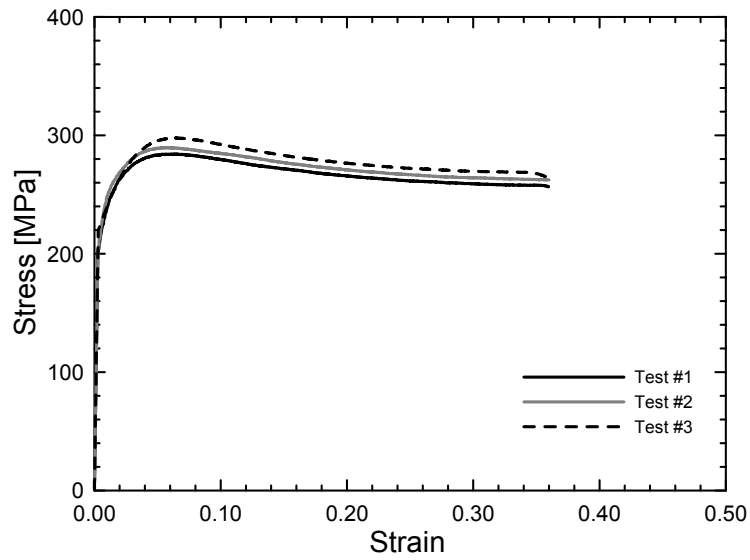


Figure 91. Compression test data repeatability:  $\dot{\epsilon} = 1.0 \text{ s}^{-1}$ ,  $T = 300 \text{ }^{\circ}\text{C}$ , rolled direction.

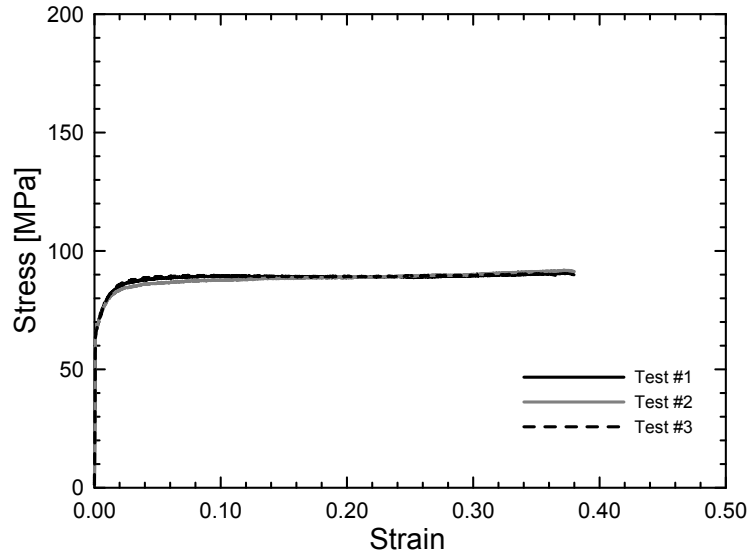


Figure 92. Compression test data repeatability:  $\dot{\epsilon} = 1.0 \text{ s}^{-1}$ ,  $T = 450 \text{ }^\circ\text{C}$ , rolled direction.

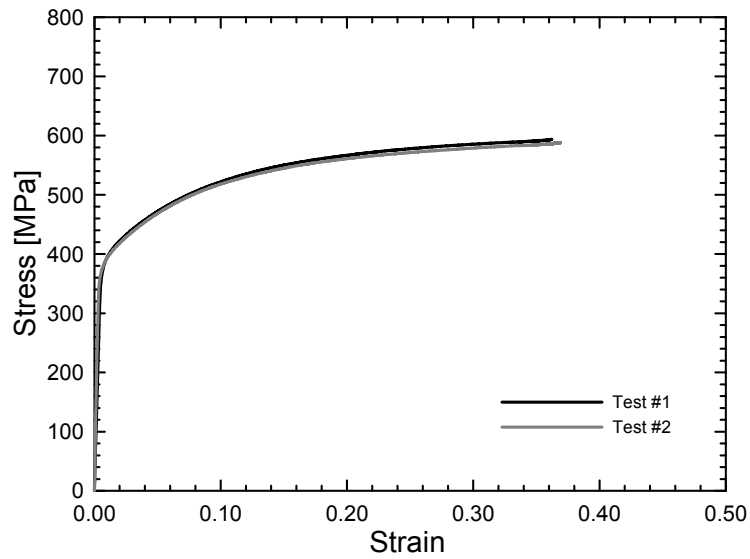


Figure 93. Compression test data repeatability:  $\dot{\epsilon} = 1.0 \text{ s}^{-1}$ , room temperature, transverse direction.

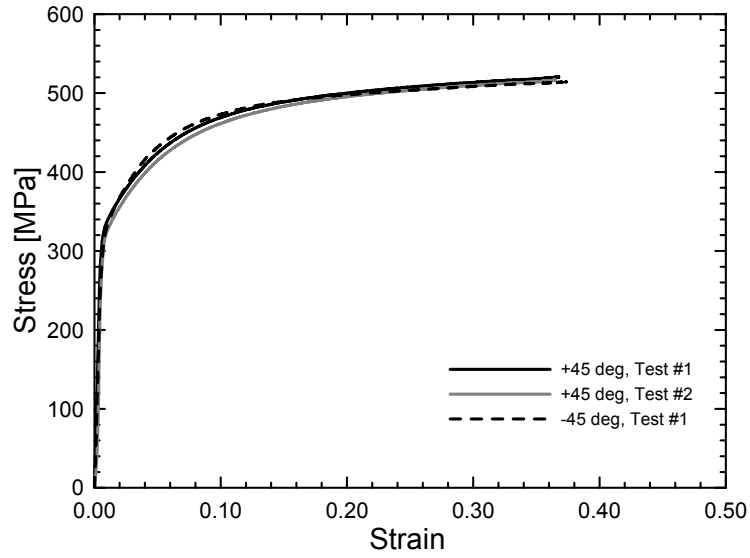


Figure 94. Compression test data repeatability:  $\dot{\epsilon} = 1.0 \text{ s}^{-1}$ , room temperature, +/- 45° direction.

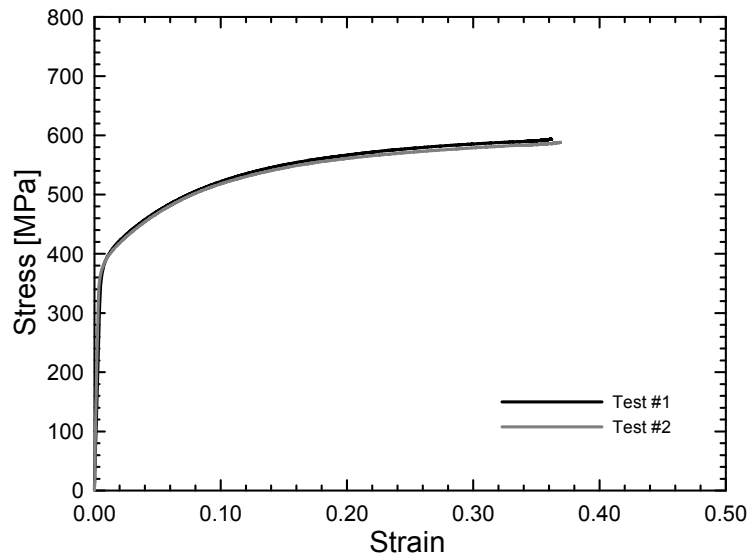


Figure 95. Compression test data repeatability:  $\dot{\epsilon} = 1.0 \text{ s}^{-1}$ , room temperature, thickness direction.

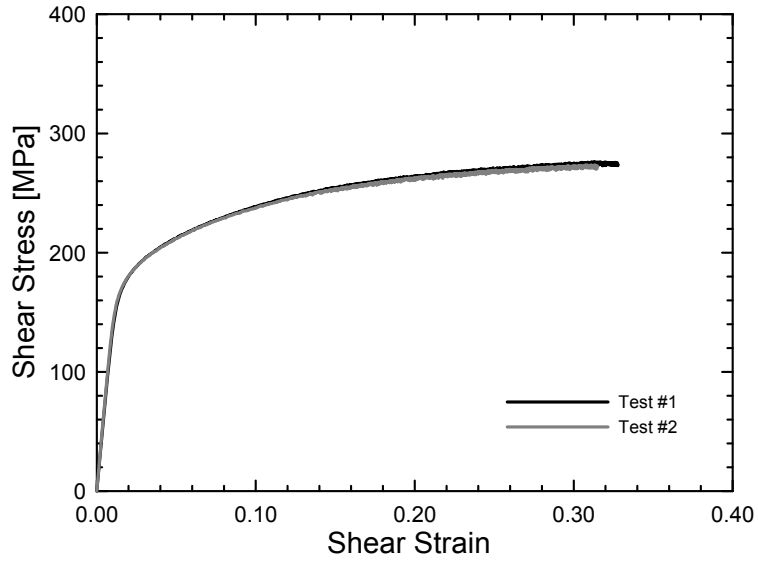


Figure 96. Torsion test data repeatability:  $\dot{\gamma} = 1.732 \times 10^{-4} \text{ s}^{-1}$ , room temperature.

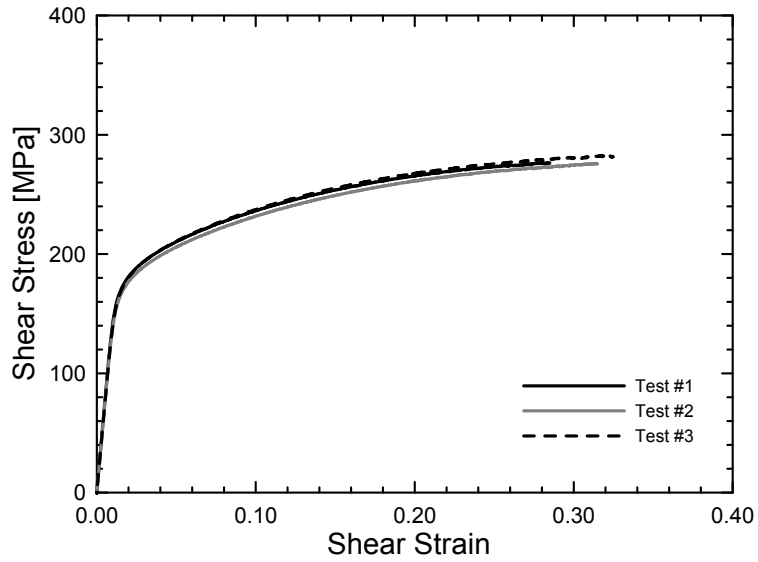


Figure 97. Torsion test data repeatability:  $\dot{\gamma} = 1.732 \times 10^{-2} \text{ s}^{-1}$ , room temperature.

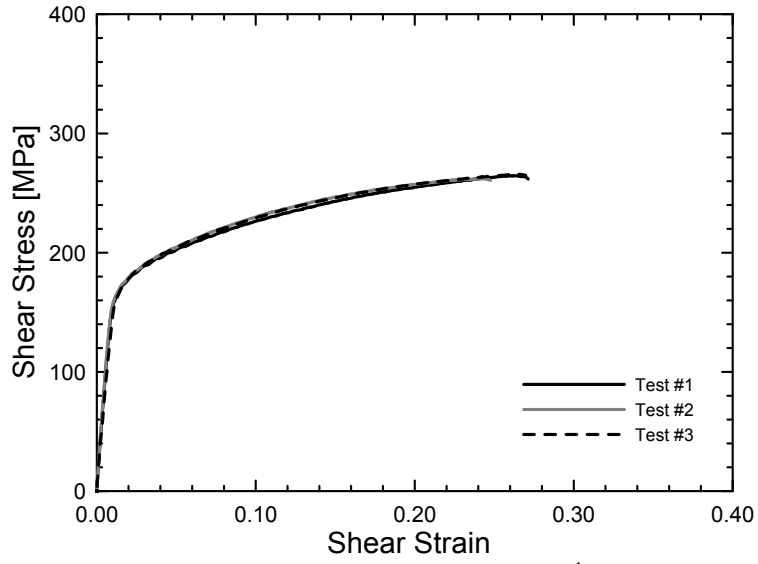


Figure 98. Torsion test data repeatability:  $\dot{\gamma}=1.732 \text{ s}^{-1}$ , room temperature.

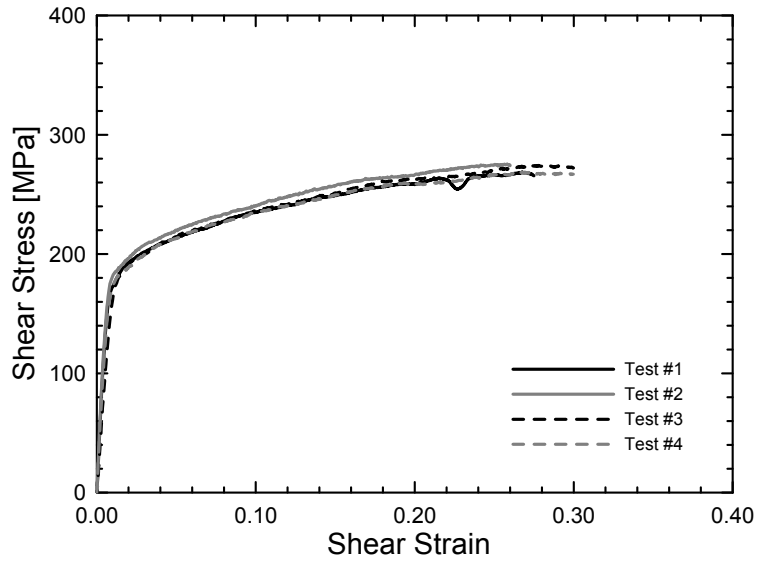


Figure 99. Torsion test data repeatability:  $\dot{\gamma}=925.0 \text{ s}^{-1}$ , room temperature.

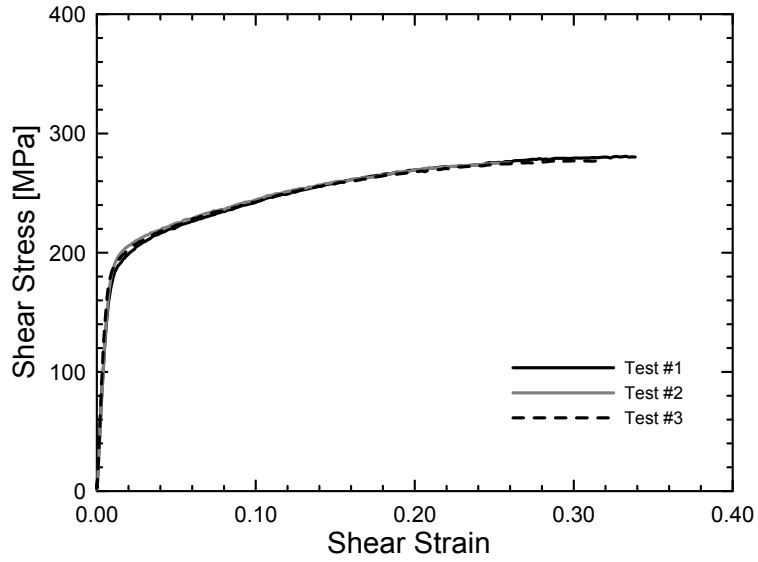


Figure 100. Torsion test data repeatability:  $\dot{\gamma}=5050.0 \text{ s}^{-1}$ , room temperature.

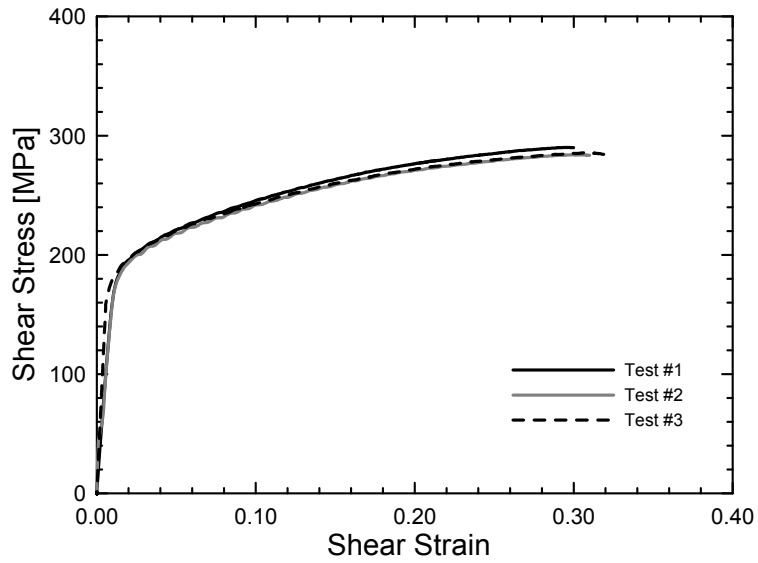


Figure 101. Torsion test data repeatability:  $\dot{\gamma}=1.732 \text{ s}^{-1}$ ,  $T = -50 \text{ }^{\circ}\text{C}$ .

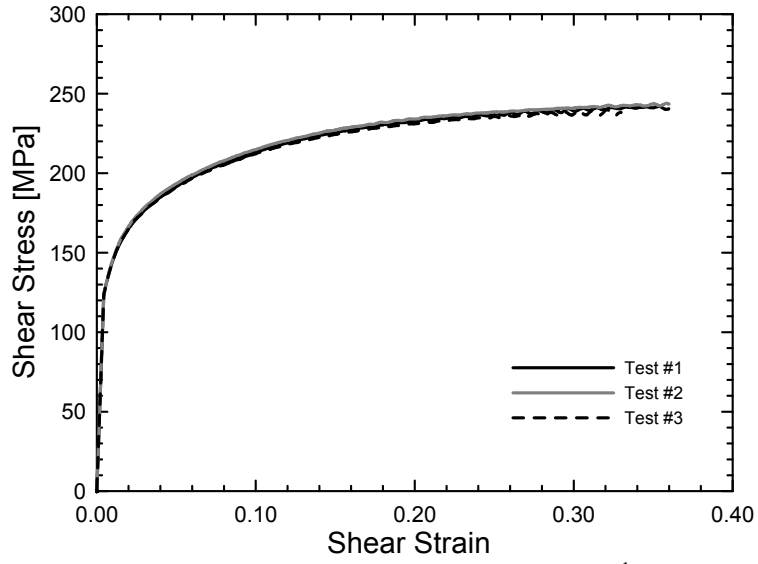


Figure 102. Torsion test data repeatability:  $\dot{\gamma}=1.732 \text{ s}^{-1}$ ,  $T=150 \text{ }^{\circ}\text{C}$ .

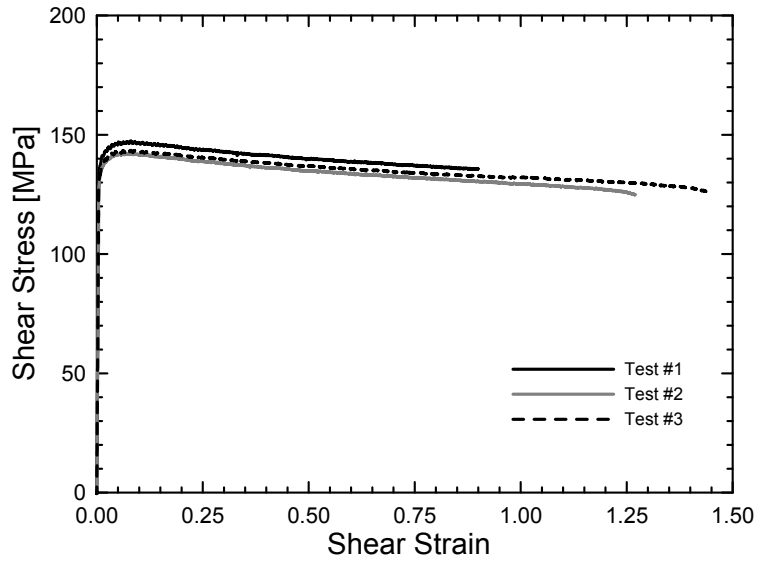


Figure 103. Torsion test data repeatability:  $\dot{\gamma}=1.732 \text{ s}^{-1}$ ,  $T=300 \text{ }^{\circ}\text{C}$ .

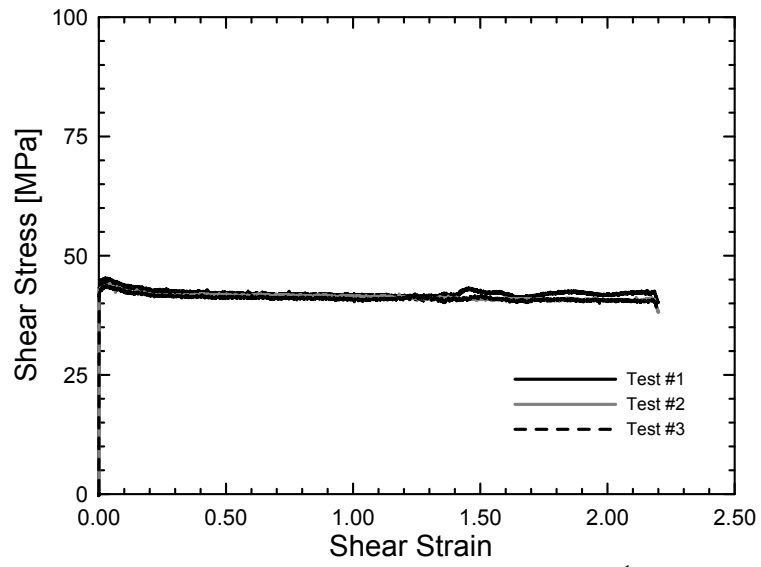


Figure 104. Torsion test data repeatability:  $\dot{\gamma}=1.732 \text{ s}^{-1}$ ,  $T=450 \text{ }^{\circ}\text{C}$ .

## Appendix B: Finite Element Meshes Used for the Tension Ductile Fracture Test Series

Finite element meshes used for the tension ductile fracture test series are shown in this appendix. Results from simulations of these experiments are used with the experimental data to construct fracture locus data points for 2024-T351 aluminum. The mesh used for the plane stress specimen with a smooth gage section is shown in Figure 48 (a).

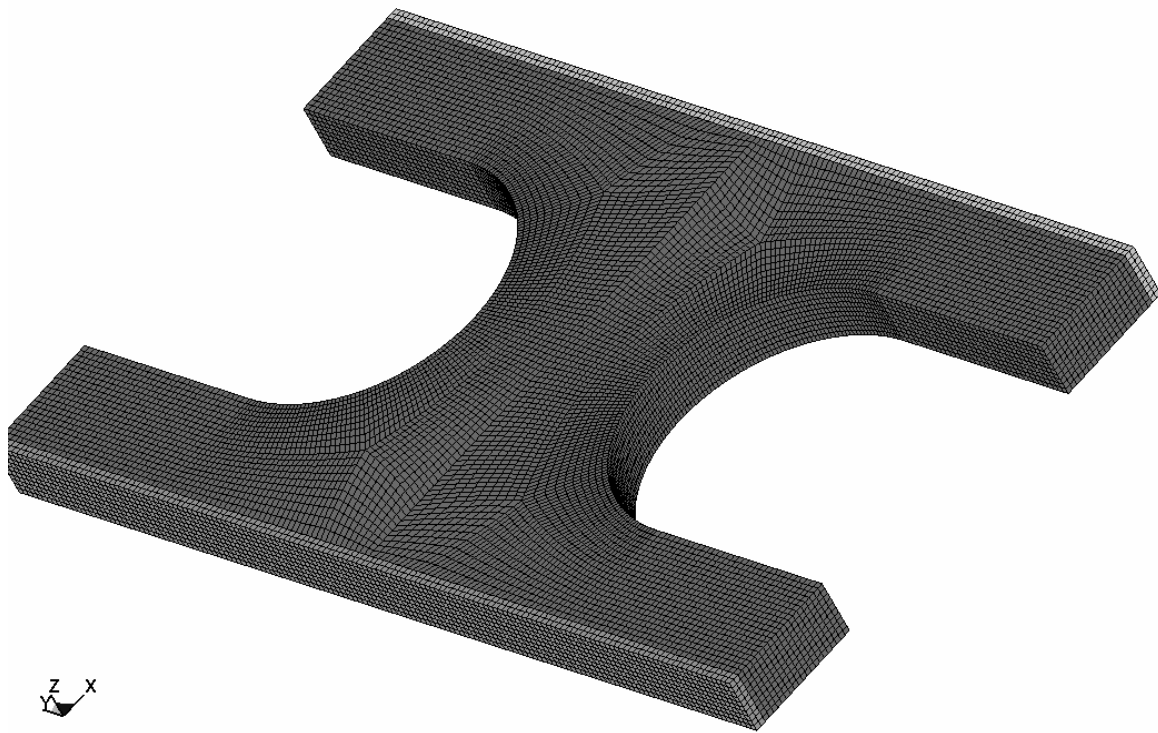


Figure 105. Mesh for plane stress tension specimen with a 1.984 mm radius notch.



Figure 106. Mesh for plane stress tension specimen with a 0.396 mm radius notch.

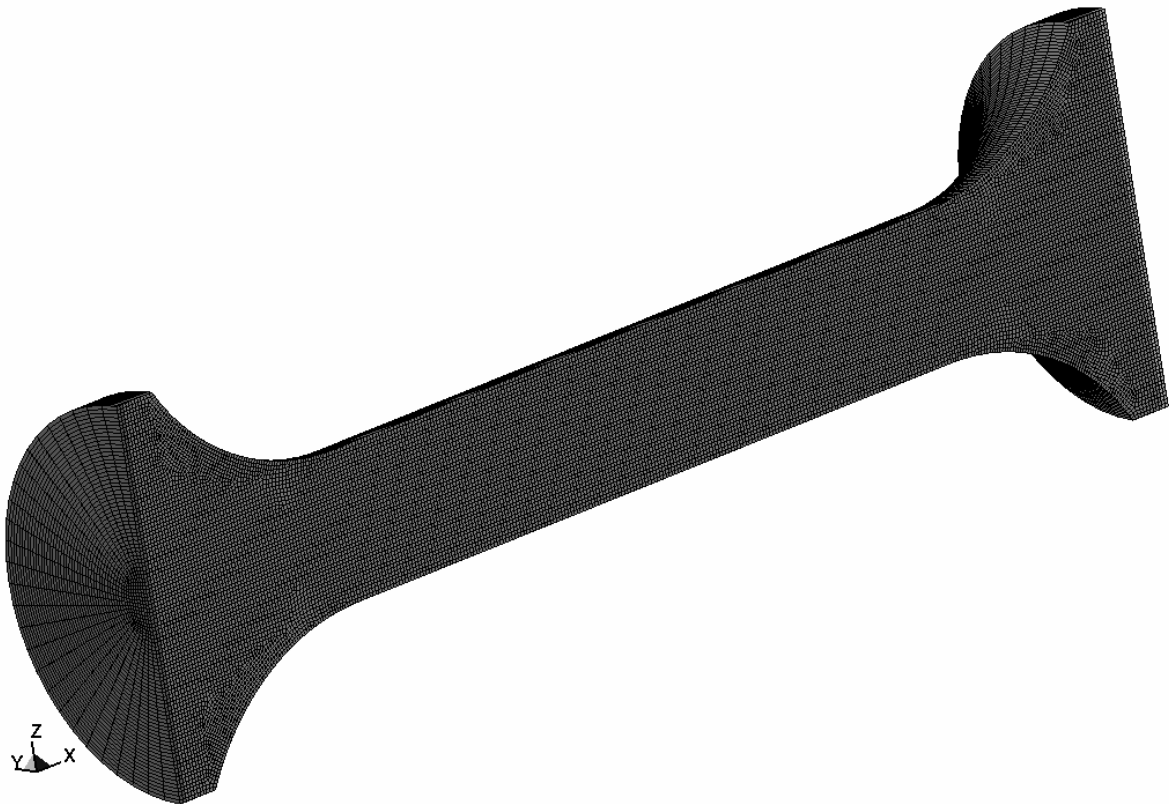


Figure 107. Mesh for axisymmetric, smooth tension specimen (section view).

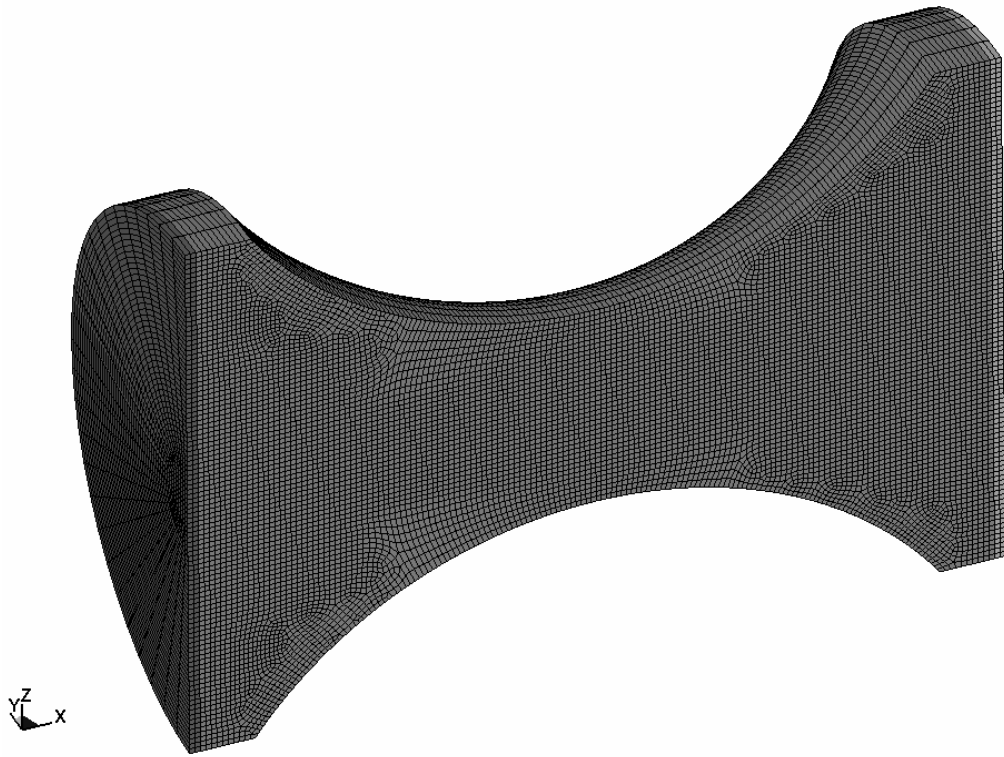


Figure 108. Mesh for axisymmetric tension specimen with a 9.144 mm radius notch (section view).

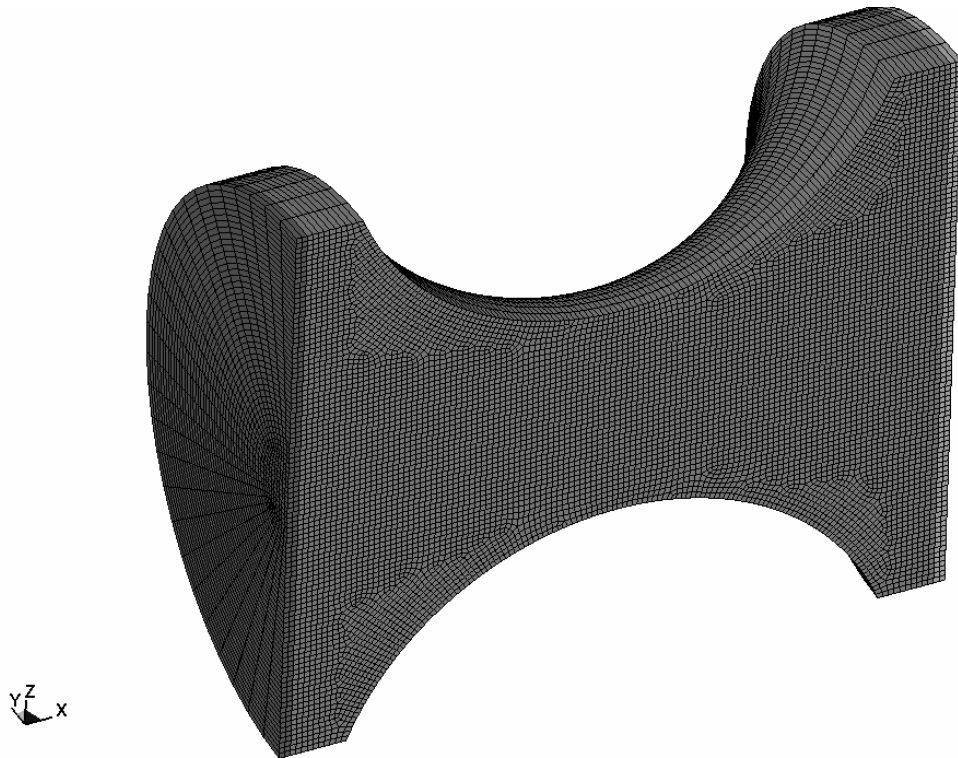


Figure 109. Mesh for axisymmetric tension specimen with a 6.096 mm radius notch (section view).

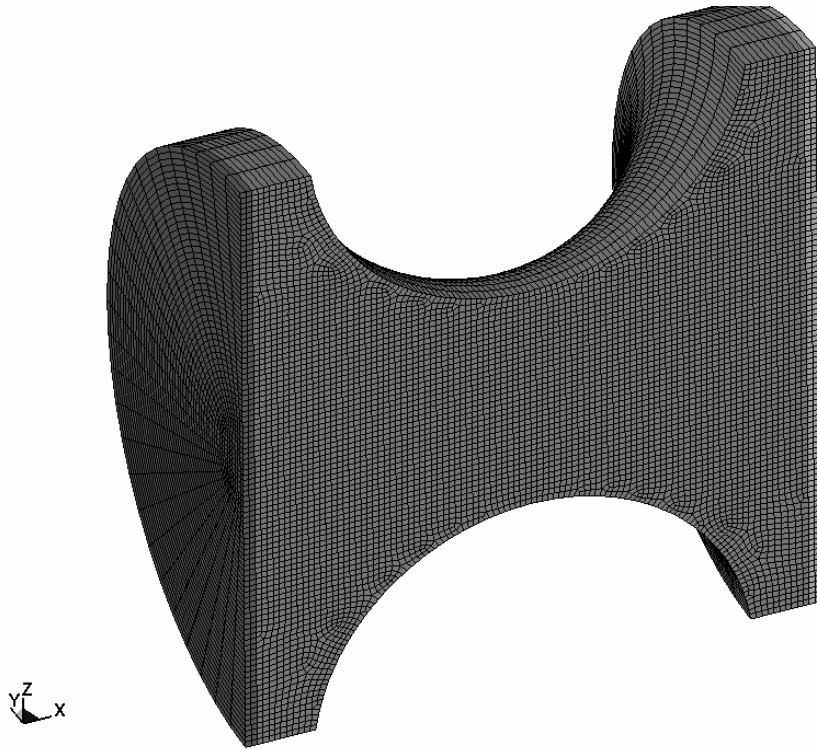


Figure 110. Mesh for axisymmetric tension specimen with a 4.470 mm radius notch (section view).

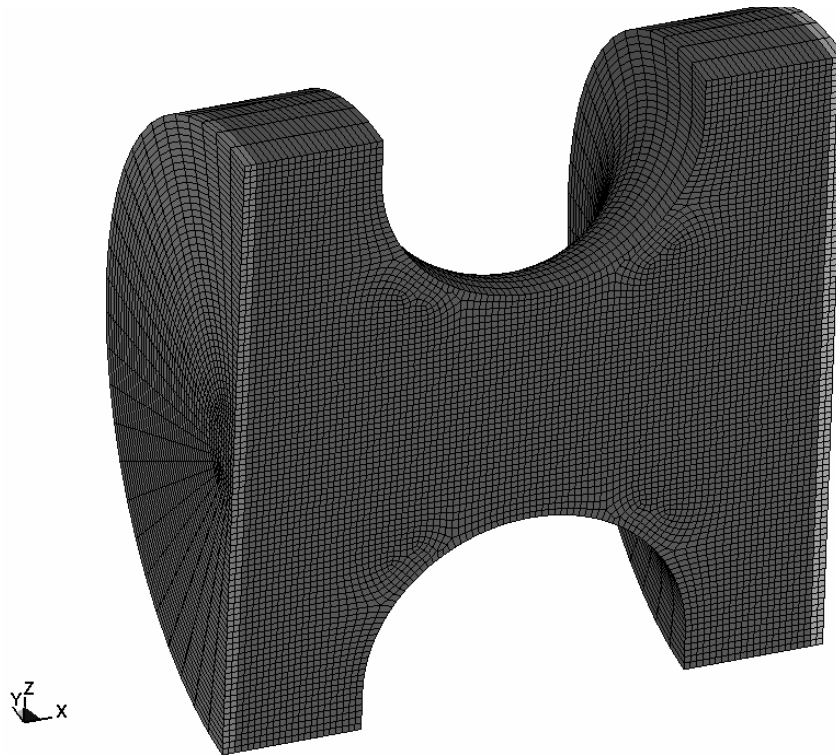


Figure 111. Mesh for axisymmetric tension specimen with a 3.048 mm radius notch (section view).

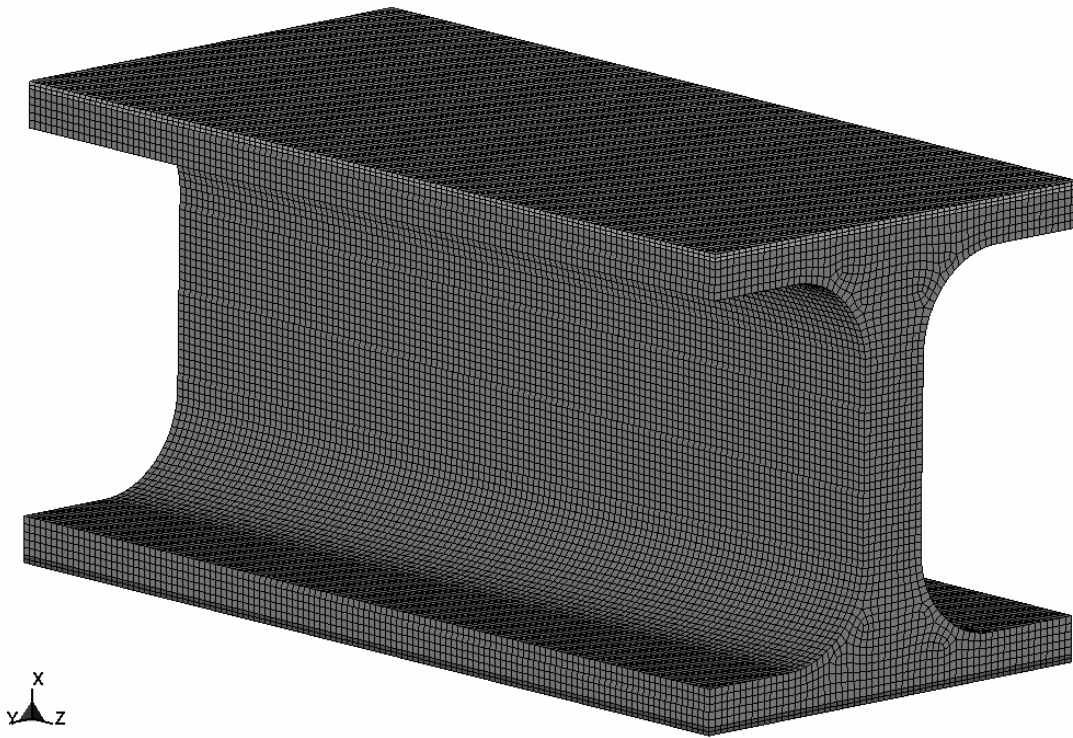


Figure 112. Mesh for plane strain tension specimen with a smooth gage section.

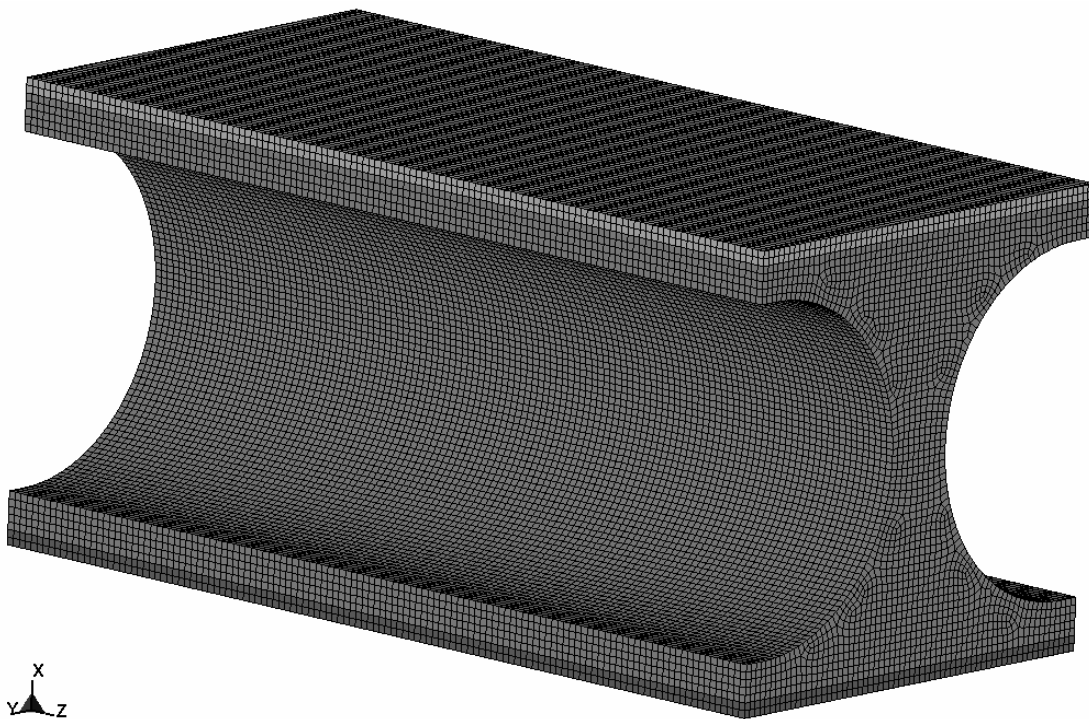


Figure 113. Mesh for plane strain tension specimen with a 4.763 mm radius notch.

## Appendix C: Comparison of Simulated and Experimental Data from Tension Ductile Fracture Tests

Additional data from the tension ductile fracture test series are presented in this appendix. For each experiment outlined in Tables 3, 4 and 5, the maximum and minimum principal surface strain contours measured with 3D DIC are compared to those from the numerical simulations. The experimental surface strains represent the image taken just prior to specimen fracture.

Force, strain and stress state data are also plotted versus displacement for each experiment. Experimental force and surface strain data are compared to simulation results. Equivalent plastic strain and triaxiality, Lode parameter and product triaxiality data presented in the plots are taken from an internal element in the simulation in the region of specimen fracture. These data are used to construct fracture locus data points using the methods described in Chapter 7.

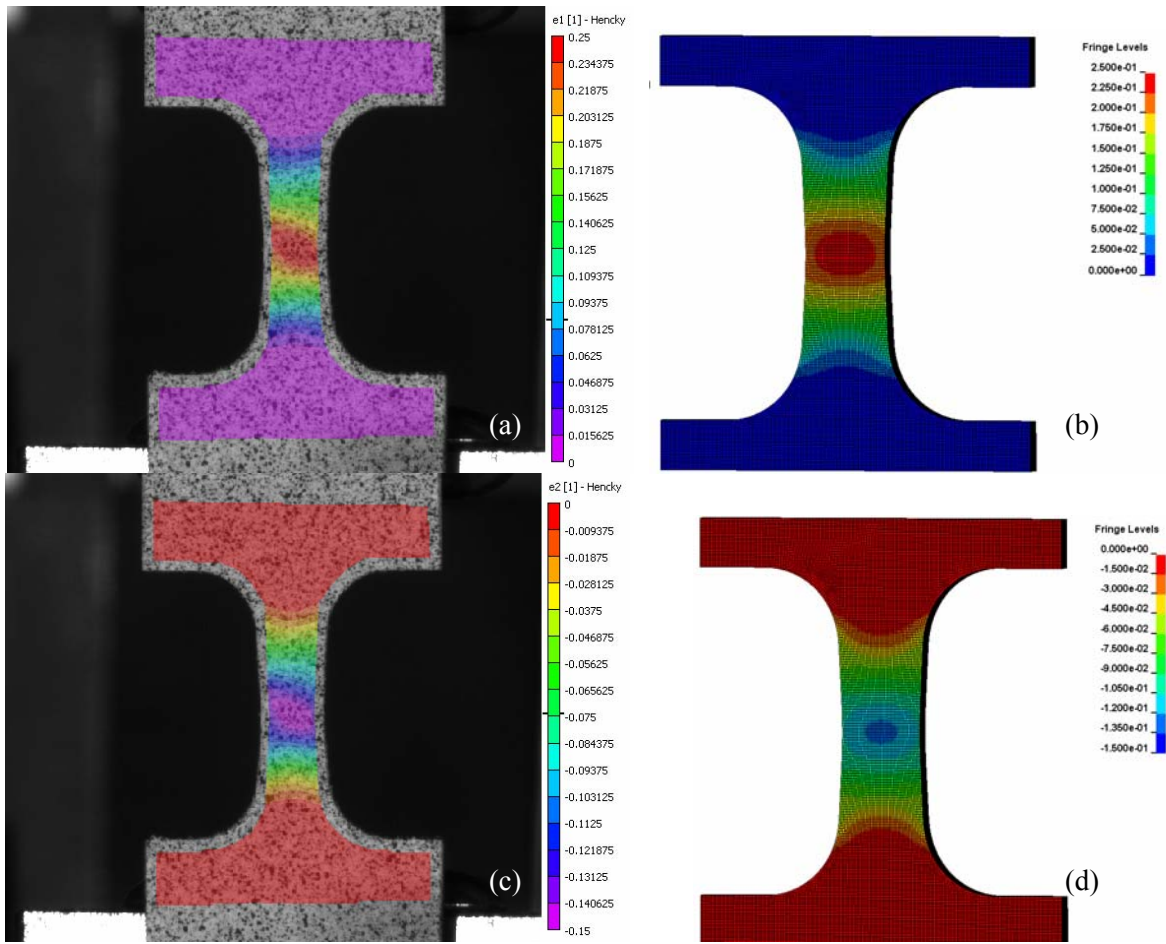


Figure 114. Comparison of specimen surface strains, plane stress specimen with smooth gage section: (a) DIC max. principal strain, (b) simulation max. principal strain, (c) DIC min. principal strain, (d) simulation min. principal strain.

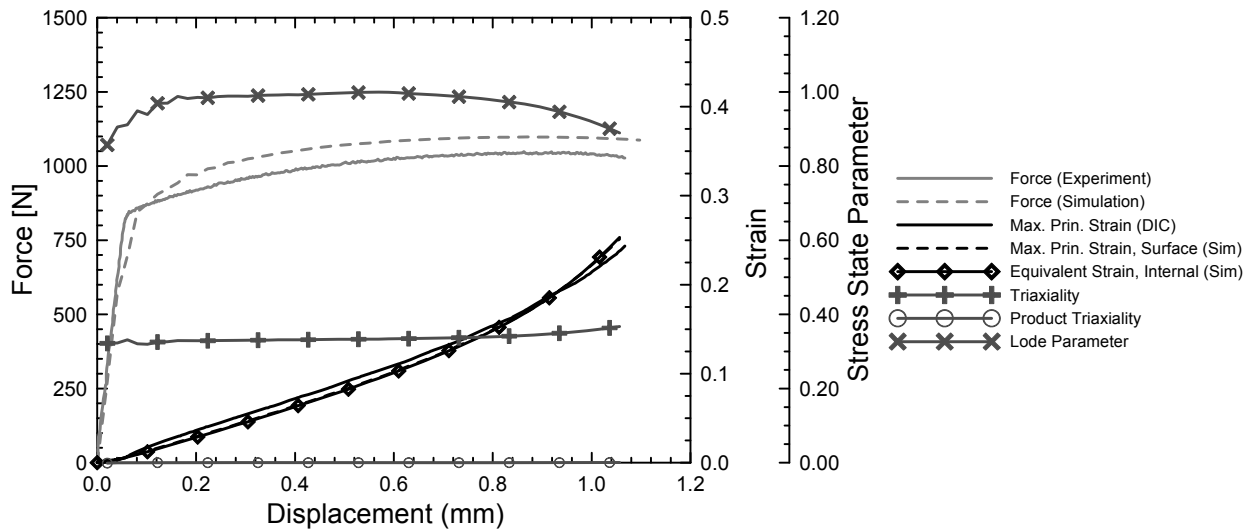


Figure 115. Experimental and simulated data for a plane stress specimen with a smooth gage section.

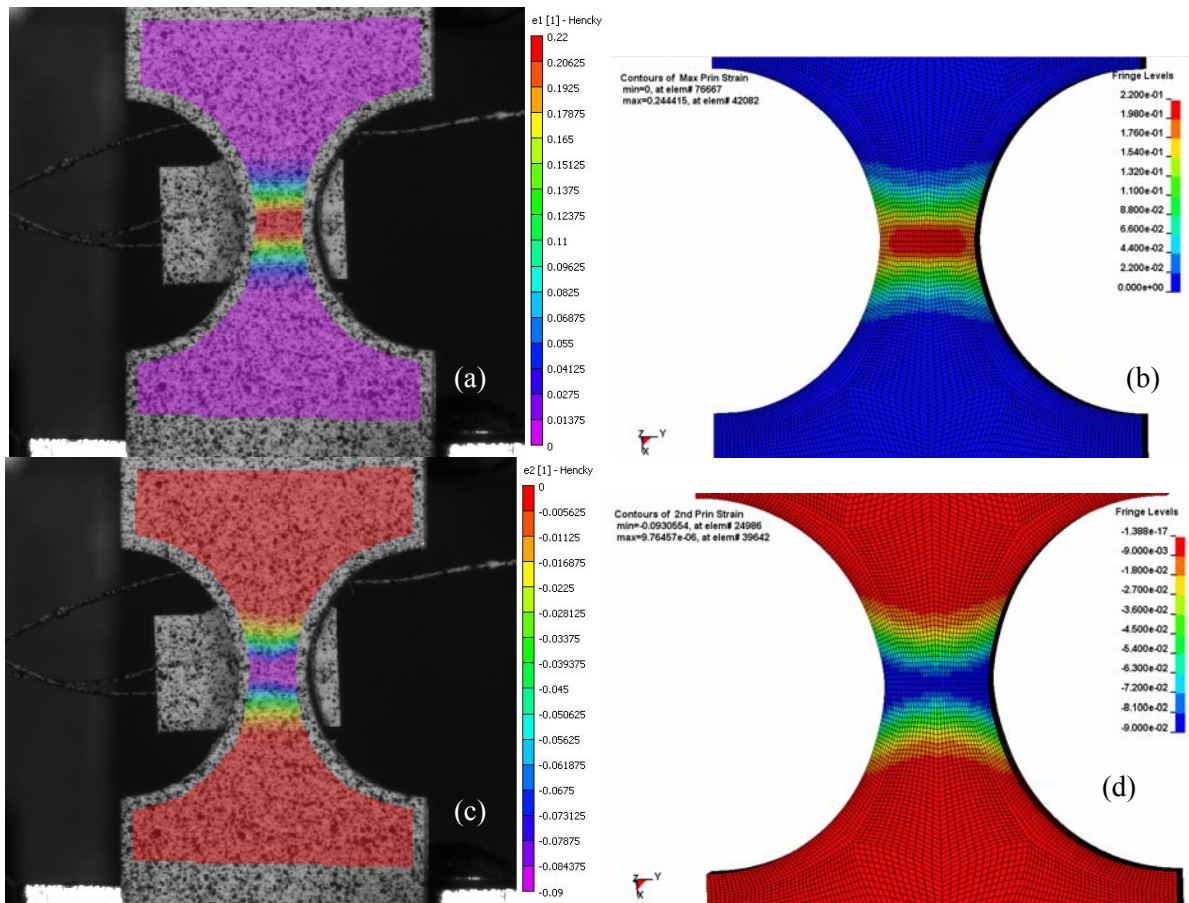


Figure 116. Comparison of specimen surface strains, plane stress specimen with 4.763 mm radius notch: (a) DIC max. principal strain, (b) simulation max. principal strain, (c) DIC min. principal strain, (d) simulation min. principal strain.

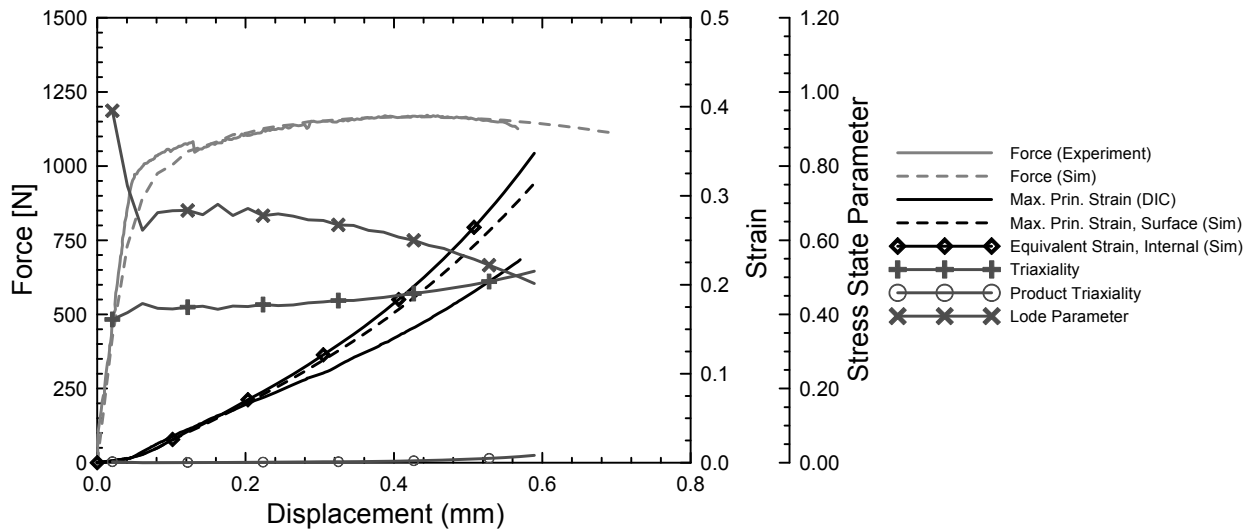


Figure 117. Experimental and simulated data for a plane stress specimen with a 4.763 mm radius notch.

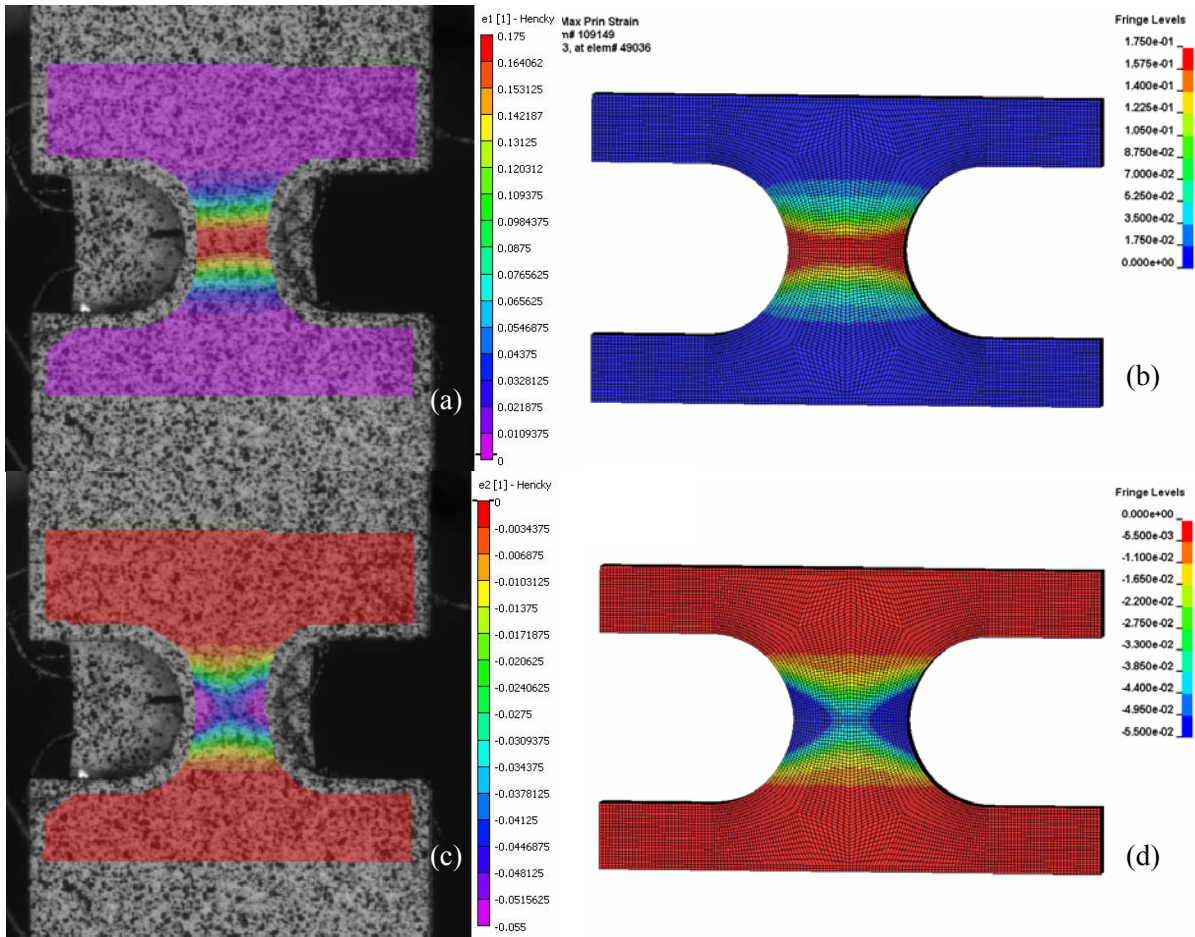


Figure 118. Comparison of specimen surface strains, plane stress specimen with 1.984 mm radius notch: (a) DIC max. principal strain, (b) simulation max. principal strain, (c) DIC min. principal strain, (d) simulation min. principal strain.

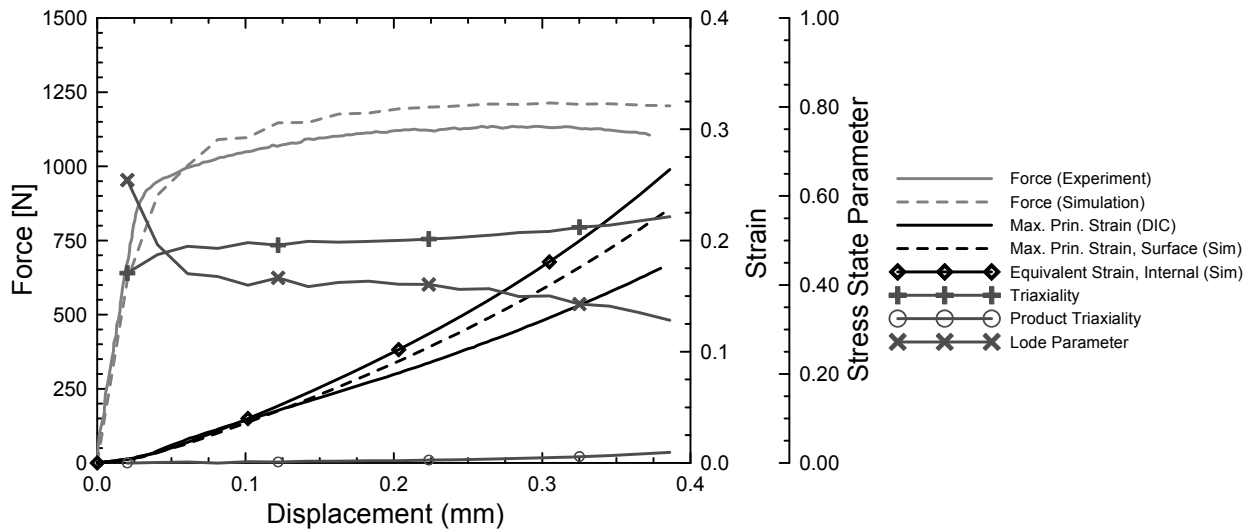


Figure 119. Experimental and simulated data for a plane stress specimen with a 1.984 mm radius notch.

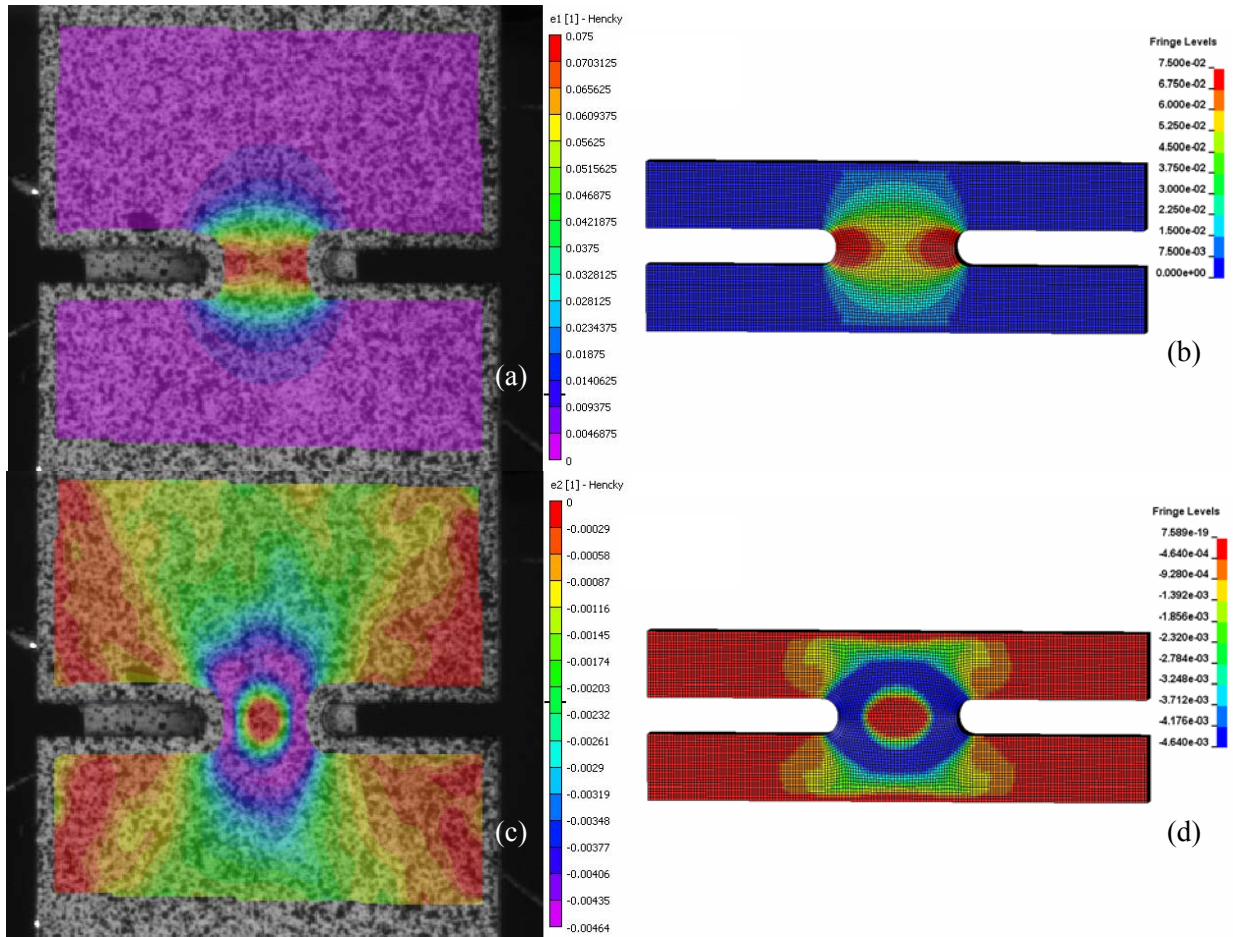


Figure 120. Comparison of specimen surface strains, plane stress specimen with 0.396 mm radius notch: (a) DIC max. principal strain, (b) simulation max. principal strain, (c) DIC min. principal strain, (d) simulation min. principal strain.

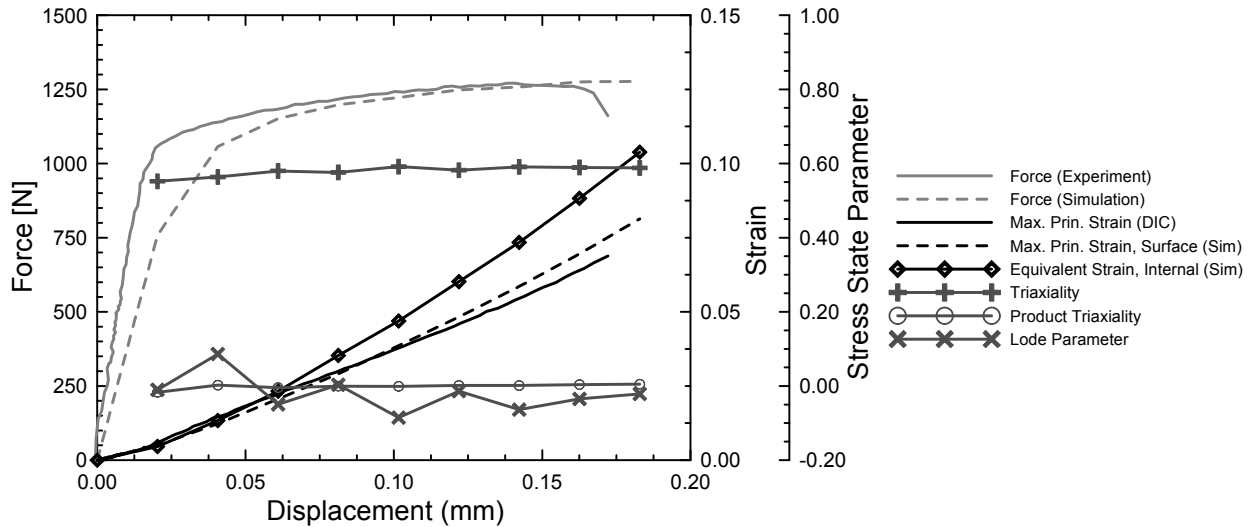


Figure 121. Experimental and simulated data for a plane stress specimen with a 0.396 mm radius notch.

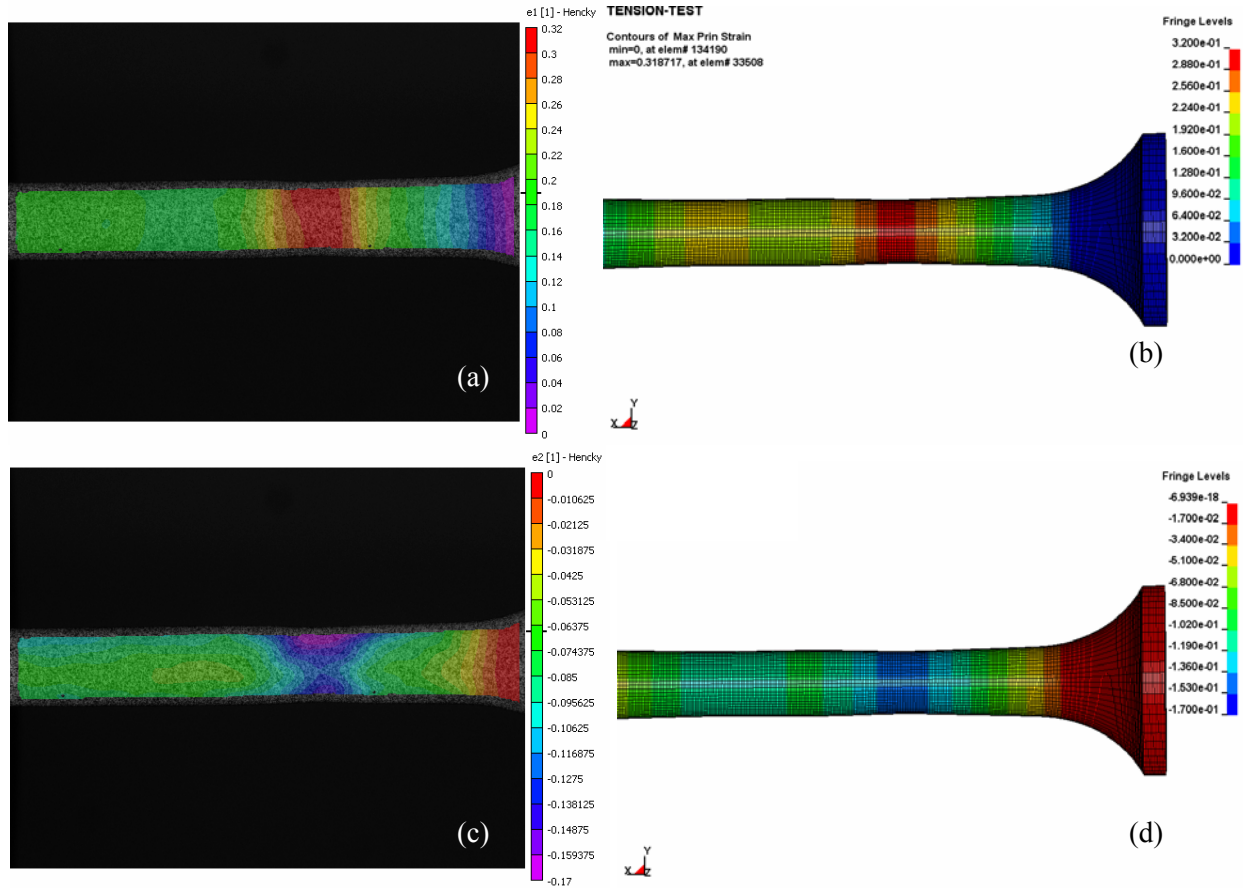


Figure 122. Comparison of specimen surface strains, axisymmetric specimen with a smooth gage section: (a) DIC max. principal strain, (b) simulation max. principal strain, (c) DIC min. principal strain, (d) simulation min. principal strain.

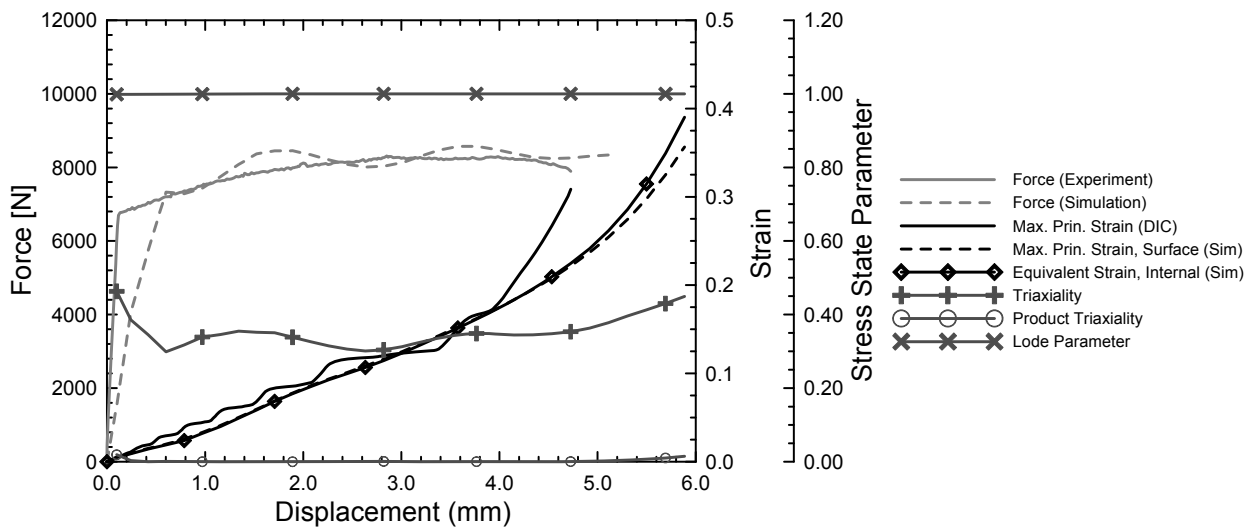


Figure 123. Experimental and simulated data for an axisymmetric specimen with a smooth gage section.

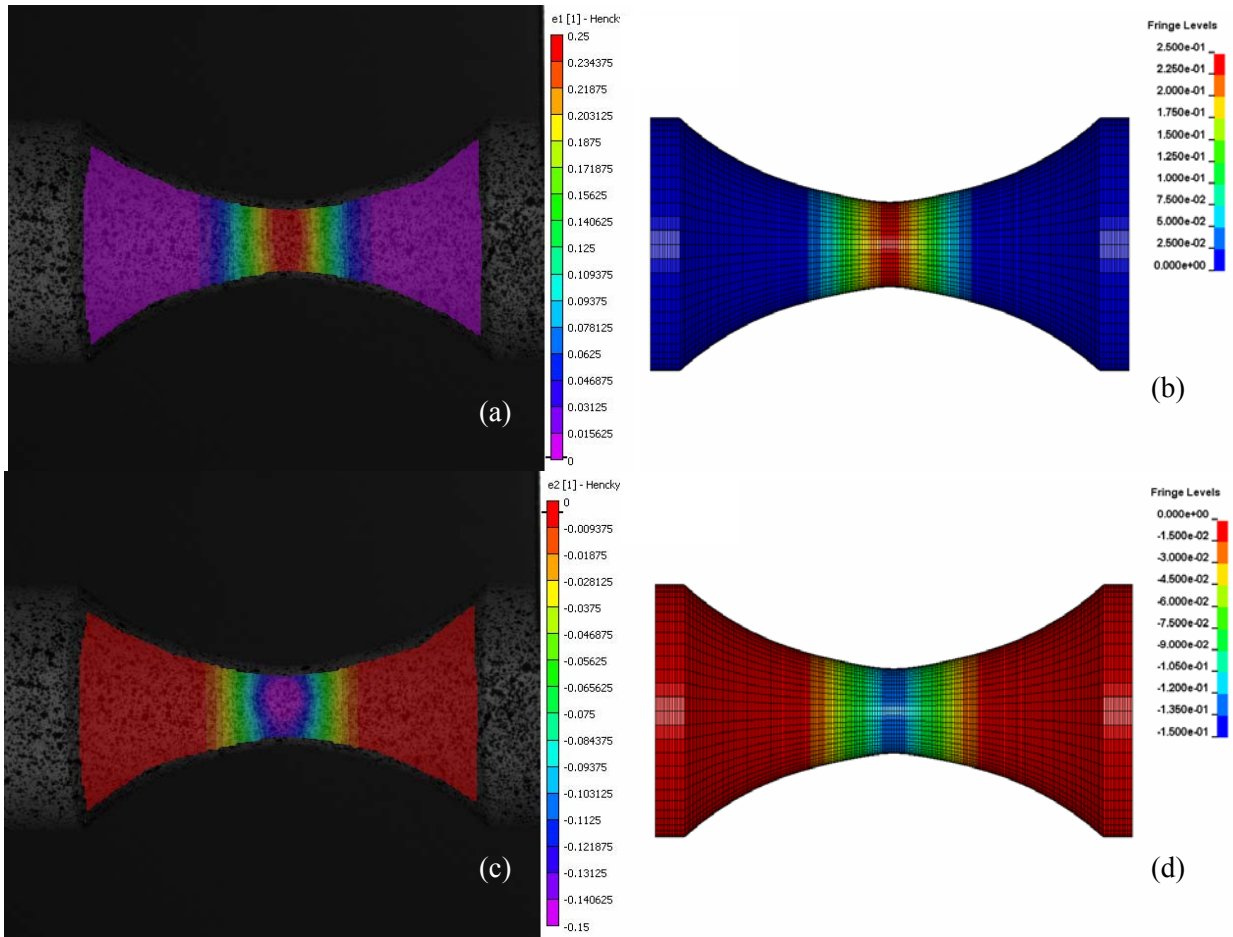


Figure 124. Comparison of specimen surface strains, axisymmetric specimen with a 14.503 mm radius notch: (a) DIC max. principal strain, (b) simulation max. principal strain, (c) DIC min. principal strain, (d) simulation min. principal strain.

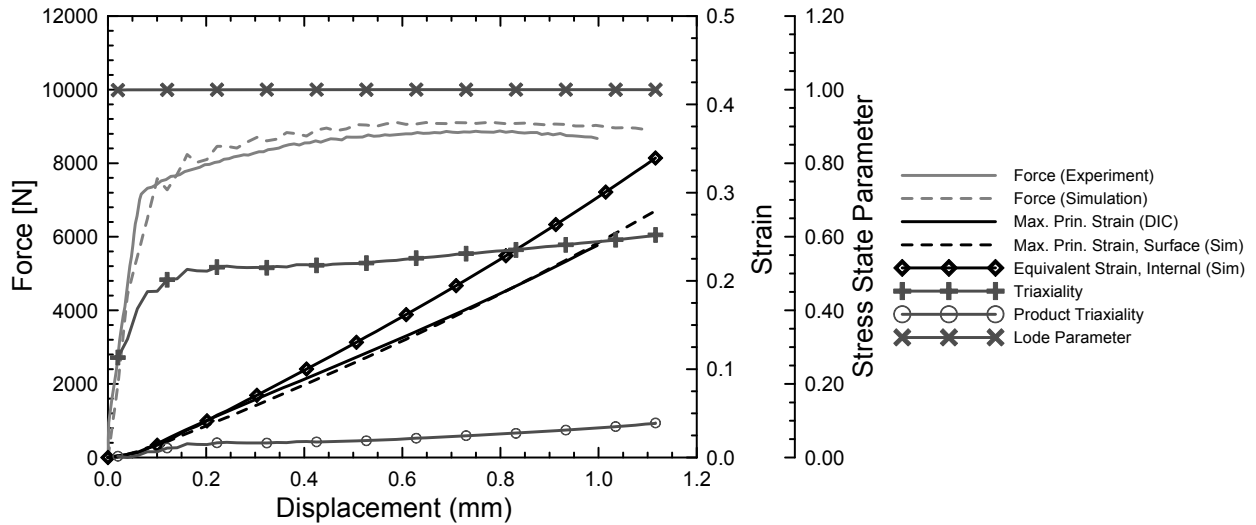


Figure 125. Experimental and simulated data for an axisymmetric specimen with a 14.503 mm radius notch.

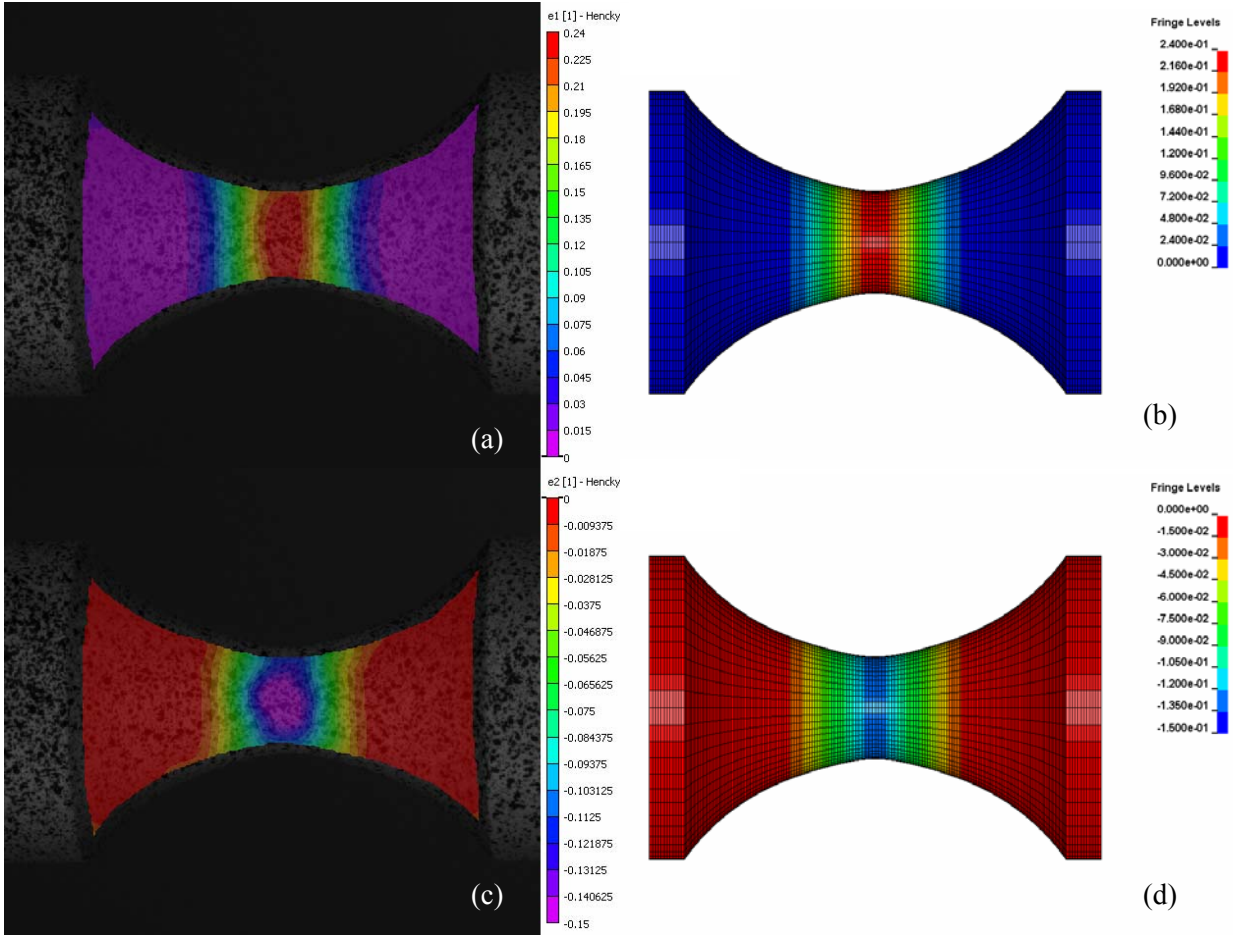


Figure 126. Comparison of specimen surface strains, axisymmetric specimen with a 9.144 mm radius notch: (a) DIC max. principal strain, (b) simulation max. principal strain, (c) DIC min. principal strain, (d) simulation min. principal strain.

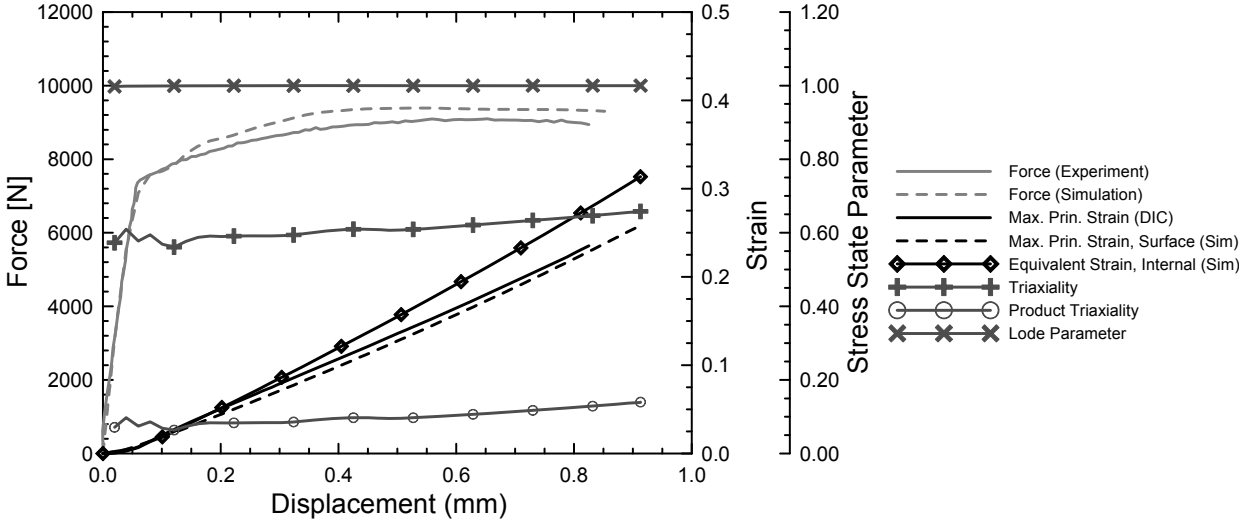


Figure 127. Experimental and simulated data for an axisymmetric specimen with a 9.144 mm radius notch.

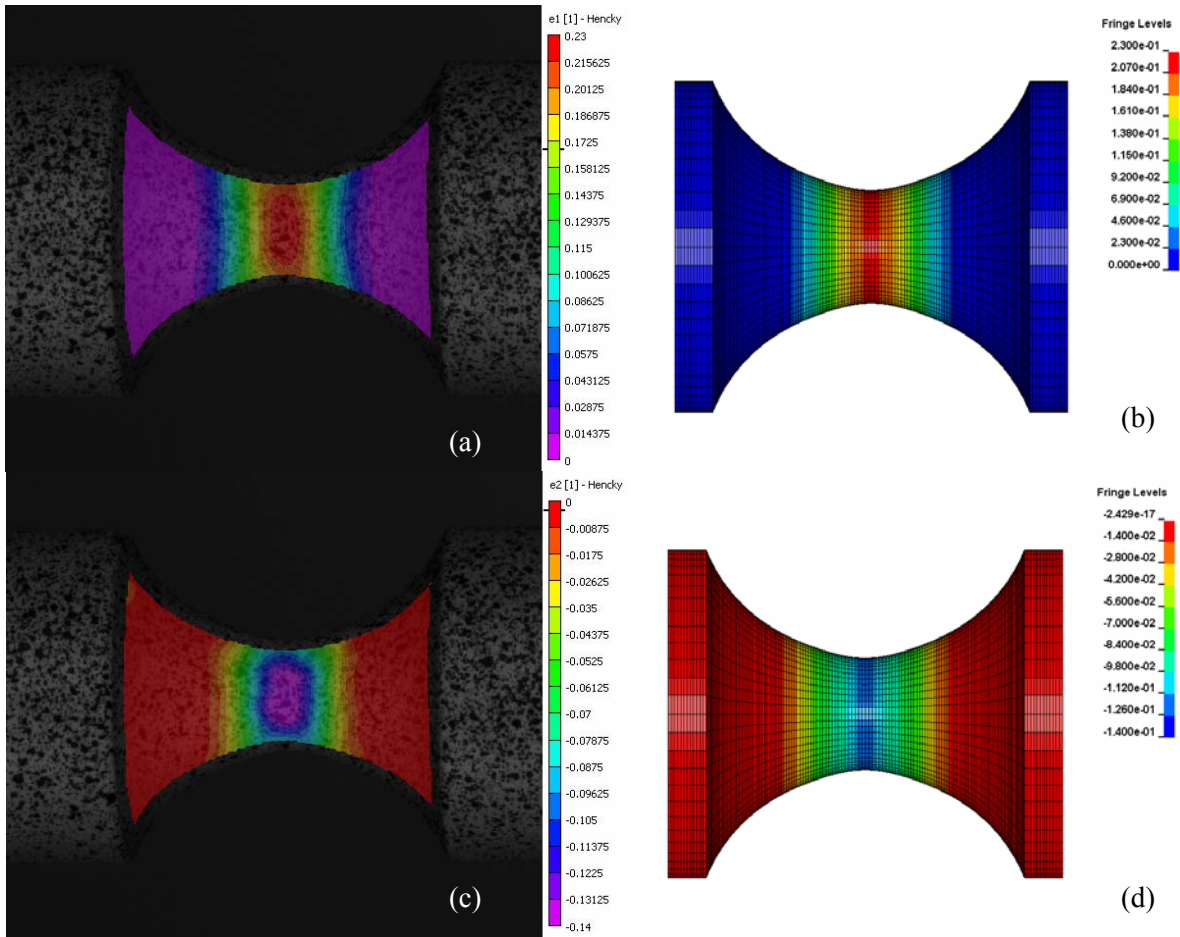


Figure 128. Comparison of specimen surface strains, axisymmetric specimen with a 6.096 mm radius notch: (a) DIC max. principal strain, (b) simulation max. principal strain, (c) DIC min. principal strain, (d) simulation min. principal strain.

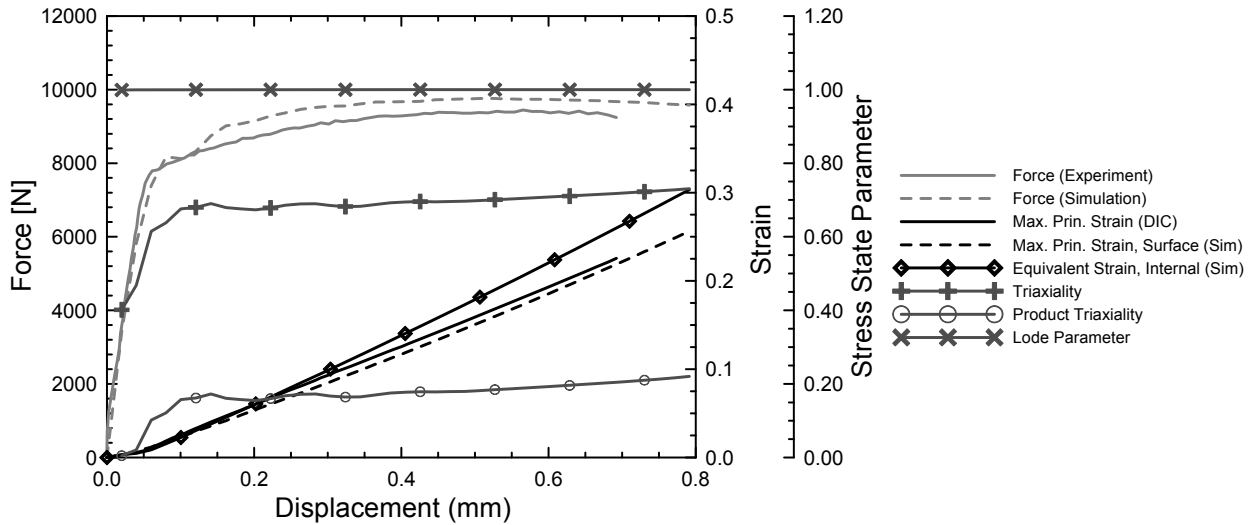


Figure 129. Experimental and simulated data for an axisymmetric specimen with a 6.096 mm radius notch.

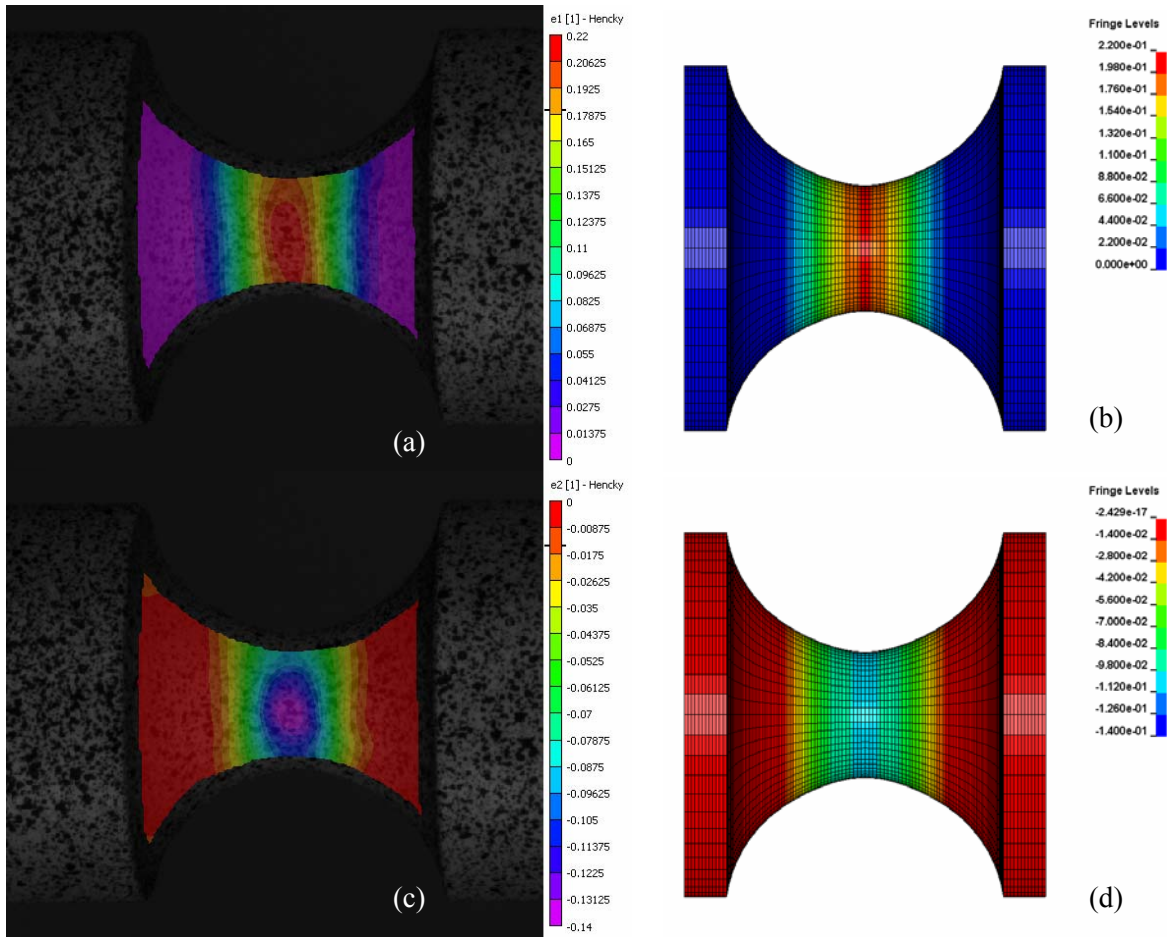


Figure 130. Comparison of specimen surface strains, axisymmetric specimen with a 4.470 mm radius notch: (a) DIC max. principal strain, (b) simulation max. principal strain, (c) DIC min. principal strain, (d) simulation min. principal strain.

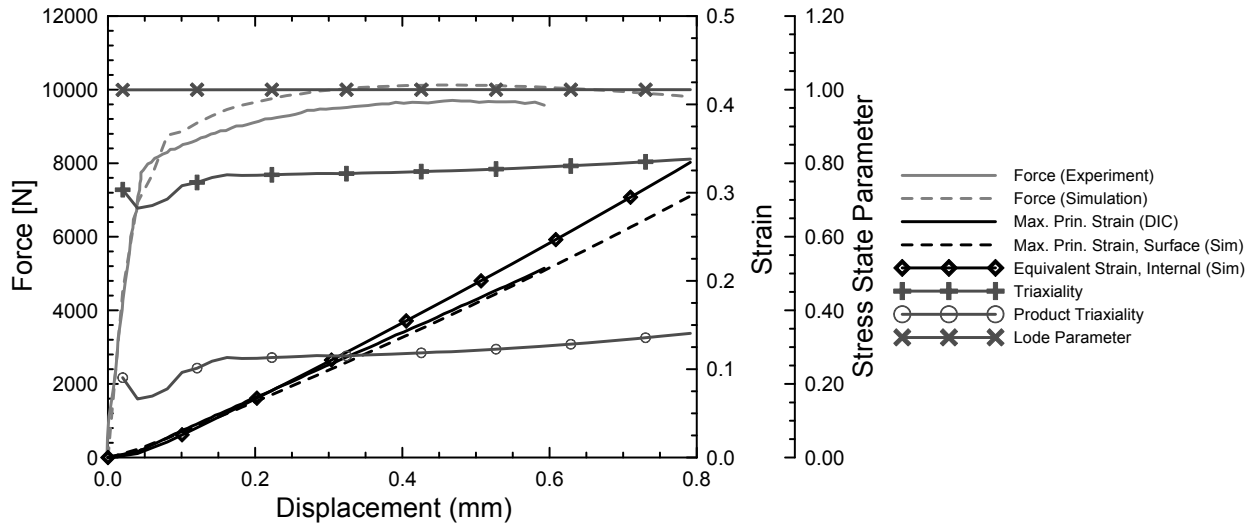


Figure 131. Experimental and simulated data for an axisymmetric specimen with a 4.470 mm radius notch.

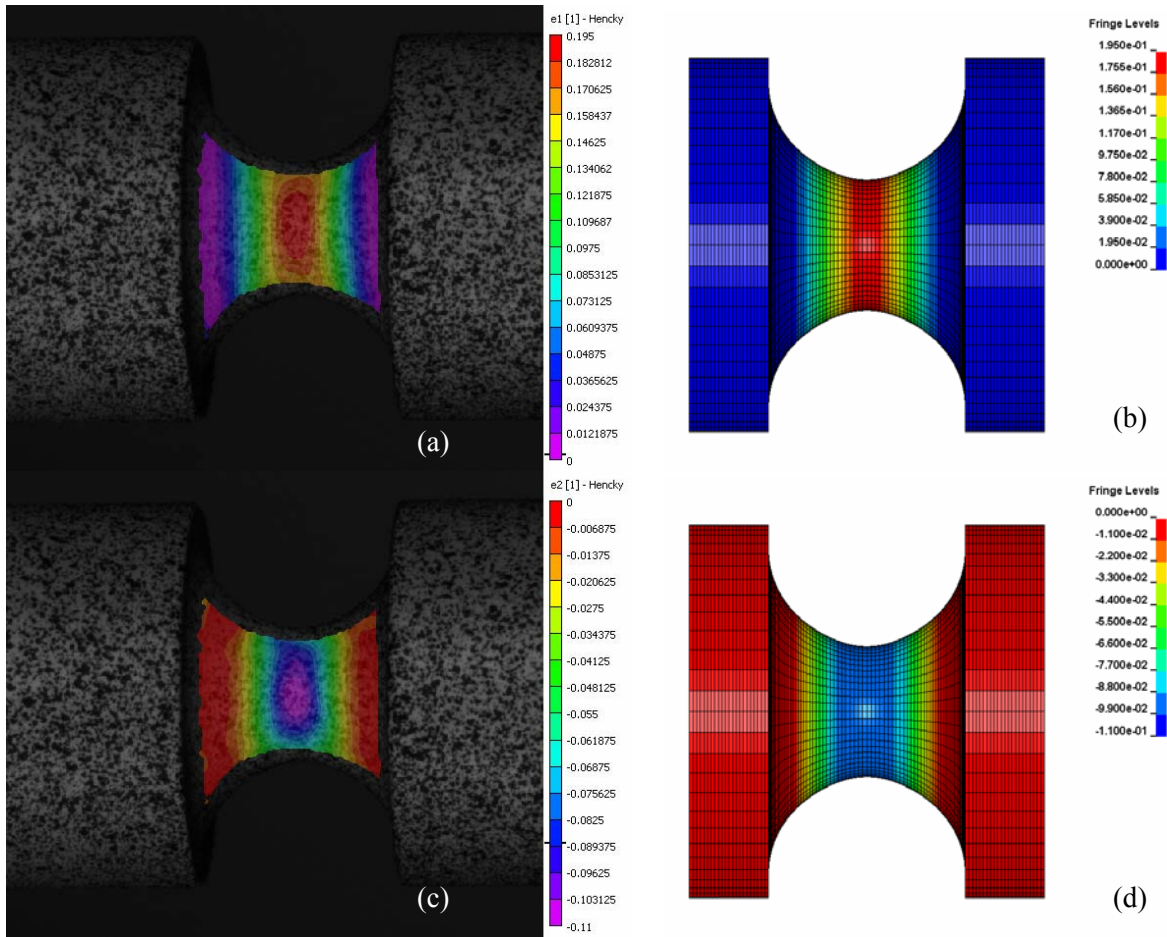


Figure 132. Comparison of specimen surface strains, axisymmetric specimen with a 3.048 mm radius notch: (a) DIC max. principal strain, (b) simulation max. principal strain, (c) DIC min. principal strain, (d) simulation min. principal strain.

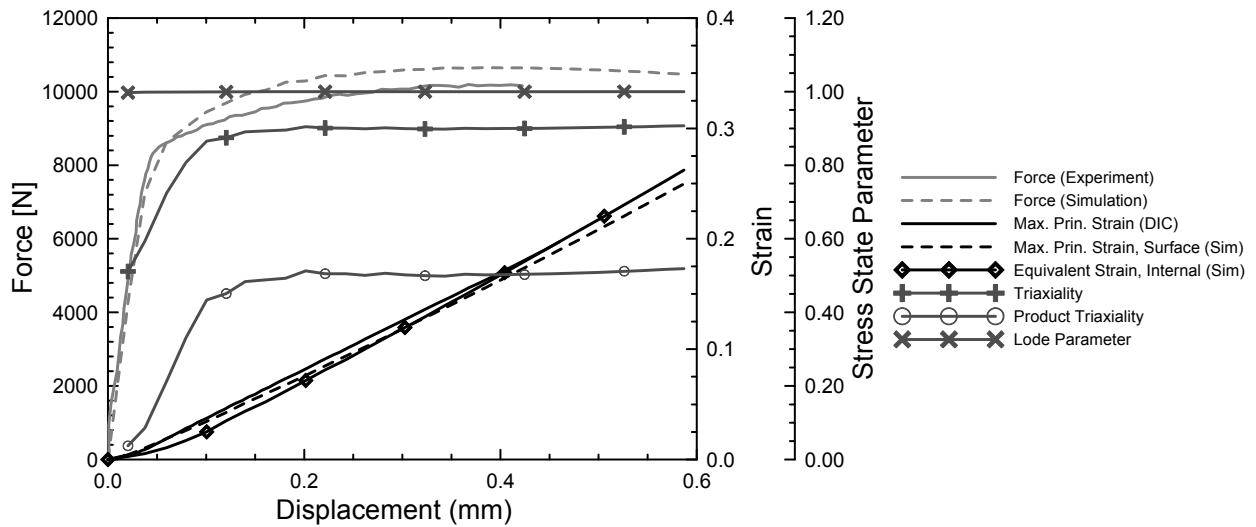


Figure 133. Experimental and simulated data for an axisymmetric specimen with a 3.048 mm radius notch.

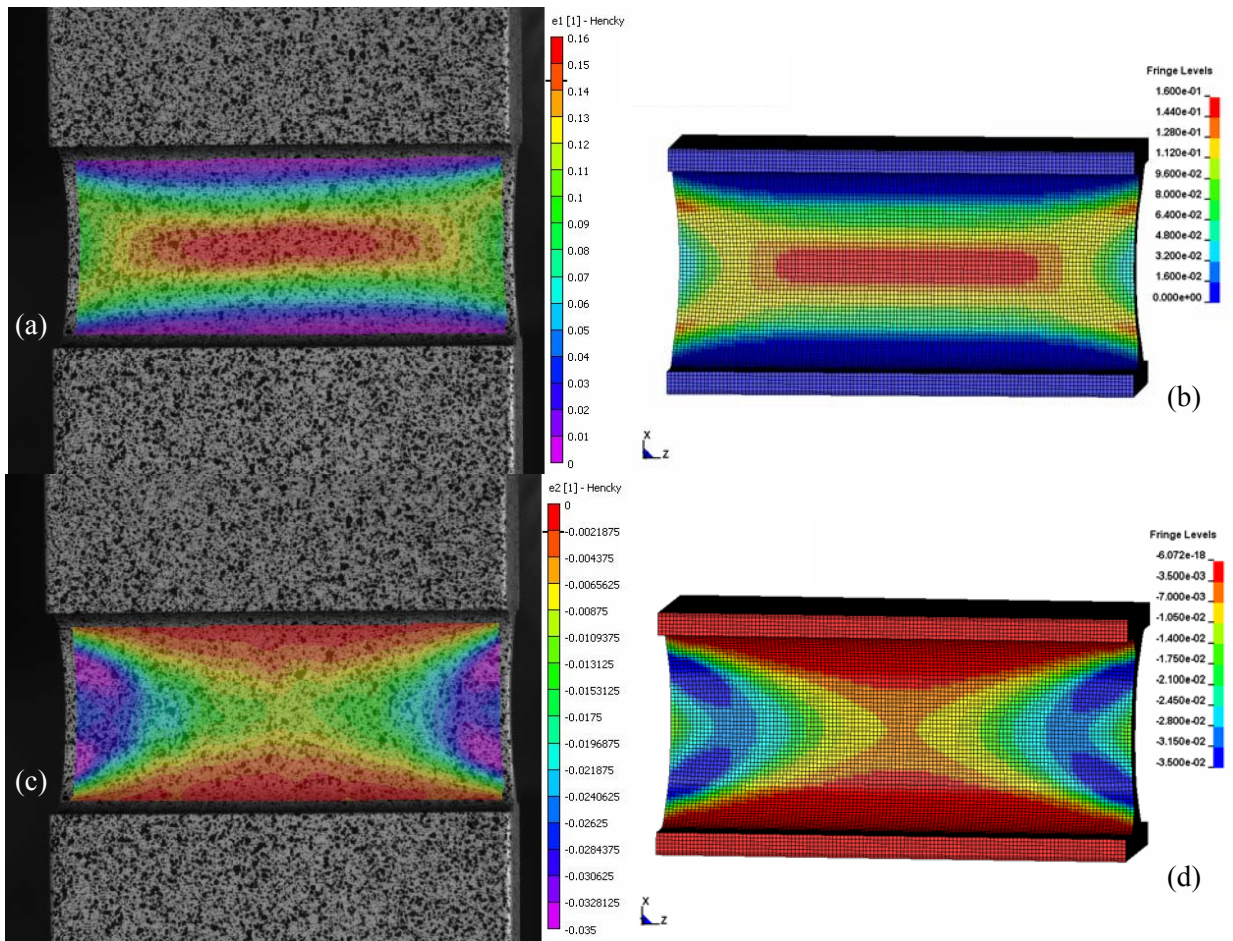


Figure 134. Comparison of specimen surface strains, plain strain specimen with a smooth gage section: (a) DIC max. principal strain, (b) simulation max. principal strain, (c) DIC min. principal strain, (d) simulation min. principal strain.

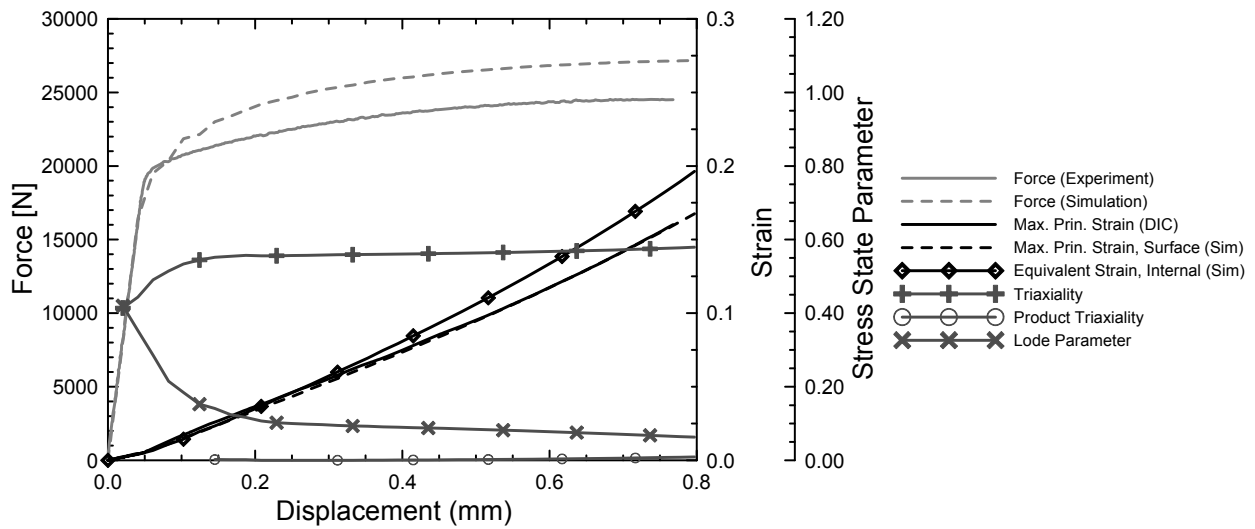


Figure 135. Experimental and simulated data for a plane strain specimen with a smooth gage section.

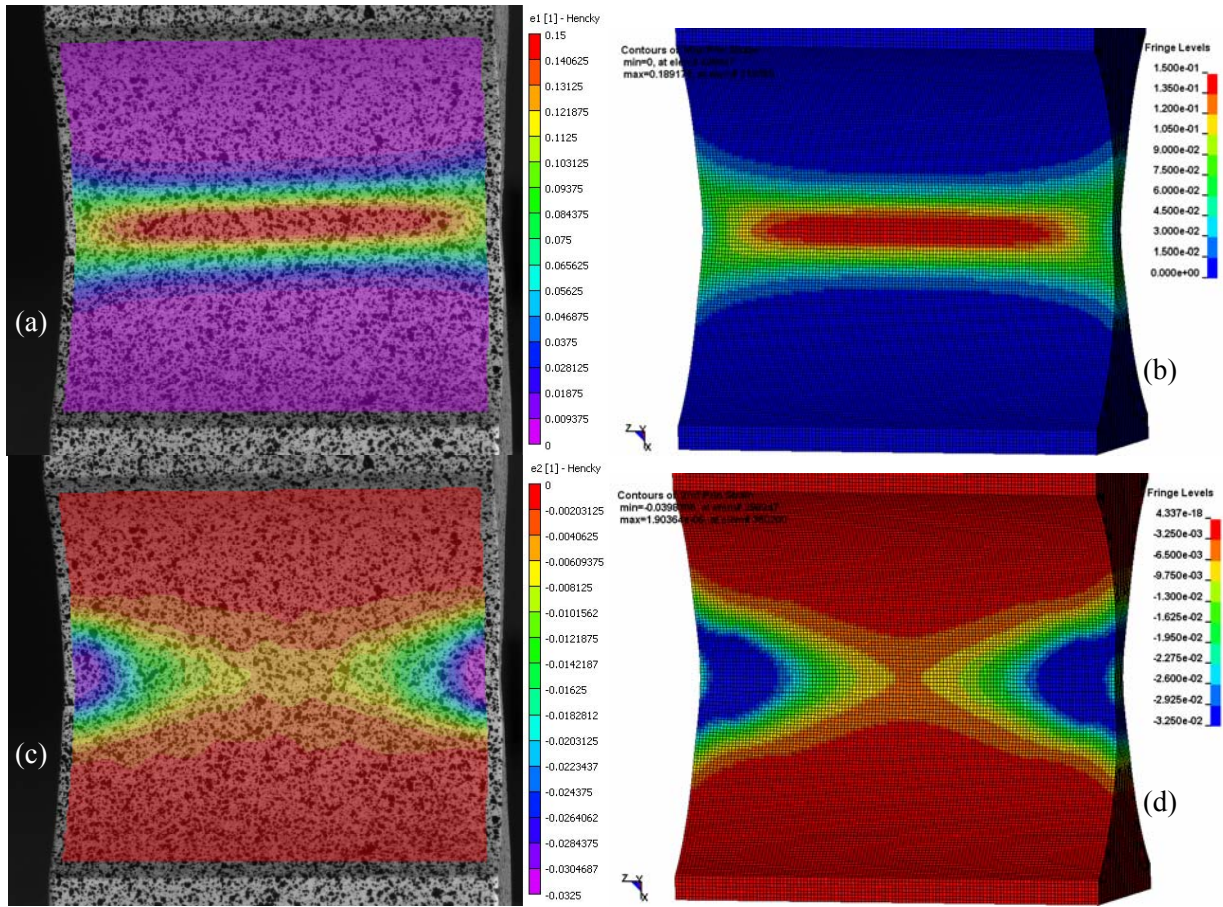


Figure 136. Comparison of specimen surface strains, plane strain specimen with 13.97 mm radius notch: (a) DIC max. principal strain, (b) simulation max. principal strain, (c) DIC min. principal strain, (d) simulation min. principal strain.

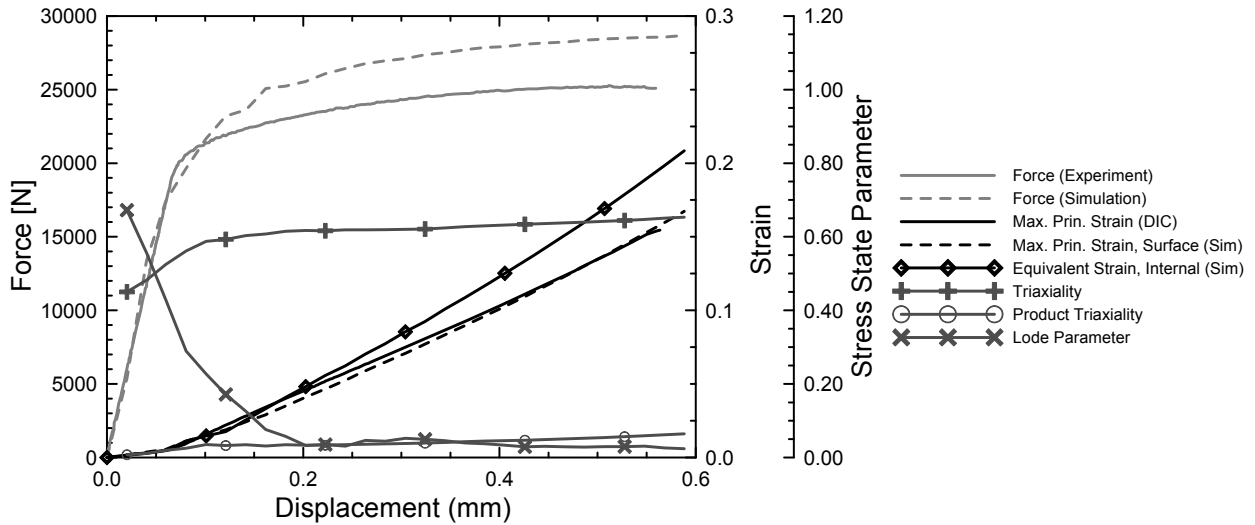


Figure 137. Experimental and simulated data for a plane strain specimen with a 13.970 mm radius notch.

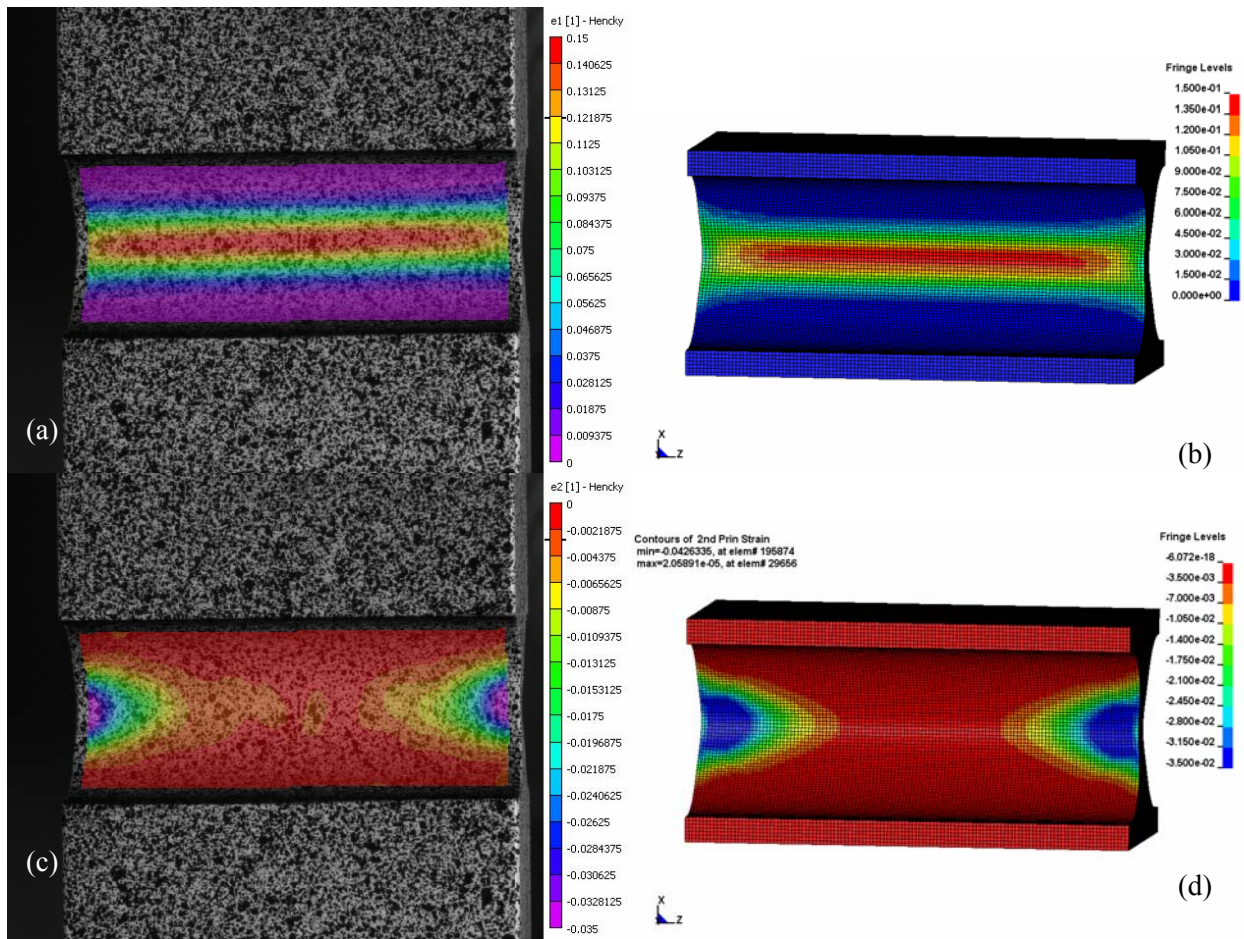


Figure 138. Comparison of specimen surface strains, plane strain specimen with 4.763 mm radius notch: (a) DIC max. principal strain, (b) simulation max. principal strain, (c) DIC min. principal strain, (d) simulation min. principal strain.

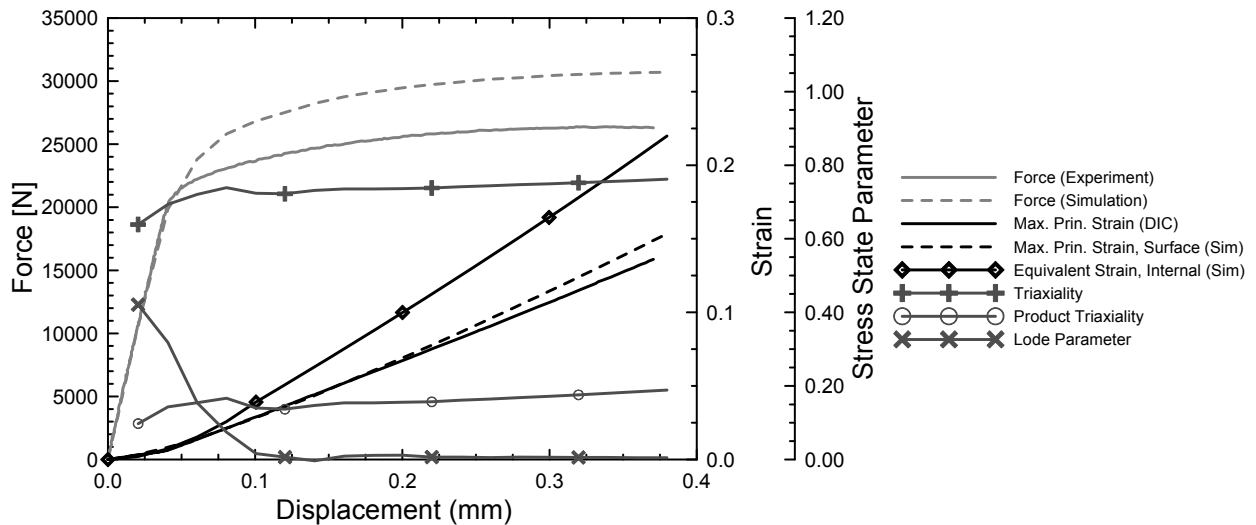


Figure 139. Experimental and simulated data for a plane strain specimen with a 4.763 mm radius notch.

## Appendix D: Additional Experimental Data for Combined Loading Experiments

This appendix contains additional data from the combined loading and pure shear experiments conducted in the ductile fracture test program. The experimental program is summarized in Table 6. Maximum and minimum principal surface strains measured using 3D DIC are presented with stress-state and strain history data for each different load case. Surface strains and history data from a combined tension-torsion experiment with  $\frac{\sigma_x}{\tau_{xy}} = 1.974$  are shown in Figure 20 and Figure 70, respectively. Data

from a combined tension-torsion experiment with  $\frac{\sigma_x}{\tau_{xy}} = 0.868$  are shown in Figure 140 and Figure 141.

Pure torsion data are shown in Figure 142 and Figure 143 and combined compression – torsion experimental data are presented in Figure 144 and Figure 145, respectively. Each history plot in this appendix contains shear, axial stress, stress triaxiality, Lode parameter and product triaxiality records. In addition, maximum principal and minimum principal specimen surface strains from DIC measurements are plotted.

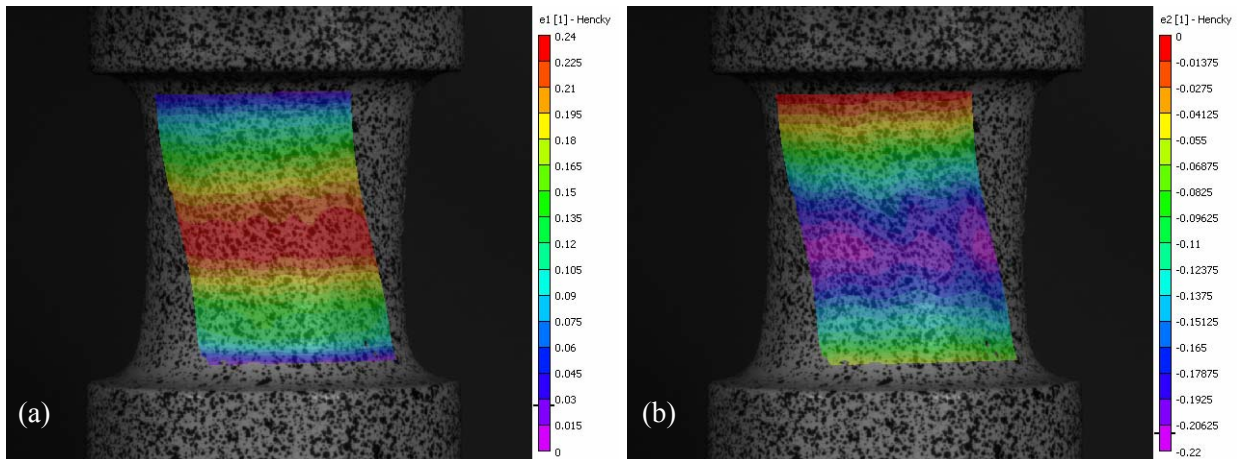


Figure 140. Surface strains on a combined tension – torsion specimen,  $\frac{\sigma_x}{\tau_{xy}} = 0.868$ : (a) max. principal strain, (b) min. principal strain.

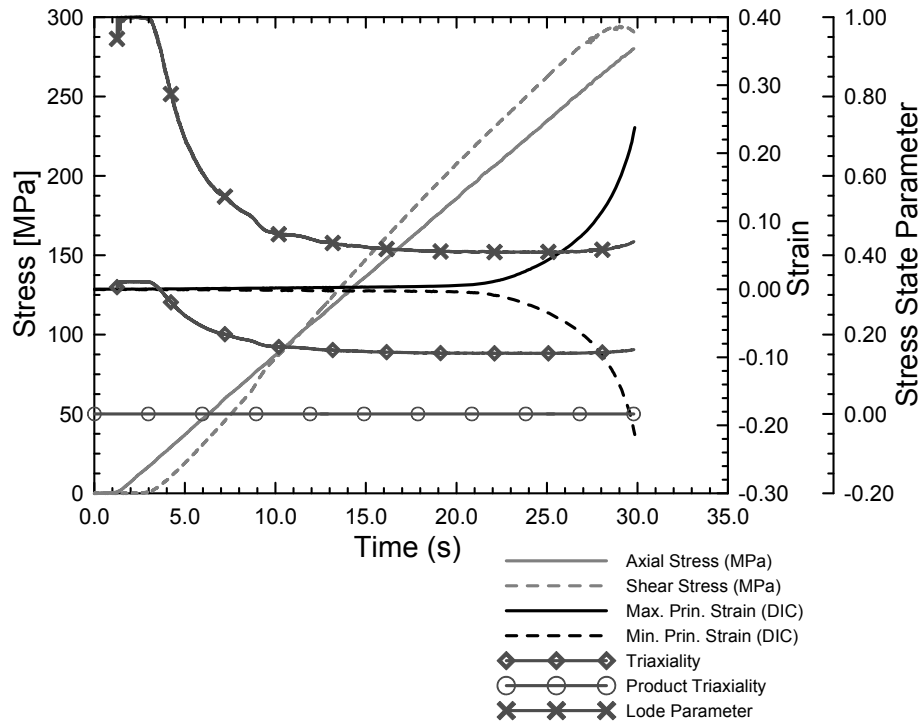


Figure 141. Combined loading experimental data,  $\frac{\sigma_x}{\tau_{xy}} = 0.868$ .

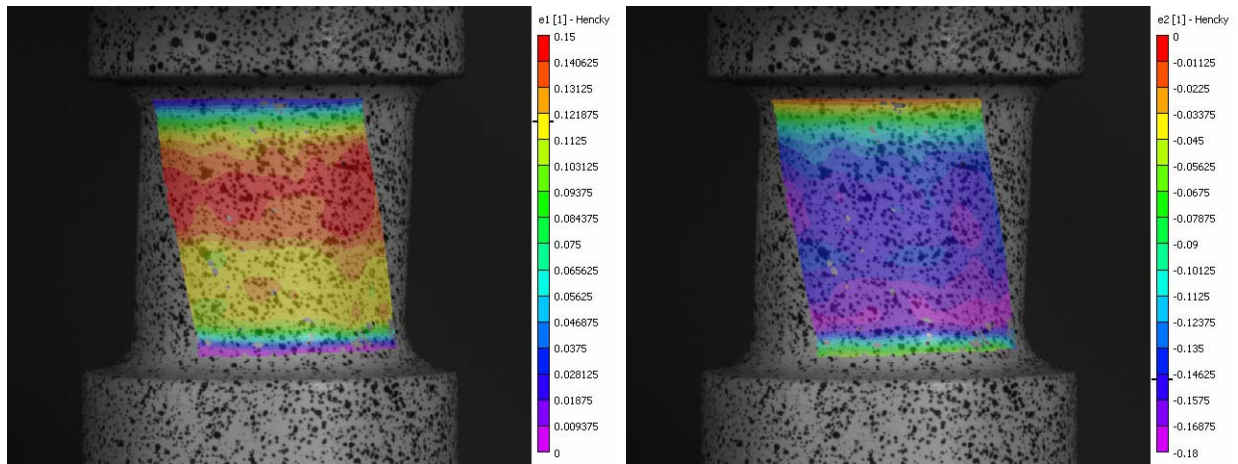


Figure 142. Surface strains on a pure shear (torsion) specimen,  $\frac{\sigma_x}{\tau_{xy}} = 0.0$ : (a) max. principal strain, (b) min. principal strain.

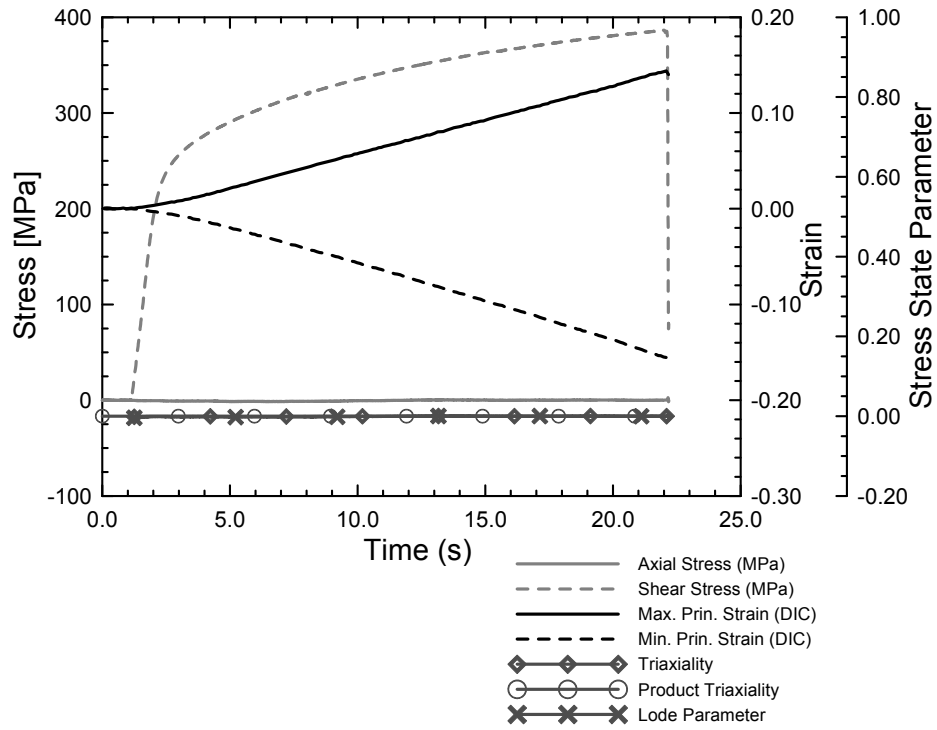


Figure 143. Pure shear (torsion) experimental data,  $\frac{\sigma_x}{\tau_{xy}} = 0.0$ .

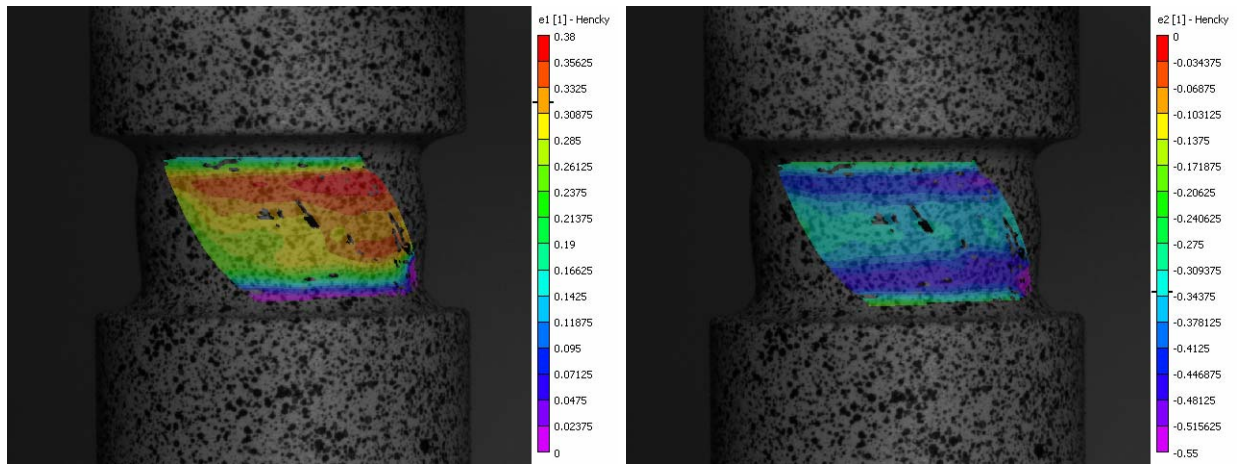


Figure 144. Surface strains on a combined compression – torsion specimen,  $\frac{\sigma_x}{\tau_{xy}} = -0.868$ : (a) max. principal strain, (b) min. principal strain.

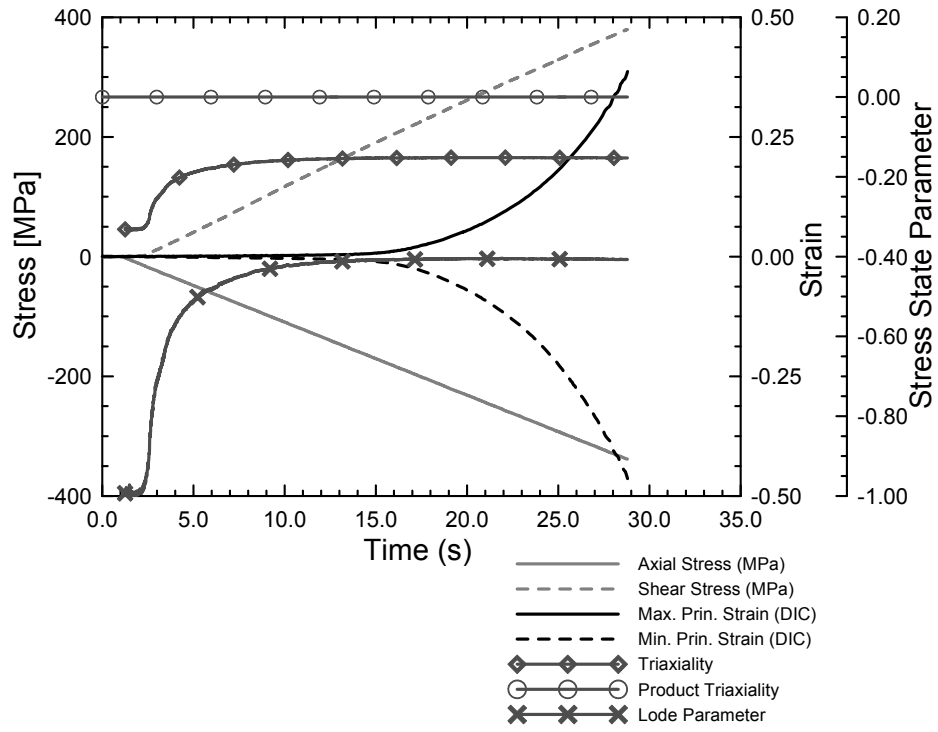


Figure 145. Combined loading experimental data,  $\frac{\sigma_x}{\tau_{xy}} = -0.868$ .

## Appendix E: Additional Views of the Fracture Locus for 2024-T351 Aluminum

Additional views of the fracture locus for 2024-T351 aluminum generated in Chapter 7 are presented here. In all plots, the equivalent plastic fracture strain ( $\bar{\epsilon}_f^p$ ) is plotted versus stress triaxiality ( $\sigma^*$ ) and the Lode parameter ( $\mu$ ). Data points are indicated by solid black circles and the surface is generated using biharmonic spline interpolation.

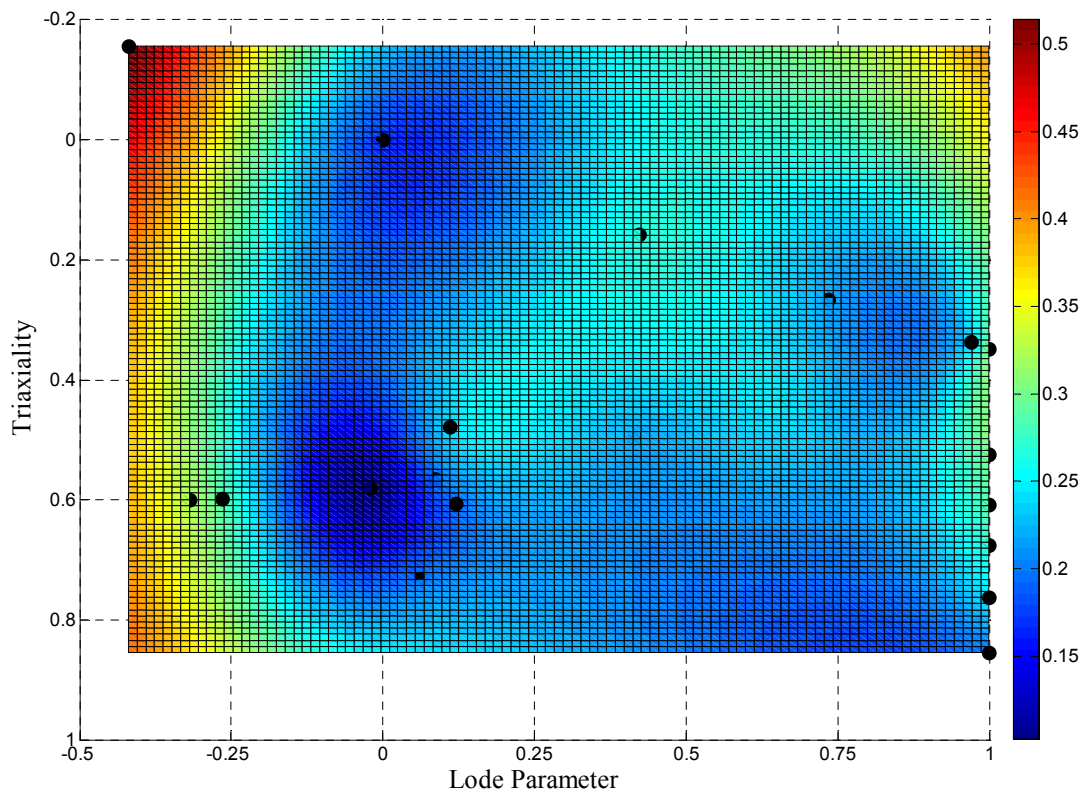


Figure 146. Fracture locus for 2024-T351 aluminum, top view.

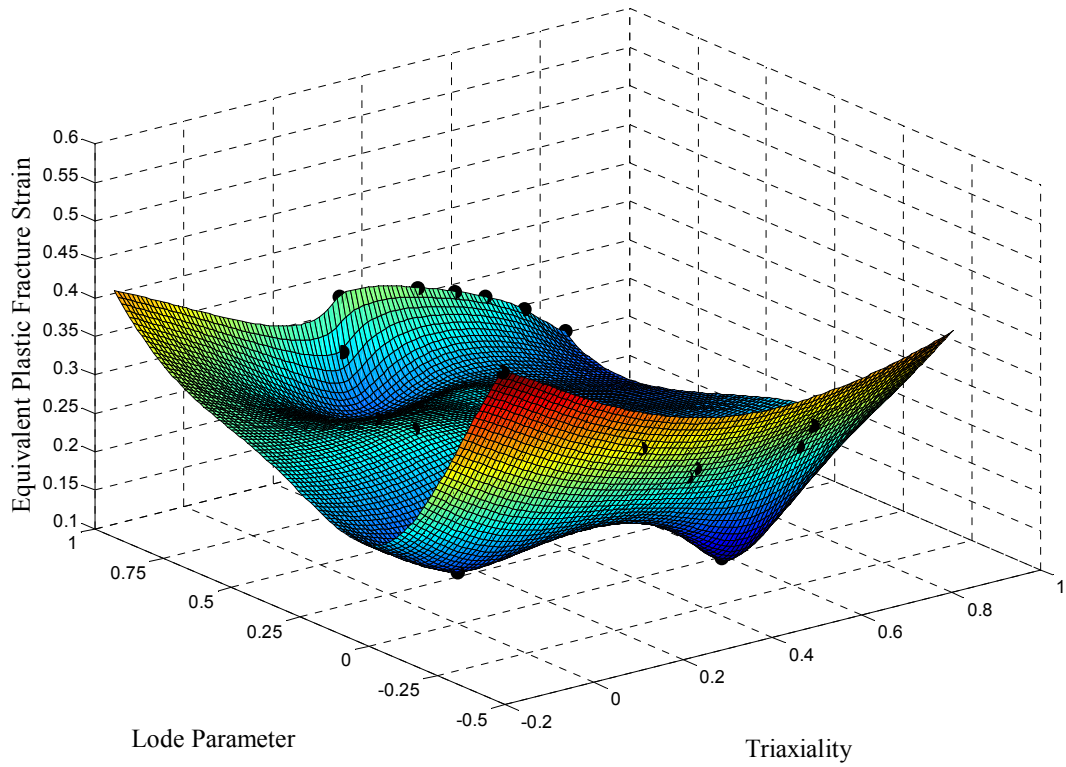


Figure 147. Fracture locus for 2024-T351 aluminum, 3D view #1.

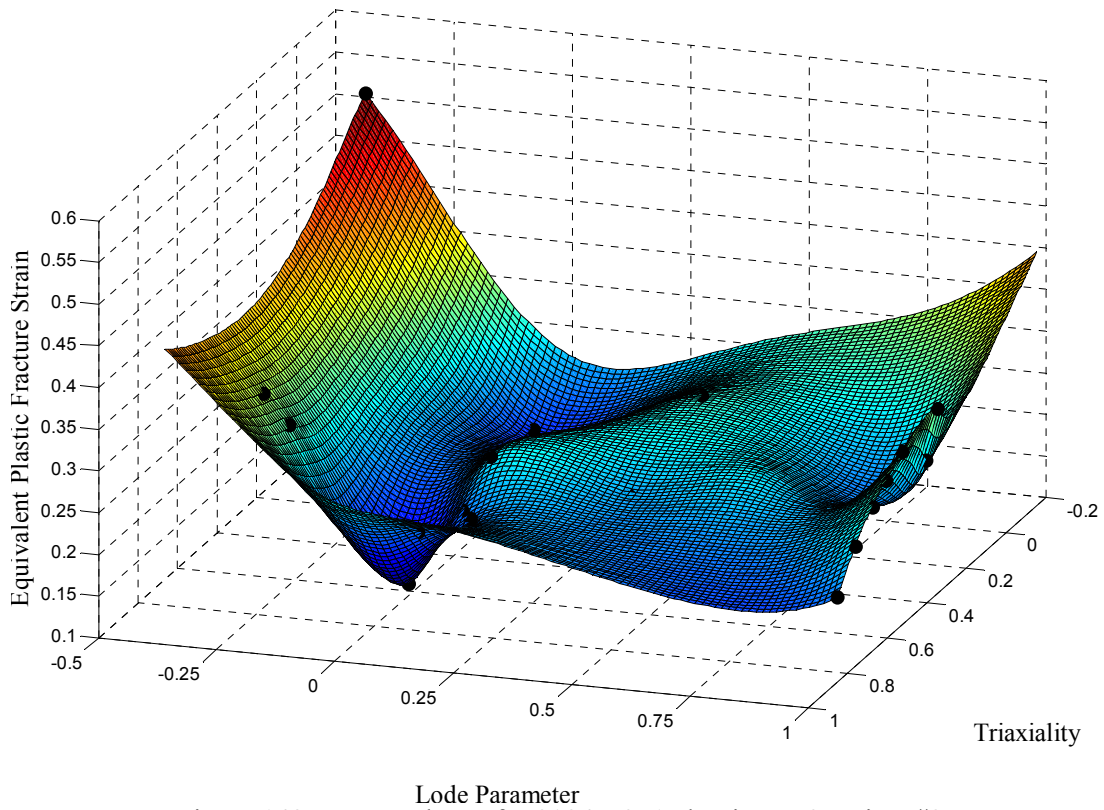


Figure 148. Fracture locus for 2024-T351 aluminum, 3D view #2.

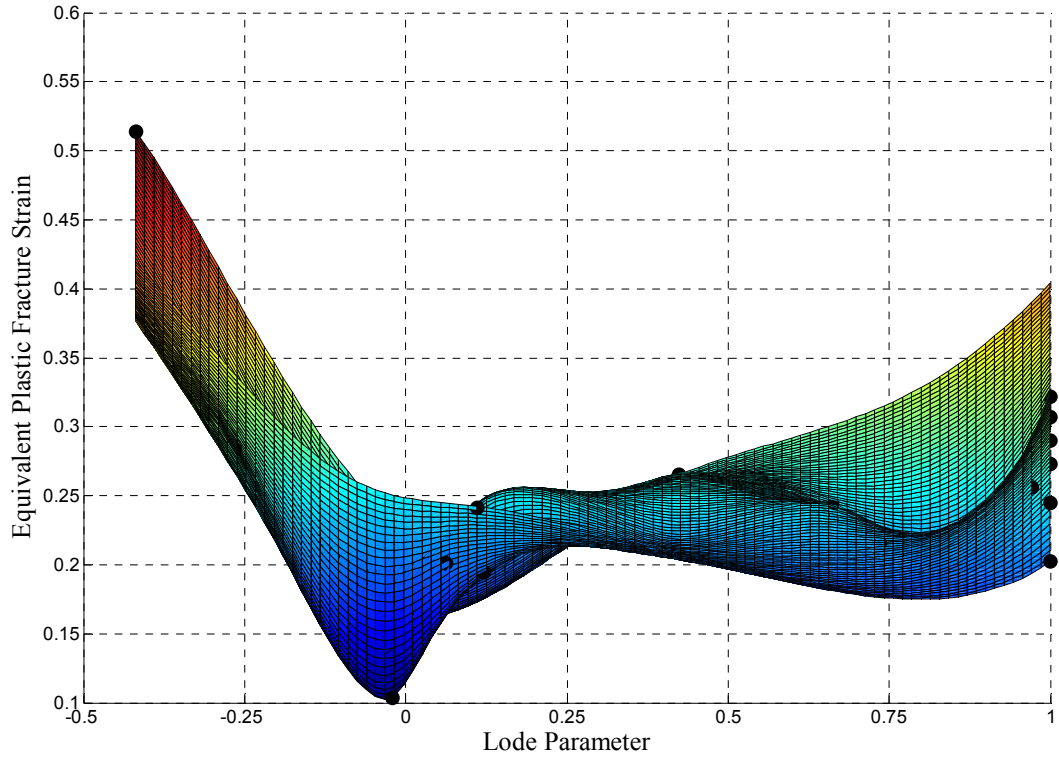


Figure 149. Fracture locus for 2024-T351 aluminum, side view #1.

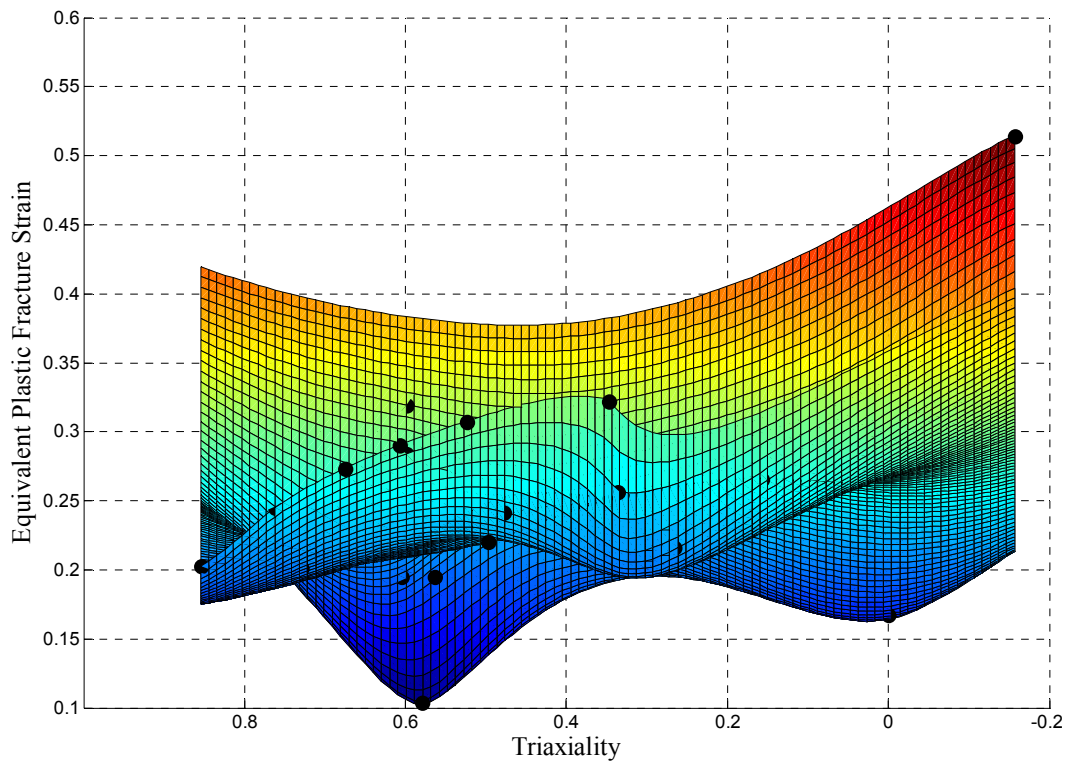


Figure 150. Fracture locus for 2024-T351 aluminum, side view #2.

## References

- [1] LSTC, LS-DYNA Keyword User's Manual, Volumes I and II, Version 971, Livermore Software Technology Center (LSTC), Livermore, CA, 2007.
- [2] ABAQUS < [http://www.simulia.com/products/abaqus\\_fea.html](http://www.simulia.com/products/abaqus_fea.html)>
- [3] AUTODYN < <http://www.ansys.com/products/explicit-dynamics/autodyn/default.asp>>
- [4] Anderson A., et al., User's Manual for ALE3D, Lawrence Livermore National Laboratory, 2003.
- [5] Hertel E.S. Jr, Bell R.L., Elrick M.G., Farnsworth A.V., Kerley G.I., McGlaun J.M., Petney S.V., Silling S.A., Taylor P.A., Yarrington L., "CTH: a software family for multi-dimensional shock physics analysis". *Proceedings of the 19th International Symposium on Shock Waves*, 1993.
- [6] Johnson, G.R., Cook, W.H., "A Constitutive Model and Data for Metals Subjected to Large Strains, High Strain Rates and High Temperatures", *Proceedings of the 7th International Symposium on Ballistics*, The Hague, The Netherlands, April 1983.
- [7] Johnson, G.R., Cook, W.H., "Fracture Characteristics of Three Metals Subjected to Various Strains, Strain Rates, Temperatures and Pressures", *Engineering Fracture Mechanics*, Vol. 21, 1985, pp31-48.
- [8] Steinberg, D.J., Cochran, S.G., Guinan, M.W., "Constitutive Model for Metals Applicable at High Strain Rate", *Journal of Applied Physics*, Vol. 51, 1980, pp1498-1504.
- [9] Zerilli, F.J.; Armstrong, R.W. "Dislocation-Mechanics-Based Constitutive Relations for Material Dynamics Calculations." *Journal of Applied Physics*. Vol. 61, 1987, pp1816-1825.
- [10] Follansbee, P.S., Kocks, U.F., "Constitutive Description of the Deformation of Copper Based on the Use of the Mechanical Threshold Stress as an Internal State Variable", *Acta Metallurgica*, Vol. 36, 1988, p81-93.
- [11] Gurson, A.L., "Continuum Theory of Ductile Rupture by Void Nucleation and Growth: Part I – Yield Criteria and Flow Rules for Porous Ductile Media", *Journal of Engineering Materials and Technology*, Vol. 99, 1977, pp 2-15.
- [12] Tvergaard, V., "Ductile Fracture by Cavity Nucleation between Larger Voids", *Journal of the Mechanics and Physics of Solids*, Vol. 30, 1982, pp265-286.
- [13] Horstemeyer, M.F., Gokhale, A.M., "A Void-Crack Nucleation Model for Ductile Metals", *International Journal of Solids and Structures*, Vol. 36, 1999, pp5029-5055.
- [14] Lundin, S.J., et al. "Uncontained Engine Debris Fire Mitigation Test – Fuselage-Mounted Engines", Final Report to the U.S. Department of Transportation, Federal Aviation Administration, Report #DOT/FAA/AR-05/3, February, 2005.

- [15] Frankenberger, C.E., "Large Engine Uncontained Debris Analysis", Final Report to the U.S. Department of Transportation, Federal Aviation Administration, Report #DOT/FAA/AR-99/11, May, 1999.
- [16] Zukas, J.A., et al., *Impact Dynamics*, John Wiley and Sons, New York, 1982.
- [17] Borvik, T., Hanssen, A.G., Langseth, M., Olovsson, L., "Response of Structures to Planar Blast Loads – A Finite Element Engineering Approach", *Computers and Structures*, Vol 87, 2009, pp507-520.
- [18] Kurtaran, H., Buyuk, M., Eskandarian, A., "Design Automation of a Laminated Armor for Best Impact Performance Using Approximate Optimization Method", *International Journal of Impact Engineering*, Vol. 29, 2003, pp397-406.
- [19] Rosenberg, Z., Ashuach, Y., Yeshurun, Y., Dekel, E., "On the Main Mechanisms for Defeating AP Projectiles, Long Rods and Shaped Charge Jets", *International Journal of Impact Engineering*, Vol 36, 2009, pp588-596.
- [20] Schwer, L.E., Hacker, K., Poe, K., "Perforation of Metal Plates: Laboratory Experiments and Numerical Simulations", *Proceedings of the 9<sup>th</sup> International LS-DYNA Users Conference*, Dearborn, MI, June, 2006.
- [21] Seidt, J.D., Gilat, A., Klein, J.A., Leach, J.R., "High Strain Rate, High Temperature Constitutive and Failure Models for EOD Impact Scenarios", *Proceedings of the 2007 SEM Annual Conference and Exposition on Experimental and Applied Mechanics*, Springfield, MA, June, 2007.
- [22] Katayama, M., Takeba, A., Toda, S., Kibe, S., "Analysis of Jet Formation and Penetration by Conical Shaped Charge with the Inhibitor", *International Journal of Impact Engineering*, Vol. 23, 1999, pp443-454.
- [23] Wu, J., Liu, J., Du, Y., "Experimental and Numerical Study on the Flight and Penetration Properties of Explosively-Formed Projectile", *International Journal of Impact Engineering*, Vol. 34, 2007, pp1147-1162.
- [24] Gilmour, K. R., Leacock, A. G., Ashbridge, M.T.J., "The Influence of Plastic Strain Ratios on the Numerical Modelling of Stretch Forming", *Journal of Material Processing Technology*, Vol. 152, 2004, pp. 116-125.
- [25] Huh, H., Kang, W.J., "Crash-Worthiness Assessment of Thin-Walled Structures with the High Strength Steel Sheet", *International Journal of Vehicle Design*, Vol. 30, 2002, pp.1-21.
- [26] Walker, J.D., "From Columbia to Discovery: Understanding the Impact Threat to the Space Shuttle", *International Journal of Impact Engineering*, Vol. 36, 2009, pp. 303-317.
- [27] Sutton, M., Orteu, J.-J., Schreier, H.W., *Image Correlation for Shape, Motion and Deformation Measurements*, Springer, New York, NY, 2009.
- [28] Li, P., Siviour, C.R., Petrinic, N., "The Effect of Strain Rate, Specimen Geometry and Lubrication on Responses of Aluminum AA2024 in Uniaxial Compression Experiments", *Experimental Mechanics*, Vol. 48, 2008.
- [29] Hodowany, J., Ravichandran, G., Rosakis, A.J., Rosakis, P., "Partition of Plastic Work into Heat and Stored Energy in Metals", *Experimental Mechanics*, Vol. 40, No. 2, June 2000.
- [30] Johnson, G.R., Hoegfeldt, J.M., Linholm, U.S., Nagy, A., "Response of Various Metals to Large Torsional Strains Over a Large Range of Strain Rates – Part 2: Less Ductile Metals", *Transactions of the ASME*, Vol. 105, January 1983, pp48-53.

- [31] Lesuer, D. R., “Experimental Investigations of Material Models for Ti-6Al-4V Titanium and 2024-T3 Aluminum”, Final Report, U.S. Department of Transportation, Federal Aviation Administration, Contract No. DTFA03-97-Z-90007, Report No. DOT/FAA/AR-00/25, September 2000.
- [32] Zhao, D., Lampman, S., “Effects of Temperature, Hot Tension and Compression Testing”, Mechanical Testing, Vol. 8, ASM Handbook, ASM International, 2000.
- [33] Barlat, F., Lege, D. J., Brem, J.C., “A Six-Component Yield Function for Anisotropic Materials”, *International Journal of Plasticity*, Vol. 7, 1991, pp 693-712.
- [34] Gilmour, K. R., Leacock, A. G., Ashbridge, M.T.J., “The Determination of the In-Plane Shear Characteristics of Aluminum Alloys”, *Journal of Testing and Evaluation*, JTEVA, Vol. 29, No. 2, March 2001, pp.131-137.
- [35] Banabic, D., Bunge H.-J., Pohlandt, K., Tekkaya, A.E., *Formability of Metallic Materials*, Springer-Verlag, Berlin, 2000.
- [36] Hammond, R.I., Proud, W.G., Goldrein, H.T., Field, J.E., “High-Resolution Optical Study of the Impact of Carbon-Fibre Reinforced Polymers with Different Lay-Ups”, *International Journal of Impact Engineering*, Vol. 30, 2004, pp 69-86.
- [37] Chen, J.K., Allahdadi, F.A., Carney, T.C., “High-Velocity Impact of Graphite/Epoxy Composite Laminates”, *Composite Science and Technology*, Vol. 57, 1997, pp 1369-1379.
- [38] Rossikhin, YU.A., Shitikova, M.V., “Dynamic Response of a Pre-Stressed Transversely Isotropic Plate to Impact by an Elastic Rod”, *Journal of Vibration and Control*, Vol. 15, 2009, pp 25-51.
- [39] Radchenko, A.V., Kobenko, S.V., Marzenyuk, I.N., Khorev, I.E., Kanel, G.I., Fortov, V.E., “Research on Features of Behaviour of Isotropic and Anisotropic Materials under Impact”, *International Journal of Impact Engineering*, Vol. 23, 1999, pp745-756.
- [40] Kothari, M., Anand, L., “Elasto-Viscoplastic Constitutive Equations for Polycrystalline Metals: Application to Tantalum”, *Journal of the Mechanics and Physics of Solids*, Vol. 46, No. 1, 1998, pp 51-83.
- [41] Plunkett, B., Cazacu, O., Lebensohn, R.A., Barlat, F., “Elastic-Viscoplastic Anisotropic Modeling of Textured Metals and Validation using the Taylor Cylinder Impact Test”, *International Journal of Plasticity*, Vol. 23, 2007, pp 1001-1021.
- [42] Grytten, F., Børvik, T., Hopperstad, O.S., Langseth, M., “Low Velocity Perforation of AA5083-H116 Aluminum Plates”, *International Journal of Impact Engineering*, Vol. 36, 2009, pp 597-610.
- [43] Pereira, J.M., Revilock, D.M., Ruggeri, C.M., “Ballistic Impact Testing of Al 2024 Sheet and Plate”, NASA Glenn Research Center, Draft report to be submitted to the Federal Aviation Administration.
- [44] Nandwana, K., “Effect of Anisotropic Material Model on Ballistic Impact of 0.5” Thick Al 2024 Plates”, Project Report submitted to the Department of Mechanical Engineering at The Ohio State University in partial fulfillment of the Degree Master of Science, April, 2009.
- [45] Dodd, B., Bai, Y., *Ductile Fracture and Ductility with Applications to Metalworking*, Harcourt Brace Jovanovich publishers, London, 1987.
- [46] McClintock, F.A., “A Criterion for Ductile Fracture by the Growth of Holes”, *Journal of Applied Mechanics*, Vol. 35, 1968, pp363-371.

- [47] Rice, J.R., Tracey, D.M., “On the Ductile Enlargement of Voids in Triaxial Stress Fields”, *Journal of the Mechanics of Physical Solids*, Vol. 17, 1969, pp 201-217.
- [48] Hancock, J.W., Mackenzie, A.C., “On the Mechanisms of Ductile Failure in High-Strength Steels Subjected to Multi-Axial Stress-States”, *Journal of the Mechanics of Physical Solids*, Vol. 24, 1976, pp 147-169.
- [49] Mackenzie, A.C., Hancock, J.W., Brown, D.K., “On the Influence of State of Stress on Ductile Failure Initiation in High Strength Steels”, *Engineering Fracture Mechanics*, Vol. 9, 1977, pp167-188.
- [50] Bridgman, P.W., *Studies in Large Plastic Flow and Fracture, with Special Emphasis on the Effects of Hydrostatic Pressure*, Harvard University Press, Cambridge, 1964.
- [51] Hopperstad, O.S., Børvik, T., Langseth, M., Labibes, K., Albertini, C., “On the Influence of Stress Triaxiality and Strain Rate on the Behaviour of a Structural Steel. Part I. Experiments”, *European Journal of Mechanics A/Solids*, Vol. 22, pp 1-13.
- [52] Børvik, T., Hopperstad, O.S., Berstad, T., “On the Influence of Stress Triaxiality and Strain Rate on the Behaviour of a Structural Steel. Part II. Numerical Study”, *European Journal of Mechanics A/Solids*, Vol. 22, pp 15-32.
- [53] Bau, Y., Wierzbicki, T., “On Fracture Locus in the Equivalent Strain and Stress Triaxiality Space”, *International Journal of Mechanical Sciences*, Vol. 46, 2004, pp 81-98.
- [54] Bau, Y., Wierzbicki, T., “A Comparative Study on Various Ductile Crack Formation Criteria”, *Journal of Engineering Materials and Technology*, Vol. 126, 2004, pp 314-324.
- [55] Bau, Y., “Dependence of Ductile Crack Formation in Tensile Tests on Stress Triaxiality, Stress and Strain Ratios”, *Engineering Fracture Mechanics*, Vol. 72, 2005, pp 505-522.
- [56] Bonora, N., Gentile, D., Pirondi, A., Newaz, G., “Ductile Damage Evolution under Triaxial State of Stress: Theory and Experiments”, *International Journal of Plasticity*, Vol. 21, 2005, pp 981-1007.
- [57] Mohr, D., Henn, S., “Calibration of Stress-Triaxiality Dependent Crack Formation Criteria: A New Hybrid Experimental-Numerical Method”, *Experimental Mechanics*, Vol. 47, 2007, pp 805-820.
- [58] Barsoum, I., Faleskog, J., “Rupture Mechanisms in Combined Tension and Shear – Experiments”, *International Journal of Solids and Structures*, Vol. 44, 2007, pp 1768-1786.
- [59] Xue, L., “Damage Accumulation and Fracture Initiation in Uncracked Ductile Solids Subject to Triaxial Loading”, *International Journal of Solids and Structures*, Vol. 44, 2007, pp 5163-5181.
- [60] Carney, K.S., DuBois, P.A., Buyuk, M., Kan, S., “Generalized, Three-Dimensional Definition, Description, and Derived Limits of the Triaxial Failure of Metals”, *Journal of Aerospace Engineering*, Vol. 22, 2009.
- [61] Lee, Y-W, Woertz, J.C., Wierzbicki, T., “Fracture Prediction of Thin Plates under Hemi-Spherical Punch with Calibration and Experimental Verification”, *International Journal of Mechanical Sciences*, Vol. 46, 2004, pp.751-781.
- [62] Grytten, F., Borvik, T., Hopperstad, O.S., Lanseth, M., “Quasi-Static Perforation of Thin Aluminum Plates”, *International Journal of Impact Engineering*, Vol. 36, 2009, pp486-497.

- [63] Walters, C.L., “Dynamic Bulging Technique for Testing Fracture in Intermediate Strain Rates”, *Proceedings of the 2009 SEM Annual Conference and Exposition on Experimental and Applied Mechanics*, Albuquerque, NM, June, 2009.
- [64] Zurek, A.K., “The Study of Adiabatic Shear Band Instability in a Pearlitic 4340 Steel Using a Dynamic Punch Test”, *Metallurgical and Materials Transactions A*, Vol. 25A, 1994, pp.2483-2489.
- [65] Roessig, K.M., Mason, J.J., “Adiabatic Shear Localization in the Dynamic Punch Test, Part I: Experimental Investigation”, *International Journal of Plasticity*, Vol. 15, 1999, pp.241-262.
- [66] Dabboussi, W., Nemes, J.A., “Modeling of Ductile Fracture Using the Dynamic Punch Test”, *International Journal of Mechanical Sciences*, Vol. 47, 2005, pp.1282-1299.
- [67] Roessig, K.M., Mason, J.J., “Adiabatic Shear Localization in the Dynamic Punch Test, Part II: Numerical Simulations”, *International Journal of Plasticity*, Vol. 15, 1999, pp.241-262.
- [68] Meyers, M.A., Andrade, U.R., Chokshi, A.H., “The Effect of Grain Size on the High-Strain, High-Strain-Rate Behavior of Copper”, *Metallurgical and Materials Transactions A*, Vol. 26 A, 1995, pp.2881-2893.
- [69] Staab, G. H., Gilat, A., “A Direct-Tension Split Hopkinson Bar for High Strain-Rate Testing”, *Experimental Mechanics*, Vol. 31, 1991, pp 232-235.
- [70] Gray, G.T., “Classic Split-Hopkinson Pressure Bar Testing”, *Mechanical Testing*, Vol. 8, *ASM Handbook*, ASM International, 2000.
- [71] Gilat, A. “Torsional Kolsky Bar Testing”, *Mechanical Testing*, Vol. 8, *ASM Handbook*, ASM International, 2000.
- [72] Nicholas, T., “Tensile Testing of Materials at High Rates of Strain”, *Experimental Mechanics*, Vol. 21, 1981, pp177-185.
- [73] Sutton, M.A., McNeil, S.R., Schreier, H.W., “Digital Image Correlation: Principles, Developments and Hands-on Experiment” Notes from a short course presented at the 2008 Society for Experimental Mechanics Conference, Orlando, FL.
- [74] Malvern, L.E., *Introduction to the Mechanics of a Continuous Medium*, Prentice-Hall, Inc., Englewood Cliffs, New Jersey, 1969.
- [75] Semiatin, S.L., Jonas, J.J., *Formability and Workability of Metals: Plastic Instability and Flow Localization*, American Society for Metals, Metals Park, OH, 1984.
- [76] Lesuer, D. R.; Kay, G. J.; LeBlanc, M. M., “Modeling Large-Strain, High Rate Deformation in Metals”, Lawrence Livermore National Lab., Livermore, CA., Report: UCRL-JC-134118, July 20, 2001.
- [77] Kahn, A.S., Huang, S., *Continuum Theory of Plasticity*, John Wiley and Sons, 1995, p 6.
- [78] MATLAB Help Manual, version R2006b.